

Biological and Medical Physics, Biomedical Engineering

Larry A. DeWerd
Michael Kissick *Editors*

The Phantoms of Medical and Health Physics

Devices for Research and Development

 Springer

Biological and Medical Physics, Biomedical Engineering

Series Editor

Elias Greenbaum, Oak Ridge, USA

Editorial Board

Masuo Aizawa, Yokohama, Japan
Olaf S. Andersen, New York, USA
Robert H. Austin, Princeton, USA
James Barber, London, England
Howard C. Berg, Cambridge, USA
Victor Bloomfield, St. Paul, USA
Robert Callender, Bronx, USA
Britton Chance, Philadelphia, USA
Steven Chu, Berkeley, USA
Louis J. DeFelice, Nashville, USA
Johann Deisenhofer, Dallas, USA
George Feher, San Diego, La Jolla, USA
Hans Frauenfelder, Los Alamos, USA
Ivar Giaever, Troy, USA
Sol M. Gruner, Ithaca, USA
Judith Herzfeld, Waltham, USA
Mark S. Humayun, Los Angeles, USA
Pierre Joliot, Paris, France
Lajos Keszthelyi, Szeged, Hungary
Robert S. Knox, Rochester, USA
Aaron Lewis, Jerusalem, Israel
Stuart M. Lindsay, Tempe, USA
David Mauzerall, New York, USA
Eugenie V. Mielczarek, Fairfax, USA
Markolf Niemz, Mannheim, Germany
V. Adrian Parsegian, Bethesda, USA
Linda S. Powers, Tucson, USA
Earl W. Prohofsky, West Lafayette, USA
Andrew Rubin, Moscow, Russia
Michael Seibert, Golden, USA
David Thomas, Minneapolis, USA

For further volumes:

<http://www.springer.com/series/3740>

The fields of biological and medical physics and biomedical engineering are broad, multidisciplinary and dynamic. They lie at the crossroads of frontier research in physics, biology, chemistry, and medicine. The Biological and Medical Physics, Biomedical Engineering Series is intended to be comprehensive, covering a broad range of topics important to the study of the physical, chemical and biological sciences. Its goal is to provide scientists and engineers with textbooks, monographs, and reference works to address the growing need for information.

Books in the series emphasize established and emergent areas of science including molecular, membrane, and mathematical biophysics; photosynthetic energy harvesting and conversion; information processing; physical principles of genetics; sensory communications; automata networks, neural networks, and cellular automata. Equally important will be coverage of applied aspects of biological and medical physics and biomedical engineering such as molecular electronic components and devices, biosensors, medicine, imaging, physical principles of renewable energy production, advanced prostheses, and environmental control and engineering.

Larry A. DeWerd · Michael Kissick
Editors

The Phantoms of Medical and Health Physics

Devices for Research and Development

 Springer

Editors

Larry A. DeWerd
Michael Kissick
Wisconsin Institutes for Medical Research
University of Wisconsin–Madison
Madison
USA

ISSN 1618-7210 ISSN 2197-5647 (electronic)
ISBN 978-1-4614-8303-8 ISBN 978-1-4614-8304-5 (eBook)
DOI 10.1007/978-1-4614-8304-5
Springer New York Heidelberg Dordrecht London

Library of Congress Control Number: 2013953254

© Springer Science+Business Media New York 2014

This work is subject to copyright. All rights are reserved by the Publisher, whether the whole or part of the material is concerned, specifically the rights of translation, reprinting, reuse of illustrations, recitation, broadcasting, reproduction on microfilms or in any other physical way, and transmission or information storage and retrieval, electronic adaptation, computer software, or by similar or dissimilar methodology now known or hereafter developed. Exempted from this legal reservation are brief excerpts in connection with reviews or scholarly analysis or material supplied specifically for the purpose of being entered and executed on a computer system, for exclusive use by the purchaser of the work. Duplication of this publication or parts thereof is permitted only under the provisions of the Copyright Law of the Publisher's location, in its current version, and permission for use must always be obtained from Springer. Permissions for use may be obtained through RightsLink at the Copyright Clearance Center. Violations are liable to prosecution under the respective Copyright Law. The use of general descriptive names, registered names, trademarks, service marks, etc. in this publication does not imply, even in the absence of a specific statement, that such names are exempt from the relevant protective laws and regulations and therefore free for general use.

While the advice and information in this book are believed to be true and accurate at the date of publication, neither the authors nor the editors nor the publisher can accept any legal responsibility for any errors or omissions that may be made. The publisher makes no warranty, express or implied, with respect to the material contained herein.

Printed on acid-free paper

Springer is part of Springer Science+Business Media (www.springer.com)

Contents

1	Introduction to Phantoms of Medical and Health Physics	1
1.1	Introduction	1
1.2	History	2
1.3	Phantom Materials	3
1.4	Dosimetry Phantoms	4
1.4.1	Phantom Construction	5
1.4.2	Dosimeters	6
1.4.3	Computational Phantoms	7
1.5	Imaging Phantoms	8
1.6	Scope of the Text	9
1.6.1	Radiation Therapy Phantoms	9
1.6.2	X-ray Imaging Phantoms	10
1.6.3	Non-ionizing Radiation Phantoms	10
1.6.4	Nuclear Medicine Phantoms	11
1.6.5	Health Physics and Computational Phantoms	11
1.7	Conclusion	12
	References	12

Part I Phantoms of Radiation Therapy

2	Radiation Therapy Dosimetry Phantoms	17
2.1	Introduction	17
2.1.1	Need for Therapeutic Dosimetry Phantoms	18
2.1.2	Overall Design Goals	18
2.1.3	Literature Review	18
2.2	Common Concepts for Dosimetry Phantoms	19
2.2.1	Classification	19
2.2.2	Phantom Geometry	20
2.2.3	Phantom Composition	20
2.2.4	Phantom Coordinate Systems	22
2.2.5	Dose Measurement System Components	22
2.2.6	Phantom Measurements	23

2.3	Water Phantoms	24
2.3.1	Construction of Water Phantoms	24
2.3.2	Characteristics of Water Phantoms	25
2.3.3	Use of Water Phantoms.	25
2.3.4	Examples of Water Phantoms	26
2.4	Non-Water Phantoms	27
2.4.1	Construction of Non-Water Phantoms	27
2.4.2	Characteristics of Non-Water Phantoms	27
2.4.3	Examples of Non-Water Phantoms	28
2.4.4	Use of Non-Water Phantoms	29
2.5	Integrated Device Phantoms.	30
2.5.1	Construction of Integrated Phantoms.	30
2.5.2	Characteristics of Integrated Phantoms	31
2.5.3	Examples of Integrated Phantoms.	32
2.5.4	Use of Integrated Phantoms.	32
2.6	Therapeutic Clinical Uses	32
2.6.1	Installation and Acceptance Testing	33
2.6.2	Calibration and Commissioning	34
2.6.3	Periodic Performance Monitoring.	34
2.6.4	Planned Patient Dose Validating.	34
2.7	Future Directions	35
2.7.1	Automated Data Collection, Analysis, and Management	35
2.7.2	Materials that More Closely Mimic the Behavior of Tissue	35
2.7.3	Variable Density Distribution (Deformable) Phantoms.	36
2.7.4	High-Resolution 3D Data Acquisition in Parallel	36
2.7.5	In vivo Dose Measurement During Treatment Delivery.	36
	References	37

3 Anthropomorphic Phantoms for Radiation Oncology

	Medical Physics	39
3.1	Introduction	39
3.2	Anthropomorphic Body Phantoms	40
3.2.1	ART Phantom	41
3.2.2	RANDO [®] Phantom.	42
3.2.3	ATOM [®] Dosimetry Phantom.	43
3.2.4	Custom Body Phantoms	44
3.3	Anthropomorphic Body-Part Phantoms	45
3.3.1	Commercially Available Anthropomorphic Body-Part Phantoms	46

- 3.3.2 Anthropomorphic Body-Part Phantoms Developed by a QA Service Organization or Institution for Their Own QA Purposes 47
- 3.4 Summary 49
- References 50
- 4 Motion Phantoms for Radiotherapy 53**
 - 4.1 Introduction 53
 - 4.2 Motion in Radiation Therapy 54
 - 4.2.1 Prostate Motion 55
 - 4.2.2 Respiratory Motion 56
 - 4.2.3 Other Treatment Sites Affected by Motion 58
 - 4.3 Quality Assurance Using Motion Phantoms 59
 - 4.3.1 Measuring Patient Motion 59
 - 4.3.2 Accounting for Motion Amplitude 60
 - 4.3.3 Measuring the Impact of Motion Frequency. 60
 - 4.3.4 Testing Motion Management Techniques 61
 - 4.4 Motion Phantom Designs. 61
 - 4.4.1 Overview of Motion Phantom Requirements 61
 - 4.4.2 Commercial Motion Phantoms 62
 - 4.4.3 Custom Motion Phantoms 65
 - 4.4.4 Motion Phantoms of the Future 68
 - 4.5 Dosimetry with Motion Phantoms. 69
 - References 70
- 5 Phantoms in Brachytherapy 77**
 - 5.1 Introduction 77
 - 5.2 Brachytherapy Dosimetry 78
 - 5.2.1 Experimental Measurements 78
 - 5.2.2 Radiation Transport Simulations. 79
 - 5.3 Therapy Simulation and Imaging Phantoms 81
 - 5.3.1 Surgical Simulation 81
 - 5.3.2 Brachytherapy Imaging 82
 - 5.3.3 Contouring Phantoms 84
 - 5.3.4 Equipment Compatibility. 84
 - 5.4 Future of Brachytherapy Phantoms 84
 - References 85

Part II Imaging Phantoms

- 6 Imaging Phantoms: Conventional X-ray Imaging Applications . . . 91**
 - 6.1 Anthropomorphic Phantom for X-ray Imaging 92
 - 6.1.1 Head/Neck Phantom 92
 - 6.1.2 Torso Phantoms 97

6.1.3	Whole Body Phantom	100
6.2	Phantoms for Acceptance and QC Tests	101
6.2.1	Radiographic Systems	102
6.2.2	Fluoroscopic Systems	111
6.3	Vendor-Specific QA Tools	116
6.3.1	Agfa Auto QC Tools	116
6.3.2	Carestream DirectView Total Quality Tool for DR/CR System	117
6.3.3	Fuji FCR 1 Shot Phantom	117
6.3.4	Fuji FCR 1 Shot Phantom Plus	118
6.3.5	GE Quality Assurance Process	119
6.4	Future Development on Imaging Phantoms	119
6.5	Web Resources	121
	References	121
7	Computer Tomography Phantom Applications	123
7.1	Historical Perspective	123
7.2	Acceptance and Quality Control Testing	124
7.2.1	Phantoms for Accessing Dosimetry	124
7.2.2	Phantoms for Accessing Image Quality	127
7.3	Use of Phantoms in the Accreditation Process	129
7.4	Anthropomorphic Phantoms for CT Applications	130
7.5	Phantoms for Investigation of Specific Imaging and Dosimetry Issues	134
7.6	Perspectives on Phantom Developments for Image Quality and Dosimetry in CT	135
	References	137
8	Mammography Phantoms	143
8.1	Introduction	143
8.2	Phantoms for Imaging	144
8.2.1	Phantom for Quality Control and Accreditation Programs	144
8.2.2	Contrast–Detail Phantom	148
8.3	Phantoms for Dosimetry	150
8.4	Anthropomorphic Phantoms for Mammographic Imaging	151
8.5	Standard Phantom Use in the Future	153
	References	153
9	Phantoms for Ultrasound Experimentation and Quality Control	159
9.1	Background	159
9.2	Physical Parameters Required for Ultrasound Phantoms	161
9.2.1	Sound Speed (Density and Acoustic Impedance)	162

9.3	Attenuation	165
9.4	Scattering	166
9.5	Mechanical Properties	167
9.6	Multi-Modality Phantoms Based on TM Gels	167
9.7	Applications of Phantoms in Ultrasound	168
9.8	Image Quality Control.	170
9.9	Doppler Phantoms	172
9.9.1	Current/Future Developments.	173
9.10	Summary	174
	References	175
10	Phantoms for Magnetic Resonance Imaging	181
10.1	Introduction	181
10.2	General MRI Phantom Construction	182
10.3	American College of Radiology Accreditation Phantom	183
10.4	Alzheimer’s Disease Neuroimaging Initiative Phantom	187
10.5	National Institute of Standards and Technology Phantom	188
10.6	Magnetic Field Homogeneity Phantom	189
10.7	Proton Relaxation Phantoms	190
10.8	Diffusion Phantoms	192
10.9	Temperature Considerations.	194
	References	196
11	Nuclear Medicine and PET Phantoms	201
11.1	Introduction	201
11.2	Mathematical Phantoms.	203
11.2.1	Internal Radiation Dosimetry	203
11.2.2	Image Reconstruction and Processing	205
11.3	Physical Phantoms	207
11.3.1	Calibrations	208
11.3.2	Thyroid Uptake Scans.	208
11.3.3	Standardized Uptake Value Calibration.	208
11.4	Quality Assurance and Acceptance Testing	209
11.4.1	Gamma Camera QC	209
11.4.2	SPECT QC	212
11.4.3	PET Phantoms	213
11.5	Anthropomorphic Physical Phantoms	216
11.6	Preclinical Imaging Phantoms	218
11.7	Other Approaches to Physical Phantoms	219
11.8	Summary.	221
	References	221

Part III Computational Phantoms

12 Computational Phantoms for Organ Dose Calculations in Radiation Protection and Imaging.	225
12.1 Introduction	225
12.2 Computational Geometries Used for Phantoms.	227
12.3 The Evolution of Computational Phantoms	229
12.3.1 First-Generation Stylized Phantoms (Prior to the 1990s).	229
12.3.2 Evolution of Stylized Phantoms	231
12.3.3 Second-Generation Voxel Phantoms (from late 1980 to Early 2000s).	234
12.3.4 BREP Phantoms from 2000s to Present.	241
12.4 Applications of Computational Phantoms at RPI	245
12.5 Monte Carlo Methods and Computer Codes.	245
12.6 Non-ionizing Radiation Applications.	246
12.7 Discussion and Conclusion	247
References	249
13 Applications of Computational Phantoms	263
13.1 Introduction	263
13.2 Computational Phantoms in Medical Physics	265
13.2.1 Applications to Radiation Therapy	265
13.2.2 The Applications to CT Imaging	270
13.2.3 The Applications to Nuclear Medicine	271
13.3 Computational Phantoms in Health Physics	273
13.3.1 Applications to Regulatory Procedures	274
13.3.2 Applications to Environmental Exposures	276
13.3.3 Applications to Nuclear Power Plant Exposures	277
13.4 Discussion	278
References	280
Index	285

Contributors

Bryan Bednarz Department of Medical Physics, University of Wisconsin, Madison, WI 53705, USA, e-mail: bbednarz2@wisc.edu

Evan J. Boote Spectrum Health Hospitals, Grand Rapids, MI, USA, e-mail: Evan.Boote@spectrumhealth.org

Paulo R. Costa Department of Nuclear Physics, University of São Paulo, Rua do Matão, Travessa R, 187, São Paulo, SP 05508-090, Brazil, e-mail: pcosta@if.usp.br

Larry A. DeWerd Department of Medical Physics, University of Wisconsin, Madison, WI 53705, USA, e-mail: ladewerd@wisc.edu

David S. Followill Radiological Physics Center, UT M. D. Anderson Cancer Center, 1515 Holcombe Boulevard, Unit 607, Houston, TX, USA, e-mail: dfollowi@mdanderson.org

Sean P. Frigo Department of Medical Physics, Wisconsin Institutes for Medical Research, 1111 Highland Avenue, Room 1005, Madison, WI 53705-2275, USA, e-mail: frigo@wisc.edu

X. George Xu Nuclear Engineering Program, Rensselaer Polytechnic Institute, Troy, NY, USA, e-mail: xug2@rpi.edu

Michael Kissick Department of Medical Physics, University of Wisconsin, Madison, WI 53705, USA, e-mail: mwkissick@wisc.edu

Michael Lawless Department of Medical Physics, University of Wisconsin, Madison, WI 53705, USA

Mark Madsen Department of Radiology, University of Iowa, Iowa City, IA, USA, e-mail: mark-madsen@uiowa.edu

Travis McCaw Department of Medical Physics, University of Wisconsin, Madison, WI 53705, USA

Kwan-Hoong Ng Department of Biomedical Imaging, University of Malaya Research Imaging Center, University of Malaya, Kuala Lumpur, Malaysia, e-mail: ngkh@ummc.edu.my

Mark J. Rivard Department of Radiation Oncology, Tufts Medical Center, 800 Washington Street, Boston, MA 02111, USA, e-mail: mrivard@tuftsmedicalcenter.org

Reed Selwyn Department of Radiology, Uniformed Services University of the Health Sciences, Bethesda, MD 20814, USA; Department of Medical Physics, University of Wisconsin, Madison, WI 53705, USA, e-mail: reed.selwyn@usuhs.edu

John J. Sunderland Department of Radiology, University of Iowa, Iowa City, IA, USA

Alessandra Tomal Institute of Physics, Federal University of Goiás, Campus Samambaia, Caixa Postal 131, Goiânia 74001-970, Brazil, e-mail: alessandra_tomal@yahoo.com.br

Yun Yang Department of Radiation Oncology, Duke University Medical Center, 3295, Durham, NC 27710, USA

Chai-Hong Yeong Department of Biomedical Imaging, University of Malaya Research Imaging Center, University of Malaya, Kuala Lumpur, Malaysia

Chapter 1

Introduction to Phantoms of Medical and Health Physics

Larry A. DeWerd and Michael Lawless

1.1 Introduction

Phantoms, devices that represent the human body, have been used in medical physics and health physics since the beginning. Soon after the discovery of X-rays, news of the medical benefits of radiation quickly spread. The first X-ray image of a human was taken of Prof. Wilhelm Roentgen's wife's hand in 1896 [1]. However, the harmful effects of high radiation doses became apparent as erythema and cell squamation were common side effects associated with the early use of medical radiation. People were reluctant to volunteer to receive radiation for experimental reasons. Consequently, physicists developed phantoms to simulate patients in order to make dosimetric measurements and to test the limitations of their systems.

The design and composition of a phantom are determined entirely by the purpose the phantom is to serve. A phantom that has been developed to evaluate the dose delivered to a patient during radiation therapy treatments will be drastically different from a phantom designed to test the imaging limits of a kilovoltage radiographic system. The purpose of the phantom will dictate the physical design of the phantom, such as the size, shape, composition, and other details of the phantom such as composition. It will also determine whether or not the phantom is to contain dosimeters (for example, TLDs or ion chambers) and what type of other elements would best suit the given situation.

The materials within a phantom are often intended to simulate human tissue. However, the properties of these materials vary with the energy of the radiation incident upon them. Thus, while something may be tissue equivalent over a given energy range, it may not be tissue equivalent over all energies. As a result, a phantom designed for use in megavoltage X-ray beams will often be made from different materials than a phantom designed for kilovoltage beams.

L. A. DeWerd (✉) · M. Lawless

Department of Medical Physics, University of Wisconsin, Madison, WI 53705, USA
e-mail: ladewerd@wisc.edu

Phantoms have become popular and are used in all aspects of medical physics applications. Simple, water-based phantoms exist to measure the output of megavoltage therapy beams. More complicated, anthropomorphic phantoms are used to test the ability of the megavoltage beams to accurately deliver a treatment. Imaging phantoms have been designed to test the limitations of X-ray imaging systems. These typically test the achievable resolution of the X-ray beam and the detector system, as well as the amount of contrast needed to distinguish objects from one another. Similar phantoms exist to test the same properties of ultrasound (US), computed tomography (CT), magnetic resonance imaging (MRI), and positron emission tomography (PET) systems. Computational phantoms have also been developed for use in computer simulations. Phantoms can also be designed to test the effects of positional errors and organ motion for both imaging and therapy applications. The various types of phantoms will be discussed in detail in the later chapters of this text.

1.2 History

Once the use of ionizing radiation became popular, the need for phantoms soon became apparent. Early in the twentieth century, it was recognized that in order to quantify the dose delivered to a tissue of interest, the measurement should be made on the tissue itself [2]. When the harmful effects of radiation were realized, the need for tissue substitutes became clear, and the concept of phantoms was born. The earliest phantoms were comprised of water or wax. The geometry of the phantoms remained fairly simple with water tanks and blocks of wax for measurements of radioactive sources or X-ray beams.

While water was (and still is) a very good approximation of the human tissues, wax presented a number of problems. Firstly, the formulations of wax varied significantly depending on the type of wax used. Thus, there was a lack of consistency among the early measurements. It was also soon discovered that wax deviated from tissue equivalency at the low energies. To alleviate this, materials with high atomic numbers were added to the wax mixtures. While this improved the radiological properties of the waxes, there was still a fair degree of variability that remained.

Wood was proposed as a potential tissue substitute and was fairly popular during the late 1930s, with use continuing in some capacities to the 1970s. There were similar problems with wood as there was with wax, as a degree of variability also exists among different samples of wood.

Around halfway through the twentieth century, an interest in developing geometrically realistic anthropomorphic phantoms occurred. A number of different anthropomorphic phantoms were developed which produced a variety of whole body phantoms as well as phantoms that covered smaller segments of the body. However, the inconsistency of tissue equivalent materials still presented a large obstacle at the time. In the 1960s, two advanced anthropomorphic phantoms were

introduced. Stacey et al. [3] and Alderson et al. [4] both developed phantoms, known as the TemexTM phantom and the Rando[®] phantom, respectively, that contained real human skeletons embedded in a tissue substitute. The phantoms were sliced axially, and the Rando[®] phantom allowed for the insertion of thermoluminescent dosimeters (TLDs) into cavities to measure the dose distribution.

While the phantoms discussed up to this point have been designed for dosimetry of radiotherapy treatments, a number of phantoms were developed for imaging systems. In the 1970s, a number of mammography phantoms were developed along with phantoms for CT, radiography and image intensifier systems. However, some imaging phantoms were developed as early as the late 1940s. Improvements and variations of these early imaging phantoms have been developed, but their main purpose has remained to test the various aspects of image quality of the system in question. Phantoms were also developed for non-ionizing applications such as US and MRI. Like the phantoms designed for testing systems that make use of ionizing radiation, the main parameters of concern are the related to the quality of the image produced by the system.

Phantoms have become more complex and more reliable over time as the materials used to manufacture them have become more reliable and reproducible. New tissue substitutes like epoxy resins and polyurethanes have allowed for phantoms of higher quality and greater reproducibility. This progression has also led to the development of phantoms that accurately mimic tissues over a wider range of energies.

With the rise in popularity of computer simulations in the field of medical physics, there came a need to represent the human body in these simulations. The detail and complexity of the computational phantoms have increased with the increased computing capacity of the available technology. Advanced imaging modalities such as CT and MRI have aided in the creation of these complex computational phantoms. The development of these phantoms have been accompanied by the rise of complex radiation transport codes, and together they have led to improved radiation dosimetry and measurement. Doses can be calculated to a variety of different tissues using these mathematical phantoms, such as the Virtual Man [5].

1.3 Phantom Materials

The selection of the appropriate materials is critical to the design and function of any type of phantom. In most cases, a phantom is meant to simulate some form of tissue, such as muscle, bone, or lung. Another very common simulated material is water, as the use of liquid water can prove to be difficult and cumbersome in certain situations. The simulated tissues all have different properties, both physically and radiologically, and the goal of the phantom materials is to represent these physical and radiological properties as accurately as possible.

There are a number of properties that can be used as a measure of the tissue equivalence of a phantom. The physical density (ρ) and effective atomic number (Z_{eff}) can both be used as relatively crude assessments of a material's tissue equivalence. While these parameters provide insight into the physical properties of the material in question, they do little to describe the material's radiological properties. The electron density (ρ_e) of a material is a more detailed parameter that provides more insight into how a material will behave in a radiation field. The most widely used and commonly accepted parameter to gauge tissue equivalence is the mass energy-absorption coefficient (μ_{en}/ρ) as it gives an indication as to how much energy is deposited locally in the tissue of interest [6, 7]. Ideally, a material will accurately represent as many of the aforementioned properties of the tissue that is being simulated. However, this can be very difficult to achieve, and one should primarily aim to simulate the radiological properties of the tissue of interest.

In most cases, there are materials available that simulate tissues very accurately, yet there are a number of caveats that should be kept in mind when phantoms are being used. The radiological properties of a material are often highly dependent on the energy of the radiation incident upon it. Thus, a material may accurately simulate a tissue in a given energy range, but could differ significantly in other energy ranges. It is common to see phantom materials separated by the energy range in which they should be used, such as the kilovoltage (diagnostic) energies or the megavoltage (treatment) energies. There are also materials available that have been developed to simulate tissues in both the diagnostic and the treatment energy ranges. However, even within a given energy range, the spectrum of the beam being used is often very wide, causing error to always be present to some degree.

It should be noted that the previous discussion is in reference to phantoms that are to be used in fields of ionizing radiation. That mass energy-absorption coefficient of a material would not necessarily be an accurate measurement of tissue equivalence for MRI or US purposes as these two imaging modalities operate on different physical principles.

1.4 Dosimetry Phantoms

Dosimetry phantoms are used when there is a need to simulate the conditions of a procedure in order to measure dose at certain points of interest. It is clearly impractical and dangerous to place an actual human in the beam to take measurements, and perhaps even more impractical to place dosimeters inside a human to make the measurements. This was the impetus for the first dosimetry phantoms, as tanks of water or slabs of tissue equivalent materials were designed to hold dosimeters and allow for measurements “in tissue” without any unnecessary exposure to the people involved.

1.4.1 Phantom Construction

As discussed earlier, the first phantoms were fairly simple, consisting of slabs of wax or tanks of water. These phantoms, while seemingly unsophisticated in design, continue to be used in many aspects of dosimetry. While wax slabs have fallen out of use, slabs of other materials (e.g., epoxy-based materials), such as Virtual WaterTM and Solid Water[®], have remained popular. Their advantage lies in their simplicity and ease of reproducibility. Their position in a beam can be easily replicated, so measurements can be made under the same conditions at different institutions and at different times. Water tanks also allow for an essentially infinite number of locations at which to place a dosimeter. The tanks allow for scanning of the beam with ionization chambers. The advanced positioning systems have been developed in order to allow for precise movement of the dosimeters within the water tank. The slab phantoms, while obviously more rigid in their design, can also be modified to hold dosimeters at number of different locations. Other rather simplistic geometries also exist for various purposes. For example, a simple cylindrical phantom is commonly used for the measurement of the computed tomography dose index (CTDI) [8]. Similarly, a uniform spherical phantom is typically used for Gamma Knife[®] dosimetry [9] because these shapes match the device's natural symmetry.

As discussed in the previous section, as time progressed, the need for phantoms that more accurately simulate the human body became increasingly evident. This led to the development of anthropomorphic phantoms. These phantoms were designed to physically resemble a body part of interest. These phantoms provide a more accurate representation of a human body which allows for dose measurements that correlate much better with the dose distribution within the human body. Another aspect of simulating the body is simulating aspects of how it moves, and phantoms have been designed to simulate these motions.

Regardless of the physical shape of the phantom, there is often an interest in introducing inhomogeneities into the phantom. It intuitively follows that more complex anthropomorphic phantoms employ more complex material distributions. However, this is not always the case. The aforementioned Rando[®] phantom has a detailed physical shape, but the only materials simulated in the phantom are bone, lung, and soft tissue. Similarly, some phantoms with simple exterior geometries can contain detailed internal structures [10]. One could even use various thicknesses of different slab phantoms to create a slab phantom with planar inhomogeneities. Phantoms that are anthropomorphic in their outward physical shape do not necessarily contain anatomically accurate internal structures, such as the RSVP Phantom[®] Head made by The Phantom Laboratory or the Radiological Physics Center's (RPC) head and neck intensity-modulated radiation therapy (IMRT) phantom. Both of these phantoms have specific purposes and have been designed to optimally and efficiently make the measurements for which they are designed.

Phantom design and construction are dictated by the phantom's purpose. Reference phantoms tend to be simpler in design for ease of reproducibility.

Phantoms designed for treatment verification purposes tend to more accurately simulate a human patient, though this is certainly not always the case. In certain cases, a detailed internal anatomy would be superfluous, while in others detailed internal structures are necessary to accurately simulate the procedure of concern.

1.4.2 Dosimeters

Any dosimetry phantom must inherently contain at least one dosimeter in order to measure the dose within the phantom. There are a number of possible dosimeters that can be used in this instance and each possesses a number of advantages and disadvantages.

Ionization chambers are commonly used for a number of reasons, including stability, negligible energy response, and their calibration to primary standards [11]. While ionization chambers are capable of providing dose at point, that dose value is a result of volume averaging. The use of a chamber should be avoided in areas where there is a steep dose gradient to avoid averaging over a large range of doses. Smaller chambers can be used to minimize this effect, but this decreases the output signal of the chamber and can also introduce a number of other problems [12]. The presence of the chamber's air cavity in the phantom can alter the field compared to when the chamber is not present, which can affect the dose measurements at locations near the chamber. Also, irradiation of the chamber stem and cable can cause leakage current which can affect readings. Ultimately, the reliability and flat energy response of ion chambers makes them well suited for dosimetry measurements in phantom. One simply must be aware of the shortcomings of ion chambers and account for them appropriately.

TLDs are also used frequently in phantoms. These solid state, integrating detectors vary in size and shape but share certain characteristics. They are generally fairly small and can be made as small as $(1 \times 1 \times 1)$ mm³ cubes. This small size allows for high spatial resolution and for measurement of fairly steep dose gradients when used properly. Many TLD formulations are also approximately tissue equivalent, which eliminates the field perturbation concerns present with ion chambers as discussed above. Most TLDs remain fairly linear up to about 1 Gy [13]. TLDs can also exhibit a rather severe energy response, particularly at lower energies [14, 15]. The use of TLDs can be tedious as their use involves a reliable annealing process and careful handling. However, if handled properly, precision less than 5 % can be achieved [16]. TLDs are well suited to phantom dosimetry as they are small, reliable, and tissue equivalent, integrating dosimeters. One must be aware of the both the dose and energy response of the TLD formulation being used, so as to avoid making errors in the dosimetric measurement.

Film dosimeters are commonly used in order to obtain a dose distribution with high spatial resolution. The two types of film are used for dosimetry purposes are radiographic film and radiochromic film. Radiographic film has been used extensively for dosimetric purposes, and the American Association of Physicists in

Medicine (AAPM) Task Group 69 [17] has published a detailed report on the use of radiographic film. Radiographic film is straightforward to use and can provide excellent measurements of dose distribution due to its extremely high spatial resolution. However, the response of any particular film can vary quite drastically due to variations in the film production process. It has also been observed that fluctuations in processor conditions can have rather severe effects on the optical density of the film. Because most films are composed of silver halide, which has a high atomic number, there is a significant energy response that must be accounted for when using radiographic film for dosimetry purposes. Despite these potential pitfalls, radiographic film can be used reliably as long as the appropriate precautions and corrections are taken into account.

The primary advantages of radiochromic film are that it is approximately tissue equivalent, and it can provide excellent spatial resolution. Additionally, it does not require a processor in order to develop. The report of AAPM Task Group 55 [18] covers radiochromic film dosimetry in detail. In 2012, the AAPM approved Task Group 235 in order to update the report of TG-55 to include a more detailed review of the literature and further investigate radiochromic film dosimetry. Radiochromic film has been shown to have a number of problems, such as an orientation dependence and similar batch non-uniformities to those of radiographic films.

There are a number of other possible dosimeters that can be used in phantoms that are not discussed here. MOSFETs and diodes have been used for dose measurements at a point. There are a number of gels available that can provide three-dimensional dose distributions within a phantom. Each dosimeter has its own advantages and drawbacks. The proper choice of a dosimeter for use in a phantom requires a knowledge of quantity to be measured and an analysis of the advantages and disadvantages of each type of dosimeter being considered. One must always be conscious of the limitations of the dosimeter being used in order to obtain accurate and reliable dosimetric measurements. A thorough analysis of dosimeter choices has been performed by Low et al. [11], and the reader is referred there for further detail.

1.4.3 Computational Phantoms

Computer simulations of radiation treatments and measurements have become increasingly popular as computer technology has become more efficient. In order for these simulations to be relevant and useful, accurate representations of the irradiation conditions are necessary. Furthermore, if one desires to compare two different simulations, it is helpful if the same geometry is used. This has led to the development of computational phantoms. Computational phantoms can be as complex or as simple as the physical sample that they are trying to represent. They can simulate anything from a simple slab phantom to anatomically accurate humans.

In many situations, the calculations performed using the computational phantoms are compared to actual measurements. This can be useful to validate a Monte Carlo transport code, or if the code has already been validated, it can be used to verify a measurement technique or to generate correction factors. Generally, these types of simulations involve relatively simple geometries and are most commonly used in the realm of radiotherapy. The complex and detailed full body phantoms are used frequently in health physics applications. A number of whole body computational phantoms have been developed over the years. Recently, the International Commission of Radiological Protection (ICRP) has designed two reference computational phantoms, one male and one female [19]. The NORMAN phantom was developed from MRI data from a single patient by Dimbylow [20] and Xu et al. [5] developed the VIP-Man computational phantom. There are a number of other computational phantoms that have been developed, and comparisons have been performed to assess their performance relative to one another [21]. These are all typically used to assess organ dose and other quantities of interest in health physics. Computational phantoms are discussed in greater detail in [Chaps. 12](#) and [13](#).

1.5 Imaging Phantoms

Since the 1980s, the amount of man-made radiation exposure per person has nearly doubled [22]. This is due in large part to the increased usage of diagnostic and interventional medical procedures. These systems have become a popular means to effectively and noninvasively diagnose a patient in almost any circumstance. However, this increased exposure has raised many concerns about the risks associated with medical imaging procedures. Ideally, it would be possible to minimize the dose to the patient while maintaining the image quality required to gather the necessary information. While dosimetric phantoms would be used to assess the dose from these procedures, most phantoms used in imaging systems provide an assessment of image quality.

There are a number of factors that determine whether or not an object will be visible in a medical image. From a simple radiograph to a CT scan, the size, shape, and radiation absorption properties of the structure and of the surrounding material affect whether or not that structure will be seen. Ultimately, the quantity of interest is the contrast of the structure, which is dependent upon the aforementioned factors. The spatial resolution of a system is also a quantity that is typically tested when evaluating performance.

Imaging phantoms need to address many of the same issues as dosimetry phantoms. Phantom materials must be chosen appropriately to properly simulate the tissues of interest. In order to generate any sort of useful image, at least two materials are needed. Many phantoms that wish to test the contrast limitations of a system will have a phantom which contains objects of various sizes and contrasts. These phantoms are often of relatively simple geometries and have been used for

multiple imaging modalities. An example of a phantom of this type is the Catphan[®] phantom developed by The Phantom Laboratory for the assessment of performance of CT scanners. It contains objects of varying size and contrast in order to test the contrast resolution of the scanner. It also contains a line pair per cm gauge to test the spatial resolution of the system. There are a number of other tests this phantom is capable of performing. Phantoms such as these can be used not only to test the limitations of the CT equipment, but also the reconstruction algorithm being used [23]. Similar phantoms have been developed to test the limitations of radiography [24], MRI [25], PET [26], and US [27] systems.

In many imaging procedures, there is a desire to have a phantom that presents a more realistic situation. As a result, there are anthropomorphic phantoms that are shaped like human body parts, and they often contain highly detailed internal anatomy. The internal anatomy of these phantoms is often far more comprehensive than in dosimetric phantoms. This is because at the lower photon energies used in imaging procedures, smaller changes in material compositions have larger effects on attenuation properties. Thus, the difference between muscle and water may be relatively small at the megavoltage energies used in external beam therapy, but can be rather noticeable at the kilovoltage energies used in imaging. There are also anthropomorphic phantoms that are used to simulate dynamic procedures such as the injection of a contrast agent. Imaging phantoms have also been developed that contain unrealistic Fourier-based patterns to assess different properties of the imaging system such as the modulation transfer function. The various types and applications of imaging phantoms will be addressed in further detail in [Chaps. 6–10](#).

1.6 Scope of the Text

This text is designed to provide an overview of the phantoms used in the past, present, and future of medical and health physics applications. There is a great deal of variety in both the physical design and the purpose of the phantoms used in the field. A brief overview of the topics to be covered in the text will be provided here, with detailed discussions to follow in later chapters.

1.6.1 Radiation Therapy Phantoms

Phantoms used in radiation therapy are almost always dosimetry phantoms although imaging phantoms are of increasing importance in therapy. The dosimetry phantoms include the water and epoxy-based slab phantoms that are used for reference purposes as well as the anthropomorphic phantoms that more accurately represent the human body. Some phantoms used in radiation therapy have been designed to simulate patient motion that occurs during radiotherapy treatments.

These can be used to assess the effectiveness of techniques designed to limit the effects of patient motion on treatment delivery.

Radiation therapy phantoms are used in brachytherapy applications. Dosimetry phantoms are used in order to characterize properties of brachytherapy seeds. These properties are later used for treatment planning purposes in clinical treatments. Because brachytherapy seeds are often of lower energy, the selection of the phantom material can have significant influence on how dose is distributed through the phantom. Thus, having a material that accurately mimics the material of interest is of critical importance. Deeper discussion of the phantoms used in radiation therapy will be provided in [Chaps. 2–5](#).

1.6.2 X-ray Imaging Phantoms

A variety of phantoms are necessary to properly assess the characteristics of an imaging system. Conventional X-ray imaging, which includes radiography and fluoroscopy, and CT make use of phantoms of various designs and purposes. Anthropomorphic phantoms can be used to simulate patient images, which can be helpful when determining what X-ray tube settings should be used in a given situation or even when training new technologists or radiologists. Both conventional X-ray and CT systems must undergo acceptance testing and regular quality assurance (QA) procedures in order to ensure the systems are performing adequately and will continue to do so in the future. Phantoms have been designed to test all of the parameters necessary for assessing system performance. As these systems make use of ionizing radiation, the dose delivered to the patient during the procedure is of interest and is meant to be kept as low as possible. Dosimetry phantoms have been designed specifically to assess the dosimetric properties of both CT and conventional X-ray systems.

Mammography is a modality of particular concern for a number of reasons. It is a very common procedure as many women receive regular mammograms as a part of breast cancer screening. Also, breast cancer is the most common type of cancer in women [28], which magnifies the importance of a properly function screening system. Like the other X-ray imaging modalities, phantoms have been designed specifically for the assessment of mammography systems. Anthropomorphic phantoms, image quality phantoms, and dosimetry phantoms have all been developed specifically for use in mammography.

1.6.3 Non-ionizing Radiation Phantoms

While they may not make use of ionizing radiation, US and MRI systems must still be evaluated to ensure proper image quality is being maintained. Because these modalities make use of properties other than the radiological properties of the

material, there are different considerations that must be taken into account when designing phantoms for these systems. The US application relies primarily on the speed of sound in a given material to produce its images and MRI relies on the relaxation rates of different tissues. Thus, tissue equivalency for US or MRI is defined quite differently than in imaging that utilizes ionizing radiation. Despite these differences in material properties, the physical design of phantoms and the techniques used to assess image quality and system performance of US and MRI can be quite similar to those of X-ray imaging modalities. Also, both US and MRI make use of anthropomorphic phantoms to simulate a medical procedure or experiment as accurately as possible.

1.6.4 Nuclear Medicine Phantoms

Nuclear medicine involves the injection of radioactive materials into the body for imaging or therapeutic purposes. Common procedures include heart perfusion scans, bone density scans, functional imaging of the brain, and thyroid cancer treatments. Nuclear medicine imaging systems undergo similar testing as that described for the other imaging modalities. Phantoms are used to test the system's detection limitations, its spatial resolution, and its uniformity [29]. Anthropomorphic phantoms have also been developed to simulate actual clinical procedures such as liver [30] or brain imaging [31]. Phantoms for nuclear medicine are unique in that they must be able to accommodate the injection of the radioactive material. Thus, phantoms are often designed to have cavities or inserts that hold the injected material during the imaging process. The phantoms used in medical imaging systems will be discussed in great detail in [Chaps. 6–11](#).

1.6.5 Health Physics and Computational Phantoms

The field of health physics investigates the dangers to those other than the patient associated with ionizing radiation. Frequently, risk of cancer induction is assessed as function of radiation dose received. There are also endpoints that are evaluated such as organ toxicities or radiation sicknesses. Assessment of these endpoints can often involve measurements of small doses or over long periods of time. Consequently, health physicists often make use of computer simulations in order to aid in this process. These simulations make use of the computational phantoms described earlier in order to provide expedient and detailed results. The computational phantoms can be used to gain some understanding of the risks associated with occupational exposures, medical imaging procedures, or from out of field dose in radiation therapy treatments. Health physics also makes use of physical phantoms in many applications. The Rando[®] phantom is used frequently to evaluate doses for health physics purposes. The BOMAB phantom [32] has also been developed

for use with whole body counters in an effort to simulate the incorporation of radioactive materials into the body. Chapters 12 and 13 provide more detail on the computational phantoms used for health physics and other applications.

1.7 Conclusion

Ultimately, the purpose of a phantom in medical physics applications is to simulate human tissue in a given procedure or experiment. While the shape and composition of a phantom can vary drastically, they generally fall into one of two categories, dosimetry phantoms and imaging phantoms. Dosimetry phantoms are designed to be able to quantify the amount of radiation received at a given point, whether it be during a therapy or imaging procedure. Imaging phantoms are used to test the limits of an imaging system and to assess the quality of the images being produced by that system.

The purpose of the phantom dictates both its form and its composition. When selecting or designing a phantom, one must carefully consider the materials to be used, the physical shape, and how these will affect what is trying to be measured in the situation of interest. There is an immense variety of phantoms available for any given application and proper selection of a phantom is dependent entirely on the situation in which it is to be used. New phantoms are continually being developed to utilize new technologies and being used in different ways to serve new and exciting purposes in the field of medical physics.

References

1. Trevert, E. (1896). *Something about X Rays for everybody*. Lynn: Bubier Publishing.
2. Kienbock, R. (1906). On the quantimetric method. *Arch Roentgen Ray*, 11, 17.
3. Stacey, A. J., Bevan, A. R. & Dickens, C. W. (1961). A new phantom material employing depolymerised natural rubber. *British Journal of Radiology*, 34, 510–515.
4. Alderson, S. W., Lanzl, L. H., Rollins, M., & Spira, J. (1962). An instrumented phantom system for analog computation of treatment plans. *The American Journal of Roentgenology, Radium Therapy, and Nuclear Medicine*, 87, 185.
5. Xu, X.G., Chao, T.C., & Bozkurt, A. (2000). VIP-man: an image-based whole-body adult male model constructed from color photographs of the visible human project for multi-particle Monte Carlo calculations. *Health Physics*, 78(5), 476–486.
6. Hill, R., Holloway, L., & Baldock, C. (2005). A dosimetric evaluation of water equivalent phantoms for kilovoltage x-ray beams. *Physics in Medicine and Biology*, 50(21), N331–N334.
7. Pantelis, E., Karlis, A. K., Kozicki, M., Papagiannis, P., Sakelliou, L., & Rosiak, J. M. (2004). Polymer gel water equivalence and relative energy response with emphasis on low photon energy dosimetry in brachytherapy. *Physics in Medicine and Biology*, 49(15), 3495–3514.
8. Pernicka, F. (1990). CT dosimetry using a TL technique. *Radiation Protection Dosimetry*, 34(1–4), 271–274.

9. Somigliana, A., Cattaneo, G. M., Fiorino, C., Borelli, S., del Vecchio, A., Zonca, G., et al. (1999). Dosimetry of gamma knife and linac-based radiosurgery using radiochromic and diode detectors. *Physics in Medicine and Biology*, 44(4), 887–897.
10. Han, Y., Shin, E. H., Lim, C., Kang, S. K., Park, S. H., Lah, J. E., et al. (2008). Dosimetry in an IMRT phantom designed for a remote monitoring program. *Medical Physics*, 35(6), 2519–2525.
11. Low, D. A., Moran, J. M., Dempsey, J. F., Dong, L., & Oldham, M. (2011). Dosimetry tools and techniques for IMRT. *Medical Physics*, 38(3), 1313–1338.
12. McEwen, M. R. (2010). Measurement of ionization chamber absorbed dose k factors in megavoltage photon beams. *Medical Physics*, 37(5), 2179–2193.
13. Attix, F. H. (1968). *Introduction to radiological physics and radiation dosimetry*. Weinheim: Wiley.
14. Nunn, A. A., Davis, S. D., Micka, J. A., & DeWerd, L. A. (2008). LiF: Mg, Ti TLD response as a function of photon energy for moderately filtered x-ray spectra in the range of 20–250 kVp relative to Co. *Medical Physics*, 35(5), 1859–1869.
15. Carrillo, R. E., Pearson, D. W., Deluca, P. M., Jr, Mackay, J. F., & Lagally, M. G. (1996). Response of calcium fluoride to 275–2,550 eV photons. *Radiation Measurements*, 26(1), 75–82.
16. DeWerd, L., Bartol, L., & Davis, S. (2009). Thermoluminescence dosimetry. In D. W. O. Rogers & J. E. Cygler (Eds.), *Clinical dosimetry measurements in radiotherapy* (pp. 815–840). Madison: Medical Physics Publishing.
17. Pai, S., Das, I. J., Dempsey, J. F., Lam, K. L., LoSasso, T. J., Olch, A. J., et al. (2007). TG-69: Radiographic film for megavoltage beam dosimetry. *Medical Physics*, 34(6), 2228–2258.
18. Niroomand-Rad, A., Blackwell, C. R., Coursey, B. M., Gall, K. P., Galvin, J. M., McLaughlin, W. L., et al. (1998). Radiochromic film dosimetry: Recommendations of AAPM radiation therapy committee task group 55. *Medical Physics*, 25(11), 2093–2115.
19. ICRP. 2009. Adult reference computational phantoms. ICRP Publication 110. *Annual of ICRP*, 39(2).
20. Dimbylow, P. J. (1999). FDTD calculations of the whole-body averaged SAR in an anatomically realistic voxel model of the human body from 1 MHz to 1 GHz. *Physics in Medicine and Biology*, 42(3), 479–490.
21. Capello, K., Kedzior, S., & Kramer, G. H. (2012). Voxel phantoms: The new ICRP computational phantoms: How do they compare? *Health Physics*, 102(6), 626–630.
22. Schauer, D. A., & Linton, O. W. (2009). NCRP Report No. 160, ionizing radiation exposure of the population of the United States, medical exposure—are we doing less with more, and is there a role for health physicists? *Health Physics*, 97(1), 1–5.
23. Ghetti, C., Ortenzia, O., & Serrelli, G. (2012). CT iterative reconstruction in image space: A phantom study. *Physica Medica*, 28(2), 161–165.
24. Yamaguchi, M., Fujita, H., Bessho, Y., Inoue, T., Asai, Y., & Murase, K. (2011). Investigation of optimal display size for detecting ground-glass opacity on high resolution computed tomography using a new digital contrast-detail phantom. *European Journal of Radiology*, 80(3), 845–850.
25. Ihalainen, T. M., Lönnroth, N. T., Peltonen, J. I., Uusi-Simola, J. K., Timonen, M. H., Kuusela, L. J., et al. (2011). MRI quality assurance using the ACR phantom in a multi-unit imaging center. *Acta Oncologica*, 50(6), 966–972.
26. DiFilippo, F. P., Price, J. P., Kelsch, D. N., & Muzic, R. F., Jr. (2004). Porous phantoms for PET and SPECT performance evaluation and quality assurance. *Medical Physics*, 31(5), 1183–1194.
27. Madsen, E. L., Zagzebski, J. A., Macdonald, M. C., & Frank, G. R. (1991). Ultrasound focal lesion detectability phantoms. *Medical Physics*, 18(6), 1171–1180.
28. Siegel, R., Naishadham, D., & Jemal, A. (2012). Cancer statistics, 2012. *CA: A Cancer Journal for Clinicians*, 62(1), 10–29.

29. Sokole, E. B., Graham, L. S., Todd-Pokropek, A., Wegst, A., Robilotta, C. C., & Krisanachinda, A. (2003). *IAEA quality control atlas for scintillation camera systems*. Vienna: International Atomic Energy Agency.
30. Lima Ferreira, F. C., & Souza, D. D. N. (2011). Liver phantom for quality control and training in nuclear medicine. *Nuclear Instruments and Methods in Physics Research, Section A: Accelerators, Spectrometers, Detectors, and Associated Equipment*, 652(1), 791–793.
31. Li, H. J., & Votaw, J. R. (1998). Optimization of PET activation studies based on the SNR measured in the 3-D Hoffman brain phantom. *IEEE Transactions on Medical Imaging*, 17(4), 596–605.
32. Kramer, G. H., Burns, L., & Noel, L. (1991). The BRMD BOMAB phantom family. *Health Physics*, 61(6), 895.

Part I
Phantoms of Radiation Therapy

Chapter 2

Radiation Therapy Dosimetry Phantoms

Sean P. Frigo

2.1 Introduction

The successful use of high-energy external beam radiation for therapeutic purposes depends critically on the spatial distribution of absolute dose within the patient. The primary reason for this is that the energy deposition itself is three dimensional in nature, where particles not only affect the immediate interaction site, but also deposit some of their energy into the surrounding area. Because this process is not entirely local, it is unavoidable that healthy tissue in the neighborhood of the target tissue will receive dose as well. Thus, healthy tissue dose tolerance often becomes a limiting factor to treatment success. Precise knowledge and control of the dose distribution allow one to approach this intrinsic limit closely and in a controlled manner, thereby maximizing the radiation's therapeutic effect.

The treatment process entails designing a 3D dose distribution through the use of imaging data for the modeling of anatomy and dose deposition. The accuracy of this process needs to be validated through measurement of dose. For many reasons, measurements are taken not directly with the patient, but instead using various representative objects. These act as a surrogate to the patient anatomy and are called a “phantom patient” or simply a phantom. Mosby's Medical Dictionary defines a phantom as “a mass of material similar to human tissue used to investigate the effect of radiation beams on human beings. Phantom materials can range from water to complex chemical mixtures that faithfully mimic the human body as it would interact with radiation” [1].

S. P. Frigo (✉)

Department of Medical Physics, University of Wisconsin–Madison, Wisconsin Institutes for Medical Research, 1111 Highland Avenue, Room 1005, Madison, WI 53705-2275, USA
e-mail: frigo@wisc.edu

2.1.1 Need for Therapeutic Dosimetry Phantoms

There are primarily two uses of therapeutic dosimetry phantoms: (1) characterization and calibration of delivered external radiation beams and (2) validation of numerical dose modeling and design through treatment planning. Ideally, one would like to be able to measure the dose distribution within a patient in real time during beam delivery and adjust the dose as necessary during delivery. Before one gets to this point, the planning and delivery systems need to be designed and validated using inanimate test objects. One advantage to this approach is the objects can receive repeated amounts of dose. Additionally, test objects allow one to create simplified geometries and densities in order to more readily interpret measurements and compare with calculation..

2.1.2 Overall Design Goals

A phantom for therapeutic dose measurement must satisfy a number of basic design goals related to materials first and geometry second. For materials, they must

1. Be similar to tissue such that measurements can be mapped to dose to tissue.
2. Have composition that can be well characterized and readily available.
3. Allow for easy traceability to reference standards.
4. Be robust to radiation damage.
5. Exhibit reproducible and well-understood response with regard to radiation type and energy.

For geometries, they must

1. Accommodate delivered beam field sizes and shapes.
2. Allow the establishment of 3D locations.
3. Be easy to transport, set up, align, and take down in an accurate and efficient manner.

For phantoms placed in routine use, the design must be rugged enough to allow repeated handling and use by technical staff.

2.1.3 Literature Review

Historically, phantoms have been created out of necessity as part of an overall measurement activity. Consequently, most studies in the literature to date focus on the application of phantoms to investigate various topics such as dose algorithm accuracy and absolute dose calibration, instead of dedicated comprehensive reviews.

Reports of phantom use appeared in the early twentieth century by Krönig [2], Quimby [3], and Failla [4]. Materials such as water and beef muscle were explored in these early works. The study by Quimby demonstrated the degree of water equivalency to various types of tissue [3]. A historical overview is presented by White [5].

A number of technical reports cite minimum phantom requirements for calibration such as AAPM TG-51 [6] and IAEA TRS-398 [7], or heterogeneity considerations in AAPM TG-65 [8]. In addition, ICRU Report 44 discusses phantom composition [9]. The use of phantoms is cited in a number of standard books in the field [10–12].

This chapter will focus on the current design and use of phantom test objects and related devices to measure both relative and absolute dose distributions. The goal is to understand basic needs of their use, limitations, and benefit to ensure that each patient receives the intended therapeutic dose. A number of commercial examples are cited in this chapter. Mention of a specific device or vendor does not constitute endorsement; nor is the collection of cited vendors or devices to be considered exhaustive.

2.2 Common Concepts for Dosimetry Phantoms

Dose measurement entails not only an object to respond to the radiation beam (phantom) but also components to detect that response. So, the concepts and characteristics of phantom objects themselves are part of a bigger picture of what constitutes a dose measurement system. We will point out this important aspect of overall integration as necessary.

2.2.1 *Classification*

There are a number of natural categories in which to classify phantoms. One is where the detector is located. The other is how configurable or flexible its use is.

2.2.1.1 Active Versus Passive Phantoms

Dosimetry phantoms can be classified as either active or passive, depending on whether the detector is on the inside or outside of the phantom object. Active phantoms have the detector within the body of the object. Examples include an ion chamber within a water tank, or an activated nucleon or molecule whose emission is analyzed. A passive phantom is one that is placed in the beam's path, and the detector is external to the object. An example of this type is used to calibrate EPID dosimetry systems [13], where entrance and exit X-rays are analyzed to determine

the deposited dose within the object. Another example is the use of proton transmission tomography to determine mass stopping powers within the object [14]. Two very common detectors, ion chambers and film, can be utilized in either active or passive configurations.

2.2.1.2 Modular Versus Integrated Phantoms

Another phantom classification determines whether the phantom material and detector were integrated or modular. In an integrated device, the detectors are rigidly affixed within the phantom material matrix in well-defined locations. Often, supporting electronics are also contained within the same packaging. Examples include planar diode and ion chamber arrays. A modular device, on the other hand, allows placement of the detector at different locations within the medium. Examples include ion chambers in water tanks or solid plastic stacks and film jackets in selected planes within the sheets of material. Modular phantoms allow for more user flexibility when selecting measurement locations and geometries.

2.2.2 Phantom Geometry

The choice of phantom geometry may affect measurement results. Dimensions must satisfy assumptions for scattering, both external to the phantom, e.g., during beam generation in the linac head (angular acceptance criterion), and also near boundaries on the side or bottom (transport criterion). Examples of the former are in the measurement of relative output factors and the latter in calibration activities. Besides overall size, phantom shape may be of consideration as well. In many cases, calculated dose for a simple fixed external beam at a single angle assumes a flat surface, but in cases for rotational beam delivery, e.g., in volume-modulated arc therapy (VMAT), other shapes such as cylindrical phantoms are employed.

2.2.3 Phantom Composition

The majority of dosimetry phantoms in routine clinical use break down along the two major types of material media employed: water or non-water. Water is common due to its being a major tissue component as well as its suitability for calibration standards. Water is readily available and has a known uniform composition. The use of non-water materials is motivated by setup efficiency, compatibility with film, and as a component for integrated phantoms. A number of factors need to be considered when comparing data from one phantom material to another, in particular relative to water, and this leads to what one may refer to as an “equivalency problem” in phantom design and use [5, 9, 15].

2.2.3.1 Modality and Energy Considerations

In choosing phantom geometry and materials, one must contemplate the radiation interaction mechanism(s) with the material, as well as subsequent transport processes. This is due to differences in primary interaction mechanisms for neutral (photon) versus charged particles (electrons, ions). As an example, a material that is similar in mass density, but differs in atomic number, may exhibit significantly different absorption mechanisms for photons, especially for those below 1 MeV or far above 10 MeV, because of the difference between the photoelectric effect, Compton scattering, and pair production primary interaction pathways. Similarly, the transport of energy from primary interaction sites through electron scatter, for example, can also affect both local dose and non-local dose.

2.2.3.2 Length Scaling for Phantoms

Because water is the primary reference medium, all other mediums are mapped to water using two types of length scaling. The first, water-equivalent depth or radiological depth, is a mass-density-scaled path through a heterogeneous object. This calculation is used to determine the depth in water which would have the same amount of radiation absorption as for traversing the material up to the given depth in the object. This is very helpful to connect calibration measurements taken in water to calculations in heterogeneous objects. The second mapping is the water-equivalent distance, where the path through a heterogeneous object is stopping-power scaled. This calculation is used to determine what the charge particle range in water would be given the composition and distance in the heterogeneous object to the location of interest. This is very important to determine the necessary beam range (energy) in proton therapy.

2.2.3.3 Phantom Dose Equivalency

Dose equivalency means measuring dose for a specific geometry in a non-water medium and connecting this to a potentially different geometry in water. If the two geometries were fixed, then this can be accomplished by a simple transference measurement. However, in order to span more geometries, a multiple-step approach can be used. The first is to utilize scaled distances. The second is to use relative absorption/interaction. The third is to scale transport and scattering. Historically, the approach was to employ simple scaling calculations using established empirical relationships, e.g., in dose “hand calculations.” The limitations in this approach are overcome using more sophisticated dose modeling methods as employed within treatment planning systems, with the most accurate being the use of Monte Carlo methods. The term “tissue equivalency” is also applied to phantoms to describe the similarity of physical properties, including electron

density and radiation absorption coefficient. Dose equivalency focuses on comparing how similar final dose distributions compare. Often, tissue-equivalent phantoms will exhibit dose equivalency as well.

2.2.4 Phantom Coordinate Systems

In ultimately treating a patient, a number of coordinate systems are defined, including ones for the imaging, planning, delivery, and measurement systems, as well as one for the patient itself. Thus, it is important to understand the phantom coordinate system definition and how it relates in particular to both the planning and delivery coordinate systems. This is significant in two places: during equipment setup and for any subsequent data processing and analysis.

2.2.5 Dose Measurement System Components

A phantom can be considered a component of a dose measurement system. Often, the terms are used synonymously. A dose measurement system has the following components:

1. **Medium**
This is the specific material and geometry with which the radiation beam interacts and generates either a directly detected signal or is modified and subsequently measured, producing an indirectly detected signal.
2. **Detector**
Particles liberated after radiation interaction with the medium are collected by the detector. This is often in the form of electrical charge from scattered electrons, but also could be visible light, etc.
3. **Processor**
Signals from the detector often need to be amplified, digitized, and then scaled and converted to the appropriate dose quantity through application of a calibration coefficient.
4. **Positioner**
Water tank dose measurement systems have positioning devices which can place and determine the detector location, usually in three dimensions. Each motion axis has a motor and position sensor. All axes are managed by a dedicated controller that sends each axis to a set location and also reads back the actual location (they may not be exactly the same). Solid phantoms do not have positioner components.
5. **Data handler**
Ultimately, the measured signal and position data need to be managed. This and subsequent analysis and processing are done in dedicated software tools that act as the front end to the data measurement system.

2.2.6 Phantom Measurements

2.2.6.1 Setup and Alignment

Accurate and well-understood phantom positioning is critical to obtaining meaningful measurement results. Institutions should define setup protocols as necessary for this purpose. In particular, 3D water tanks must go through an alignment and leveling procedure prior to measurement. Often, the tank vendor will provide instructions and tools to ensure proper setup, but ultimately, the user needs to verify proper setup and alignment before proceeding with performing measurements. Since these activities are time-consuming, alternatives to 3D water tanks are often used when possible.

2.2.6.2 Relative and Absolute Dosimetry

All major calibration protocols generate calibration coefficients that are expressed in terms of dose to water. Calibration phantoms must be able to accommodate reference geometries defined by protocols, as well as dose-to-water transference. The latter is necessary to generate absolute dose calibrations of detectors such as ion chambers and also of treatment delivery system output. The requirement of relative dosimetry, on the other hand, is that one is able to accurately measure the ratio of dose at one location to that of a chosen reference location within the phantom.

2.2.6.3 Detectors and Devices

The main purpose of radiation dosimetry phantoms for therapeutic use is to measure dose. One must therefore consider the detection process and devices used. In its most general, detection involves either the direct or indirect detection of liberated electrons.

Direct detectors produce charge that then can be immediately amplified and counted by electronic circuits. Examples of direct detectors are ion chambers or diodes. When the detector is embedded within the phantom material, the detector composition should match that of the phantom material as closely as possible. Differences in composition can perturb measured charge, and then, this must be considered in converting measured charge to absorbed dose.

Indirect detectors ultimately analyze a signal related to dose deposition within the phantom. Examples include reading the optical density of film emulsion agents such as silver halides [12], the MR signal from a molecule in a gel matrix [16], or emission from activation of an O^{18} nucleus by proton nuclear activation [17].

2.2.6.4 Data Processing and Agreement

Measured data from phantoms need to be processed in some form. The processing can be broken down along the lines of where it is done: by the device or by the user, and foreground versus background. Low-level background processing starts with the fundamentally detected signal where amplification, background subtraction, etc. are performed by the device electronics. High-level background processing can include the automatic subtraction of position shifts, coordinate transformations, application of scaling factors or calibration coefficients, filtering and smoothing, and so on.

Foreground processing is actively performed by the user and software tools. This most often entails analysis of some form. One example is the determination of scan profile parameter values as defined by protocols, e.g., flatness, penumbra, or symmetry. Another example is the comparison between measured and calculated data. This last activity is the ultimate endpoint for one of the two primary phantom uses: to validate dose calculation and delivery. The most basic data comparison is the use of a local point-wise percent difference calculation, calculated at the same location. However, in dosimetry, usually this is modified to a non-local percent difference calculation, where the difference is calculated at a given location, but the percentage is determined by dividing by a specified value such as the overall maximum. This relaxes the accuracy requirements in low-signal areas. Since measurement in high-dose gradient regions is very sensitive to positioning errors, distance-to-agreement and gamma analyses are utilized instead. These latter methods apply not only to 1D (point) data, but also to 2D (planar) and 3D (volumetric) data as well.

2.3 Water Phantoms

In this section, we will describe phantoms whose medium is water. These phantoms play a central role in absolute dosimetry calibration of machine output. They also allow for the systematic inspection of many important beam shape properties such as symmetry and flatness, as they are readily observed in a uniform medium. Water also is chosen because it is a dominant component in many types of tissue, simple in chemical composition, and readily available.

2.3.1 Construction of Water Phantoms

A typical 3D water phantom dose measurement system consists of the following:

1. A tank made of a clear material such as PMMA (PlexiglassTM).
2. A water subsystem containing a reservoir, pump, and transfer line, or instead a simple drain valve.

3. A lift cart.
4. A positioning system of one or more axes either driven manually or automatically. Each axis has a motor and position sensor which are driven and read by a controller.
5. A detector such as an ion chamber or diode.
6. Data handling system that collects, calibrates, converts, and analyzes data such as profiles.

Simpler variants that offer manual detector positioning for point dose measurement still contain many of the above properties in their construction. Although early water phantoms were fabricated in-house with specific tasks in mind, they now have become widely available and those employed in routine clinical use often are obtained commercially. In general, all have similar construction, with tanks having clear walls made of acrylic, open to the top.

2.3.2 Characteristics of Water Phantoms

A 3D scanning system is able to position the detector to any point within the available limits of the scan axes. Coordinated positioning and signal acquisition is called scanning. The output data are in the terms of a profile, which is represented as an array of position and signal values. The signal values often are expressed in arbitrary units and digital numbers or can have a calibration coefficient applied so the end result is in terms of absolute dose. This last step is routinely applied in the data handling software or can be done outside of the acquisition system by the user. Often, profile data are plotted on a relative scale. Examples are lateral profile scans perpendicular to the beam central axis scaled to the central axis value; longitudinal (depth) profile scans often are rescaled relative to their maximum value or a standard reference depth.

2.3.3 Use of Water Phantoms

Water phantoms are used to determine machine output. Charge measured at a reference depth and geometry is converted to dose through a calibration protocol. Relative machine output is determined by measuring dose in water for various machine settings (beam geometries), whereby the measured charge is compared to the standard reference geometry defined for absolute calibration. Often, a table of “output factors” is the end result of this activity.

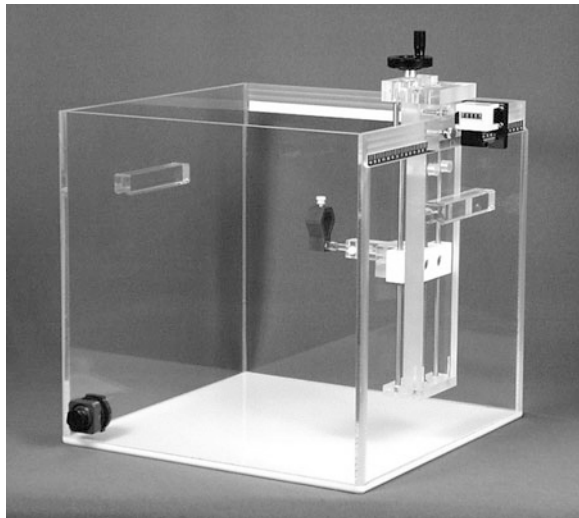
Scanning water phantoms are used to generate beam profile data for the use in determining dose at locations other than the calibration point. Profile data are used for dose calculations using simple scaling (hand calculation), or as guidance to more sophisticated model-based calculations in treatment planning systems.

Attention must be paid to the type of water used. From a dosimetric standpoint, there is no clinically significant difference in using distilled versus tap water direct from a ground or surface source. However, tap water may contain minerals from the source or supply lines. Any deposition of mineral films may interfere with positioning mechanisms. For this reason, dedicated 3D scanning systems should only use distilled water. Simple calibration phantoms with less sensitive mechanisms can be used with tap water, providing that the water is clear and colorless and does not leave any residue after the tank is emptied and dried. Ideally, water tanks and reservoirs should not be left filled for extended periods of time. The walls of some tanks may deform, as they are designed to hold water only for typical use periods, not months. Water stored for extended periods of time may develop algae contamination. It is recommended that for longer-term storage, the water be treated with a small amount of hydrogen peroxide or other mild algacide agent. Even then, water reservoirs that are filled over time should be periodically flushed.

2.3.4 Examples of Water Phantoms

We close this section by citing two typical examples of water phantoms in common use. The first is a tank with a single simple manual positioner. This allows dose measurement in 1D along the depth direction. It is useful for output and inspection of depth-dose curve stability during monthly quality assurance (QA). See Fig. 2.1. The second example is that of a 3D scanning system. A 3D scanning system can move the detector to a programmed location within the accessible volume. Coordinated scans are made to measure dose profiles either lateral or longitudinal to the radiation beam axis.

Fig. 2.1 A typical water tank and manual 1D positioning system. (Image courtesy of CNMC Company)



2.4 Non-Water Phantoms

Despite water's primary role, it does not fulfill all the needs of dosimetric measurement. Foremost is that patient composition is not uniform, hence the need for heterogeneous phantom materials. Secondly, water is limited to planar surface geometries aligned to gravity. Water is more difficult to handle and not compatible with many detectors unless special waterproofing is applied. Additionally, the setup and handling of water tanks are often time-consuming. Thus, solid materials are utilized for the medium when possible or necessary. A very common application is in their use as "check phantoms" for relative QA measurement, e.g., morning machine output. Baseline measurement values are established, and readings are compared for percent deviation from the baseline as part of the check.

Non-water phantoms can be categorized according to whether they are engineered or naturally fabricated. Naturally fabricated phantoms entail essentially a butcher's section of animal tissue. Engineered phantoms are those fabricated using a host of materials to dosimetrically mimic either water or tissue, at least on a relative level. Engineered phantoms can be categorized further by material and geometry and whether they are permanently integrated with detectors. The latter will be discussed in [Sect. 2.5](#).

2.4.1 Construction of Non-Water Phantoms

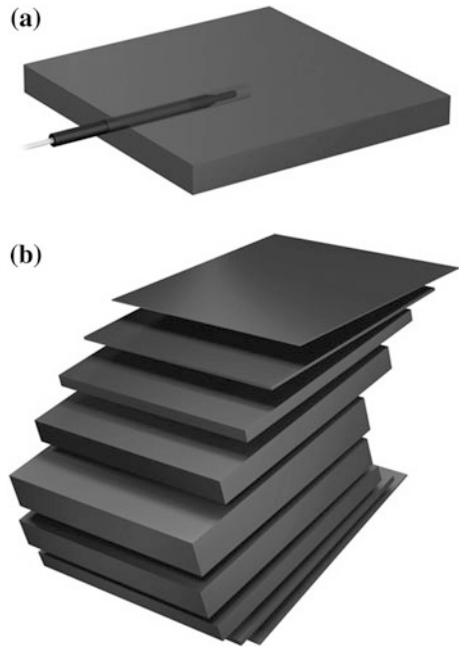
Engineered phantoms typically come in two exterior geometries. The first is a stack of sheets usually $30 \times 30 \text{ cm}^2$ with thicknesses ranging from approximately 0.2–5.0 cm, as shown in [Fig. 2.2](#). Individual sheets may contain cavities which are designed to accept a specific detector which fits closely into the cavity, such as a Farmer or parallel plate ion chamber. More complex geometries are machined or molded to dedicated exterior shapes, ranging from a simple sphere to mimicking the surface of a human body [[18](#)].

2.4.2 Characteristics of Non-Water Phantoms

There are two solid material categories used. One is a mixture of compounds in an epoxy resin and the latter a solid single compound such as poly(methyl methacrylate) (PMMA) (acrylic) [[9](#), [15](#)]. Common trade names for PMMA are PlexiglasTM or LuciteTM. Early solid phantoms were simple blocks of PMMA. However, this material over time will exhibit changes from radiation exposure, and due to its composition, many properties are not as close to liquid water or tissue as desired.

Engineered phantom composition is either uniform or variable. A stack of water-equivalent sheets as a replacement for a water tank is intended to be

Fig. 2.2 A solid water slab showing a receptacle for an ion chamber (a) and a stack of slabs (b). (Images courtesy of Standard Imaging)



uniform, as well as an object machined out of a single piece of material. More complex engineered phantoms will contain well-defined regions where the composition is usually uniform, typically intended to mimic various tissue classes such as lung, muscle, adipose, muscle, and bone. More simply, one may construct a phantom object out of dedicated sheets to represent specific tissue types as well. Since non-water phantom material comes in slabs, this allows very flexible use of film. Jackets can be sandwiched between sheets for many measurements such as planar dose.

When selecting non-water phantoms, it is important to consider a number of characteristics. These include intended (design) physical properties such as composition, mass density, electron density, and temperature dependence; accuracy and uniformity in manufacture; and response to radiation absorption particle transport. Manufacturers often offer certification of phantom properties, but the user is responsible for understanding how well a specific phantom compares with water and to characterize each phantom through acceptance testing.

2.4.3 Examples of Non-Water Phantoms

There are a number of commercial sources of non-water material and phantoms. Examples of these include Gammex Solid WaterTM, Standard Imaging Blue WaterTM, Med-Cal Virtual WaterTM, PTW RW3TM, and CIRS Plastic WaterTM.

With these products, one can typically achieve calibration accuracy on the level of 0.5–1.0 % to true dose. Manufacturers of ion chambers offer slabs paired with specific models to ensure proper detector fit, which is critical for accurate and reproducible results. An example of an acrylic phantom is the PTW ICRU Acrylic Calibration PhantomTM.

A very useful engineered phantom is the anthropomorphic (RandoTM) phantom. The surface and interior regions mimic human anatomy. Materials that represent soft tissue are chosen to have an effective atomic number that closely resembles muscle with randomly distributed fat [18]. This phantom is discussed in detail in another chapter.

It is often desirable to configure the phantom density through the means of exchangeable plugs. An example of this type is the CIRS Model 062M Electron Density PhantomTM, which allows one to place tissue-equivalent materials at different locations [19]. This type of phantom often is used to calibrate CT scanner data for later mapping to mass density or stopping-power values within a treatment planning system.

Another type of phantom is termed an animal tissue phantom or “Meat Market” phantom. Often for ease of handling, the phantom is frozen. Butchered pieces of turkey, ham, pig head, beef steak, or leg of lamb have been utilized. Figure 2.3 shows the use of a leg of lamb for proton transmission measurements as part of planning system commissioning [20]. In this case, the phantom was used to provide a realistic heterogeneous object to study the proton range calculations in a planning system.

2.4.4 Use of Non-Water Phantoms

Although most non-water phantoms are very simple in structure, the critical nature of radiation measurement requires some vigilance in their use. As mentioned earlier, it is important to ensure that the detector fits snugly into its cavity, and so the material should be machined specifically for the employed detector. On first use, it is advisable to image the phantom with the detector inserted using kV radiography and to make a reference mark on the detector indicating its full placement into the material. In addition, plugs are often provided for insertion into the detector cavity when a detector is not being utilized. Detectors and cavities are visible in the examples in Fig. 2.2.

Upon receipt of the non-water phantom, acceptance testing should be performed. Composition uniformity is best checked through acquisition of a computed tomography (CT) scan and inspection of CT number variation. This determines density uniformity, including identifying possible air pockets. Another test is to check the material response to a given beam relative to water. For ion beams, e.g., protons, the variation in a slab’s water-equivalent thickness (WET) is directly proportional to the variation in material density, and therefore, values of

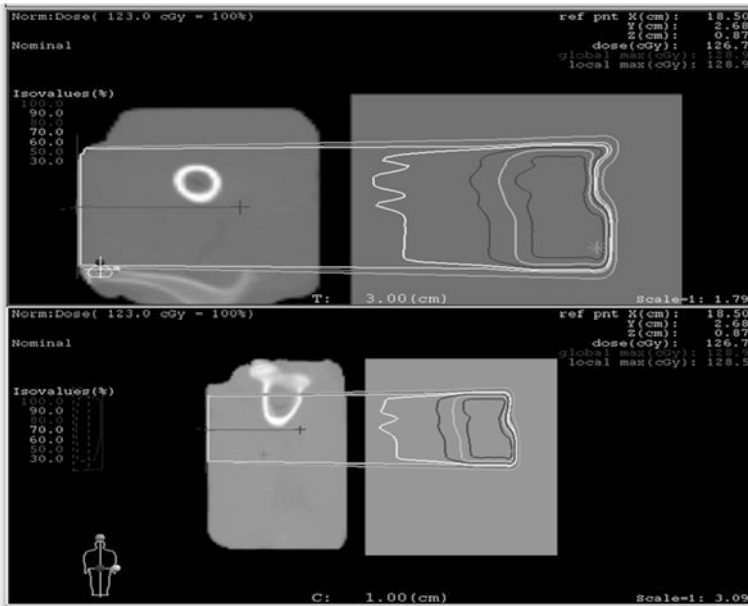


Fig. 2.3 Example dose distribution measured in solid water using an animal tissue phantom setup for calculated proton range validation. (Courtesy of Niek Schreuder)

1–3 % are not uncommon [21]. In this case, for range measurements, one should calibrate the WET of each slab and use the same slabs in the same order through QA processes that involve range measurement and comparison with calculations.

2.5 Integrated Device Phantoms

Integrated device phantoms are parts of a dose measurement system where the response material (medium) and probe (detector) act as one unit and designed for one or more specific measurement goals. The simplest example is an ion chamber residing into a milled cavity in a slab of non-water material, as mentioned earlier. However, here we will focus on devices that contain multiple detectors and often have built-in electronics as well.

2.5.1 Construction of Integrated Phantoms

Integrated devices are a single unit consisting of a chassis, water-equivalent material, detectors, internal connections, electronics, and data/power connectors. The bodies are often marked to indicate location of the detectors as well as

alignment and orientation. In this configuration, the material and geometry typically are fixed. Because of these additional components, there is more metal present, and this can affect the dose measurement or limit the applicability to well-defined measurement setups. In earlier devices, metal could lead to scatter and attenuation in undesirable ways. Recent devices have shown improvement in this area.

2.5.2 Characteristics of Integrated Phantoms

Integrated devices allow for greatly reduced measurement session time. Setup often entails placing the device on top of a treatment table and aligning to the beam center and perhaps connecting one cable. This simple operation allows for routine use by clinical technicians. The units are designed to withstand repeated handling from daily use.

Dose measurement requires a sufficient amount of solid material to achieve scatter equilibrium. Devices often have a built-in over layer of fixed physical thickness from the entrance surface to the detector elements. Often it is important to know and to consider this amount of water-equivalent distance when setting up the device and later interpreting measurements or comparing with calculation. Often, slabs of non-water phantom material are placed on the entrance surface of the device to place the detection elements at a desired water-equivalent depth.

Integrated device phantoms typically utilize either ion chambers or diodes for detectors. These are built-in and at fixed locations. Diodes allow for smaller measurement volumes than ion chambers and hence may offer the potential for higher spatial resolution. However, diodes are susceptible to radiation-induced changes that cause their response to change with time. They also may exhibit energy and temperature dependence and be affected by low-energy scatter. Ion chambers do not have these issues, but require larger detection element volumes to produce usable signal-to-noise levels. For either detector type, it is possible to perform both relative and absolute calibrations. A central location is assigned an absolute calibration and is propagated to the other detectors through relative calibration. At a minimum, dose distribution measurement of profiles, planes, or volumes using a device with a detector array must have at least a relative calibration performed.

Proper use of integrated device phantoms requires an understanding of their intended use and limitations. Because of the fixed materials and detector geometry, this may place restrictions on field size or beam orientation. One should be mindful of boundary detectors which may not have sufficient scatter conditions present during measurement. Similarly, all detectors could suffer from insufficient backscatter. If identified, this latter condition may be remedied by placement of slabs of non-water phantom material to the side or underneath the device.

2.5.3 Examples of Integrated Phantoms

Most integrated devices in clinical use are obtained commercially due to their specialized design and production. Examples of linear (1D) arrays include the Sun Nuclear ProfilerTM and IBA ZebraTM. The former is a diode array for rapid measurement of beam profiles, which is useful for real-time feedback during linac beam steering. The ZebraTM is an array of parallel plate ion chambers for measurement of charged particle depth-dose curves, including Bragg and spread-out Bragg peak analysis. Patient dose distribution QA necessitates the use of planar (2D) arrays. Example devices for this task include the Sun Nuclear MapCheckTM (diode) and the IBA MatriXXTM (ion chamber). A simpler 2D device for daily linac energy and output constancy measurement includes Standard Imaging Beam CheckerTM. Devices also exist that measure dose over a volume; examples of these quasi-3D arrays include the Sun Nuclear ArcCHECKTM and ScandiDos Delta 4TM. Figure 2.4 shows both the prototype and eventual engineered product for the Sun Nuclear ArcCHECKTM [22].

2.5.4 Use of Integrated Phantoms

Integrated devices are used for delivery system and patient-specific QA. The first devices were constructed to facilitate frequent machine measurements. An example is the daily check of output and symmetry constancy of linac beams. Additionally, as the number of detectors increased, less frequent (monthly) measurement of beam parameter constancy became more feasible. One could then readily not only measure symmetry, but flatness and field size as well.

With the advent of delivery techniques such as intensity-modulated radiotherapy (IMRT) and VMAT, the need arose for end-to-end validation that the delivered dose to the patient was as modeled in the planning system. Integrated devices have played a key role in verifying accurate dose delivery to an increasing fraction of patients receiving modulated beam treatments. In fact, without this verification step, it would have been impossible to otherwise manually verify complex dose distributions that arise from complex delivery sequences.

2.6 Therapeutic Clinical Uses

Dosimetric phantoms play a key role in evaluating the entire treatment chain, from imaging to planning to delivery. Two primary uses arise: (1) Full end-to-end tests where dose is delivered to a phantom, and the measured dose is compared to that calculated by the planning system and (2) tests targeted to individual portions of the treatment chain, such as the planning system itself.

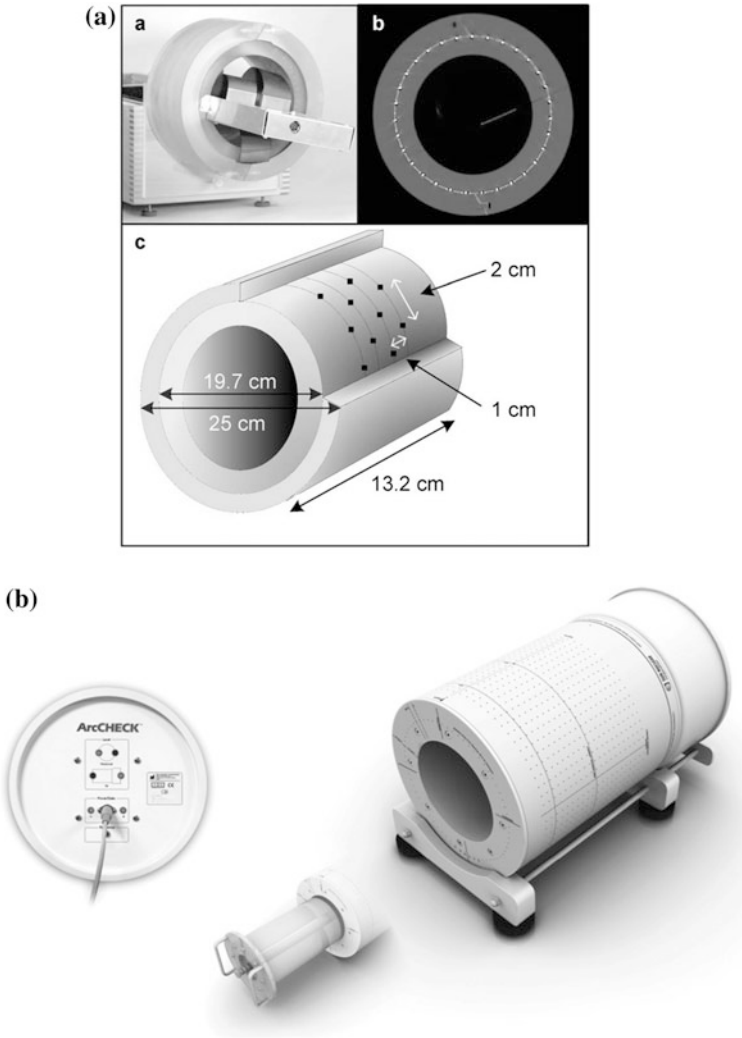


Fig. 2.4 An integrated device phantom prototype (a) (from Fig. 2.1 in Letourneau et al.) that is now sold commercially as the ArcCHECK™ from Sun Nuclear (b). (Upper image reprinted with permission from the American Association of Physicists in Medicine and lower image courtesy of Sun Nuclear)

2.6.1 Installation and Acceptance Testing

Vendors often will use phantoms to verify the performance or to guide adjustment of equipment during the on-site installation process. Water tanks are often used to measure and adjust linac beam profile properties such as symmetry and flatness.

Film inside solid water is used to establish and verify geometric positioning and alignments.

Acceptance testing occurs after initial installation of a component in the treatment chain, and before the item is commissioned and employed for treatment. Here, phantom measurements can be used to ensure that the device meets design specifications agreed upon between the facility and the device vendor. An example is the inspection of linac beam properties using a 3D scanning system, or spoke measurements with film to verify radiation isocenter.

2.6.2 Calibration and Commissioning

After a component in the treatment chain is installed and accepted, two things must still be done, and they both involve phantom use. The first is to perform any necessary calibrations of the device itself, e.g., the adjustment of linac output using the TG-51 protocol [6]. The second is to generate necessary data for absolute dosimetric calculations. These data can be as simple as a point dose measurement at a specific location, but typically extends to tables of output factors and a library of longitudinal and lateral beam profiles for machine settings that span those available during clinical use.

2.6.3 Periodic Performance Monitoring

Once the treatment chain is established through installation/acceptance testing and calibration/commissioning, the performance must remain stable to within predefined levels. Phantoms are used for periodic measurement of output stability, e.g., during monthly linac quality assurance (QA). In addition, scans of phantoms that are run through the planning process play a role in treatment planning system QA as well. The performance monitoring activities are often similar to those used earlier, but the goal is to inspect performance stability with respect to initially established benchmark measurements, as opposed to the establishment of those values. When possible, simpler phantoms which require less setup time and are easy to handle are employed. Performance stability means transfer factors can be generated, for example, so solid water phantoms or integrated devices can be used instead of water tanks.

2.6.4 Planned Patient Dose Validating

In addition to being used for general system performance, phantoms play a role in ensuring accurate treatment specific to an individual patient. Typically, an end-to-end

measurement verifies both planning and delivery as part of patient-specific QA. A classic example is patient-specific measurements for IMRT or VMAT delivery using a solid water stack with film and an ion chamber. This combination can check both the absolute dose at a point and the relative dose in the plane of the film. When a new treatment technique is being established in a clinic, often every patient will have specific measurements. This serves to further test the implementation of new planning and delivery tools or techniques. Later on, when baselines are more firmly established, it is common practice to then measure patients that are outside the span of existing measurements, or for complicated cases with challenging geometry and dose objectives. A number of reports give practical guidelines on how to test dose calculation algorithms in a TPS through the use of inhomogeneous phantoms [23].

2.7 Future Directions

There are a number of areas in phantom or dose measurement system design that are under development as we have not yet reached ultimate design or use goals as stated in the beginning of this chapter. We conclude by discussing these here.

2.7.1 Automated Data Collection, Analysis, and Management

Although many dose measurement systems based on integrated phantoms allow some automation and analysis, often there are manual steps in setting these up or in subsequently performing them. For repetitive measurements, or for making a large group of systematic measurements, progress is needed to automate tasks. In addition, large amounts of data over potentially long periods of time necessitate a dedicated data management system for this purpose.

2.7.2 Materials that More Closely Mimic the Behavior of Tissue

The composition of solid phantom materials needs to be optimized to best approximate actual tissue response to radiation. Advances in imaging and dose calculations will drive the need to create more complex and more configurable test objects both for dose verification and also for educational purposes.

2.7.3 Variable Density Distribution (Deformable) Phantoms

In order to test algorithms that perform deformation of dose distributions, one needs phantom objects that deform in a controlled and known manner. This will allow for the easy validation of software that employs deformation transformations both to mass density and to dose distributions. Recent progress has been made by Niu et al. [24].

2.7.4 High-Resolution 3D Data Acquisition in Parallel

There is no routine means to measure a 3D dose distribution at high spatial resolution over entire treated volumes at a high frequency in a clinical setting. This is desirable because the dose distribution in the patient is three dimensional. Calculated models of the patient dose distribution in treatment plans are also three dimensional. Current practice is limited to a sampling of the dose distribution through measurements that produce 1D or 2D arrays of data.

Recent progress has been reported in 3D dose measurement with the use of a phantom with a Presage gel insert analyzed using optical CT imaging [25]. A comparison with 2D planar dose measurements indicated the benefit from measuring the entire treated volume, producing a more complete verification. With a 3D measurement, one can generate DVH curves, and with proper deformation mapping, one can visualize dose relative to the patient's anatomy. Although not a direct patient dose measurement, this work has demonstrated progress toward that goal.

2.7.5 In vivo Dose Measurement During Treatment Delivery

Although progress has been made in the in vivo measurement of dose during delivery, e.g., with EPID-based methods [13], the ultimate goal of routinely measuring the entire patient delivered dose in 3D incrementally still is not routinely available, especially with adequate time resolution. Ideally, one would want to build up the measured dose distribution as delivery progresses, compare with the planned (intended) dose, and instruct corrections to the delivery of the remainder of the prescribed fraction to account for any deviation from intended dose due to patient and/or delivery system performance fluctuations. This process sometimes is termed as dose-guided radiation therapy (DGRT). Current methods rely on CT imaging at time of simulation or prior to treatment and so are not quite real time as desired.

References

1. O'Toole, M. (Ed.). (2012). *Mosby's medical dictionary* (9th ed.). St. Louis: Elsevier/Mosby.
2. Krönig, B., & Friedrich, W. (1922). *The principles and physics of radiation therapy*. New York: Rebman Co.
3. Quimby, E. H., Copeland, M. M., & Woods, R. C. (1934). The distribution of Roentgen rays within the human body. *American Journal of Roentgenology. Radiation Therapy*, 32, 534.
4. Failla, G., Quimby, E. H., & Dean, A. (1922). Some problems of radiation therapy. *American Journal of Roentgenology*, 9, 479.
5. White, D. R. (1978). Tissue substitutes in experimental radiation physics. *Medical Physics*, 5, 467.
6. Almond, P. R., Biggs, P. J., Coursey, B. M., Hanson, W. F., Hug, M. S., Nath, R., et al. (1999). AAPM's TG-51 protocol for clinical reference dosimetry of high-energy photon and electron beams. *Medical Physics*, 26, 1847.
7. Andreo, P., Burns, D. T., Hohlfield, K., Huq, M. S., Kanai, T., Laitano, F., Smyth, V. G., & Vynckier, S. (2000). Absorbed dose determination in external beam radiotherapy: An international code of practice for dosimetry based on standards of absorbed dose to water. International Atomic Energy Agency (IAEA) Report TRS-398.
8. Papanikolaou, N., Battista, J. J., Boyer, A. L., Kappas, C., Klein, E., Mackie, T. R., et al. (2004). *Tissue inhomogeneity corrections for megavoltage photon beams*, *American Association of Physicists in Medicine (AAPM) Report 85*. Madison: Medical Physics Publishing.
9. Tissue Substitutes in Radiation Dosimetry and Measurement, International Commission on Radiation Units (ICRU) (1989). Report 44. Oxford: Pergamon Press, ICRU (Bethesda, MD).
10. Hendee, W. R., Ibbott, G. S., & Hendee, E. G. (2005). *Radiation therapy physics* (3rd ed.). Hoboken: Wiley.
11. Kahn, F. M. (2009). *The physics of radiation therapy* (4th ed.). Baltimore: Lippincott Williams and Wilkins.
12. Podgorsak, E. H. (Ed.). (2005). *Radiation oncology physics: A handbook for teachers and students*. Vienna: International Atomic Energy Agency.
13. van Elmpt, W., McDermott, L., Nijsten, S., Wendling, M., Lambin, P., & Mijnheer, B. (2008). A literature review of electronic portal imaging for radiotherapy dosimetry. *Radiotherapy and Oncology*, 88, 289.
14. Schulte, R. W., Bashkirov, V., Li, T., Liang, Z., Mueller, K., Heimann, J., et al. (2004). Conceptual design of a proton computed tomography system for applications in proton radiation therapy. *IEEE Transactions on Nuclear Science*, 51, 866.
15. Hill, R. F., Brown, S., & Baldock, C. (2008). Evaluation of the water equivalence of solid phantoms using gamma ray transmission measurements. *Radiation Measurements*, 43, 1258.
16. Pavoni, J. F., Pike, T. L., Snow, J., DeWerd, L., & Baffa, O. (2012). Tomotherapy dose distribution verification using MAGIC-f polymer gel dosimetry. *Medical Physics*, 39, 2877.
17. Studenski, M. T., & Xiao, Y. (2010). Proton therapy dosimetry using positron emission tomography. *World Journal of Radiology*, 2, 135.
18. Alderson, S.W., Lanzl, L. H., Rollins, M., & Spira, J. (1962). An instrumented phantom system for analog computation of treatment plans. *Am. J. Roentg.* 87:185. (See also: <http://www.phantomlab.com/products/rando.php>).
19. CIRS Electron Density Phantom (see: <http://www.cirsinc.com/products/modality/24/electron-density-phantom/>).
20. Zheng, Y., Kang, Y., Zeidan, O., Keole, S., Pankuch, M., & Schreuder, N. (2012). How much is the proton range uncertainty? An end-to-end study using various animal tissues, presented at PTCOG-51, Seoul, Korea.
21. Zhang, R., Taddei, P. J., Fitzek, M. M., & Newhauser, W. D. (2010). Water equivalent thickness values of materials used in beams of protons, helium, carbon and iron ions. *Physics in Medicine and Biology*, 55, 2481.

22. Létourneau, D., Publicover, J., Kozelka, J., Moseley, D. J., & Jaffray, D. (2009). Novel dosimetric phantom for quality assurance of volumetric modulated arc therapy. *Medical Physics*, *36*, 1813.
23. IAEA-TECDOC-1583. (2008). Commissioning of radiotherapy treatment planning systems: testing for typical external beam treatment techniques. IAEA, Vienna, Austria, 2008. (Available from: http://www-pub.iaea.org/MTCD/publications/PDF/te_1583_web.pdf).
24. Niu, C. J., Foltz, W. D., Velec, M., Moseley, J. L., Al-Mayah, A., & Brock, K. K. (2012). A novel technique to enable experimental validation of deformable dose accumulation. *Medical Physics*, *39*, 765.
25. Oldham, M., Thomas, A., O'Daniel, J., Juang, T., Ibbott, G., Adamovics, J., et al. (2012). A quality assurance method that utilizes 3D dosimetry and facilitates clinical interpretation. *International Journal of Radiation Oncology Biology Physics*, *84*, 540.

Chapter 3

Anthropomorphic Phantoms for Radiation Oncology Medical Physics

David S. Followill

3.1 Introduction

The use of phantoms in radiation oncology by medical physicists as a substitute for human tissue has been in use for many decades. The various types of phantoms used have evolved with time in terms of shape, material and composition. Basic calibration and output constancy phantoms used in the clinic have been simple blocks of wood, solid plastic cubes, solid acrylic or polystyrene plastic phantoms cut into slabs, water tanks of all sizes and currently a variety of water equivalent plastics. Regardless of the number of solid phantoms available to the medical physicist, since 1983 with the publication of the Task Group report 21 [1], the liquid water phantom has been the preferred phantom for calibrations and dosimetry measurements (as described in Chap. 2). No other readily available phantom comes closer to simulating actual human soft tissue than the liquid water phantom.

Even though the water phantoms used for calibration simulate most human soft tissues and is easy to use, it does not provide a realistic representation of the shape of the human body, differences in tissue densities and the spatial mass density distributions between different organ sites within the body. As such, anthropomorphic phantoms were built and reported on as early as 1924. These early phantoms were humanoid in shape and contained different tissue equivalent materials such as “wax-plastic”, bags of talc, plywood, Mix D plastic and sawdust and rice [2–6]. The ICRU report 44 on “Tissue Substitutes in Radiation Dosimetry and Measurement” and ICRU report 48 on “Phantoms and Computational Models in Therapy, Diagnosis and Protection” give a detailed history of the early and current anthropomorphic phantoms [7, 8]. The version of the anthropomorphic phantom used today was developed over 50 years ago which was described by

D. S. Followill (✉)

Radiological Physics Center, U. T. M. D. Anderson Cancer Center, 1515 Holcombe Blvd,
Unit 607, Houston, TX, USA

e-mail: dfollowi@mdanderson.org

Stacey et al. in 1961 [9] and Alderson et al. back in 1962 [10]. The term “anthropomorphic” is defined as “ascribing human form and/or attributes to an object that is not human”. Most all anthropomorphic phantoms are normally designed and made to closely resemble the shape and size of the human body, whether male, female, adult or child. In addition, these anthropomorphic phantoms have to be constructed of materials that not only simulated human tissue densities, but also the radiation interactions within the tissue equivalent materials.

Since these phantoms are designed for dosimetry measurements they had to have the ability to accommodate radiation dosimeters in multiple locations. These anthropomorphic phantoms are not recommended for routine dosimetry measurements of actual patients due to the variability between the phantoms and the patients, but they are excellent phantoms to verify a particular new treatment process, dose calculation algorithm or to make dose measurements at locations far from the treatment fields. This verification process may include some if not all of the following components:

1. imaging of a heterogeneous human-like phantom,
2. transfer of the images to the treatment planning system,
3. contouring targets and organs at risk (OAR),
4. dosimetry data in the planning system,
5. dose calculation algorithm used by the planning system,
6. transfer of the treatment plan to the treatment unit, and
7. delivery of the planned doses.

This verification process is also known as an, “end to end”, treatment verification.

3.2 Anthropomorphic Body Phantoms

There are currently three versions of the anthropomorphic cross sectional dosimetry body phantoms available to the radiotherapy medical physicist. The first is the “Alderson Radiation Therapy phantom (ART phantom)” offered by Radiology Support Devices (Long Beach, CA). This phantom is a modified version of the earlier original Alderson RANDO phantom built and described by Alderson et al. back in 1962 [10]. The second body phantom is the “RANDO[®]” body phantom offered by The Phantom Lab (Salem, NY) and this phantom is very similar in design to the original Alderson RANDO phantom. The third body phantom is the “ATOM[®]Dosimetry Phantom” offered by Computerized Imaging Reference Systems, Inc (CIRS) (Norfolk, VA). The ATOM phantom is unique in that it can be provided in different sizes ranging from a newborn to adult. All three of the commercially available types of body phantoms are designed to hold various types of radiation dosimeters depending on the needs of the medical physicist.

3.2.1 ART Phantom

As mentioned above, the ART anthropomorphic body phantom (Fig. 3.1) (Radiology Support Devices Inc., Long Beach, CA) is the descendant of the original Alderson RANDO phantom [10]. This phantom can be supplied either as a male (175 cm tall, 73.5 kg) or female (155 cm, 50 kg). The phantom includes cross sectional slices from the apex of the head to just below the groin. Several key improvements over the original Alderson RANDO phantom have been made and they include using tissue equivalent materials that follow the ICRU 44 specifications in terms of a stable homogeneous composition in the desired anatomical shape that has both non-radiation properties (electrical conductivity, thermal and mechanical properties) and radiation related properties (appropriate attenuation and scatter properties) to simulate human tissue (ICRU 1989). The human skeleton has been replaced with a skeleton that comes from a highly detailed polymer molding from a human skeleton which reproduces the shape, mass density, and attenuation coefficient of cortical bone and spongiosa. The replacement of the human skeleton with a manufactured one allows for more continuity between phantoms. Campbell and Almond compared the location and size of the human skeleton in 3 Alderson RANDO phantoms and found a considerable difference between the 3 phantoms [11]. The molded bone equivalent material also takes care of the reduced bone density problem associated with human skeletons due to the loss of the marrow [12]. The lungs are molded from syntactic foam and have an average density of 0.3 g/cm^3 . The soft tissue equivalent material conforms to the ICRU standards and where necessary is cut away to generate air cavities such as in

Fig. 3.1 Alderson radiation therapy phantom (ART phantom) provided by radiology support devices (RSD)



the nasal cavity region. Various realistically shaped breast sizes are provided that can be attached to the female phantom or if a large female is desired, the male phantom can be made to accommodate breasts.

The ART phantoms are cut in 2.5 cm cross sectional slices. Matrices of holes in either a 3×3 or 1.5×1.5 cm grid can be drilled to accommodate TLD capsules. The holes, when they do not contain TLD, are filled with bone-, lung- or soft tissue-equivalent pins. The phantom plastics are rigid enough to be drilled to custom fit an ion chamber if the medical physicist so desires.

3.2.2 RANDO[®] Phantom

The RANDO[®] phantom (Fig. 3.2) (The Phantom Laboratory, Salem, NY) closely simulates the original Alderson Rando phantom. This phantom can be supplied either as a male (175 cm tall, 73.5 kg) or female (163 cm, 54 kg). The phantom includes cross sectional slices from the apex of the head to just below the groin.

Fig. 3.2 RANDO[®] Phantom provided by the phantom laboratory



Unlike the ART phantom, each RANDO[®] phantom contains a human skeleton. These human skeletons provide the asymmetry in the bony structure and distorted joints normally found in a patient. However, because the skeletons are not all the same size, they are adjusted slightly to fit in the phantom mold when each phantom is made. The lungs are hand molded and custom placed in each ribcage for each phantom. They have the same effective atomic number as the soft tissue equivalent material, but with a density equal to that of median respiratory rate ($\sim 0.35 \text{ g/cm}^3$). The soft tissue equivalent material is a urethane formulation that is equivalent to muscle with randomly distributed fat. Similar to the ART phantom, the female or male RANDO[®] phantom can be accommodated with naturally shaped breasts, ranging in sizes from A through E.

The RANDO[®] phantoms are cut in 2.5 cm cross sectional slices. Film can be sandwiched between slices if desired. Matrices of holes can also be custom drilled or the medical physicist can accept the standard grid sizes of either 3×3 or 1.5×1.5 cm. Holes are never drilled where there is bone and the holes can be 2, 5, or 6 mm in diameter. Mix D plugs are offered to fill the holes when dosimeters are not inserted. The phantom plastics are rigid enough to be drilled to custom fit an ion chamber or other dosimeter if the medical physicist so desires.

3.2.3 ATOM[®] Dosimetry Phantom

The ATOM[®] phantoms (Fig. 3.3) (CIRS, Inc., Norfolk, VA) come in six different sizes; adult male (173 cm tall, 73 kg), adult female (160 cm, 55 kg), pediatric

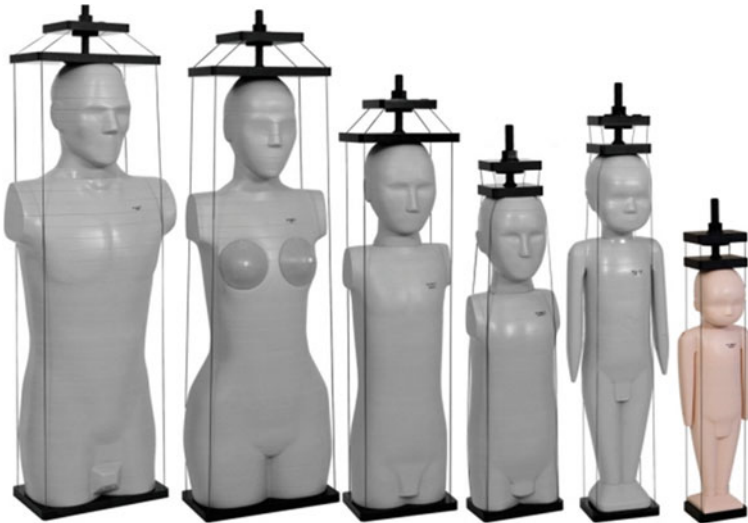


Fig. 3.3 The ATOM[®] phantoms provided by computerized imaging reference systems (CIRS), Inc

newborn (51 cm, 3.5 kg), pediatric 1 year (75 cm, 10 kg), pediatric 5 years (110 cm, 19 kg) and pediatric 10 years (140 cm, 32 kg). Of the three commercial providers of body phantoms, these are the only pediatric body phantoms offered [13]. The phantoms includes cross sectional slices from the apex of the head to just below the groin except for the newborn and pediatric 1 year phantoms which include the legs and arms. Leg and arm attachments are also available upon request for the other 4 ATOM[®] phantoms. All ATOM[®] phantoms are made from the CIRS tissue equivalent epoxy resins. The bone tissue equivalent material is homogeneous and customized to vary in density from 1.41 g/cm³ for the newborn to 1.6 g/cm³ for the adult phantoms depending on the phantom simulated age since human skeleton density varies as a person ages. Human skeletons are not used. The ATOM[®] phantoms are all constructed of CIRS tested proprietary tissue equivalent materials. The linear attenuation coefficients for soft/bone tissue equivalent and lung equivalent materials are within 1 and 3 % of actual soft tissue/bone and lung tissue, respectively. The lung equivalent tissues are made to be low density inhale (0.2 g/cm³), but higher densities are available on special order. Similar to the other body phantoms, the female or male ATOM[®] phantom can be accommodated with naturally shaped breasts, ranging in sizes of 190 or 350 cm³ for the female phantom and 350 cm³ for the male phantom. In addition, supine breasts, shaped as when a patient would be lying on their back are available in three sizes: small (400 cm³ B–C cup), medium (800 cm³ D cup) and large (1,200 cm³ DD cup).

The ATOM[®] phantoms are cut in 2.5 cm cross sectional slices. CIRS has identified on each slice a mapping of the average location of 22 different radio-sensitive organs. This allows the medical physicist to customize the placement of the dosimeter holes to only those locations that are crucial and desired. In addition to the customized dosimeter hole placement, the medical physicist can also have a standard grid of either 3 × 3 or 1.5 × 1.5 cm of holes drilled in each slice. The holes can be 2, 5, 7 or 10 mm in diameter. Holes are filled, when not containing a dosimeter, with custom plugs made of the appropriate tissue equivalent material depending on where the holes are located and what dosimeters are being used. The ATOM[®] phantoms can be prepared to hold a variety of dosimeters including various shaped and sized TLD, OSLD nanoDots, MOSFETs, film, ion chambers or diodes. The medical physicist simply needs to discuss the specific requirements needed for the phantom with the CIRS staff.

3.2.4 Custom Body Phantoms

While the three anthropomorphic body phantoms described in detail above are precisely made and are very human-like, they do have disadvantages. They are extremely expensive, may not be configured in every possible manner and when assembled are very heavy. A clinic should clearly define the benefits and need for purchasing an anthropomorphic body phantom and compare these against the price

of the phantom. Not only will the phantom be expensive, but does the clinic have the equipment and knowledge to analyze the dosimeters normally placed in the body phantoms, i.e., TLD. The dosimetry system may be an extra cost.

There have been other researchers who have developed anthropomorphic body phantoms in an attempt to bypass the disadvantages listed above. Hasanzadeh and Abedelahi built their own anthropomorphic body phantom using a human skeleton and paraffin (plus NaCl) that would accommodate TLD at various locations [14]. Lehmann et al. [15] developed and reported on an anthropomorphic body phantom called the “radiation phantom with humanoid shape and adjustable height (RPHAT)”. The unique characteristic of this body phantom was designed to have an adjustable thickness to address the range of patient thicknesses encountered in the clinic. The height adjustment comes from the fact that the phantom is sliced in the coronal direction instead of the axial direction. The phantom had additional coronal phantom slices that could be inserted in the center of the phantom to increase the thickness as needed [15]. Commercial phantoms may be sliced in the sagittal or coronal direction but only by special order. Despite the expense of the commercial body phantoms, and with a few exceptions, they appear to be the standard anthropomorphic body phantom that the medical physics community continues to use. The need for ideal tissue equivalent materials and the capability to modify the phantoms to the user’s specifications seems to outweigh the cost of these phantoms.

3.3 Anthropomorphic Body-Part Phantoms

Instead of purchasing a complete body phantom, there is often the need to have an anthropomorphic phantom for just a section or part of the body to assess a specific treatment modality or treatment target. Examples of this would be the need for only a head phantom for stereotactic radiotherapy for brain lesions or a thorax for the evaluation of a moving target in a low density organ to evaluate the heterogeneity corrected dose calculations for an SBRT treatment. To address this need for smaller more specific anthropomorphic phantoms, numerous anthropomorphic body-part phantoms have been developed. All of these smaller phantoms have the same requirements as the larger body phantoms such as appropriate tissue equivalent materials and the ability to contain dosimeters of various types depending on the need of the medical physicist. The vast majority of these anthropomorphic body-part phantoms are solid and are primarily made of tissue equivalent plastics. However, there are some body-part phantoms that have plastic shells and are water filled where there might be soft tissue. There are two classifications of anthropomorphic body-part phantoms: those that can commercially purchased for individual use and those that were developed by a quality assurance (QA) service organization or by an individual institution for their own QA purposes.

3.3.1 Commercially Available Anthropomorphic Body-Part Phantoms

Similarly to the anthropomorphic body phantoms, the body-part phantoms are available from a variety of vendors, for several body-parts and that will accommodate various dosimeters. In Table 3.1, a list of the primary vendors and body-part phantoms available from each is listed. The manufacturers of the large body phantoms capitalized on their specific expertise and experience with their own specific tissue equivalent materials when designing and building the smaller body-part phantoms.

Some of the common features for the body-part phantoms listed in Table 3.1 are that they all can accommodate multiple dosimeters depending on the accessories purchased with the phantom. The CIRS, SI, RSD and Modus phantoms are solid and the Phantom Lab is liquid filled. All of the phantoms can hold either TLD or film with the exception of the Modus QUASARTM phantom which only has inserts for ion chambers. The CIRS and SI phantoms can accommodate 3D dosimeters (gels), diodes, MOSFETs and ion chambers with the exception of the CIRS SRS Head phantom, which can not accommodate diodes or MOSFETs. The Phantom Lab phantoms have inserts for TLD, gels, film and ion chambers.

All of the anthropomorphic body-part phantoms that are commercially available are made of appropriate tissue equivalent materials. Some are more heterogeneous than others, but that is by design depending on the body part and the number of heterogeneous tissue structures located within that body-part. All of these phantoms will serve the medical physicist's need, however it is critical that the physicist be capable of taking the dosimeter readings and precisely being able to determine dose from those readings. The most sophisticated and expensive anthropomorphic phantom will be useless if the physicist can not perform the measurements and dosimeter analysis correctly.

Table 3.1 Major commercial providers of anthropomorphic body-part phantoms

Vendor	Body-part			
	Head	Thorax	Moving thorax	Pelvic
Radiology support devices (RSD)	SRS head phantom	–	Dynamic breathing phantom	–
The phantom lab	SRS RSVP phantom TM head	–	–	IMRT RSVP Phantom TM Pelvis
Comp. imaging ref. sys. (CIRS)	SRS head	Thorax phantom	Dynamic thorax phantom	IMRT pelvic 3D phantom
Modus medical devices	–	QUASAR TM body phantom	QUASAR TM body phantom	QUASAR TM body phantom
Standard imaging (SI)	LUCY [®] 3D QA phantom	–	–	–

3.3.2 Anthropomorphic Body-Part Phantoms Developed by a QA Service Organization or Institution for Their Own QA Purposes

Typically this class of anthropomorphic phantom was designed with a single purpose in mind. For example, the Radiological Physics Center (RPC) developed its IMRT spine phantom with the sole purpose of credentialing institutions for participation in a specific spine metastases clinical trial, while de Almeida et al. [16] developed a gynecological pelvic phantom for dose delivery verification and education at their institution. These phantoms are normally not available for purchase, but may be used by many institutions and medical physicists as a part of the QA service being offered.

One such organization that provides phantoms for a service, specifically for NCI funded clinical trial QA, is the RPC. The RPC uses lightweight mailable anthropomorphic phantoms (Fig. 3.4) to evaluate treatment delivery at institutions wanting to participate in NCI sponsored clinical trials. The phantoms simulate lesions to be treated in the brain, head and neck, prostate, liver, spine or lung areas, and allow verification of 3D-CRT, SBRT and IMRT plans. The RPC currently has 65 anthropomorphic body-part phantoms in use. The brain, head and neck, pelvis, spine and thorax RPC phantoms have been described in detail [17–20]. The phantoms contain imageable targets as well as organs at risk whose location and densities are similar to the tissues within the body-part being simulated as seen in Fig. 3.5. Densities and dimensions provide realistic conditions for dose constraints used during the planning and delivery process. A reciprocating table, which is able to reproduce different breathing cycles, is also included when a technique to account for target motion, as might be seen with lung or liver targets, is required for credentialing. Participating institutions are instructed to image the phantom, plan a treatment following guidelines, perform all the QA procedures used in clinic and deliver the plan as if it were a patient.

Fig. 3.4 The RPC IMRT H&N, pelvis and lung phantoms



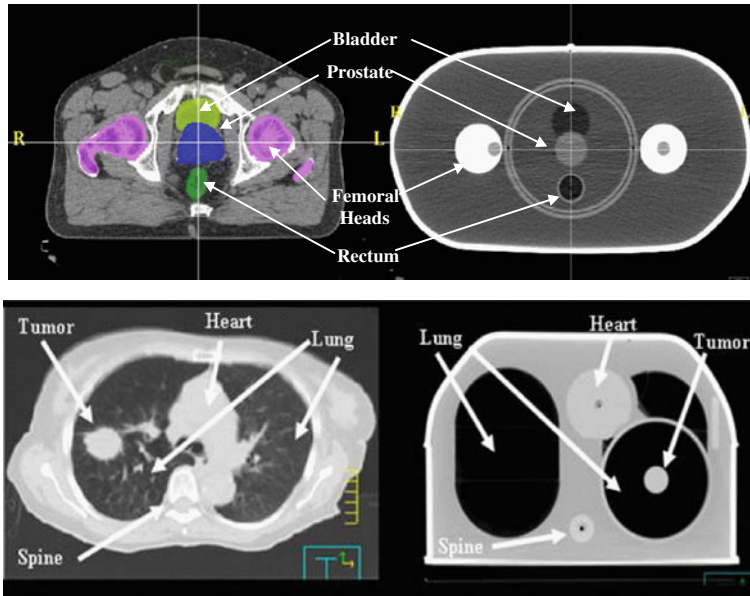


Fig. 3.5 RPC pelvis and lung phantoms with corresponding patient anatomy

The RPC is not the only QA service to use anthropomorphic body-parts. Harrison et al. [21] described the use of a pelvic phantom for an Australian multicenter radiotherapy dosimetry comparison [22]. The Australian pelvic phantom was a solid phantom that had structures representing bone, organ and backfill and it could accommodate the placement of TLD and an ion chamber at various locations. The gynecological pelvic phantom described by de Almeida et al. was a water filled acrylic phantom modeled after the pelvic region of the female Alderson Rando phantom. The unique characteristic of this phantom was that it allowed the placement of tandem and ovoids along with an insert for an ion chamber so that it could be placed at the bladder, rectum and point A locations. Another IMRT head and neck phantom, different from the RPC design, was developed and used by a Belgian-French task group called Groupe Oncologie Radiotherapie Tete Et Cou (GORTEC) to perform a multicenter IMRT dosimetry audit of IMRT delivery. The GORTEC phantom was a solid homogeneous dedicated head and neck polystyrene phantom where ion chambers could be placed at seven different locations coinciding with target and OAR locations. The anthropomorphic body-part phantoms listed above are just a few of the many that are developed at individual institutions for the purpose of performing their own end to end QA of a specific treatment or to verify their treatment planning system's dose calculation accuracy.

With the recent increase in the number of proton radiotherapy centers, the delivery of accurate proton doses to patients has become a topic of concern within

the clinical trial community. The RPC has developed three anthropomorphic body-part phantoms to be used as end to end quality audits for proton therapy of sites in the brain, lung and pelvis. These phantoms are nearly identical to the RPC's other phantoms with the exception that the head phantom is solid and all three phantoms contain proton equivalent plastics. Unlike photon and electron radiotherapy where the planning system dose calculation depends on the CT number versus electron density curve, proton therapy planning system dose calculations depend on the CT number versus relative stopping power (RSP) Ratio. As such the plastics that were good tissue equivalent materials for photons and electrons may not be appropriate for protons because they do not fall on the CT number versus RSP for human tissues. An example of this is the use of high impact polystyrene for photons as a soft tissue substitute, however for protons polystyrene has an RSP that is approximately 10 % different than soft tissue of the same CT number. The RPC and Moyers et al. [23] have made numerous measurements of various plastics to determine which ones are suitable tissue equivalents for proton therapy. Plastics that fall on or very near to the curve representing real human tissues are viewed as being tissue equivalent for proton therapy. Therefore, caution is necessary when using current commercial or QA service anthropomorphic phantoms for proton therapy dosimetry verification. The incorrect plastics can result in large errors in dose and dose distribution.

3.4 Summary

As described, there are numerous options available to the radiotherapy medical physicist in terms of anthropomorphic phantoms. The choice of which to use is highly dependent on the specific needs of the physicist and the specific treatments to be verified. Decisions have to be made as to whether a body phantom is necessary or perhaps a body-part phantom is all that is needed. The type of dosimeter to be placed within the phantom that the physicist knows how to analyze correctly may also play a role as to which phantom is the best fit for your clinic. Regardless of the many variables to choose from, there is no better human substitute than an anthropomorphic phantom for verifying, by means of dose measurements, the complete "end to end" dose delivery process.

Future anthropomorphic phantoms will become even more complex. As radiation oncology enters the era of adaptive radiation therapy (ART), phantoms will be needed to verify the delivery of a radiation dose to a moving or changing target using the imaging systems found on therapy units. These phantoms will not only have structures that can be visualized with kV and MV X-rays, but will have to include some aspect of target position change with time and be able to accommodate dosimeters. The introduction of 3D dosimetry will pose additional challenges in that they are not always tissue equivalent. Finally, the use of charged particle therapy, i.e., protons and carbon ions, will require further investigations as to the suitability of the phantom materials to be used as tissue substitutes.

References

1. Task Group 21, American Association of Physicists in Medicine. (1983). A protocol for the determination of absorbed dose from high-energy photon and electron beams. *Medical Physics*, 10, 741.
2. Westman, A. (1924). A simplified dosimetric method in gynecological deep roentgenotherapy. *Acta Radiologica*, 3, 68.
3. Jensen, A. (1945). Dose measurements in roentgen irradiation of the female pelvis. *Acta Radiologica*, 26, 99.
4. Nahon, J. R., & Hawkes, J. B. (1954). Energy distribution in the thorax during multiple field and rotational therapy. *The American journal of roentgenology*, 72, 819.
5. Wheatley, B. M., & Lister, W. C. (1957). The construction of the phantom. In Court-Brown, W. M., & Doll, R. (Eds.), *Leukaemia and aplastic anaemia in patients irradiated for ankylosing spondylitis, medical research council special report series no. 295*, London: Her Majesty's Stationery Office.
6. Jacobs, M. L., & Pape, L. (1961). Dosimetry for a total-body irradiation chamber. *Radiology*, 77, 788.
7. ICRU 44, (1989). International Commission on Radiation Units and Measurements, *Tissue substitutes in radiation Dosimetry and measurement*, ICRU Report 44, Bethesda, MD: International Commission on Radiation Units and Measurements.
8. ICRU 48, (1992). International Commission on Radiation Units and Measurements, *Phantoms and computational models in therapy, diagnosis and protection*, ICRU Report 48, Bethesda, MD: International Commission on Radiation Units and Measurements.
9. Stacey, A. J., Bevan, A. R., & Dickens, C. W. (1961). A new phantom material employing depolymerised natural rubber. *British Journal of Radiology*, 34, 510.
10. Alderson, S. W., Lanzl, L. H., Rollins, M., & Spira, J. (1962). An instrumented phantom system for analog computation of treatment plans. *The American Journal of Roentgenology*, 87, 185.
11. Campbell, D. W., & Almond, P. R. (1970). A comparison study of the anatomical differences between three RANDO phantoms. *Physics Investigation*, 94, 198.
12. Somerwil, A., & van Kleffens, H. J. (1977). Experience with the Alderson RANDO phantom. *British Journal of Radiology*, 50, 295.
13. Varchena, V. (2002). Pediatric phantoms. *Pediatric Radiology*, 32, 280.
14. Hasanzadeh, H., & Abedelahi, A. (2011). Introducing a simple tissue equivalent anthropomorphic phantom for radiation dosimetry in diagnostic radiology and radiotherapy. *Journal Paramedical Sciences*, 2, 25.
15. Lehmann, J., Stern, R. L., Levy, J., Daly, T. P., Hartmann-Siantar, C. L., & Goldberg, Z. (2004). Radiation phantom with humanoid shape and adjustable thickness (RPHAT)'. *Physics in Medicine and Biology*, 49, N125.
16. de Almeida, C. E., Rodriguez, M., Vianello, E., Ferreira, I. H., & Sibata, C. (2002). An anthropomorphic phantom for quality assurance and training in gynaecological brachytherapy. *Radiotherapy and Oncology*, 63, 75.
17. Stovall, M., Balter, P., Hanson, W. F., & Cole, A. (1995). Quality audit of radiosurgery dosimetry using mailed phantoms. *Medical Physics*, 22, 1009.
18. Molineu, A., Followill, D. S., Balter, P. A., Hanson, W. F., Gillin, M. T., Huq, M. S., et al. (2005). Design and implementation of an anthropomorphic quality assurance phantom for intensity-modulated radiation therapy for the radiation therapy oncology group. *International Journal of Radiation Oncology Biology Physics*, 63, 577.
19. Followill, D. S., Evans, D. R., Cherry, C., Molineu, A., Fisher, G., Hanson, W. F., et al. (2007). Design, development, and implementation of the radiological physics center's pelvis and thorax anthropomorphic quality assurance phantoms. *Medical Physics*, 34, 2070.

20. Caruthers, D., Ibbott, G. S., & Followill, D. S. (2009). Commissioning a new anthropomorphic spine and lung phantom for the remote validation of treatment plans for institutions participating in RTOG 0631. *Medical Physics*, *36*, 2651.
21. Harrison, K. M., Ebert, M. A., Kron, T., Howlett, S. J., Cornes, D., Hamilton, C. S., et al. (2011). Design, manufacture and evaluation of an anthropomorphic pelvic phantom purpose-built for radiotherapy dosimetric intercomparison. *Medical Physics*, *38*, 5330.
22. Ebert, M. A., Harrison, K. M., Howlett, S. J., Cornes, D., Bulsara, M., Hamilton, C. S., et al. (2011). Dosimetric intercomparison for multicenter clinical trials using a patient based anatomic pelvic phantom. *Medical Physics*, *38*, 5167.
23. Moyers, M. F., Sardesai, M., Sun, S., & Miller, D. W. (2010). Ion stopping powers and CT numbers. *Medical Dosimetry*, *35*, 179.

Chapter 4

Motion Phantoms for Radiotherapy

Michael Kissick and Travis McCaw

4.1 Introduction

In both diagnostic and therapeutic applications of medical radiation, there are issues related to patient or organ motion. Motion can degrade image quality or interfere with the delivery of the desired dose distribution. In either case, phantoms are used to explore the issues related to motion before the procedure is applied to the patient. There is a variety of motion phantoms commercially available to address quality control and research needs. Furthermore, virtually no end of in-house motion phantoms has been constructed for use in more specialized investigations. It would be impossible to discuss in any depth the limitless options and varieties of motion phantoms that have been conceived and used. This chapter focuses on applications of motion phantoms to an area of medical physics that requires an ever-increasing characterization of sensitivity to motion: external beam radiation therapy. The various aspects of motion phantom design criteria are discussed as an example of how to approach motion phantom use for other applications of interest.

In general, an understanding of the motion of interest is required, after which a phantom with motion capability needs to be constructed to explore and characterize the implications of this motion for the delivered dose. This chapter is organized as follows: (1) common motion parameters and sites affected by motion are discussed; (2) quality assurance techniques are discussed by reviewing methods to measure motion, the impact of common motion parameters, and the testing of motion management techniques; (3) motion phantom designs are reviewed in terms of requirements, commercial designs, custom designs, and what the future may bring; and (4) the dosimetry associated with motion phantoms is reviewed briefly.

M. Kissick (✉) · T. McCaw

Department of Medical Physics, University of Wisconsin, Madison, WI 53705, USA
e-mail: mwkissick@wisc.edu

As intensity-modulated radiation therapy (IMRT) has advanced and become more prominent, the need for motion and positioning phantoms has also increased. IMRT allows for the delivery of escalated doses to the planning target volume (PTV) while sparing more of the surrounding organs at risk (OAR), creating substantial dose gradients at the PTV boundaries. Treatment margins, as defined in the ICRU 50 and ICRU 62 reports [1, 2], are often incorporated into the PTV or the clinical target volume (CTV) to ensure that the gross tumor volume (GTV) is sufficiently covered by the prescription dose. The use of inadequate treatment margins can result in underdosed regions of the PTV, which could potentially compromise local tumor control [3]. Normal tumor motion, such as respiratory-induced motion, can extend the probability density function of the PTV beyond the coverage of the treatment margins, creating regions of over- and under-dosage within the PTV. Tumor motion can occur both during (intrafraction) and between (interfraction) treatment fractions. Dose errors related to patient setup and registration can be included in this discussion since these errors can be thought of as a motion with zero frequency.

Motion phantoms are useful for a variety of medical physics purposes, both imaging and therapy, but this chapter will concentrate on their use in radiation therapy. However, there is overlap between imaging and therapy, and this overlap can be expected to grow in the future. For example, positron emission tomography (PET) is used for cancer diagnosis, staging, and treatment planning, and the same types of motion phantoms that are used for therapy investigations can be used for PET investigations [4].

Imaging motion phantoms are often custom designed to improve the use of four-dimensional computed tomography (4DCT). Of course, motion phantoms can be used in many other medical applications such as cardiac surgery to improve robotic-assisted surgery. Many studies can now be accomplished with only a computer simulation, opening the door to highly advanced anthropomorphic phantoms that also include cardiorespiratory motion. These virtual phantoms have been made from the visible male and female data sets from the National Library of Medicine [5].

4.2 Motion in Radiation Therapy

For fractionated radiotherapy treatments, there are three general types of motion: organ motion related to patient setup errors, organ motion occurring between fractions, and organ motion occurring within a fraction. Relative to a phantom designed to simulate these motions, the first two are equivalent, effectively making two types of motion: interfraction and intrafraction.

Without any loss of generality, any motion in time, $X(t)$, can be decomposed into a Fourier series of sinusoidal functions, such as

$$X(t) = A \sin(\omega t + \delta) \quad (1)$$

where A is the motion amplitude, ω is the motion frequency, t is time, and δ is the initial phase. A good motion phantom allows one to check for the dosimetric impact of each of these components of motion. It should be noted that the errors in the initial phase are equivalent to setup or registration errors, or, if $\omega = 0$, interfraction motion. In this way, each fraction could have a different initial phase, which is often assumed to be random.

The most severe intrafraction motion generally occurs in the abdominal region. The treatment sites that are most susceptible to interfraction motion are those sites adjacent to the digestive system [6], especially the prostate, seminal vesicles, gynecological tumors, bladder, and rectum. Perhaps the most common example of motion is thoracic motion, which occurs primarily due to respiration, affecting the lungs, liver, kidneys, pancreas, and also the prostate. The prostate and the lung are discussed here as examples of interfraction and intrafraction motion, respectively.

4.2.1 Prostate Motion

The prostate is a good example of a site that often undergoes rotational, as well as translational, motion. For example, Roeske et al. [7] found the standard deviations (SD) of motions along the anterior–posterior (AP), lateral, and superior–inferior (SI) axes to be 2.7, 0.9, and 1.7 mm, respectively. Rotational SDs about the AP, lateral, and SI axes were 1.3° , 4.0° , and 2.1° , respectively. The magnitude of the motion SDs primarily correlated with rectal volume. Note that the SDs represent the variations from the expected positions. The mean positions are often close to zero and smaller than the SDs [6]. These SDs represent the resolution required of a motion phantom to exactly reproduce the motion. Based on the results of Langen and Jones [6], the largest observed displacement of the prostate was 20 mm, and the average SD of displacement along the AP, SI, and lateral axes was 3.0, 2.9, and 1.1 mm, respectively.

A prostate motion phantom design needs to resolve the above motions. Additionally, the required motion resolution may be impacted by the method used to monitor or track prostate motion. Common motion-tracking techniques include portal imaging [8], electronic portal imaging with an implanted marker [9], computed tomography (CT) scans [7, 10], gold seeds [11], and ^{125}I seeds [12].

It should be stressed that prostate motion can be fairly random, and it can occur within a fraction, as well. Intrafraction motion can interfere with the beam modulation, creating dosimetric errors that may not be sufficiently addressed with increased margins. These issues will be discussed in greater detail in the context of lung motion. The temporal behavior of prostate motion can vary rapidly, due to bowel gas for example. Considering that external beam radiation therapy treatments of the prostate usually occur over many fractions, dose errors due to prostate motion during a fraction are mostly averaged away by the many fractions comprising the treatment. The prostate moves primarily between fractions and that

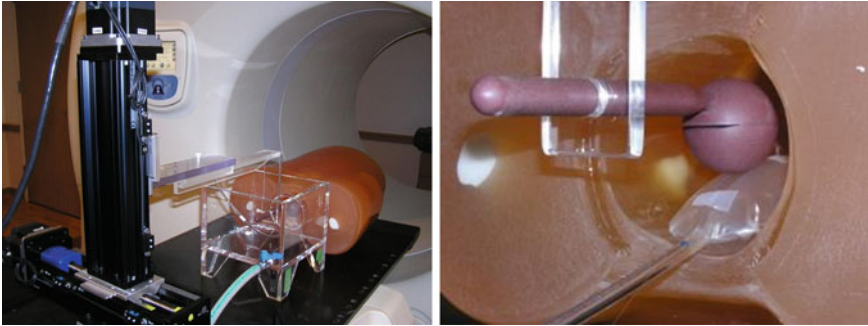


Fig. 4.1 Experimental setup for the design and development of a prostate motion monitoring system. The motion phantom arm attaches to the WUSTL 4D motion phantom and moves within an anthropomorphic phantom (Kyoto Kagaku, Inc., Japan). The setup is shown entering the TomoTherapy Hi-Art IITM machine bore

requires daily localization of the CTV, usually with CT, radiopaque markers, portal images, or megavoltage CT (MVCT) in the case of helical tomotherapy (HT).

Prostate motion phantoms must simulate not only natural motion of the prostate, but also controlled motion, such as in the presence of a rectal balloon [13]. Note that Patel et al. [13] used ultrasound localization, so a motion phantom that tests positioning accuracy with their technique would also need to be compatible with ultrasound.

One may also want to model deformation or some aspects of relative motions within a phantom. An example of such a phantom is shown in Fig. 4.1. A Virtual WaterTM (Med-Cal, Verona, WI) phantom with a space for film insertion is made to move in a realistic pattern both within an anthropomorphic phantom (Kyoto Kagaku, Inc., Japan) and in a water tank. The anthropomorphic phantoms produced by Kyoto Kagaku, Inc. are designed for imaging and described elsewhere in this text, but they are used here to investigate small and linearizable dose perturbations induced by target motion. In this way, heterogeneity in the presence of bone, prostate, water, and air (rectal balloon) is accurately simulated.

4.2.2 Respiratory Motion

The frequency power spectrum of respiratory motion is very different from that of prostate motion. Specifically, respiration is cyclical. While there is randomness associated with respiration, the dominant behavior is nearly sinusoidal. If 3D conformal treatment techniques are used, then the frequency spectrum is of little importance, except for low-frequency drifts that have a motion period on the order of the length of the treatment fraction. Neglecting randomness for now, respiratory motion is often modeled with the following function [14]:

$$X(t) = A\cos^{2n}(\pi t/\tau + \pi/2) \quad (2)$$

where A is the amplitude of motion along a given direction, X ; n is an integer; and τ is the period. The exponent of the cosine function governs the asymmetry of the breathing waveform. George et al. [15] found that using $2n = 4$ shows good agreement with patient data, but setting $2n = 1$ agrees nearly as well. Therefore, a motion phantom should be able to produce motion patterns of the form of Eq. (2) in order to model realistic motion. If possible, a phantom capable of fully programmable motion is preferable in order to most accurately model patient motion. For instance, the Washington University in St. Louis (WUSTL) 4D motion phantom is fully programmable for 3D translations [16]. It uses stepping motors that are capable of producing motion speeds typical of respiration. The phantom is highly accurate and can support in excess of 10 lbs.

The WUSTL 4D motion phantom has been used in conjunction with anthropomorphic phantoms, for instance in the work of Kissick et al. [17] investigating why HT lung treatments without active motion management are robust to dose errors. A spherical, Virtual WaterTM tumor phantom with a slit for radiochromic film was placed at the end of the motion stage of the WUSTL 4D motion phantom and moved within a LUNGMANTM (Kyoto Kagaku, Inc., Japan) chest phantom. This configuration is shown in Fig. 4.2.

A study by Kashani et al. [18] accounted for deformation of the lung tissue and surrounding vasculature due to respiration. This study also acknowledged a need for programmable motion to accurately model the irregularities of respiratory motion waveforms. However, another approach to producing random motion is to take the Fourier transform of a realistic motion waveform [i.e., Eq. (2)] and compute the relative weights for each frequency. Then, use those weights to sum each motion frequency component modeled with Eq. (1).

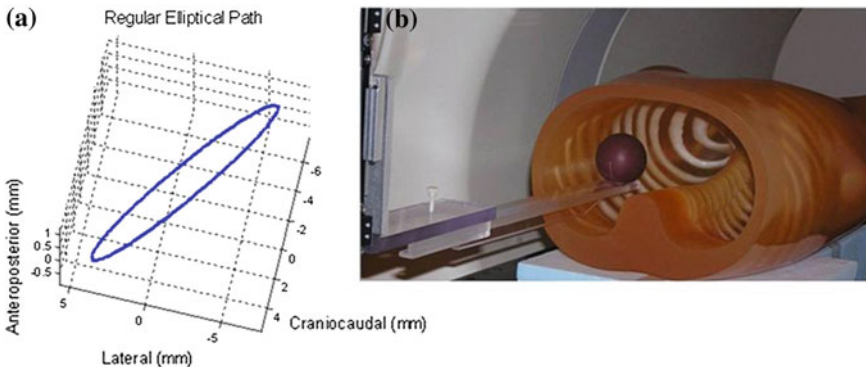


Fig. 4.2 Pictured is a phantom setup to demonstrate the capability of HT to deliver a plan to a moving tumor without motion management. The motion trace programmed for the lung tumor phantom inside the anthropomorphic chest phantom (LUNGMANTM, Kyoto Kagaku, Inc., Japan) is shown in (a). The motion phantom arm attaches to the WUSTL 4D motion phantom and is shown in (b) as it enters the Tomotherapy Hi-Art IITM machine bore

The spatial patterns of lung tumor motion can be complicated. By tracking implanted markers, Seppenwoolde et al. [19] found a wide variety of elliptical patterns to the motion. Erratic behavior in time and space is present within each fraction for respiratory motion. Additionally, the initial phase of motion from fraction to fraction is highly random. However, this interfraction positional randomness has the benefit of averaging out dose variations introduced by interplay between dynamic modulation and tumor motion over many fractions [20].

The amplitude of lung motion is largest in the lower lobe, closer to the diaphragm. The motion of the diaphragm along the craniocaudal axis varies widely, from 7 to 38 mm, with an average close to 10 mm [6]. More extensive information about the amplitude of lung motion can be found in Seppenwoolde et al. [19].

Apart from the lungs, another organ that moves largely with respiration is the liver. Liver motion has been measured with nuclear medicine techniques using ^{99}Tc [21, 22] and with CT [23].

4.2.3 Other Treatment Sites Affected by Motion

While lung and prostate treatments are the most prominent examples of sites that are susceptible to motion complications, several other treatment sites also undergo motion. For many of these other sites, the mechanisms are the same as for prostate motion (often caused by bowel movements) or lung motion (caused by respiration). For example, motion of the seminal vesicles, bladder, and rectum is induced in a manner similar to the prostate. In addition, other sites in the lower abdominal region move in similar irregular patterns, such as gynecological tumors. In this region, motion can be controlled passively with the use of rectal balloons and urinary catheter balloons, but there is often residual motion that needs to be investigated with a phantom that can simulate this motion. Likewise, in addition to the lung, there are several sites that move with respiration, such as the liver, the kidneys, and the pancreas. The same respiratory motion waveform that is used for lung motion likely applies to these sites also, but the amplitude of motion and hysteresis will differ.

A comprehensive review of motion patterns for all treatment sites was assembled by Langen and Jones [6]. Langen and Jones found that the corpus uteri can move 3 to 15 mm along the SI axis and 0 to 9 mm along the AP axis at the 95 % confidence level, due primarily to changes in bladder and rectal volume. Balloons are used in these organs to reduce the volume variation, thereby reducing motion of nearby treatment sites. The seminal vesicles move about 1 mm in both the AP and the SI directions, and about 0.5 mm laterally, but all of these motions can exceed 1 cm [6]. Sites subject to respiratory motion have been studied more thoroughly. The liver moves as much as the lower lobe of the lung, because of its close proximity to the diaphragm, but the motion is almost exclusively along the SI axis with a magnitude of 2 to 3 cm [6]. The kidneys and the pancreas both follow a similar motion pattern.

In addition to intrafraction organ motion, all treatment sites are also subjected to interfraction motion, which is primarily the result of patient setup uncertainties. Many studies of setup uncertainties have been completed, but most consider only particular treatment units or techniques, such as an investigation of the MVCT guidance of HT using an anthropomorphic phantom [24]. In that study, it was determined that the automated registration procedure is typically precise to within 1 mm. However, occasional large errors occurred, so a manual check of each registration is required.

The use of motion phantoms can be further generalized to include the investigation of various motion management techniques, such as proper margins [25]. Active motion management techniques—such as optical imaging, X-ray imaging, surrogate markers for 4DCT, immobilization devices, and active breathing control—are outlined and reviewed by Webb [26].

4.3 Quality Assurance Using Motion Phantoms

A major use of a motion phantom is the evaluation and quality assurance of techniques that manage patient motion during treatment. Such techniques include the measurement and prediction of tumor motion and the determination of the correlation between the motion of internal organs and external markers.

4.3.1 *Measuring Patient Motion*

Using the Varian[®] Real-time Position Management[™] (RPM) system (Varian Medical Systems, Palo Alto, CA), Vedam et al. [27] explored the correlation between the motion of internal organs and external markers in the context of respiratory-gated radiotherapy treatments. For stereotactic radiosurgery, a great deal of precision and accuracy in positioning is required. Optical imaging of passive infrared reflectors, placed on the phantom as they would be on a patient [28], can be used to evaluate the utility of the optical system.

In addition to the optical technique of the Varian[®] RPM[™] system, another technique is to measure with X-ray imaging [29]. Fiducial markers are implanted in the prostate, for example, and the movement is tracked with fluoroscopy. The issues that a motion phantom can be used to explore are how many fiducials are needed, and how well the motion correlates with other measurements. The fiducial markers can potentially shift, and quality control should be used to investigate these issues. Implanted fiducial markers have been used to measure lung motion also [19]. Tumors can also be located with ultrasound [30], and this technique is often used for registration confirmation. A motion phantom can be used in this context to explore the precision of ultrasound imaging for registration verification. Respiratory monitoring can also be accomplished with non-imaging devices such

as a spirometer [31]. It would be more difficult to use a motion phantom for this case, unless the sense of the motion is broadened to include moving something that changes air volume simultaneously with tumor position to test the correlation of tumor motion with changes in air volume.

4.3.2 Accounting for Motion Amplitude

The current approach to account for tumor motion in external beam radiotherapy, even with advanced IMRT, is the expansion of treatment margins. There are various approaches to determine the appropriate size of the enlarged margin, such as using a 4DCT to measure the actual tumor path [32, 33]. A useful approach involves registration of the tumor to an average motion position and using statistical approaches to optimize the margin size [25]. Phantoms are essential for the evaluation of margin sizes prior to clinical use to ensure proper coverage of the PTV in the presence of motion.

4.3.3 Measuring the Impact of Motion Frequency

The American Association of Physicists in Medicine Task Group 76 report [34] recommends that respiratory motion management should be used when the motion amplitude of the target exceeds 5 mm. However, considering motion only in the context of amplitude and margins neglects the possibility of internal cold spots and the loss of tumor control that they might cause [3, 35]. The reason is that interplay [20, 36, 37] dynamics are a function of frequency. By ignoring frequency, the assumption is made that there is no interplay, perhaps even before it is explored and determined to be negligible. Such an assumption was acceptable when there was no IMRT, and motion effects were limited to the blurring of field penumbra. When motion effects are determined to be only at the boundary, then adding a margin to account for motion is an acceptable solution. However, it is of the opinion of the authors of this chapter that one should not assume that frequency is negligible until it is demonstrated to be so.

Based on the work of Kissick et al. [37, 38] with HT, as well as studies by other investigators, dose errors in the radiation planning treatment volume (PTV) can be minimized by applying planning and delivery constraints that will avoid spatial and temporal interference between dynamic intensity modulation of the radiation beam and patient motion during IMRT [39]. Work in this area is timely because of the likely emergence of dose painting for non-uniform, ‘theragnostic’ dose prescriptions, and the effort devoted to the planning and delivery of these treatments.

4.3.4 Testing Motion Management Techniques

There are a number of new technologies that have been developed to minimize and correct for complications that arise from patient motion and positioning errors. An excellent review is provided by Webb [26]. Other reviews also exist for specific motions, such as the review of respiratory motion by Keall [40]. A motion phantom is useful for exploring all approaches to motion management, including passive strategies (i.e., enlarged margins) and active strategies, such as the re-assortment of beamlet weights used by HT motion management [41]. In all cases, a controlled motion is required to connect the dose errors to the motion characteristics.

Motion phantoms are used to explore optimal margin size, such as that proposed by Van Herk [25]. Only with a controlled motion can the trade-off between a reduced duty cycle and sharp dose gradients from gating be explored. Motion is often tracked with a surrogate device. A 4DCT is used to connect the surrogate motion to the organ or tumor motion of interest. There are always questions that need to be explored, such as how many external surrogate markers (infrared reflectors) are needed for an accurate and precise application of the Varian[®] RPM[™] system [15]. Internal markers are often used to record the motion paths of various voxels in vivo [19]. Internal markers can move, however, and a motion phantom can be used to explore the resulting dose error.

No matter how motion is tracked, whether by optical reflectors, X-ray attenuation in high atomic number implants, ultrasound, electromagnetic transponders, 4DCT with on board cone beams, or any other method, the accuracy of the motion-tracking system must be explored with a separate surrogate motion stage. Such a surrogate stage is included with the Washington University 4D Phantom [16], and it should exist for all programmable advanced motion phantoms.

4.4 Motion Phantom Designs

Depending on the intended use of the phantom, a motion phantom must satisfy certain mechanical specifications. Mechanical requirements of a motion phantom for different applications and the specifications of select commercial and custom motion phantoms are discussed in this section.

4.4.1 Overview of Motion Phantom Requirements

A motion phantom requires a motor and a translation device to make a more traditional type of phantom move relative to the laboratory frame for which the treatment is prepared. The motor can be as simple as a rotary motor with a cam shaft for simple harmonic motion. A more sophisticated motion stage would have a

stepping or servomotor connected to a linear actuator. The actuator would translate or rotate the dosimetry system, which could be any of a range of phantoms. It is common to use Solid WaterTM or an anthropomorphic phantom with thermoluminescent dosimeter (TLD) chips or film (radiochromic or radiographic) embedded.

The motion needs to be controlled by some type of control circuit, typically a computer, so the user can achieve a high level of accuracy in the amplitude, frequency, initial phase, and start and stop times of the motion. To create realistic motions with randomness or positional drifting (i.e., low-frequency components), computer-programmable motors are preferable. The level of precision and accuracy required depends upon the expected dose distribution and the sensitivity of the final outcome to dose inaccuracies. For example, an optical-tracking system may be precise to a fraction of a millimeter. One may wish to know the position to within that measurement precision. On the other hand, the penumbra of a megavoltage X-ray beam is on the order of millimeters. Therefore, one could argue that error less than a millimeter is negligible. The same thinking also applies to timing and frequency. Many motion studies sample motion at 30 Hz [6].

Another requirement of motion phantoms is the dimensional degrees of freedom: up to three orthogonal translations and three orthogonal rotations, all of which can potentially be modulated in time. Usually, only a subset of these degrees of freedom is required. Even a simple one-dimensional motion phantom is useful for motion sensitivity studies. Any motion phantom that can accurately move another phantom at 30 Hz position specification with sub-millimeter accuracy and precision should cover nearly all applications for motion issues in radiation therapy.

4.4.2 Commercial Motion Phantoms

A variety of motion phantoms are available commercially to address research and clinical needs. The majority of commercial motion phantoms can be categorized as either a motion platform or a thorax motion phantom. A motion platform has a moving stage that translates and/or rotates the phantom of interest, permitting motion studies with static phantoms. Thorax motion phantoms are thorax phantoms with dynamic components that mimic respiratory motion. Examples of both types of motion phantoms are discussed in the following sections, focusing on their technical specifications and examples of their use in the literature.

4.4.2.1 Motion Platforms

The respiratory gating platform (Standard Imaging (SI), Middleton, WI) is a motion platform capable of one-dimensional sinusoidal motion. The technical specifications for this motion phantom are summarized in Table 4.1 [42]. The period and amplitude of motion are independently controlled. The respiratory gating phantom has a weight capacity of 32 kg and can fasten to imaging and treatment couches for

Table 4.1 Technical specifications for the SI respiratory gating platform

Period of oscillation	2–6 s
Period resolution	0.5 s
Period accuracy	± 0.2 s
Period repeatability	± 0.1 s
Motion amplitude	5–40 mm
Translational resolution	5 mm
Translational accuracy	± 0.5 mm
Translational repeatability	± 0.5 mm

improved positioning stability. Investigations utilizing this phantom include studies of 4DCT data sets, specifically the correlation of uncertainties [43] and the development of a semiautomatic maximum intensity projection algorithm [44].

The QUASARTM programmable respiratory motion platform [45] (Modus Medical Devices, Inc., London, Ontario, Canada) can reproduce one-dimensional sinusoidal and patient respiratory waveforms. Additionally, this motion platform can create a lateral hysteresis motion of up to 1 cm in amplitude for investigations with phase separation. A chest wall platform moves in the AP direction to model surrogate motion patterns for motion-tracking systems and gating investigations. The included software allows the user to display and edit motion waveforms, which can be created or imported from motion-tracking systems. This phantom has a weight capacity of 20 kg.

The dynamic platform 008 PL [46] (CIRS, Inc., Norfolk, VA) can produce programmable motion in the SI direction with an amplitude of up to ± 25 mm. An independently controlled, programmable chest wall platform moves in the AP direction with a maximum amplitude of ± 25 mm. Both motions are produced with an accuracy of ± 0.1 mm. The motion control software provides a graphical interface with which the following motion waveforms can be programmed: $\sin(t)$, $1-2\cos^4(t)$, $1-2\cos^6(t)$, sawtooth, and sharkfin. The dynamic platform has a weight capacity of 32 kg.

For fully programmable motion in three dimensions, there is the WUSTL 4D phantom [16]. The WUSTL 4D phantom has a motion stage that can move along three orthogonal axes. Motion along each axis is independently controlled and fully programmable, allowing for arbitrary motion in three dimensions. Custom motion trajectories can be specified at fifty positions per second with ± 0.2 mm positioning accuracy. Additionally, the WUSTL 4D phantom has a second motion stage capable of motion in the anterior–posterior direction for modeling of surrogate motion waveforms. The WUSTL 4D phantom has been utilized for numerous studies, including motion investigations of tomotherapy treatments [17, 38, 47], evaluations of electromagnetic tumor-tracking and kV imaging localization [48–52], and evaluation of dynamic MLC tumor-tracking treatments [53]. In addition to one-dimensional sinusoids and patient motion traces, which can be achieved with the motion platforms discussed previously, these studies also use three-dimensional patient motion traces, one-dimensional sinusoids with added randomness, and raster scanning.

4.4.2.2 Thorax Motion Phantoms

Contrary to motion platforms, which translate a separate phantom of interest, thorax motion phantoms model the human thorax and have the capability of producing respiratory motions. The moving parts are commonly interchangeable inserts designed for diagnostic and therapeutic studies. The QUASARTM programmable respiratory motion phantom [54] (Modus Medical Devices, Inc., London, Ontario, Canada) is a 12 kg acrylic phantom with an oval shape. A chest wall platform provides surrogate motion in the AP direction. Cylindrical cedar wood inserts ($\rho = 0.4 \text{ g/cm}^3$) are used to model lung tissue and can be translated in the SI direction. One-dimensional motion waveforms can be created, or imported from a motion-tracking system and edited, using the included software. Inserts are available for 4DCT and PET/CT imaging, film and ion chamber measurements, and with the tumor located off-axis. The QUASARTM respiratory motion rotation stage [54] (Modus Medical Devices, Inc., London, Ontario, Canada) is available as an attachment, allowing rotations of the inserts up to $\pm 30^\circ$. Several studies have been completed using the QUASARTM programmable respiratory motion phantom to model respiratory motion as a one-dimensional sinusoid, including investigations of target volume definitions in the presence of motion [55, 56], the impact of intrafraction motion on intensity-modulated treatments [57–59], and a real-time position and dose monitoring system [60].

The dynamic thorax phantom [61] (CIRS, Inc., Norfolk, VA) is similar in design to the QUASARTM programmable respiratory motion phantom, but it also more accurately models the tissues of the thorax. The dynamic thorax phantom is a 17.2 kg epoxy phantom, oval in shape, with an anthropomorphic spine. The phantom material is designed to be tissue equivalent in the energy range from 50 keV to 25 MeV. A cylindrical insert with an off-axis tumor model translates along and rotates about the SI axis, thereby generating motion in three dimensions. Motion control software allows the user to create motion trajectories that follow one of five built-in waveforms (see Table 4.2 for motion specifications), or import and edit respiratory motion traces. Interchangeable inserts accommodate MOSFET dosimeters, microionization chambers, film, PET/CT targets, and gel dosimeters. An independently controlled surrogate motion platform models chest wall (AP) or diaphragmatic (SI) motion. The three-dimensional motion capabilities of the dynamic thorax phantom have been used in studies of MV fluoroscopy for

Table 4.2 Motion specifications for the CIRS dynamic thorax phantom

SI motion amplitude	$\pm 25 \text{ mm}$
AP/lateral motion amplitude (via rotation)	$\pm 10 \text{ mm}$
Linear motion accuracy	$\pm 0.1 \text{ mm}$
Rotational motion accuracy	$\pm 0.2 \text{ degrees}$
Motion period accuracy	5 ms
Surrogate motion amplitude	$\pm 25 \text{ mm}$
Built-in motion waveforms	$\sin(t)$, $1-2\cos^4(t)$, $1-2\cos^6(t)$, sawtooth, sharkfin

verification of gated treatments [62], 4D digital tomosynthesis for image-guided therapy [63], and positron-emitting fiducial markers for tumor-tracking [64]. The dynamic thorax phantom has also been used to model one-dimensional motion for studies of dose verification using an electronic portal imaging device to track tumor motion [65], using PRESAGETM dosimeters to verify gated treatments [66], multiple breath-hold cone-beam CT for image-guided therapy [67], and variability in treatment margin definition due to target motion [68, 69].

Of the commercially available thorax motion phantoms, the dynamic breathing phantom [70] (Radiology Support Devices, Inc., Long Beach, CA) most accurately models the anatomy of the thorax and deformation due to respiratory motion. The dynamic breathing phantom is a humanoid torso composed of elasticized versions of the soft tissue materials used in the Alderson radiation therapy phantom (Radiology Support Devices, Inc., Long Beach, CA), including lungs, skin, and sub-dermis. Additionally, rigid bones are incorporated that move with respiration. Respiratory motion is controlled by programming the air pressure within the lungs, creating chest wall motion in excess of 1 cm. A tumor model within one of the lungs follows an independently programmed motion, controlled by a pneumatic motion actuator. The phantom can execute 5–20 breaths per minute according to one of the following waveforms: $\sin^2(t)$, $\sin^4(t)$, $\sin^6(t)$, $1 - \sin^4(t)$, $1 - \sin^6(t)$. Court et al. [71] used the dynamic breathing phantom with a custom tumor model to reproduce a one-dimensional patient motion trace for an investigation of dose errors due to interplay for numerous treatment techniques and treatment planning systems.

4.4.3 Custom Motion Phantoms

For investigations in which commercial motion phantoms are unavailable or insufficient, motion phantoms of varying complexities can be created in-house. This section addresses examples of custom motion phantoms in the literature, with an emphasis on the considerations of phantom design.

The simplest of motion phantoms can be created with a rotary drive motor connected to a translation stage. Such a phantom is capable of one-dimensional sinusoidal oscillation with adjustable period and amplitude of motion. Using a rod for a translation stage, Ford et al. [72] constructed an oscillator to investigate respiration-correlated spiral CT. With a similar phantom, Keall et al. [73] studied the feasibility of using dynamic MLC modulation to track tumor motion. An oscillator with a wider range of applications can be constructed by using a platform on rails as the translation stage [74, 75].

Oscillators are favorable as motion phantoms for their simplicity, but they are limited to sinusoidal motion at constant angular velocity. A more advanced motion platform, such as that constructed by Fitzpatrick et al. [76], is capable of programmable, irregular, one-dimensional motion. Instead of a rotary drive motor, Fitzpatrick et al. used a stepper motor driven by a motor controller. The stepper

motor was connected to the motion stage by a linear actuator. Stepper motors are capable of accurate positioning and are best suited for moving static loads at low accelerations. Applying large torques with a stepper motor can result in a loss of rotor positioning control. The torque that the system experiences can be regulated with displacement feedback, but the use of displacement feedback can produce a positioning delay. Decreasing the pitch of the linear actuator can also reduce the torque required from the stepper motor. However, a lower pitch requires a greater angular velocity from the stepper motor, thereby reducing the torque that the motor can apply without loss of positioning control. In addition to the mechanical capabilities of the drive system, the memory of the stepper motor controller also needs to be considered for the generation of irregular motion. The motor controller used in this study was designed for short or cyclical motion profiles; no additional trajectories could be added once the motion began. To circumvent this limitation, Fitzpatrick et al. segmented the time–displacement coordinate pairs defining the motion trajectory. Each segment of coordinates was approximated with a second-order polynomial, effectively reducing each segment of coordinate pairs to a single pair. This approach also smooths high-frequency noise from patient motion traces, thereby reducing the stress on the motor [76].

Litzenberg et al. [77] designed a similar one-dimensional motion stage to meet the quality assurance needs of four-dimensional treatment planning and delivery. Specifically, the motion platform was designed to achieve spatial resolutions of 1 mm and temporal resolutions of 2–30 Hz for the evaluation of CT imaging, electromagnetic tracking, and fluoroscopic imaging. A polycarbonate stage was translated with a ball-screw electric cylinder linear actuator. The linear actuator was connected by a belt to an AC servomotor with position-encoded feedback. The motor was controlled by a programmable motion controller through a servo driver. Input/output ports were included to allow communication with other devices to import motion patterns or synchronize the phantom motion with image acquisition or treatment delivery. The accuracy of the phantom motion was tested using the Varian® RPM™ system. The positional accuracy was less than 0.5 mm for motions with amplitudes up to 60 mm, velocities up to 80 mm/s, and accelerations up to 100 mm/s². The phantom motion synchronization was accurate to within 2 ms [77].

For studies utilizing irregular, two-dimensional motion patterns, Richter et al. [78] constructed a motion platform driven by a programmable industrial robot. The driven platform was a multi-layered, heterogeneous phantom designed to simulate the thoracic wall, lung tissue, and tumor. The positioning accuracy of the motion platform was verified using infrared markers and 4DCT imaging. The resolution of the 4DCT images along the direction of motion was 1.5 mm, limiting the accuracy with which the phantom position could be determined [78].

To generate fully programmable, three-dimensional motion for the verification of IMRT treatments, Nakayama et al. [79] developed a three-dimensional motion phantom. The motion phantom consisted of a three-dimensional driving mechanism, composed of three orthogonal ball-screw linear actuators; a computer control system; and phantoms for film dosimetry. The computer control system was connected

to the driving mechanism with 10 m cables to avoid exposing the radiation-sensitive circuits. The positioning accuracy of the three-dimensional motion phantom was verified using the Polaris[®] Vicra[®] system (Northern Digital, Inc., Waterloo, Ontario, Canada) [79].

While a fully programmable, three-dimensional motion platform is capable of reproducing surrogate or tumor motion traces, a single motion platform cannot be used to simulate both motions. Zhou et al. [80] developed a respiratory motion simulator with two independently controlled, fully programmable, three-dimensional motion platforms to simulate motion of the skin surface and the tumor for the quality assurance of CyberKnife[®] (Accuray, Inc., Sunnyvale, CA) treatments. The skin-motion simulator was composed of three orthogonal linear slides, while the tumor motion simulator had two linear slides and a vertically mounted linear piston actuator. The two motion simulators were each driven by a servomotor with an optical rotary encoder for positional feedback. The positional accuracy of the respiratory motion simulator was confirmed using the Optotrack motion capture system (Northern Digital, Inc., Waterloo, Ontario, Canada). It was determined that positional errors of the motion simulator, as a function of time, were the superposition of both low- and high-frequency components. The low-frequency components corresponded to the frequency of motion, while the high-frequency components were representative of the natural frequencies of the simulator. The high-frequency positioning errors can be reduced by improving the structural rigidity of the motion phantom [80].

In addition to the motion of the target relative to the treatment beam, another concern in the treatment of moving tumors is the motion of the target relative to the surrounding tissue. The non-rigid nature of the motion of soft tissue is especially important for dose verification and adaptive treatments. Deformable registration identifies equivalent points in different phases of a four-dimensional image of non-rigid motion, thereby facilitating the calculation of dose to these points. However, deformable motion phantoms are required to experimentally verify the accuracy of deformable registration algorithms. Due to the limited selection of commercially available options, deformable phantoms comprise a large portion of the in-house motion phantoms found in the literature. An example of an in-house deformable motion phantom was constructed by Kashani et al. [18]. The chest wall and cavity of a diagnostic thoracic phantom (Radiology Support Devices, Inc., Long Beach, CA) served as the body of the deformable phantom, while the abdominal insert was replaced with high-density foam to extend the existing lung insert. For consistency with published values of lung tissue attenuation, the foam was soaked in a diluted iodinated contrast agent solution. Several rigid tumor structures of known shape and varying density were placed throughout the foam insert. A Lucite diaphragm driven by a one-dimensional actuator compressed the lung insert according to programmed motion profiles. The reproducibility of the phantom deformation was confirmed with CT scans of the phantom for differing levels of compression [18]. The phantom was then modified with the placement of many small markers throughout the foam insert and used for the assessment of deformable registration algorithms [81].

A separate evaluation of deformable image registration with an in-house deformable motion phantom was completed by Serban et al. [82] Lung tissue was simulated using a natural latex balloon filled with natural sponges, dampened to more closely match the Hounsfield unit value of lung tissue. A tissue-equivalent model tumor with slits for radiochromic film was embedded in the sponge. Nylon wires and Lucite beads were placed throughout the sponge to both aid and evaluate the deformable registration process. The balloon was placed within a Lucite cylinder to model the thoracic cavity, and the space surrounding the balloon was filled with water to model the chest wall. A piston attached to a programmable motor compressed the balloon [82]. This phantom was also used to evaluate the RAD-POS real-time position monitoring and dose measuring system (Best Medical Canada, Ottawa, Ontario, Canada) [83].

A deformable motion phantom similar to that of Serban et al. [82] was created by Nioutsikou et al. [84] An important distinction is that the tumor model in the phantom of Nioutsikou et al. was not embedded in the sponge, but rigidly connected to the positioner gantry that compressed the sponge. Consequently, the tumor motion would match the programmed motion waveform. Furthermore, the programmable motion gantry was capable of three-dimensional motion, allowing for more complex motion patterns. By connecting the motion controller for one motion axis to the MU/64 signal from a linear accelerator, the tumor motion was correlated with dose delivery, thereby creating more reproducible intrafraction motion [84].

To verify the accuracy of four-dimensional dose calculations, Vinogradskiy et al. [85] created a deformable lung insert for the Radiological Physics Center anthropomorphic thorax phantom [86]. The lung was modeled by a cylinder filled with slices of sponges and foam. A water-equivalent tumor volume was placed in the center of the slices. The slice structure of the lung allowed for film dose measurements throughout the lung volume. A real-time controller and stepper motor driving a piston compressed the lung insert according to programmed motions. A platform attached to the piston made the system compatible with respiratory motion monitoring systems. To ensure the reproducibility of the setup, the cylindrical insert was keyed for alignment, rails within the insert guided the placement and travel of lung slices, and metal wires and pinpricks were used to register film images with calculated dose distributions [85, 87].

4.4.4 Motion Phantoms of the Future

As evidenced by the numerous examples of custom motion phantoms, currently available motion phantoms do not address all the needs of the clinical and research physicist. This section discusses potential characteristics of future motion phantoms based on observation of trends in medical physics. Radiation therapy with intensity-modulated external beams is becoming more precise with higher dose gradients. Sub-volume boosts and dose painting treatments actually create dose gradients within the PTV. The impact of motion-related uncertainties, including tissue

deformation and changing heterogeneity, is consequently amplified. Therefore, phantoms that deform and have realistic anthropomorphic features will be of even greater importance. Furthermore, the anthropomorphic features will need to be able to deform in realistic ways, including some ability to independently produce rotations and translations. Also, there are many treatment sites within the body, most of which move uniquely, so a whole-body phantom will be desirable. In order to provide quality control on a patient-specific basis for all aspects of motion, including interplay with the modulation patterns, highly programmable motion and frequency control are essential for future motion phantoms. Finally, increased flexibility in the types of dosimeters that can be inserted in the phantom will be needed to accurately measure the impact of the improved motion capabilities.

An example of a motion phantom that satisfies the above criteria has the following attributes: (1) a whole-body anthropomorphic phantom with modular and deformable components to model common treatment sites and their motions; (2) a flexible robot arm that can be attached to particular parts of the anthropomorphic phantom; (3) fully programmable motion to match patient-specific motions; and (4) compatibility with several different dosimeters. A discussion of dosimetry for motion investigations is the subject of [Sect. 4.5](#). This same phantom should also be compatible with imaging devices, such as PET/CT scanners that are used for treatment planning [4], so that motion and positioning issues can be explored in a holistic way throughout the entire treatment process.

Steidl et al. [88] developed a phantom that meets many of the criteria discussed in this section for dosimetry of scanned ion beams. An anthropomorphic chest wall phantom was created that could undergo deformable motion independent of the target. The target, located at the end of a robotic arm, was capable of fully programmable motion in six dimensions. The target consisted of a three-dimensional array of pinpoint ionization chambers interleaved with radiographic films to provide dose measurements throughout the target volume. The parts of the phantom that were irradiated were devoid of metal, making it compatible with CT imaging. A phantom such as this, extended to simulate the whole body, for photon therapy, that is tissue equivalent across the diagnostic and therapeutic energy ranges, would satisfy many of the projected needs of medical physicists in the future [88].

4.5 Dosimetry with Motion Phantoms

The choice of dosimeter is an important consideration for any measurement, impacting both the amount of data obtained and the uncertainty in the data. Contrary to static measurements of traditional (i.e., unmodulated) deliveries, where a dosimeter within the field sees a homogeneous dose distribution, dosimeters for dynamic measurements will see time-dependent dose distributions, similar to IMRT measurements. As a result, the concerns that are involved in the selection of a dosimeter for a motion investigation are similar to those for the measurement of an IMRT delivery. The selection of dosimeters for IMRT QA is

the topic of AAPM Task Group 120 [89]. At a minimum, a motion phantom should provide a point dose measurement and a planar dose measurement to permit evaluation of the delivered distribution using the gamma index [90]. Ionization chambers provide absolute point dose measurements with minimal uncertainty. TLDs [85] and MOSFETs [71] have been used for dose measurements distributed throughout a volume at the expense of increased uncertainty. Film is frequently used for planar measurements, but arrays of diodes or ionization chambers can be used with motion stages with sufficient weight capacity.

Given the potential application of motion phantoms to patient-specific QA, studies of the predictive power of gamma passing rates for IMRT QA should be considered for motion phantom dosimetry. Nelms et al. [91] demonstrated that per-beam gamma passing rates do not correlate with dose errors in anatomic regions of interest. Instead, DVH-based metrics were shown to better predict the impact of delivery errors on the patient DVH [92]. Taking these two studies into consideration, motion phantoms used for patient-specific IMRT QA should be capable of three-dimensional dosimetry to best determine the impact of patient motion on treatment delivery.

References

1. ICRU 50 (1993). Prescribing, recording, and reporting photon beam therapy. Report 50, International Commission on Radiation Units and Measurements.
2. ICRU 62 (1999). Prescribing, recording, and reporting photon beam therapy: Supplement to ICRU Report 50. Report 62, International Commission on Radiation Units and Measurements.
3. Tomé, W. A., & Fowler, J. F. (2002). On cold spots in tumor subvolumes. *Medical Physics*, 29, 1590–1598.
4. McCall, K. C., Barbee, D. L., Kissick, M. W., & Jeraj, R. (2010). PET imaging for the quantification of biologically heterogeneous tumours: Measuring the effect of relative position on image-based quantification of dose painting-targets. *Physics in Medicine and Biology*, 55, 2789–2806.
5. National Institutes of Health, (2012, December 27) *National Library of Medicine*. <http://www.nlm.nih.gov>.
6. Langen, K. M., & Jones, D. T. L. (2001). Organ motion and its management. *International Journal of Radiation Oncology Biology Physics*, 50, 265–278.
7. Roeske, J. C., Forman, J. D., Mesina, C. F., He, T., Pelizzari, C. A., Fontenla, E., et al. (1995). Evaluation and changes in the size and location of the prostate, seminal vesicles, bladder, and rectum during a course of external beam radiation therapy. *International Journal of Radiation Oncology Biology Physics*, 33, 1321–1329.
8. Balter, J. M., Sandler, H. M., Lam, K., Bree, R. L., Lichter, A. S., & Haken, R. K. T. (1997). Measurement of prostate movement over the course of routine radiotherapy using implanted markers. *International Journal of Radiation Oncology Biology Physics*, 37, 205–212.
9. Vigneault, E., Pouliot, J., Laverdiere, J., Roy, J., & Dorion, M. (1997). Electronic portal imaging device detection of radioopaque markers for the evaluation of prostate position during megavoltage irradiation: A clinical study. *International Journal of Radiation Oncology Biology Physics*, 37, 205–212.

10. Schild, S. E., Casale, H. E., & Bellefontaine, L. P. (1993). Movements of the prostate due to rectal and bladder distension: Implications for radiotherapy. *Medical Dosimetry*, *18*, 13–15.
11. Crook, J., Raymond, Y., Yang, H., & Esche, B. (1995). Prostate motion during radiotherapy as assessed by fiducial markers. *Radiotherapy and Oncology*, *37*, 35–42.
12. Althof, V. G. M., Hoekstra, C. J. M., & te Loo, H. J. (1996). Variation in prostate position relative to bony anatomy. *International Journal of Radiation Oncology Biology Physics*, *34*, 709–715.
13. Patel, R. R., Orton, N., Tomé, W. A., Chappell, R., & Ritter, M. A. (2003). Rectal dose sparing with a balloon catheter and ultrasound localization in conformal radiation therapy for prostate cancer. *Radiotherapy and Oncology*, *67*, 285–294.
14. Lujan, A. E., Balter, J. M., & Haken, R. K. T. (2003). A method for incorporating organ motion due to breathing into 3D dose calculation in the liver: Sensitivity to variations in motion. *Medical Physics*, *30*, 2643–2649.
15. George, R., Vedam, S. S., Chung, T. D., Ramakrishnan, V., & Keall, P. J. (2005). The application of the sinusoidal model to lung cancer patient respiratory motion. *Medical Physics*, *32*, 2850–2861.
16. Malinowski, K., Noel, C., Lu, W., Lechleiter, K., Hubenschmidt, J., Low, D., & Parikh, P. (2007). Development of the 4D phantom for patient-specific, end-to-end radiation therapy QA. In *Proceedings of SPIE Medical Imaging Conference*, 6510.
17. Kissick, M. W., Mo, X., McCall, K. C., Schubert, L. K., Westerly, D. C., & Mackie, T. R. (2010). A phantom model demonstration of tomotherapy dose painting delivery, including managed respiratory motion without motion management. *Physics in Medicine and Biology*, *55*, 2983–2995.
18. Kashani, R., Lam, K., Litzenberg, D., & Balter, J. (2007). Technical note: A deformable phantom for dynamic modeling in radiation therapy. *Medical Physics*, *34*, 199–201.
19. Seppenwoolde, Y., Shirato, H., Kitamura, K., Shimizu, S., van Herk, M., Lebesque, J. V., et al. (2002). Precise and real-time measurement of 3D tumor motion in lung due to breathing and heartbeat, measured during radiotherapy. *International Journal of Radiation Oncology Biology Physics*, *53*, 822–834.
20. Bortfeld, T., Jokivarsi, K., Goitein, M., Kung, J., & Jiang, S. B. (2002). Effect of intra-fraction motion dose delivery: Statistical analysis and simulation. *Physics in Medicine and Biology*, *47*, 2203–2220.
21. Weiss, P. H., Baker, J. M., & Potchen, E. J. (1972). Assessment of hepatic respiratory excursion. *Journal of Nuclear Medicine*, *37*, 21–29.
22. Harauz, G., & Bronskill, M. J. (1979). Comparison of the liver's respiratory motion in supine and upright positions: Concise communication. *Journal of Nuclear Medicine*, *20*, 733–735.
23. Balter, J. M., Ten Haken, R. K., Lawrence, T. S., Lam, K. L., & Robertson, J. M. (1996). Uncertainties in CT-based radiation therapy treatment planning associated with patient breathing. *International Journal of Radiation Oncology Biology Physics*, *36*, 167–174.
24. Boswell, S., Tomé, W., Jeraj, R., Jaradat, H., & Mackie, T. R. (2006). Automatic registration of the setup verification process for the special case of a rigid head phantom. *Medical Physics*, *33*, 4395–4404.
25. Herk, V. (2004). Errors and margins in radiation therapy. *Seminars in Radiation Oncology*, *14*, 52–64.
26. Webb, S. (2006). Motion effects in (intensity modulated) radiation therapy: A review. *Physics in Medicine and Biology*, *51*, R403–R425.
27. Vedam, S. S., Keall, P. J., Kini, V. R., & Mohan, R. (2001). Determining parameters for respiration-gated radiotherapy. *Medical Physics*, *28*, 2139–2146.
28. Tomé, W. A., Mehta, M. P., Meeks, S. L., Buatti, J. M., Bova, F. J., & Friedman, W. A. (2000). Image guided fractionated stereotactic radiotherapy. *Radiotherapy and Oncology*, *56*, S60.
29. Kitamura, K., Shirato, H., Seppenwoolde, Y., Onimura, R., Oda, M., Fujita, K., et al. (2002). Three-dimensional intrafractional movement of prostate measured during real-time tumor-

- tracking radiotherapy in supine and prone treatment positions. *International Journal of Radiation Oncology Biology Physics*, 53, 1117–1123.
30. Lattanzi, J., McNeely, S., Donnelly, S., Palacio, E., Hanlon, A., Schultheiss, T. E., et al. (2000). Ultrasound base stereotactic guidance in prostate cancer—quantification of organ motion and set-up errors in external beam radiotherapy. *Computer Aided Surgery*, 5, 289–295.
 31. Jiang, S. B., & Doppke, K. (2001). Dosimetric effect of respiratory motion on the treatment of breast cancer with tangential fields. *Medical Physics*, 28, 1228.
 32. Rietzel, E., Liu, A. K., Doppke, K. P., Wolfgang, J. A., Chen, A. B., Chen, G. T. Y., et al. (2006). Design of 4D treatment planning target volumes. *International Journal of Radiation Oncology Biology Physics*, 66, 287–298.
 33. Pan, T., Lee, T. Y., Rietzel, E., & Chen, T. Y. (2004). 4D-CT imaging of a volume influenced by respiratory motion on multi-slice CT. *Medical Physics*, 31, 333–340.
 34. Keall, P. J., Mageras, G. S., Balter, J. M., Emery, R. S., Forster, K. M., Jiang, S. B., et al. (2006). The management of respiratory motion in radiation oncology report of the AAPM Task Group 76. *Medical Physics*, 33, 3874–3900.
 35. Kissick, M. W., & Mackie, T. R. (2009). Task Group 76 Report on ‘The management of respiratory motion in radiation oncology’ [*Medical physics* 33, 3874–3900 (2006)]. *Medical Physics*, 36, 5721–5722.
 36. Yu, C. X., Jaffray, D. J., & Wong, J. W. (1998). The effects of intrafraction motion on the delivery of dynamic intensity modulation. *Physics in Medicine and Biology*, 43, 91–104.
 37. Kissick, M. W., Boswell, S. A., Jeraj, R., & Mackie, T. R. (2005). Confirmation, refinement, and extension of a study in intrafraction motion interplay with sliding jaw motion. *Medical Physics*, 32, 2346–2350.
 38. Kissick, M. W., Flynn, R. T., Westerly, D. C., Hoban, P. W., Mo, X., Soisson, E. T., et al. (2008). On the impact of longitudinal breathing motion randomness for tomotherapy delivery. *Physics in Medicine and Biology*, 53, 4855–4873.
 39. Ehler, E. D., Nelms, B. E., & Tomé, W. A. (2007). On the dose to a moving target while employing different IMRT delivery mechanisms. *Radiotherapy and Oncology*, 83, 49–56.
 40. Keall, P. (2004). 4-Dimensional computed tomography imaging and treatment planning. *Seminars in Radiation Oncology*, 14, 81–90.
 41. Lu, W., Chen, M., Ruchala, K. J., Chen, Q., Langen, K. M., Kupelian, P. A., et al. (2009). Real-time motion-adaptive-optimization (MAO) in Tomotherapy. *Physics in Medicine and Biology*, 54, 4373–4398.
 42. Standard Imaging, Inc. (2012). *Respiratory Gating Platform: Specifications*. <http://www.standardimaging.com>.
 43. Ehler, E. D., & Tomé, W. A. (2010). On correlated sources of uncertainty in four dimensional computed tomography data sets. *Technology in Cancer Research and Treatment*, 9, 299–306.
 44. Mancosu, P., Sghedoni, R., Bettinardi, V., Aquilina, M. A., Navarria, P., Cattaneo, G. M., et al. (2010). Semiautomatic technique for defining the internal gross tumor volume of lung tumors close to liver/spleen cupola by 4D-CT. *Medical Physics*, 37, 4572–4576.
 45. Modus Medical Devices, Inc. (2013). *Modus: Respiratory Motion Platform*. <http://www.modusmed.com>.
 46. Computerized Imaging Reference Systems, Inc. (2013). *Dynamic Platform Model 008PL: Products—CIRS*. <http://www.cirsinc.com>.
 47. Chaudhari, S. R., Goddu, S. M., Rangaraj, D., Pechenaya, O. L., Lu, W., Kintzel, E., et al. (2009). Dosimetric variances anticipated from breathing-induced tumor motion during tomotherapy treatment delivery. *Physics in Medicine and Biology*, 54, 2541–2555.
 48. Smith, R. L., Lechleiter, K., Malinowski, K., Shepard, D. M., Housley, D. J., Afghan, M., et al. (2009). Evaluation of linear accelerator gating with real-time electromagnetic tracking. *International Journal of Radiation Oncology Biology Physics*, 74, 920–927.
 49. Santanam, L., Noel, C., Willoughby, T. R., Esthappan, J., Mutic, S., Klein, E. E., et al. (2009). Quality assurance for clinical implementation of an electromagnetic tracking system. *Medical Physics*, 36, 3477–3486.

50. Wiersma, R. D., Riaz, N., Dieterich, S., Suh, Y., & Xing, L. (2009). Use of MV and kV imager correlation for maintaining continuous real-time 3D internal marker tracking during beam interruptions. *Physics in Medicine and Biology*, *54*, 89–103.
51. Santanam, L., Malinowski, K., Hubenschmidt, J., Dimmer, S., Mayse, M. L., Bradley, J., et al. (2008). Fiducial-based translational localization accuracy of electromagnetic tracking system and on-board kilovoltage imaging system. *International Journal of Radiation Oncology Biology Physics*, *70*, 892–899.
52. Liu, W., Wiersma, R. D., Mao, W., Luxton, G., & Xing, L. (2008). Real-time 3D internal marker tracking during arc radiotherapy by the use of combined MV-kV imaging. *Physics in Medicine and Biology*, *53*, 7197–7213.
53. Smith, R. L., Sawant, A., Santanam, L., Venkat, R. B., Newell, L. J., Cho, B., et al. (2009). Integration of real-time internal electromagnetic position monitoring coupled with dynamic multileaf collimator tracking: An intensity-modulated radiation therapy feasibility study. *International Journal of Radiation Oncology Biology Physics*, *74*, 868–875.
54. Modus Medical Devices, Inc. (2013). *Modus: Respiratory Motion Phantom*. <http://www.modusmed.com>.
55. Cuijers, J. P., Verbakel, W. F. A. R., Slotman, B. J., & Senan, S. (2010). A novel simple approach for incorporation of respiratory motion in stereotactic treatments of lung tumors. *Radiotherapy and Oncology*, *97*, 443–448.
56. Nakamura, M., Narita, Y., Sawada, A., Matsugi, K., Nakata, M., Matsuo, Y., et al. (2009). Impact of motion velocity on four-dimensional target volumes: A phantom study. *Medical Physics*, *36*, 1610–1617.
57. Ong, C., Verbakel, W. F. A. R., Cuijers, J. P., Slotman, B. J., & Senan, S. (2011). Dosimetric impact of interplay effect on RapidArc lung stereotactic treatment delivery. *International Journal of Radiation Oncology Biology Physics*, *79*, 305–311.
58. Oliver, M., Gladwish, A., Staruch, R., Craig, J., Gaede, S., Chen, J., et al. (2008). Experimental measurements and Monte Carlo simulations for dosimetric evaluations of intrafraction motion for gated and ungated intensity modulated arc therapy deliveries. *Physics in Medicine and Biology*, *53*, 6419–6436.
59. Oliver, M., Staruch, R., Gladwish, A., Craig, J., Chen, J., & Wong, E. (2008). Monte Carlo dose calculation of segmental IMRT delivery to a moving phantom using dynamic MLC and gating log files. *Physics in Medicine and Biology*, *53*, N187–N196.
60. Cherpak, A., Ding, W., Hallil, A., & Cygler, J. E. (2009). Evaluation of a novel 4D in vivo dosimetry system. *Medical Physics*, *36*, 1672–1679.
61. Computerized Imaging Reference Systems, Inc. (2013). *Dynamic Thorax Phantom Model 008A: Products—CIRS*. <http://www.cirsinc.com>.
62. Tai, A., Christensen, J. D., Gore, E., Khamene, A., Boettger, T., & Li, X. A. (2010). Gated treatment delivery verification with on-line megavoltage fluoroscopy. *International Journal of Radiation Oncology Biology Physics*, *76*, 1592–1598.
63. Maurer, J., Godfrey, D., Wang, Z., & Yin, F. (2008). On-board four-dimensional digital tomosynthesis: First experimental results. *Medical Physics*, *35*, 3574–3583.
64. Chamberland, M., Wassenaar, R., Spencer, B., & Xu, T. (2011). Performance evaluation of real-time motion tracking using positron emission fiducial markers. *Medical Physics*, *38*, 810–819.
65. Aristophanous, M., Rottmann, J., Court, L. E., & Berbeco, R. I. (2011). EPID-guided 3D dose verification of lung SBRT. *Medical Physics*, *38*, 495–503.
66. Brady, S. L., Brown, W. E., Clift, C. G., Yoo, S., & Oldham, M. (2010). Investigation into the feasibility of using PRESAGETM/optical-CT dosimetry for the verification of gating treatments. *Physics in Medicine and Biology*, *55*, 2187–2201.
67. Boda-Heggemann, J., Fleckenstein, J., Lohr, F., Wertz, H., Nachit, M., Blessing, M., et al. (2011). Multiple breath-hold CBCT for online image guided radiotherapy of lung tumors: Simulation with a dynamic phantom and first patient data. *Radiotherapy and Oncology*, *98*, 309–316.

68. Rit, S., van Herk, M., Zijp, L., & Sonke, J. (2012). Quantification of the variability of diaphragm motion and implications for treatment margin construction. *International Journal of Radiation Oncology Biology Physics*, 82, e399–e407.
69. Vergalasova, I., Maurer, J., & Yin, F. (2011). Potential underestimation of the internal target volume (ITV) from free-breathing CBCT. *Medical Physics*, 38, 4689–4699.
70. Radiological Support Devices (2009). *Radiology Support Devices | Dynamic Anatomical Respiring Humanoid Phantom*. <http://www.rsdphantoms.com/index.html>.
71. Court, L. E., Seco, J., Lu, X., Ebe, K., Mayo, C., Ionascu, D., et al. (2010). Use of a realistic breathing lung phantom to evaluate dose delivery errors. *Medical Physics*, 37, 5850–5857.
72. Ford, E. C., Mageras, G. S., Yorke, E., & Ling, C. C. (2003). Respiration-correlated spiral CT: A method of measuring respiratory-induced anatomic motion for radiation treatment planning. *Medical Physics*, 30, 88–97.
73. Keall, P. J., Kini, V. R., Vedam, S. S., & Mohan, R. (2001). Motion adaptive x-ray therapy: A feasibility study. *Physics in Medicine and Biology*, 46, 1–10.
74. Kaganaki, B., Read, P. W., Molloy, J. A., Larner, J. M., & Sheng, K. (2007). A motion phantom study on helical tomotherapy: The dosimetric impacts of delivery technique and motion. *Physics in Medicine and Biology*, 52, 243–255.
75. Jiang, S. B., Pope, C., Jarrah, K. M. A., Kung, J. H., Bortfeld, T., & Chen, G. T. Y. (2003). An experimental investigation on intra-fraction organ motion effects in lung IMRT treatments. *Physics in Medicine and Biology*, 48, 1773–1784.
76. Fitzpatrick, M. J., Starkschall, G., Balter, P., Antolak, J. A., Guerrero, T., Nelson, C., et al. (2005). A novel platform simulating irregular motion to enhance assessment of respiration-correlated radiation therapy procedures. *Journal of Applied Clinical Medical Physics*, 6, 13–21.
77. Litzenberg, D. W., Hadley, S. W., Lam, K. L., & Balter, J. M. (2007). A precision translation stage for reproducing measured target volume motions. *Journal of Applied Clinical Medical Physics*, 8, 111–118.
78. Richter, A., Wilbert, J., & Flentje, M. (2011). Dosimetric evaluation of intrafractional tumor motion by means of a robot driven phantom. *Medical Physics*, 38, 5280.
79. Nakayama, H., Mizowaki, T., Narita, Y., Kawada, N., Takahashi, K., Mihara, K., et al. (2008). Development of a three-dimensionally movable phantom system for dosimetric verifications. *Medical Physics*, 35, 1643–1650.
80. Zhou, T., Tang, J., Dieterich, S., & Cleary, K. (2004). A robotic 3-D motion simulator for enhanced accuracy in CyberKnife stereotactic radiosurgery. *International Congress Series*, 323–328.
81. Kashani, R., Hub, M., Kessler, M. L., & Balter, J. M. (2007). Technical note: A physical phantom for assessment of accuracy of deformable alignment algorithms. *Medical Physics*, 34, 2785–2788.
82. Serban, M., Heath, E., Stroian, G., Collins, D. L., & Seuntjens, J. (2008). A deformable phantom for 4D radiotherapy verification: Design and image registration evaluation. *Medical Physics*, 35, 1094–1102.
83. Cherpak, A., Serban, M., Seuntjens, J., & Cygler, J. E. (2011). 4D dose-position verification in radiation therapy using the RADPOS system in a deformable lung phantom. *Medical Physics*, 38, 179–187.
84. Nioutsikou, E., Symonds-Taylor, J. R. N., Bedford, J. L., & Webb, S. (2006). Quantifying the effect of respiratory motion on lung tumour dosimetry with the air of a breathing phantom with deforming lungs. *Physics in Medicine and Biology*, 51, 3359–3374.
85. Vinogradskiy, Y. Y., Balter, P., Followill, D. S., Alvarez, P. E., White, R. A., & Starkschall, G. (2009). Verification of four-dimensional photon dose calculations. *Medical Physics*, 36, 3438–3447.
86. Followill, D. S., Evans, D. R., Cherry, C., Molineu, A., Fisher, G., Hanson, W. F., et al. (2007). Design, development, and implementation of the Radiological Physics Center's pelvis and thorax anthropomorphic quality assurance phantoms. *Medical Physics*, 34, 2070–2076.

87. Vinogradskiy, Y. Y., Balter, P., Followill, D. S., Alvarez, P. E., White, R. A., & Starkschall, G. (2009). Comparing the accuracy of four-dimensional photon dose calculations with three-dimensional calculations using moving and deforming phantoms. *Medical Physics*, *36*, 5000–5006.
88. Steidl, P., Richter, D., Schuy, C., Schubert, E., Haberer, T., Durante, M., et al. (2012). A breathing thorax phantom with independently programmable 6D tumour motion for dosimetric measurements in radiation therapy. *Physics in Medicine and Biology*, *57*, 2235–2250.
89. Low, D. A., Moran, J. M., Dempsey, J. F., Dong, L., & Oldham, M. (2011). Dosimetry tools and techniques for IMRT. *Medical Physics*, *38*, 1313–1338.
90. Low, D. A., Harms, W. B., Mutic, S., & Purdy, J. A. (1998). A technique for the quantitative evaluation of dose distributions. *Medical Physics*, *25*, 656–661.
91. Nelms, B. E., Zhen, H., & Tomé, W. A. (2011). Per-beam, planar IMRT QA passing rates do not predict clinically relevant patient dose errors. *Medical Physics*, *38*, 1037–1044.
92. Zhen, H., Nelms, B. E., & Tomé, W. A. (2011). Moving from gamma passing rates to patient DVH-based QA metrics in pretreatment dose QA. *Medical Physics*, *38*, 5477–5489.

Chapter 5

Phantoms in Brachytherapy

Yun Yang and Mark J. Rivard

5.1 Introduction

Brachytherapy is a subfield of radiation oncology where miniature radiation sources are placed in close contact or within the human body [1]. Sources are frequently embedded surgically and can be temporarily implanted or placed permanently. Common radionuclides used for brachytherapy include ^{192}Ir , ^{137}Cs , and ^{125}I [2]. Clinical application of these sources is performed in the high-dose-rate (HDR) or low-dose-rate (LDR) regimes at $>12\text{ Gy/h}$ or $<2\text{ Gy/h}$, respectively. With HDR ^{192}Ir brachytherapy, a single source is robotically positioned for several minutes within catheters or needles implanted in the patient [3]. With LDR ^{125}I brachytherapy, dozens of sources can be permanently implanted and in direct contact with tissue [4].

Phantoms serve many purposes in the field of brachytherapy, often permitting scientific evaluation where experimentation on a human subject is not possible. Technical investigations of radionuclide choice, photon emissions, dose distributions, and surgical technique may be performed through use of brachytherapy phantoms. This chapter investigates the role of phantoms over the entire field of brachytherapy, covering radiation dosimetry, treatment simulation, and imaging.

Y. Yang
Department of Radiation Oncology, Duke University Medical Center, DUMC 3295,
Durham, NC 27710, USA

M. J. Rivard
Department of Radiation Oncology, Tufts University School of Medicine, Boston, MA,
USA

M. J. Rivard (✉)
Department of Radiation Oncology, # 246, Tufts Medical Center, 800 Washington Street,
Boston, MA 02111, USA
e-mail: mrivard@tuftsmedicalcenter.org

5.2 Brachytherapy Dosimetry

For clinical and research purposes, there is a need to evaluate radiation dose distributions in the vicinity of brachytherapy sources. This is especially common for determining AAPM TG-43 brachytherapy dosimetry parameters for subsequent clinical treatment planning. Radiation dose distributions may be characterized through experimental measurements or computational radiation transport simulations.

5.2.1 Experimental Measurements

Dosimetric measurements with phantoms represent a physical assessment of a realistic situation. This advantage is complemented by the fact that dosimetric measurements are often performed on the same source that is used clinically. A weakness of physical measurements is the correlation of the detector response to the desired quantity, e.g., absorbed dose [5]. Further, measurement of brachytherapy source dose distributions is confounded by the high dose gradients and large variation in dose rates near the source [6]. For a sufficient detector signal, detector size may be compromised, i.e., enlarged, and subsequently the spatial resolution is degraded and volume-averaging effects may arise. A key attribute of a brachytherapy dosimetry phantom is the ability to rigidly position the radiation detector at a known distance from the brachytherapy source [7]. Stiff plastics are commonly used.

Phantoms in brachytherapy dose measurements are typically designed to either mimic the circumstances of a patient treatment, are therefore composed of an assortment of materials to reflect the realistic composition, or are designed to be radiologically equivalent to water or be chemically pure to minimize uncertainties in correlating response to absorbed dose. Being radiologically equivalent to water by design minimizes the magnitude of the correlation of detector response to absorbed dose to water [8]. However, a more accurate dosimetric technique may be to use an exceedingly pure phantom material in which the correlation uncertainties are low, but the magnitude of the correction is high [9]. This is an area of active research.

Brachytherapy sources emit a wide range of photon energies, and detectors are often customized to a specific energy regime to minimize calibration uncertainties. The dosimetric influence of material heterogeneities having unit density and effective atomic numbers near seven is minimal for high-energy photon-emitting sources such as ^{192}Ir , ^{137}Cs , and ^{60}Co . For low-energy photon-emitting sources such as ^{125}I , ^{103}Pd , and ^{131}Cs , the influence of material composition due to the photoelectric effect can be striking [10]. Consequently, contaminants to the phantom material can cause significant perturbation of the measured dose distribution [11, 12]. Measurements of radiation dose distributions are influenced by the scattering environment; this effect

can be pronounced for high-energy photon-emitting sources [13]. To obtain an accurate measure of the sought dose distribution, the dosimetry investigator must be aware of the influence of phantom composition and phantom size effects [14].

The American Association of Physicists in Medicine (AAPM) provides guidance to dosimetry investigators for evaluating brachytherapy source dose distributions [15, 16]. Water is the standard reference medium in which measured dose distributions in phantom should be converted. The influence of phantom size and composition on detector response is noted, and the dosimetry investigator should specify this information in his report. Further, because of the great influence of phantom material composition on radiation attenuation and absorbed dose for low-energy photon-emitting brachytherapy sources, the dosimetry investigator is advised to chemically analyze the phantom to determine composition in comparison to the manufacturer-reported composition [15]. The sensitivity of dose to phantom composition is less pronounced for high-energy photon-emitting sources [16].

It is not easy to measure brachytherapy source dose distributions, especially in the reference phantom medium of liquid water. While there are no studies to our knowledge using water as the detector medium, there is the work at the M.D. Anderson Cancer Center in which thermoluminescent dosimeter (TLD) powder as a detector was used inside a water phantom [17, 18]. For ^{131}Cs seeds, there was good agreement of their measurements in liquid water compared to Monte Carlo methods [12, 19] also in liquid water. In addition to TLD powder, other radiation detectors for brachytherapy source dosimetry include TLD cubes (i.e., $1 \times 1 \times 1 \text{ mm}^3$) and radiochromic film [20, 21]. Each detector type will have unique handling and positioning requirements in the phantom chosen for the measurement.

While not in general use in the clinic, a new detector type utilizing polymer gels is under investigation [22–24]. An advantage of this approach is that the brachytherapy phantom and detector materials are one and the same, minimizing concerns for material heterogeneities and dose gradient changes at the detector boundary. Without concern for detector position uncertainties, polymer gel readout becomes paramount for evaluation of absorbed dose at a specified distance from a brachytherapy source. Readout methods include optical light analogous to computed tomographic (CT) reconstruction, ultrasound, and magnetic resonance imaging (MRI) using conventional equipment [25]. Also, polymer gels are sensitive to oxygen contamination and diffusion of the irradiated gel, which can blur the delivered radiation dose distribution.

5.2.2 Radiation Transport Simulations

Non-physical assessment of brachytherapy dose distributions is often performed using Monte Carlo methods for radiation transport simulations [26, 27]. Unlike physical measurements using phantoms, computational simulations of radiation

transport may include unphysical possibilities. This aspect is both disadvantageous in that a realistic environment is never present, yet can also be advantageous in numerous other ways. For example, simulations of radiation transport in expensive phantom materials or clinical circumstances may be performed—all without any of the deleterious aspects of radiation exposure. The radiological influence of changing phantom material composition by small amounts can be examined readily using Monte Carlo methods. The mass density of the phantom material can also be varied easily with Monte Carlo methods—even considering impossible phantom material designs, compositions, and mass densities. Further unreachable aspects of an experimental setup include a dosimetric assessment of individual photon energies from nuclear disintegration [28], separation of primary and scattered photons within the phantom [29], and individually analyzing the dosimetric contribution of photons and electrons penetrating the brachytherapy source capsule [30]. There also can be significant costs savings when using Monte Carlo methods in comparison with conducting dosimetric measurements in phantoms.

Computational approaches to evaluating brachytherapy source dose distributions are primarily limited by the following effects [31]:

- (a) computer power,
- (b) uncertainties in radionuclide energy spectrum,
- (c) variations in dynamic internal components, causing changes in the dose distribution,
- (d) uncertainties in atomic and nuclear data such as phantom material cross sections, and
- (e) limitations of the physics models used in the Monte Carlo code.

Over time, the influence of these limitations will diminish. Computing power has only improved over time and has become more readily available. Groups such as the National Nuclear Data Center of Brookhaven National Laboratory regularly evaluate radionuclide disintegration and subsequent photon emissions, updating the standard spectrum every few years [32]. Changes between these evaluations have been minimal over the past decade or so for the clinical radionuclides mentioned in this chapter. Though it seems obvious not to, some brachytherapy manufacturers design a source with dynamic internal components that cause the radiation dose distribution to change upon altering the source orientation. Without detailed information from the manufacturer, often including proprietary design information, the dosimetry investigator cannot adequately model the dosimetric influence of dynamic internal components. With the harmonization of medical physics and nuclear physics computational research, uncertainties in phantom material cross sections have significantly diminished in the past two decades. Consequently, there are no clinically relevant differences between the truth and current cross-sectional data. Finally, advancements in medical physics computational research has developed benchmark cases and subsequently permitted Monte Carlo code intercomparisons [32, 33]. While this is still a lively area of research, it

seems there are no significant differences among current codes for the photon energies and phantom materials in common use in brachytherapy.

An area of active research in Monte Carlo methods for estimating brachytherapy source dose distributions is development of standardized computational phantoms [34, 35]. There are computerized phantoms simulating the human body in great detail, with resolution smaller than 1 mm, and include many millions of voxels [36]. These realistic computational phantoms highlight limitations with existing treatment planning software, facilitate Monte Carlo code intercomparisons, permit assessment of new brachytherapy sources [37], and allow multimodality comparisons such as brachytherapy versus external-beam radiotherapy [38]. It is expected that their use will increase, eventually serving as high-powered test cases for clinical medical physicists to commission brachytherapy treatment planning systems [39].

5.3 Therapy Simulation and Imaging Phantoms

Phantoms may be used in brachytherapy to simulate the surgical implantation procedure, to facilitate imaging specific to brachytherapy, to evaluate consistency and accuracy for segmenting regions of interest, i.e., contouring, and to test source compatibility with new equipment before patient use.

5.3.1 Surgical Simulation

The most common disease sites for brachytherapy are prostate, breast, and gynecological sites. For the prostate, the most popular one on the market is the ultrasound prostate training phantom (Fig. 5.1), model 053-I by CIRS, Inc. This disposable phantom serves as tool to practice permanent LDR seed surgical implantation for prostate brachytherapy. It is also possible to use this phantom as a practice tool for needle placement in HDR ^{192}Ir brachytherapy.

To our knowledge, there are no surgical practice phantoms for breast brachytherapy from any manufacturer. While the CIRS, Inc., model 051 breast biopsy phantom (Fig. 5.2) could easily be modified to simulate needle placement for interstitial HDR ^{192}Ir brachytherapy, most breast brachytherapy performed today is with MammoSite-like balloons, not done interstitially.

Also to our knowledge, there are no surgical practice phantoms for gynecological brachytherapy from any manufacturer. It seems that the CIRS, Inc., model 404 female pelvis ultrasound training phantom (Fig. 5.3) could be modified to match the needle insertion resistance and bony anatomy physically present on women. In this way, an assortment of common HDR ^{192}Ir brachytherapy implantation procedures could be practiced without direct patient involvement or experimentation.

Fig. 5.1 The model 053-I ultrasound prostate training phantom by CIRS, Inc. <http://www.cirsinc.com/products/all/78/ultrasound-prostate-training-phantom/>. This phantom serves to provide imaging quality assurance, assessment of contouring proficiency, and surgical implantation proficiency



Fig. 5.2 The model 051 triple-modality breast biopsy training phantom by CIRS, Inc. <http://www.cirsinc.com/products/all/63/triple-modality-biopsy-training-phantom/>. With the embedded biopsy targets, this phantom could serve as a surgical training phantom for interstitial or balloon breast brachytherapy



Another phantom use during surgical simulation is for transpupillary illumination preceding plaque placement for episcleral brachytherapy [40]. Here, a non-radioactive plaque mockup is positioned over the region to be treated. Unlike the radioactive eye plaque that is optically opaque, the phantom device can readily pass visible light to visualize the shadow of an intraocular lesion, permitting intraoperative lesion localization. This entire process takes a couple of minutes or less.

5.3.2 *Brachytherapy Imaging*

In concert with surgical placement and practicing, phantoms specific to brachytherapy are needed for image evaluating. Many of the imaging modalities in use within a radiation therapy clinic for external-beam radiotherapy, such as X-ray CT



Fig. 5.3 The model 404 female pelvis ultrasound training phantom by CIRS, Inc. <http://www.cirsinc.com/products/new/91/female-ultrasound-training-pelvis/>. This phantom could potentially be modified to serve as a training phantom for gynecological brachytherapy, inserting cylindrical applicators, tandem and ovoid applicators, or interstitial needles

and MRI, are also available for brachytherapy. But due to the more hands-on and harried nature of brachytherapy in comparison with external-beam radiotherapy, often including a surgical component and sometimes being delivered intraoperatively, there has been less development of phantoms for imaging in brachytherapy. However, ultrasound imaging phantoms for brachytherapy have been developed. These include the aforementioned model 053 phantom and the model 045 (Fig. 5.4), both by CIRS, Inc. Proper use of this phantom for prostate ultrasound QA is outlined in the AAPM TG-128 report [41]. Further, phantoms have been used for evaluating brachytherapy seeds [42].

Fig. 5.4 The model 045 brachytherapy ultrasound QA phantom by CIRS, Inc. <http://www.cirsinc.com/products/all/71/brachytherapy-qa-phantom/>. Use of this phantom for ultrasound imaging quality assurance is extensively described in the AAPM TG-128 report



5.3.3 Contouring Phantoms

There is a growing body of literature that suggests that the process of contouring is highly subjective, with variability among physicians and over time [43]. Given the higher dose gradients and larger doses per fraction with brachytherapy in comparison with external-beam radiotherapy, brachytherapy outcomes are likely more sensitive to contouring variability. Having standardized phantoms with known segmentation can provide an opportunity to evaluate and improve contouring expertise. While the brachytherapy imaging phantoms provided by CIRS have well-defined boundaries between internal structures, these boundaries are more defined than realistic patient structures (i.e., organs) and the absolute shapes of the internal structures are not specified. This latter aspect prevents quantitative contouring assessment through established structures to monitor contouring performance within the treatment planning system.

5.3.4 Equipment Compatibility

As part of the commissioning process preceding clinical brachytherapy, several pieces of equipment (often from dissimilar manufacturers) must come together and be tested to work as expected and with high precision. It is possible that a benchtop test does not reflect the practical clinical circumstances. Differences may include the patient's elevated temperature (in comparison to ambient room temperature), patient pressure upon the brachytherapy applicator, the dynamic nature of the patient anatomy from surgery to imaging then treatment, edema at the implantation site (not to be confused with the prior item), and seepage of bodily fluids. It is important to test the intended treatment under the most realistic circumstances. Under some conditions, the source will not be present at the expected position due to changing differences in curvature depending on source location [44]. Under other conditions, such as extreme catheter curvature for a non-percutaneous biliary implant, the source cannot physically go to the desired position [45] and the treatment must be abandoned. Experience and proper training will mitigate unintended brachytherapy events.

5.4 Future of Brachytherapy Phantoms

This review highlights the areas in which phantoms are used in brachytherapy. With the advancement of technology and increasing concern for quality assurance [46], often being patient-specific activities, phantoms will take a growing role in brachytherapy [47]. Phantoms dimensions and composition have recently become standardized for specification of brachytherapy dosimetry parameter reference data

[15, 16]. As clinical brachytherapy dosimetry becomes more accurate with dose calculation algorithms beyond the conventional TG-43 formalism [48], professional societies will develop physical and computational phantoms to permit dose calculation algorithm benchmarking. This synergy among clinical, research, and development endeavors will place brachytherapy phantoms in the spotlight as a means of providing high-quality preclinical testing and quality assurance.

References

1. Nath, R., Anderson, L. L., Meli, J. A., Olch, A. J., Stitt, J. A., & Williamson, J. F. (1997). Code of practice for brachytherapy physics: Report of the AAPM Radiation Therapy Committee Task Group No. 56. *Medical Physics*, *24*, 1557–1598.
2. Ballester, F., Nath, R., & Baltas, D. (2012). *Radionuclides in Brachytherapy: Current and Potential New Sources*. In *Comprehensive Brachytherapy: Physical and Clinical Aspects*. Boca Raton, FL: Taylor & Francis.
3. Kubo, H. D., Glasgow, G. P., Pethel, T. D., Thomadsen, B. R., & Williamson, J. F. (1998). High dose-rate brachytherapy treatment delivery: Report of the AAPM Radiation Therapy Committee Task Group No. 59. *Medical Physics*, *25*, 375–403.
4. Yu, Y., Li, Z., Mellenberg, D. E., Nath, R., Schell, M. C., Waterman, F. M., et al. (1999). Permanent prostate seed implant brachytherapy: Report of the American Association of Physicists in Medicine Task Group No. 64. *Medical Physics*, *26*, 2054–2076.
5. Williamson, J. F., & Rivard, M. J. (2009). *Thermoluminescent Detector and Monte Carlo Techniques for Reference-Quality Brachytherapy Dosimetry*. In *Clinical Dosimetry for Radiotherapy: AAPM Summer School*. Madison, WI: Medical Physics Publishing.
6. Venselaar, J., Welleweerd, H., & Mijneer, B. (2001). Tolerances for the accuracy of photon beam dose calculations of treatment planning systems. *Radiotherapy and Oncology*, *60*, 191–201.
7. DeWerd, L. A., Ibbott, G. S., Meigooni, A. S., Mitch, M. G., Rivard, M. J., Stump, K. E., et al. (2011). A dosimetric uncertainty analysis for photon-emitting brachytherapy sources: Report of AAPM Task Group No. 138 and GEC-ESTRO. *Medical Physics*, *38*, 782–801.
8. Williamson, J. F., & Rivard, M. J. (2005). *Quantitative Dosimetry Methods for Brachytherapy* (2nd ed.). In *Brachytherapy Physics: Joint AAPM/ABS Summer School*. Madison, WI: Medical Physics Publishing.
9. Rivard, M. J., Meigooni, A. S., & Nath, R. (2012). *The TG-43 dose calculation formalism: Development, insights, and modernization*. In *Comprehensive Brachytherapy: Physical and Clinical Aspects*. Boca Raton, FL: Taylor & Francis.
10. Melhus, C. S., & Rivard, M. J. (2006). Approaches to calculating AAPM TG-43 brachytherapy dosimetry parameters for ^{137}Cs , ^{125}I , ^{192}Ir , ^{103}Pd , and ^{169}Yb sources. *Medical Physics*, *33*, 1729–1737.
11. Meigooni, A. S., Awan, S. B., Thompson, N. S., & Dini, S. A. (2006). Updated Solid WaterTM to water conversion factors for ^{125}I and ^{103}Pd brachytherapy sources. *Medical Physics*, *33*, 3988–3992.
12. Rivard, M. J. (2007). Brachytherapy dosimetry parameters calculated for a ^{131}Cs source. *Medical Physics*, *34*, 754–762.
13. Pérez-Calatayud, J., Granero, D., & Ballester, F. (2004). Phantom size in brachytherapy source dosimetric studies. *Medical Physics*, *31*, 2075–2081.
14. Granero, D., Pérez-Calatayud, J., Pujades-Claumarchirant, M. C., Ballester, F., Melhus, C. S., & Rivard, M. J. (2008). Equivalent phantom sizes and shapes for brachytherapy dosimetric studies of ^{192}Ir and ^{137}Cs . *Medical Physics*, *35*, 4872–4877.

15. Rivard, M. J., Coursey, B. M., DeWerd, L. A., Hanson, W. F., Huq, M. S., Ibbott, G. S., et al. (2004). Update of AAPM Task Group No. 43 Report: A revised AAPM protocol for brachytherapy dose calculations. *Medical Physics*, *31*, 633–674.
16. Pérez-Calatayud, J., Ballester, F., Das, R. K., DeWerd, L. A., Ibbott, G. S., Meigooni, A. S., et al. (2012). Dose calculation for photon-emitting brachytherapy sources with average energy higher than 50 keV: Report of the AAPM and ESTRO. *Medical Physics*, *39*, 2904–2929.
17. Tailor, R., Ibbott, G. S., & Tolani, N. (2008). Thermoluminescence dosimetry measurements of brachytherapy sources in liquid water. *Medical Physics*, *35*, 4063–4069.
18. Tailor, R., Ibbott, G., Lampe, S., Bivens-Warren, W., & Tolani, N. (2008). Dosimetric characterization of a ^{131}Cs brachytherapy source by thermoluminescence dosimetry in liquid water. *Medical Physics*, *35*, 5861–5868.
19. Wang, J., & Zhang, H. (2008). Dosimetric characterization of model Cs-1 Rev2 cesium-131 brachytherapy source in water phantoms and human tissues with MCNP5 Monte Carlo simulation. *Medical Physics*, *35*, 1571–1579.
20. Lindsay, P., Rink, A., Ruschin, M., & Jaffray, D. (2010). Investigation of energy dependence of EBT and EBT-2 Gafchromic film. *Medical Physics*, *37*, 571–576.
21. Raffi, J. A., Davis, S. D., Hammer, C. G., Micka, J. A., Kunugi, K. A., Musgrove, J. E., et al. (2010). Determination of exit skin dose for ^{192}Ir intracavitary accelerated partial breast irradiation with thermoluminescent dosimeters. *Medical Physics*, *37*, 2693–2702.
22. Maryanski, M. J., Ibbott, G. S., Schulz, R. J., & Gore, J. C. (1996). Radiation therapy dosimetry using magnetic resonance imaging of polymer gels. *Medical Physics*, *23*, 699–705.
23. McJury, M., Tapper, P. D., Cosgrove, V. P., Murphy, P. S., Griffin, S., Leach, M., et al. (1999). Experimental 3D dosimetry around a high dose-rate clinical ^{192}Ir source using a polyacrylamide gel (PAG) dosimeter. *Physics in Medicine and Biology*, *44*, 2431–2444.
24. Baldock, C., De Deene, Y., Doran, S., Ibbott, G., Jirasek, A., Lepage, M., et al. (2010). Polymer gel dosimetry. *Physics in Medicine and Biology*, *55*, R1–R63.
25. McJury, M., Oldham, M., Cosgrove, V. P., Murphy, P. S., Doran, S., O’Leach, M., et al. (2000). Radiation dosimetry using polymer gels: Methods and applications. *British Journal of Radiology*, *73*, 919–929.
26. Williamson, J. F. (2005). *Semiempirical Dosimetry Methods for Brachytherapy* (2nd Ed.). In *Brachytherapy Physics: Joint AAPM/ABS Summer School*. Madison, WI: Medical Physics Publishing.
27. Rogers, D. W. O. (2006). Fifty years of Monte Carlo simulations for medical physics. *Physics in Medicine and Biology*, *51*, R287–R301.
28. Rivard, M. J. (2001). A discretized approach to determining TG-43 brachytherapy dosimetry parameters: Case study using Monte Carlo calculations for the MED3633 ^{103}Pd source. *Applied Radiation and Isotopes*, *55*, 775–782.
29. Taylor, R. E. P., & Rogers, D. W. O. (2008). EGSnrc Monte Carlo calculated dosimetry parameters for ^{192}Ir and ^{169}Yb brachytherapy sources. *Medical Physics*, *35*, 4933–4944.
30. Ballester, F., Granero, D., Pérez-Calatayud, J., Melhus, C. S., & Rivard, M. J. (2009). Evaluation of high-energy brachytherapy source electronic disequilibrium and dose from emitted electrons. *Medical Physics*, *36*, 4250–4256.
31. DeWerd, L. A., Rivard, M. J., & Selbach, H. J. (2012). *Uncertainties Associated with Brachytherapy Source Calibrations and Dose Calculations*. In *Comprehensive Brachytherapy: Physical and Clinical Aspects*. Boca Raton, FL: Taylor & Francis.
32. Rivard, M. J., Granero, D., Perez-Calatayud, J., & Ballester, F. (2010). Influence of photon energy spectra from brachytherapy sources on Monte Carlo simulations of kerma and dose rates in water and air. *Medical Physics*, *37*, 869–876.
33. Granero, D., Vijande, J., Ballester, F., & Rivard, M. J. (2011). Dosimetry revisited for the HDR ^{192}Ir brachytherapy source model mHDR-v2. *Medical Physics*, *38*, 487–494.
34. Zaidi, H., & Xu, X. G. (2007). Computational anthropomorphic models of the human anatomy: The path to realistic Monte Carlo modeling in radiological sciences. *Annual Review of Biomedical Engineering*, *9*, 471–500.

35. Menzel, H. G., Clement, C., & DeLuca, P. (2009). ICRP Publication 110. Realistic reference phantoms: An ICRP/ICRU joint effort. A report of adult reference computational phantoms. *Ann ICRP*, *39*, 3–5.
36. Anderson, C. A., Kelley, K. C., & Goorley, J. T. (2012). Mesh human phantoms with MCNP. Los Alamos National Laboratory, Los Alamos, NM, LA-UR-12-00139:1–8.
37. Mille, M. M., Xu, X. G., & Rivard, M. J. (2010). Comparison of organ doses for patients undergoing balloon brachytherapy of the breast with HDR ^{192}Ir or electronic sources using Monte Carlo simulations in a heterogeneous human phantom. *Medical Physics*, *37*, 662–671.
38. Candela-Juan, C., Ballester-Pallarés, F., Pérez-Calatayud, J., & Rivard, M. J. (2013). Calculated organ doses using Monte Carlo simulations in a reference male phantom undergoing HDR brachytherapy applied to localized prostate carcinoma. *Med Phys* *40*:033901 (p. 8).
39. Rivard, M. J., Venselaar, J. L. M., & Beaulieu, L. (2009). The evolution of brachytherapy treatment planning. *Medical Physics*, *36*, 2136–2153.
40. Nag, S., Quivey, J. M., Earle, J. D., et al. (2003). The American Brachytherapy Society recommendations for brachytherapy of uveal melanomas. *International Journal of Radiation Oncology Biology Physics*, *56*, 544–555.
41. Pfeiffer, D., Sutlief, S., Feng, W., Pierce, H. M., & Kofler, J. (2008). AAPM Task Group 128: Quality assurance tests for prostate brachytherapy ultrasound systems. *Medical Physics*, *35*, 5471–5489.
42. Siebert, F.-A., De Brabandere, M., Kirisits, C., Kovács, G., & Venselaar, J. (2007). Phantom investigations on CT seed imaging for interstitial brachytherapy. *Radiotherapy Oncology*, *85*, 316–323.
43. De Brabandere, M., Haustermans, K., Hoskin, P., Van den Heuvel, F., & Siebert, F.-A. (2012). Prostate post-implant dosimetry: Interobserver variability in seed localisation, contouring and fusion. *Radiotherap Oncology*, *104*, 192–198.
44. Kirisits, C., Lang, S., Dimopoulos, J., et al. (2006). The Vienna applicator for combined intracavitary and interstitial brachytherapy of cervical cancer: Design, application, treatment planning and dosimetric results. *International Journal of Radiation Oncology Biology Physics*, *65*, 624–630.
45. Dvorák, J., Jandík, P., Melichar, B., Jon, B., Mergancová, J., Zoul, Z., et al. (2002). Intraluminal high dose rate brachytherapy in the treatment of bile duct and gallbladder carcinomas. *Hepato-Gastroenterology*, *49*, 916–917.
46. Thomadsen, B. R., Williamson, J. F., Rivard, M. J., & Meigooni, A. S. (2008). Anniversary paper: Past and current issues, and trends in brachytherapy physics. *Medical Physics*, *35*, 4708–4723.
47. Rivard, M. J., Beaulieu, L., & Mourtada, F. (2010). Enhancements to commissioning techniques and quality assurance of brachytherapy treatment planning systems that use model-based dose calculation algorithms. *Medical Physics*, *37*, 2645–2658.
48. Beaulieu, L., Carlsson Tedgren, Å., Carrier, J.-F., Davis, S. D., Mourtada, F., Rivard, M. J., et al. (2012). Report of the Task Group 186 on model-based dose calculation methods in brachytherapy beyond the TG-43 formalism: Current status and recommendations for clinical implementation. *Medical Physics*, *39*, 6208–6236.

Part II
Imaging Phantoms

Chapter 6

Imaging Phantoms: Conventional X-ray Imaging Applications

Kwan-Hoong Ng and Chai-Hong Yeong

An imaging phantom is a specially designed physical object that is scanned or imaged in medical imaging to evaluate, analyze, and optimize the performance of various imaging modalities. These phantoms are readily available and provide more consistent results than the use of a living subject or cadaver; their use also serves to avoid subjecting a human subject to unnecessary radiation exposure.

Imaging phantoms were originally designed for use in 2D X-ray-based imaging techniques such as radiography or fluoroscopy, and subsequently phantoms with desired imaging characteristics were developed for 3D imaging modalities such as magnetic resonance imaging (MRI), computed tomography (CT), ultrasound, positron emission tomography (PET), and other imaging modalities.

There are numerous phantoms which have been developed to test a variety of different physical parameters of imaging modalities or techniques. However, there are too many to be comprehensively covered in this chapter. We will focus on selected phantoms which meet the following criteria:

1. Extensively tested with documentation and published data;
2. Commercially and readily available;
3. Recognized by the leading bodies in the medical physics and radiology communities, such as the American Association of Physicists in Medicine (AAPM), Institute of Physics and Engineering in Medicine (IPEM), American College of Radiology (ACR), International Atomic Energy Agency (IAEA), etc.

The construction of each of these phantoms will be discussed briefly followed by specific reference to their role in conventional X-ray imaging applications, including radiography and fluoroscopy. The phantoms are discussed according to the categories of anthropomorphic phantoms, acceptance testing and quality control (QC) phantoms, as well as vendor-specific phantoms. This chapter will end

K.-H. Ng (✉) · C.-H. Yeong

Department of Biomedical Imaging and University of Malaya Research Imaging Centre,
University of Malaya, Kuala Lumpur, Malaysia
e-mail: ngkh@ummc.edu.my

with a brief discussion on research phantoms which have the potential of contributing to diagnostic imaging development. The phantoms discussed in this chapter and their main applications are summarized in Table 6.1.

6.1 Anthropomorphic Phantom for X-ray Imaging

Anthropomorphic phantoms are ideal substitute for patient selection, monitoring, training, and optimization of scanning parameters of imaging modalities. They are useful for research and development involving *in vitro* experimental validation prior to clinical application in human. Phantoms permit unlimited repetition of radiation exposure for investigation or training purposes. Optimization of image quality and radiation exposure can be achieved by using suitable phantoms that replicate the human anatomy. Some anthropomorphic phantoms are used as QA tools for initial implementations of an imaging protocol and routine QC for the imaging modality.

6.1.1 Head/Neck Phantom

6.1.1.1 CIRS Dental and Diagnostic Head Phantom

The CIRS dental and diagnostic head phantom (CIRS Inc, USA) was designed for the selection, monitoring, training, and verification of scanning parameters common to most radiological procedures requiring fine anatomical details. The phantom is ideal for determining optimum system settings, commissioning new equipment, monitoring system performance, and training in dental and panoramic X-ray, as well as CT and cone beam CT examinations. The phantom is constructed of proprietary tissue-equivalent materials, ATOM Max. It is made of tissue-simulating resins mimicking the X-ray attenuation properties of human tissue for both CT and therapy energy ranges (50 keV to 25 MeV). The phantom approximates the average male human head in both size and structure. The phantom includes detailed 3D anthropomorphic anatomy such as brain, bone, larynx, trachea, sinus, nasal cavities, and teeth. The bones contain both cortical and trabecular separations. The teeth include distinct dentine, enamel, and root structure including the nerve (Fig. 6.1).

Table 6.1 List of the available commercialized phantoms and their main applications

Phantoms	Manufacturers/ suppliers	Applications
<i>Anthropomorphic phantoms</i>		
Dental and diagnostic head phantom	CIRS Inc, USA	Determining optimum system settings, commissioning new equipment, monitoring system performance, and training in dental and panoramic X-ray, as well as CT and cone beam CT procedures
Alderson lung/chest phantom	RSD Inc, USA	Tissue equivalent phantom mimicking human lung and chest. The phantom also simulates custom pathologies of lung and chest, e.g., coronary artery irregularity and narrowing, lung tumors, and pneumonia
Multipurpose chest phantom the "LUNGMAN"	Kyoto Kagaku Co. Ltd, Japan	Tissue-equivalent phantom which can be used for either plain radiography or CT chest scanning for training, education, device assessment or evaluation, and research
Neonatal chest phantom	Gammex Inc, USA	Measure of image consistency over time, QC of image resolution and noise for CR and DR systems, optimization of radiation exposure and image quality
CIRS 3D Torso phantom	CIRS Inc, USA	Tissue equivalent phantom simulating an average male torso for medical imaging applications, training, and research
RANDO® phantoms	The Phantom Laboratory Inc, USA	Tissue equivalent whole body phantom simulating adult male and female. The phantom was initially designed for dose mapping in radiotherapy; however, there is an increasing use of the phantom in organ dose measurement and optimization in diagnostic imaging

(continued)

Table 6.1 (continued)

Phantoms	Manufacturers/ suppliers	Applications
<i>Acceptance testing and QC phantoms</i>		
<i>Radiographic system</i>		
REX X-ray test phantom	PTW, Germany	Reference phantom for QC of X-ray installations for radiographic and fluoroscopic systems. Suitable for constancy tests and acceptance tests of conventional X-ray equipments. It complies with IEC 61223-3-1
“Duke” phantom	Fluke Biomedical, USA	Quantitative measurements for image quality and performance of conventional and digital X-ray systems
ACR accredited radiography/fluoroscopy phantom	CIRS Inc, USA	Initial quality assurance (QA) assessment and routine monthly QC testing for radiography and fluoroscopy systems, personnel qualification, and clinical image quality assessment. Accredited by ACR
Radiography/fluoroscopy QC phantom	Fluke Biomedical, USA	Provide a reproducible and quantitative method for evaluating image quality and performance of radiography and fluoroscopy systems

(continued)

Table 6.1 (continued)

Phantoms	Manufacturers/ suppliers	Applications
Leeds test object	Leeds Test Object Ltd, UK	A comprehensive collection of test objects or patterns which are used to assess the performance of a wide variety of X-ray imaging systems. The performance test includes limiting spatial resolution, low-contrast sensitivity, scaling errors, high-contrast resolution, threshold contrast, display monitor setup, video voltage, image resolution uniformity, dynamic range of imaging capability, pixel mis-registration, X-ray/light beam alignment, and overall check of film processing
EZ CR/DR "DIN" test tool	Fluke Biomedical, USA	The phantom is used as a preventative maintenance QC tool. It can be used to take regularly scheduled measured data points from the image, such as line pair resolution measurements, regions of interest (ROIs), and geometry symmetry
ANSI acrylic phantoms for diagnostic X-ray including chest, abdomen/lumbar spine, skull, and extremities phantom	ANSI, USA	Tissue-equivalent phantom used for evaluation of imaging performance of the conventional X-ray systems. Conform to AAPM recommendations
CDRH LucAl phantoms including chest, abdomen/lumbar spine, and fluoroscopy phantom	CDRH, USA	Tissue equivalent phantom used for evaluation of imaging performance of the fluoroscopic systems. Conform to AAPM recommendations and established clinically
"Bona Fide Phantom" for dual energy X-ray absorptiometry (DEXA) QC	CIRS Inc, USA	QC tool for DEXA scanners to check linearity of bone mineral density over the clinical range

(continued)

Table 6.1 (continued)

Phantoms	Manufacturers/ suppliers	Applications
<i>Fluoroscopic system</i>		
Cardiovascular fluoroscopic benchmark phantom	CIRS Inc, USA	To evaluate and standardize image quality of catheterization or cardiovascular fluoroscopy procedures
Fluoroscopic contrast imaging phantom	Fluke Biomedical, USA	To evaluate image quality and performance of the fluoroscopy system
Rotating spoke test tool	Ludlum Measurements Inc, USA	To evaluate performance of the fluoroscopy systems on screen image lag, motion blur, contrast, and related distortions encountered in fluoroscopic examinations
<i>Vendor-specific phantoms</i>		
Carestream total quality tool for CR/DR system	Carestream Health Inc, USA	To verify that all Carestream CR or DR detectors within a facility are operating within the specified range
Fuji FCR 1 shot phantom	Fujifilm, USA	Enables a system-wide quality analysis by incorporating eight performance tests into a single exposure for Fujifilm CR and DR systems
Fuji FCR 1 shot phantom plus	Fujifilm, USA	Advanced QC program with automated tests, software, and reports specifically for use with Fujifilm CR and DR systems as well as the QC workstations
GE quality assurance phantom (QAP)	GE Healthcare, UK	Comprehensive QA program includes a series of performance tests associated with automated analyzing software for scheduled QC program on the DR systems. It includes a flat-field phantom

Legends

AAPM American Association of Physicists in Medicine

ACR American College of Radiology

ANSI American National Standards Institute

CDRH Center for Devices and Radiological Health

CIRS Computerized Imaging Reference Systems

GE General Electric

RSD Radiology Support Device

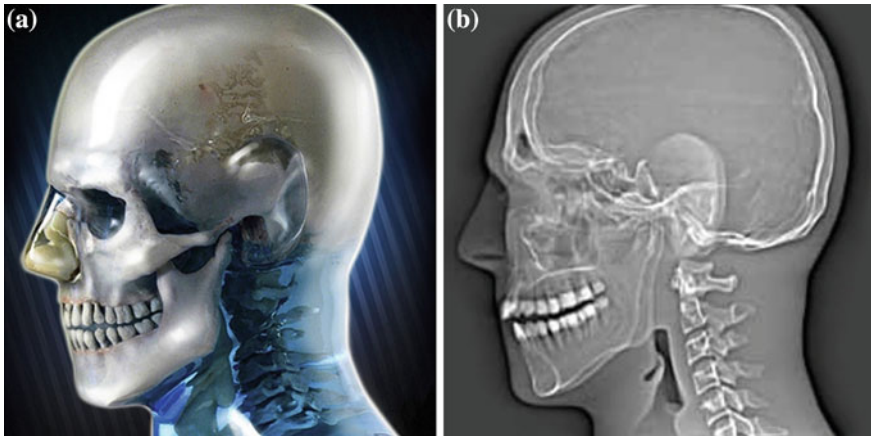


Fig. 6.1 **a** The left lateral view of the CIRS dental and diagnostic head phantom. **b** Plain X-ray image of the phantom. (Images courtesy of CIRS Inc, USA)

6.1.2 Torso Phantoms

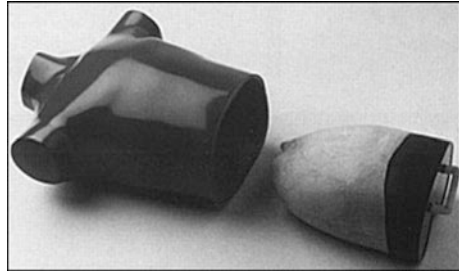
6.1.2.1 Alderson Lung/Chest Phantom

The Alderson lung/chest phantom (Radiology Support Device Inc, USA) extends from the neck to below the diaphragm. It is molded around a male skeleton, corresponding to the external body size of a patient, 175 cm tall and weighing 73.5 kg. The materials used to construct the phantom, known as the “RSD materials”, are equivalent to human bone and soft tissues. Animal lungs are selected to match the size of an adult male. Lungs are fixed in the inflated state and are molded to conform to the pleural cavities of the phantom. The pulmonary arteries are injected with a blood-equivalent plastic. The phantom with simulated left coronary artery reveals several areas of coronary artery irregularity and narrowing. The phantom is available either with the diaphragm permanently sealed to the interior of the phantom, fixing the lungs in place, or with a removable diaphragm, which permits the interchange of lungs and provides an unlimited number of configurations and disease simulations. The phantom is equipped with custom pathologies such as different sizes of nodules and pneumonia to demonstrate different pathological conditions of the lungs (Fig. 6.2).

6.1.2.2 Kyoto Kagaku Multipurpose Chest Phantom “LUNGMAN”

The Kyoto Kagaku chest phantom, also known as the “LUNGMAN” was developed by Kyoto Kagaku Co, Ltd, Japan. The phantom provides a life-size anatomical model of a human torso. It is a multipurpose phantom which is applicable for both plain radiography and CT imaging. The inner components of

Fig. 6.2 The Alderson lung/ chest phantom with removable diaphragm. (Image courtesy of Radiology Support Device Inc, USA)



the phantom consisting of mediastinum, pulmonary vasculature, and an abdomen block are detachable to allow insertion of mimic tumors or other lesions. The X-ray properties of the soft tissue substitute material and synthetic bones are similar to human tissues. The 3D structure of the phantom allows both posterior–anterior (PA) and lateral images to be obtained (Fig. 6.3).

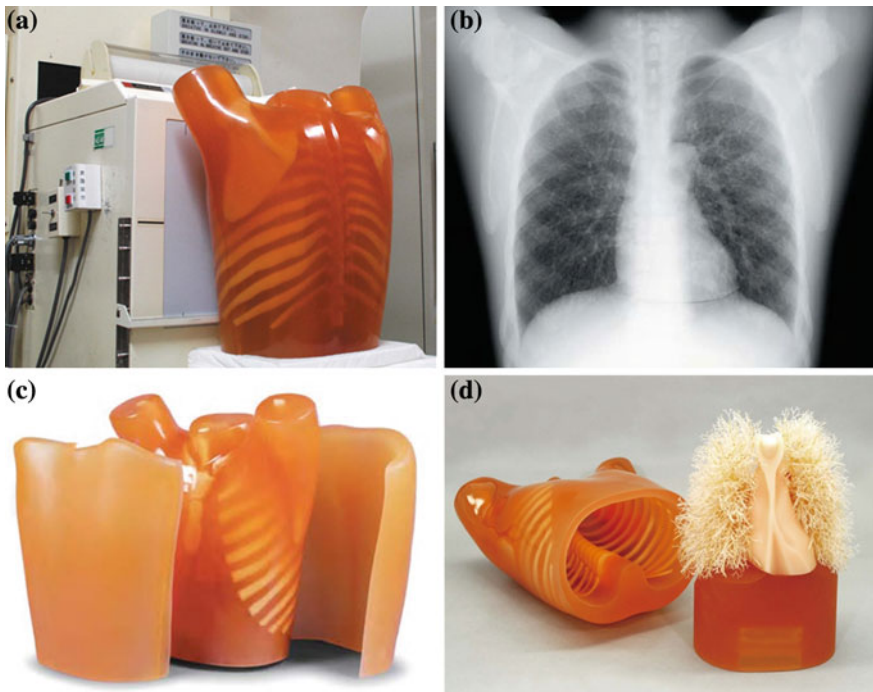


Fig. 6.3 The multipurpose chest phantom Kyoto Kagaku “LUNGMAN”. **a** Positioning of the phantom for chest radiography. **b** The resulting phantom image. **c** Phantom with the chest plates to simulate a larger body size. **d** The inner components consisting of mediastinum, pulmonary vasculature, and an abdomen block are easily detachable, allowing insertion of mimic tumors or other lesions. (Images courtesy of Kyoto Kagaku Co, Ltd, Japan)

Fig. 6.4 The Gammex neonatal chest phantom (Model 610, Gammex Inc, USA) used for QA program for computed and digital radiography. (Image courtesy of Gammex Inc, USA)



6.1.2.3 Gammex 610 Neonatal Chest Phantom

The Gammex 610 (Gammex Inc, USA) is an anthropomorphic neonatal phantom that represents a 1–2 kg neonate in its transmission characteristics, histogram, physical size, and structure. The phantom also contains clinically relevant image quality features for resolution and noise in the form of a lung with simulated pneumothorax with pleural thickening and a lung with simulated hyaline membrane disease. The phantom can be used for QA program for computed and digital radiography. Patient exposure is a concern especially in digital imaging where overexposed images could be post-processed to an acceptable level. The result often referred to as “dose creep” is especially relevant in pediatric imaging where some patients are imaged several times a day (Fig. 6.4).

6.1.2.4 CIRS 3D Torso Phantom

The CIRS anthropomorphic 3D torso phantom (CIRS Inc, USA) was designed for simulation of an average male torso for medical imaging applications. The removable organs enable the placement of dosimeters such as thermoluminescent dosimeters (TLDs) and contrast agents, etc. The phantom is fabricated using epoxy materials which have the optimal tissue simulation in the diagnostic energy range (40 keV to 20 MeV). The phantom is claimed to simulate the physical density and linear attenuation of actual tissue to within 2 % in the diagnostic energy range.

The phantom contains removable organs such as lungs, heart, liver, pancreas, kidney, and spleen. The lower portion of the phantom contains a removable, soft, bolus material simulating a mixture of 50 % adipose and 50 % muscle tissue. This insert is used to maintain the position of the organs when the phantom is placed upright. Simulated muscle material is used to layer the rib cage and vertebral column. The exterior envelope of the phantom simulates a mixture of 30 %

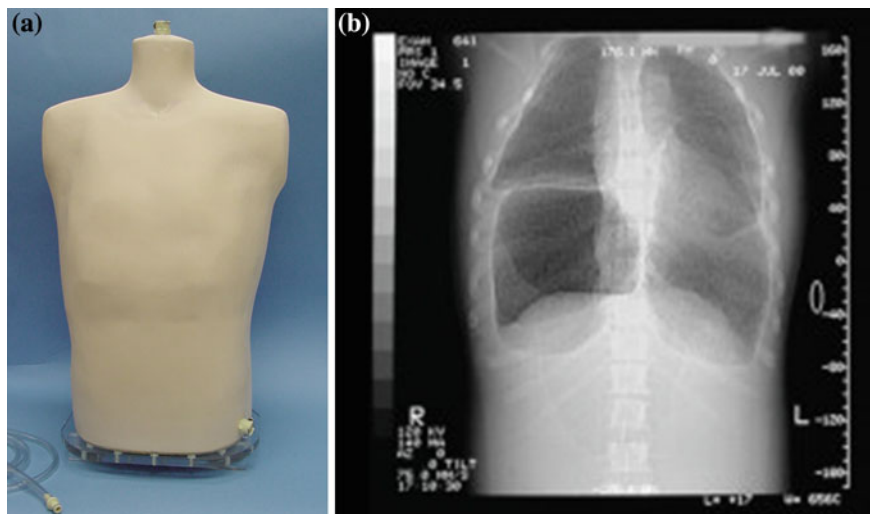


Fig. 6.5 **a** The CIRS anthropomorphic 3D torso phantom (CIRS Inc, USA). **b** Plain X-ray image shows the anterior–posterior (AP) projection of the phantom. (Images courtesy of CIRS Inc, USA)

adipose and 70 % muscle tissue. The phantom is sealed at the bottom by an acrylic plate. Water- or blood-mimicking fluid can be used to fill all the interstitial voids within the phantom (Fig. 6.5).

6.1.3 Whole Body Phantom

6.1.3.1 RANDO[®] Phantom

The RANDO[®] phantoms (The Phantom Laboratory Inc, USA) are constructed with natural human skeleton cast inside tissue-equivalent material. The soft tissue is manufactured with a proprietary urethane formulation with an effective atomic number and mass density that closely simulates muscle tissue with randomly distributed fat. There are two RANDO[®] models, RANDO[®] Man and RANDO[®] Woman. The RANDO[®] Man represents a 175-cm-tall and 73.5-kg male figure, whereas the RANDO[®] Woman represents a 163-cm-tall and 54-kg female figure. The RANDO[®] lungs are molded to fit the contours of the natural human rib cage. The lower density material in the RANDO[®] lungs is designed to simulate human lungs in a median respiratory state.

The RANDO[®] phantoms were initially designed for dose mapping applications in radiotherapy. However, its tissue equivalent properties and the whole body anatomy make it a useful phantom for diagnostic imaging applications especially

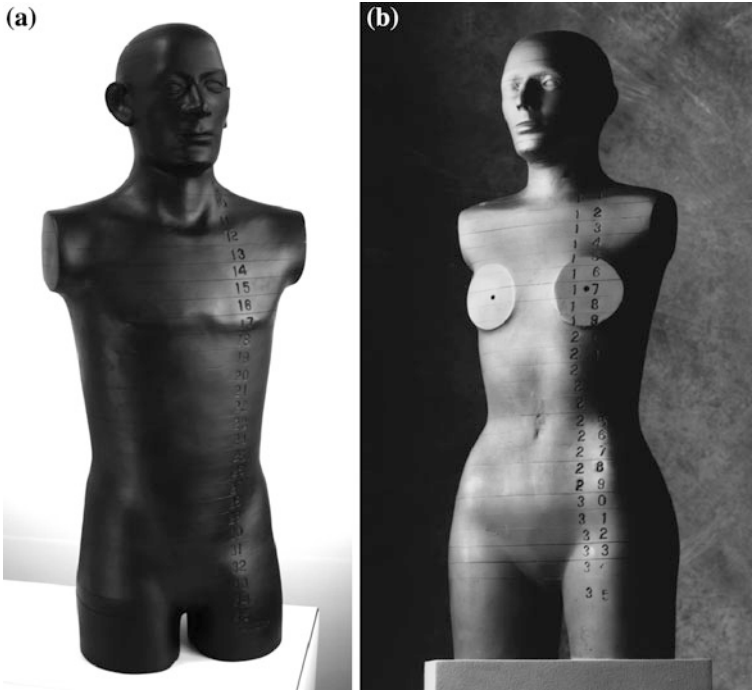


Fig. 6.6 **a** The RANDO[®] Man. **b** The RANDO[®] Woman (Images courtesy of the Phantom Laboratory, Inc, USA)

for dose measurement and optimization. *In vivo* dose measurements can be done using radiochromic films or TLDs. To facilitate dose mapping, RANDO[®] phantoms are sliced into 2.5 cm sections and equipped with standard, close-fitting Mix D plugs inserted in the holes of each section. The radiochromic films and TLDs can be placed within these sections or holes (Fig. 6.6).

6.2 Phantoms for Acceptance and QC Tests

The phantoms used for acceptance and QC tests are typically composed of material that mimics human tissue in its ability to produce absorption and scattering of radiation, i.e., they mimic radiopacity or radiolucency characteristics of human anatomy. Various phantoms have been developed for QC testing of conventional X-ray systems with respect to optical density, spatial resolution, and contrast detail. For example, a step wedge when radiographed produces a series of nearly uniform film areas with decreasing optical densities: line resolution phantoms that can be visually evaluated to estimate the smallest visible structure on film, and contrast detail phantom consisting of objects of decreasing size and

contrast (circles or parallel lines) that can be visually evaluated to assess the detectability of the features on the X-ray image.

The general requirements of an acceptable test phantom are summarized as follows:

1. The phantom material and thickness should simulate X-ray attenuation and scattering of human anatomy;
2. The phantom setup should allow exposure in clinical setting. The phantom should be of appropriate size to represent realistic X-ray field and large enough to cover automatic exposure control (AEC) detectors;
3. An ideal phantom should accommodate exposure or dose measurements during the QC test.

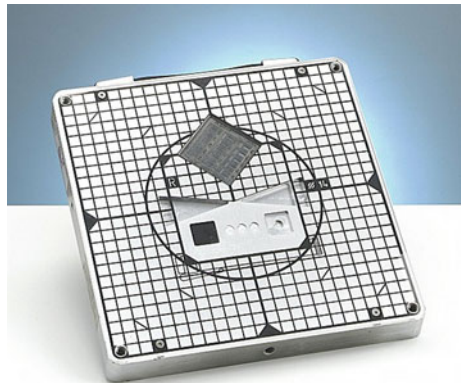
The following sections describe selected commercially available QC phantoms for both radiographic and fluoroscopic imaging systems.

6.2.1 Radiographic Systems

6.2.1.1 REX X-ray Test Phantom

The REX X-ray test phantom (PTW, Germany) is a reference phantom for QC of X-ray facilities for radiography and fluoroscopy. The phantom is suitable to be used for constancy tests and acceptance tests of X-ray equipments. It complies with the international standard IEC 61223-3-1 [1]. The phantom is constructed by a compact aluminum test object of $25 \times 25 \times 2.5$ cm dimension with well-defined structures with respect to X-ray attenuation and image quality. The REX phantom provides fast and easy control of properties, adjustment, and stability of X-ray components and imaging systems (Fig. 6.7).

Fig. 6.7 The REX X-ray test phantom (PTW, Germany). (Image courtesy of PTW, Germany)



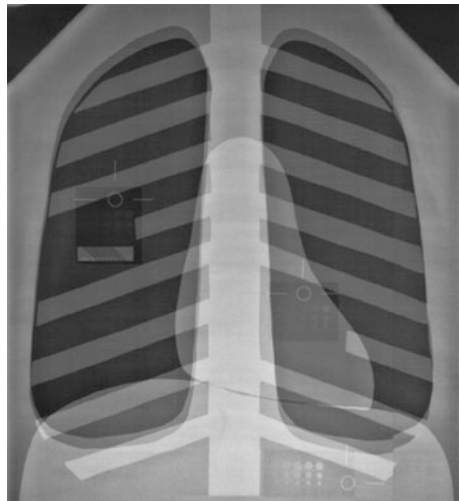
6.2.1.2 “Duke” Phantom

The “Duke” phantom (Model 07-646, Nuclear Associates, USA) is a QC phantom for conventional and digital X-ray systems. It provides quantitative measurements for evaluation of image quality and performance of the complete integrated digital system. The “Duke” phantom was developed by Chotas et al. [2] from the Duke University Medical Centre, Durham, USA, in 1997. The phantom is constructed from sheets of copper and aluminum shapes resembling frontal radiographic projections of human thoracic structures (lungs, heart, ribs, and abdomen). The components are oriented and arranged to simulate a projection of a complete thorax and are then sandwiched between additional sheets of aluminum and acrylic. The top two corners of the phantom form “shoulders” which provide a region for direct X-ray exposure of the image receptor. The “Duke” phantom is equipped with regional test objects, contrast–detail test pattern, line-pair test pattern, and stainless steel wire mesh overlaying the entire chest area.

The “Duke” phantom can be used for the following purposes:

1. QC testing of photostimulable storage phosphor CR systems
2. Digital thoracic radiography systems based on a selenium detector
3. Conventional screen–film systems
4. Routine testing of phototimer performance in all chest imaging systems (Fig. 6.8).

Fig. 6.8 The “Duke” QC phantom for conventional and digital chest X-ray. (Image courtesy of Fluke Biomedical, USA)



6.2.1.3 CIRS ACR Accreditation Radiography/Fluoroscopy (R/F) QA Phantom

The CIRS ACR accreditation R/F QA phantom (Model 903, CIRS Inc, USA) was designed for a comprehensive review of radiographic and fluoroscopic facilities and image quality programs. It was designed to be an integral part of the ACR R/F Accreditation Program. The phantom can be used for initial QA assessment and routine monthly QC testing to ensure optimal performance of the R/F systems. The phantom is manufactured from poly(methyl methacrylate) (PMMA)-equivalent epoxy that has the same X-ray attenuation properties as acrylic with significantly greater durability. The overall phantom measures $25 \times 25 \times 20.7$ cm and consists of three attenuation plates, one test object plate and a detachable stand for reproducible setup. The test objects include high-resolution copper mesh targets from 12 to 80 lines per inch and two separate contrast detail test objects (Fig. 6.9).

6.2.1.4 Radiography/Fluoroscopy QC Phantom

The R/F QC phantom (Model 07-647, Nuclear Associates, USA) was designed to provide a reproducible and quantitative method for evaluating the image quality and performance of radiographic and fluoroscopic imaging systems. The design of this phantom is based on the CDRH fluoroscopic phantom (refer Sect. 6.2.1.8). The phantom is used in determining subtle degradation in imaging performance. It can be used for QC of phototimer and automatic brightness control (ABC) consistency, as well as to verify the fluoroscopic monitor contrast and brightness adjustment. The phantom contains a 2 mm copper attenuator, which is simulating the attenuation of an average adult. The center of the phantom consists of pie-shaped wedges of varying mesh sizes for evaluating high-contrast performance. The meshes are surrounded by four low-contrast masses of different diameters ranging from 2 to 8 mm. There is a small “density difference” patch at one edge of the phantom to measure film contrast. At the opposite edge of the phantom, there are two monitor adjustment squares, each having a low-contrast square insert (Fig. 6.10).

Fig. 6.9 The CIRS ACR accreditation R/F QA phantom (Model 903, CIRS Inc, USA). (Image courtesy of CIRS Inc, USA)

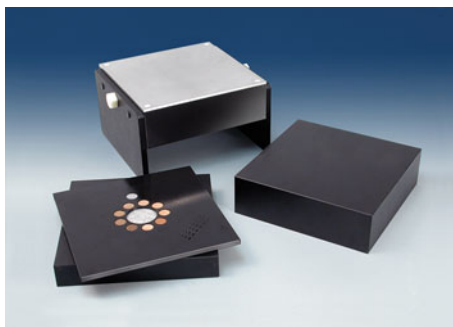
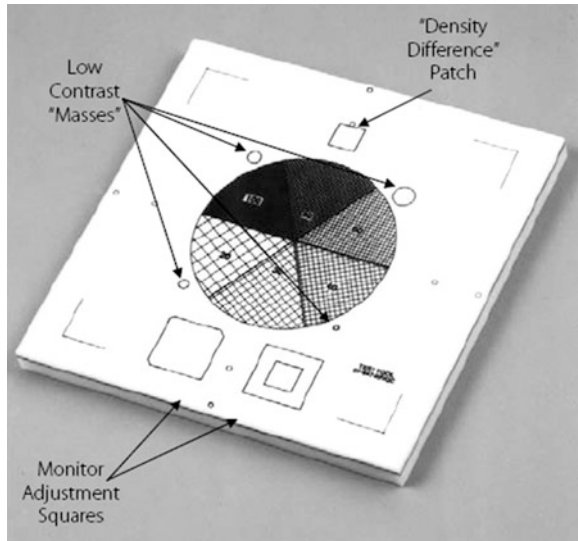


Fig. 6.10 The R/F QC phantom (Model 07-647, Nuclear Associates, USA). (Image courtesy of Fluke Biomedical, USA)



6.2.1.5 Leeds Test Objects

The Leeds test objects (Leeds Test Object Ltd, UK) are a collection of test objects or patterns which are used to assess the performance of a wide variety of X-ray imaging systems, including radiographic, fluoroscopic, digital, and mammographic systems. These objects, the first of which was manufactured in 1955, have been recommended as a clinical standard for establishing the correct operating performance of X-ray systems following their adoption for clinical use by the National Health Service (NHS), UK, in 1973 and as a testing protocol by the IPEM, UK, in 1979.

The general design and purposes of Leeds test tools are listed as following:

1. High-contrast resolution mesh: used for the evaluation of the resolution of fluoroscopic imaging systems. Plastic plates containing eight groups of wire mesh screening. The wire mesh screening should be made of copper or brass in mesh sizes ranging from 9 to 23 lines per cm for conventional fluoroscopic units and from 12 to 39 lines per cm for evaluation of cinefluoroscopy units.
2. Fluoroscopic threshold contrast test tool: used to provide a quantitative evaluation of fluoroscopic threshold contrast. It consists of two $15 \times 15 \text{ cm} \times 6.3 \text{ mm}$ thick aluminum plates. Each plate contains an array of 1.1 cm targets of varying contrast arranged in three columns. Three $15 \times 15 \text{ cm} \times 1 \text{ mm}$ copper attenuation sheets are also needed. Tables of target contrast versus kVp permit determination of target contrast at the tested fluoroscopic kVp values.
3. Centering and alignment tool: used to determine perpendicularity of the central ray of the X-ray beam. The device should be a box or cylinder whose sides are perpendicular with its bottom to within 1 degree with a centrally located vertical wire.

4. Beam restriction and sizing evaluation device: an aluminum plate with four sliding brass strips dividing the plate into quarters. Holes, at 12.7 mm intervals, should be drilled in perpendicular lines beneath the sliding brass strips. Recommended minimum size of 23 × 23 cm.

The variety of Leeds test objects with their product code, applications and standard compliance are summarized in Table 6.2.

Some examples of commonly used Leeds test objects are shown in Figs. 6.11, 6.12, 6.13, 6.14.

6.2.1.6 EZ CR/DR “DIN” Test Tool

The EZ CR/DR “DIN” test tool (Model 07-605-7777, Nuclear Associates, USA) is designed for evaluating the entire CR or DR image acquisition chain including laser beams, photomultiplier tubes, network gateways, and laser printers. It is suitable to be used as a preventive maintenance QC tool by taking regularly scheduled measured data points from the image, such as line-pair resolution measurements, ROIs, and geometry symmetry. The phantom allows a routine check on the dynamic range, contrast resolution, homogeneity, and resolution of the CR/DR systems. Quantitative measurement is applied to evaluate monitor as well as printed film image quality (Fig. 6.15).

6.2.1.7 Acrylic Phantoms for Diagnostic X-ray

The Joint Commission (TJC), USA, requires X-ray exposure measurements to be determined for commonly used projections in all radiographic suites [3]. In order to provide this information when using radiographic AEC or fluoroscopy ABC systems, specifically designed phantoms must be used. Attenuating material must be used between the focal spot and AEC or ABC detectors. Since these detectors are energy dependent, measurement of skin entrance exposure requires the use of patient-equivalent phantoms for meaningful results [4].

AAPM has recommended four special patient-equivalent phantoms for use in diagnostic radiology, i.e., chest, abdomen/lumbar spine, skull X-ray, and extremity X-ray phantoms. The phantoms have been developed by the ANSI using acrylic and the CDRH using Lucite and aluminum (LucAl). The phantoms are patient-equivalent and are specifically designed to conform to the AAPM recommendations. The designs of modified ANSI phantoms are summarized in Table 6.3.

6.2.1.8 CDRH LucAl Phantoms

The comparison between the modified ANSI phantoms and the CDRH phantoms has been carried out and documented in the AAPM Report No. 31. It is noted that

Table 6.2 List of Leeds test objects with their product code, applications and standard compliance for CR/DR, fluoroscopy, and digital subtraction fluorography (DSF) systems

Imaging modalities	Leeds test objects	Measure	Standard compliance	
CR/DR	TOR CDR	Sensitometric measurements		
		Resolution limit		
		Low-contrast large-detail detectability High-contrast small-detail detectability		
	CR DDR set	Threshold contrast		Kcare CR/DR protocol
		Scaling errors		
		Image resolution uniformity		
	PIX-13	Dynamic range		DIN 6868-13
		Resolution limit		
		Low-contrast large-detail detectability X-ray to light field alignment		
	ANSI	Image quality performance (patient equivalent)		AAPM 31
TO 12	Threshold contrast for digital spot imaging systems (a range of nine contrasts per detail size)			
TO 16	Threshold contrast for computed digital radiography systems (a range of 12 contrasts per detail size)			
TO 20	Threshold contrast for digital spot imaging systems (a range of nine contrasts per detail size)			
Fluoroscopy	TOR 18FG	Limiting spatial resolution		
		Greyscaling		
		Low-contrast detectability Circular geometry		
	SFS set	Set includes:		
		TO 10 threshold contrast test object		
		TO N3 contrast test object		
		TO GS2 greyscale test object		
		TO E1 edge test object		
	TO M1 geometry test object			
	TO MS1, TO MS3, TO MS4 mesh test objects			
Step wedge	Optical density			
Fluoro-4	Limiting spatial resolution		DIN 6868-4	
	Greyscaling			
	Low-contrast detectability Circular geometry			
TO 10	Threshold contrast for fluoroscopic X-ray systems (a range of nine contrasts per detail size)			
Digital subtraction	DSF set	Dynamic range		
		Threshold contrast		
	TO DR	Pixel misregistration Dynamic range		

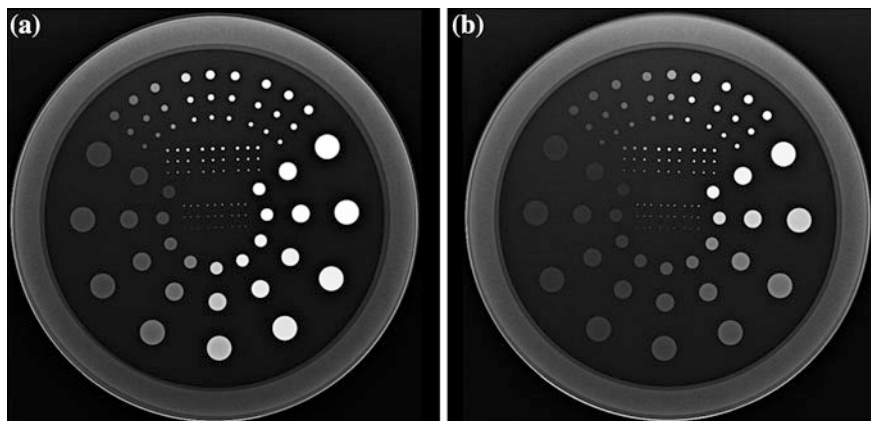


Fig. 6.11 Examples of threshold contrast test object **a** TO 10 and **b** TO 12 for digital spot imaging systems. The test object has 108 details with a range of 12 sizes (ranged 11–0.25 mm) and nine contrasts (range 0.0043–0.540 at 70 kV, 1.0 mm Cu filtration). The results are plotted on a threshold detection index curve. (Images courtesy of Leeds Test Object Ltd, UK)

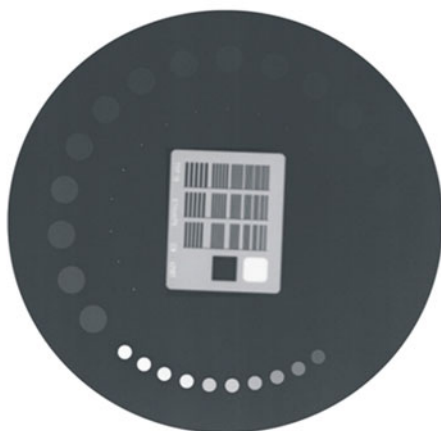


Fig. 6.12 The TOR CDR phantom used for conventional and non-subtractive digital radiography and fluoroscopy systems. After an initial grayscale check, image quality is measured by counting the number of details detected and the number of bar patterns resolved in the image. It can be used for sensitometric measurement, resolution limit, low-contrast large-detail detectability, and high-contrast small-detail detectability. (Image courtesy of Leeds Test Object Ltd, UK)

the patient equivalency of the CDRH phantoms has been established clinically [4]. The designs and constructions of the CDRH LucAl phantoms are summarized in Table 6.4.

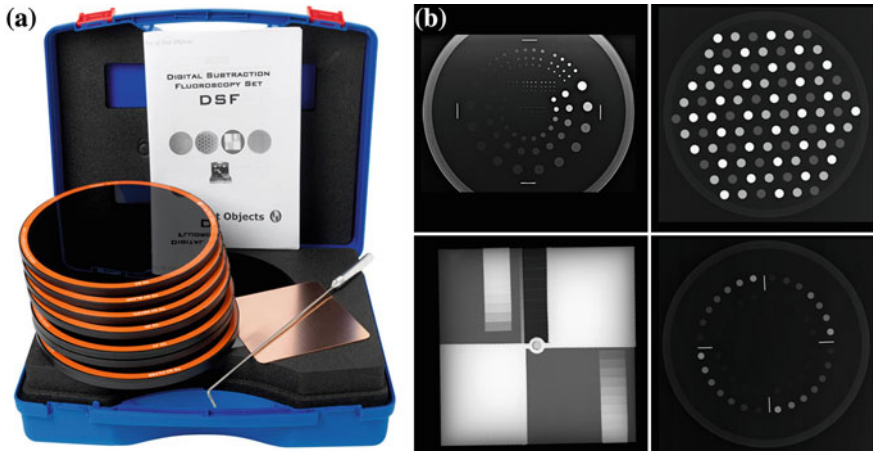


Fig. 6.13 **a** The Leeds test object set for digital subtraction fluorography (*DSF*). The set consists of four test objects: TO J3 used to check log/linear subtraction analog-to-digital converter (*ADC*) and digital-to-analog converter (*DAC*) operation, TO Q3 used to measure dynamic range of imaging capability, TO 20 to assess threshold contrast detail detectability, and TO D3 to detect systematic misregistration artefacts. **b** The *DSF* images of the Leeds test object (*top left*: TO 20; *top right*: TO D3; *bottom left*: TO J3; *bottom right*: TO Q3). (Images courtesy of Leeds Test Object Ltd, UK)

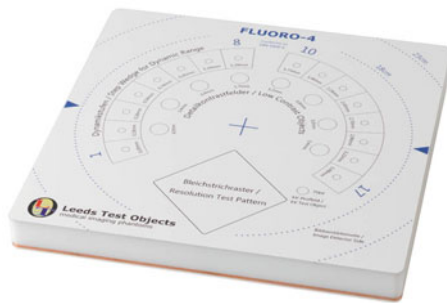


Fig. 6.14 Leeds test object Fluoro-4 phantom used to check image quality performance of digital and conventional fluoroscopy systems. Fluoro-4 should be used with either PMMA/Cu or Al attenuator plates. It can be used for quantitative assessment of limiting spatial resolution, low-contrast resolution and dynamic range of imaging capability. (Image courtesy of Leeds Test Object Ltd, UK)

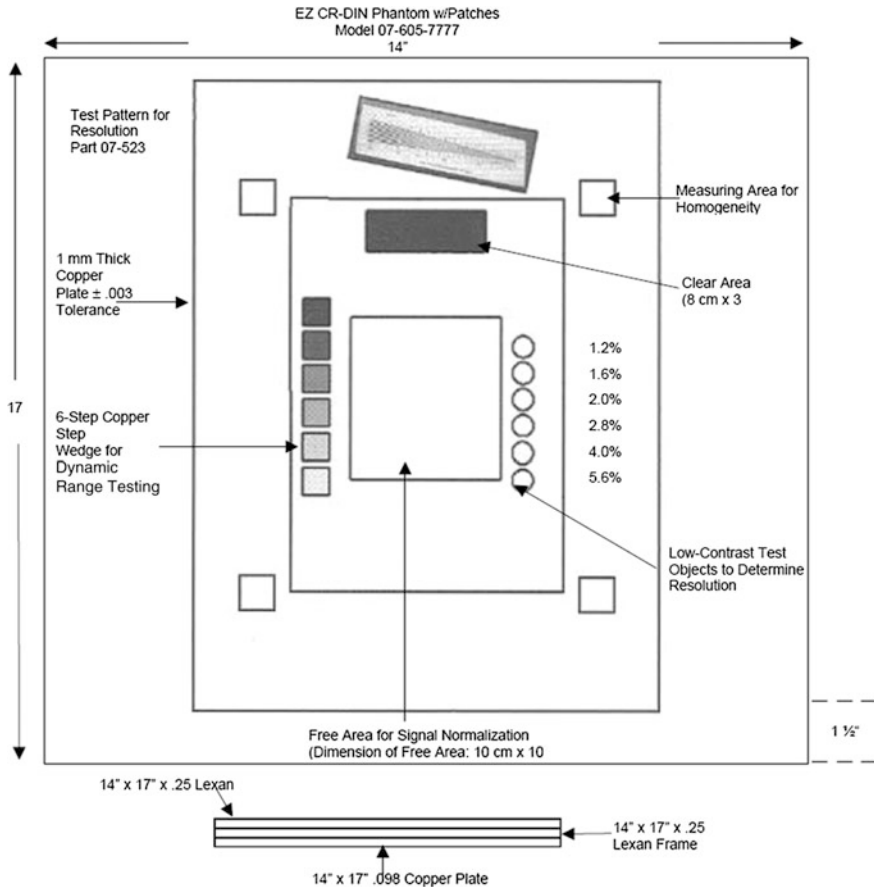



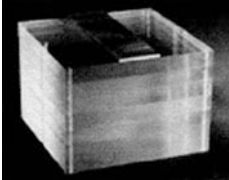
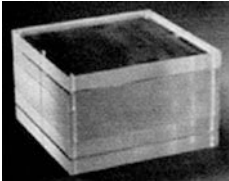
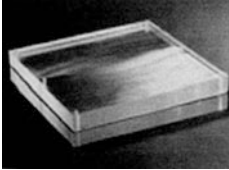
Fig. 6.15 Schematic diagram of the EZ CR/DR “DIN” test tool (Model 07-605-7777, Nuclear Associates, USA). (Image courtesy of Fluke Biomedical, USA)

6.2.1.9 Dual-Energy X-ray Absorptiometry QC Phantom

CIRS “Bona Fide Phantom”

The CIRS BFP phantom is a QC tool for DEXA scanners, which features an acrylic-embedded calcium hydroxyapatite (CHA) step wedge. The phantom has a range of densities ($0.7\text{--}1.5\text{ g cm}^{-2}$) with respect to clinical range of bone mineral density (BMD). The phantom uses a CHA insert for direct assessment of bone density accuracy. The CHA insert is compliant with Food and Drug Administration (FDA) guidelines for cross-calibration phantoms for clinical trials. The phantom is cast in acrylic and comes with its own carrying case. The case remains on the phantom during scanning and does not affect BMD readings, allowing rapid placement and removal for the phantom from the bed (Fig. 6.16).

Table 6.3 Description of the modified ANSI phantoms [4]

Phantom	Description
Chest X-ray phantom 	This phantom consists of four sheets of $30.5 \times 30.5 \times 2.54$ cm clear acrylic, one sheet of $30.5 \times 30.5 \times 1.0$ mm and one sheet of $30.5 \times 30.5 \times 2.0$ mm aluminum (type 1100 alloy), and spacers to provide a 5.08 cm air gap
Abdomen/Lumbar spine phantom 	This phantom consists of seven sheets of $30.5 \times 30.5 \times 2.54$ cm clear acrylic for a total thickness of 17.78 cm. The phantom has been modified to include a $7.0 \times 30.5 \times 4.5$ mm thick piece of aluminum (type 1100 alloy) in order to provide additional attenuation in the spinal region
Skull X-ray phantom 	This phantom has the same configuration as the chest phantom, but without the air gap. The phantom consists of four sheets of $30.5 \times 30.5 \times 2.54$ cm clear acrylic, one sheet of 30.5×30.5 cm \times 1.0 mm and one sheet of 30.5×30.5 cm \times 2.0 mm aluminum (type 1100 alloy), and a center sheet of $30.5 \times 30.5 \times 5.08$ cm clear acrylic
Extremity X-ray phantom 	This phantom consists of one 30.5×30.5 cm \times 2.0 mm piece of aluminum (type 1100 alloy) sandwiched between two sheets of $30.5 \times 30.5 \times 2.54$ cm clear acrylic

6.2.2 Fluoroscopic Systems

6.2.2.1 CIRS Cardiovascular Fluoroscopic Benchmark Phantom

The CIRS cardiovascular fluoroscopic benchmark phantom (Model 901 NEMA-SCA&I, CIRS Inc, USA) was designed to evaluate and standardize catheterization image quality in cardiovascular fluoroscopy. It is the product of collaboration between the Society for Cardiac Angiography and Interventions (SCAI) and the National Electric Manufacturers Association (NEMA). The phantom configuration is compliant with the performance standard of NEMA XR 21 [5]. The phantom is manufactured from PMMA with X-ray absorption properties similar to soft tissue at diagnostic energies. It contains a variety of static and dynamic test targets for objective assessment of resolution, motion unsharpness, and radiation exposure.

Table 6.4 Description of the CDRH LucAl phantoms [4]

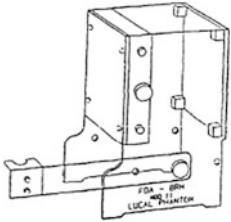
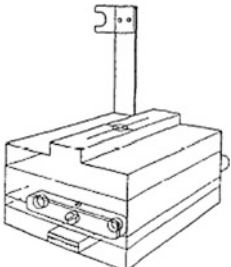
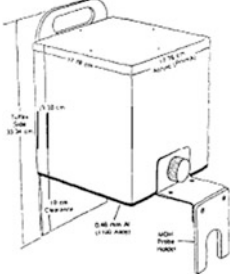
Phantom	Description
<p data-bbox="138 213 417 243">CDRH LucAl chest phantom</p> 	<p data-bbox="605 213 1038 508">This phantom consists of two sheets of $2.54 \times 25.4 \times 0.95$ cm clear acrylic, one sheet of $25.4 \times 25.4 \times 5.4$ cm clear acrylic, one sheet of $2.54 \times 25.4 \times 0.25$ mm aluminum (type 1100 alloy), one sheet of $25.4 \times 25.4 \times 0.16$ mm aluminum (type 1100 alloy), and a 19 cm air gap. Clinical testing of the phantom has shown it to be equivalent to a 23 cm patient for the PA chest projection [12]</p>
<p data-bbox="138 513 582 543">CDRH LucAl abdomen/lumbar spine phantom</p> 	<p data-bbox="605 513 1038 830">This phantom consists of 25.4×25.4 cm pieces of clear acrylic totaling 16.95 cm thick in the soft tissue region and one $6.99 \times 25.4 \times 0.46$ cm strip of aluminum (type 1100 alloy) and 18.95 cm total clear acrylic thickness for the spinal region</p>
<p data-bbox="138 836 582 866">CDRH LucAl fluoroscopy phantom</p> 	<p data-bbox="605 836 1038 1187">This patient-equivalent phantom of uniform thickness consists of a 17.78 cm thick acrylic block, one fluoroscopic image quality test object, one lead stop plate and one copper attenuation plate. The base of the phantom is comprised of two type-1100 aluminum plates, each 2.3 mm thick. The phantom has four lead beads embedded on top, to be used as collimation orientation points. It stands on two legs, approximately 10.16 cm off the tabletop. One leg is specially designed as a probe holder</p>

Fig. 6.16 The CIRS “Bona Fide Phantom” used for QC test in DEXA systems. (Image courtesy of CIRS Inc, USA)



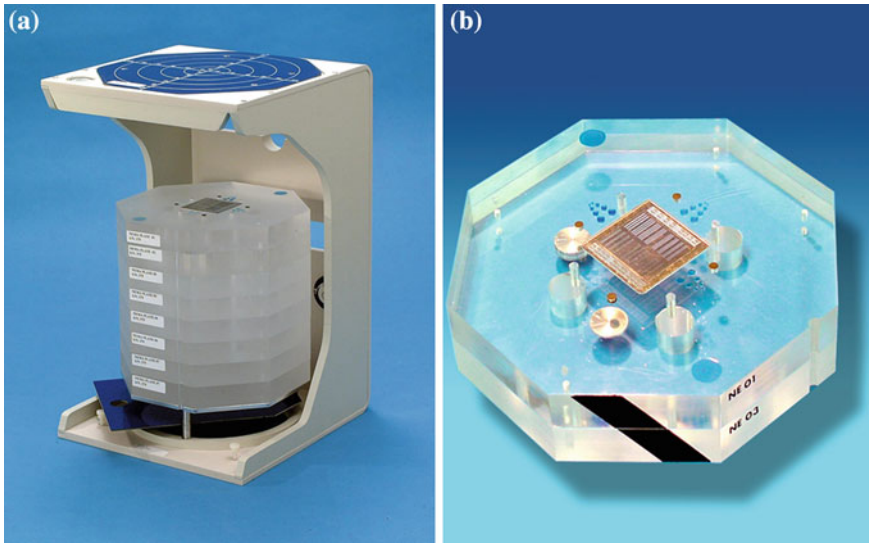


Fig. 6.17 **a** Complete set of the CIRS cardiovascular fluoroscopic benchmark phantom (Model 901, CIRS Inc, USA). **b** Close-up view of the central target assembly (NE 01) and working thickness plate (NE 03) as part of the assembly of the phantom. (Image courtesy of CIRS Inc, USA)

The sectional design allows for configuration of thicknesses from 5 to 30 cm, simulating PA thicknesses from infants to large adult patients (Fig. 6.17).

6.2.2.2 Fluoroscopic Contrast Imaging Phantom

The fluoroscopic contrast imaging phantom (Model 07-643, Nuclear Associates, USA) is a test tool to evaluate image quality and optimal performance of a fluoroscopy system. It can be used to check the dynamic range of the video system and overall system performance, as well as the radiographic film range and density. The phantom has an outer diameter of 23 cm and thickness of 1.28 cm. It weighs 1.26 kg (Fig. 6.18).

6.2.2.3 Fluoroscopic Imaging Test Phantom

The fluoroscopic imaging test phantom (Model 07-653, Nuclear Associates, USA) can be used to evaluate, adjust, and optimize fluoroscopic video cameras, brightness systems, and image processing systems. It provides a test pattern enabling the precise adjustment of many critical parameters of the fluoroscopic system such as video level, contrast, peak whites, black level, shading or vignette correction, automatic brightness, sweep linearity, frequency response, and aperture

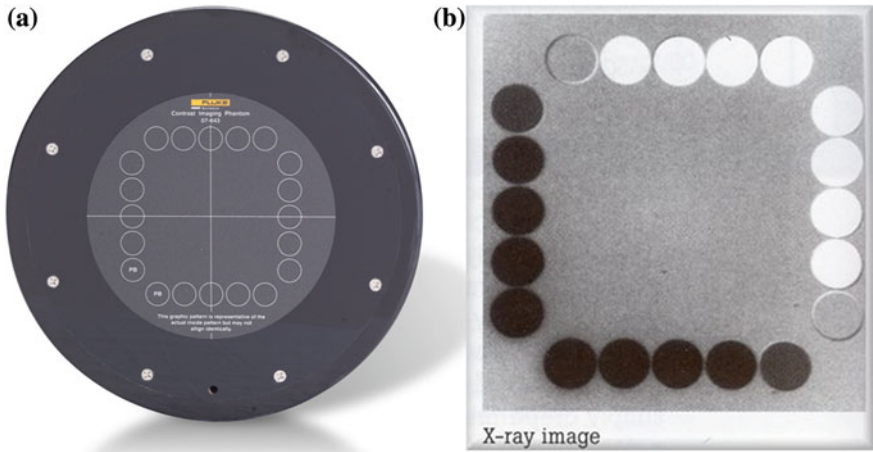


Fig. 6.18 a The fluoroscopy contrast imaging phantom (Model 07-643, Nuclear Associates, USA). b Plain X-ray image of the phantom. (Image courtesy of Fluke Biomedical, USA)

Fig. 6.19 The fluoroscopy imaging test phantom (Model 07-653, Nuclear Associates, USA). (Image courtesy of Fluke Biomedical, USA)

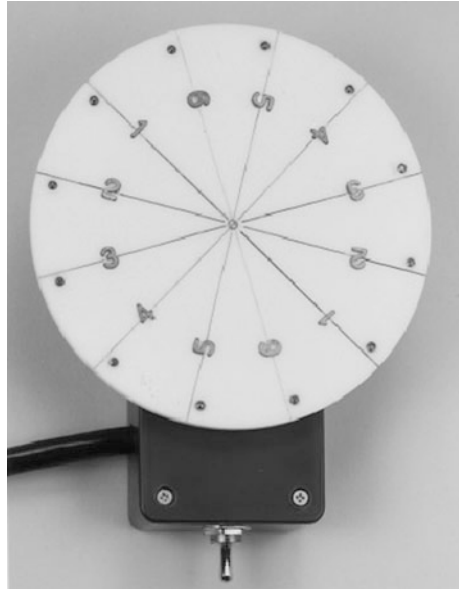


correction. The phantom has an outer diameter of 22.78 cm and thickness of 1.28 cm. It weighs 1.86 kg (Fig. 6.19).

6.2.2.4 Ludlum Rotating Spoke Test Tool

The rotating spoke test tool (Model L-629, Ludlum Medical Physics, USA) was designed to evaluate the performance of the fluoroscopic imaging systems. The tool demonstrates screen image lag, motion blur, contrast, and related distortions encountered in fluoroscopic examinations. When combined with aluminum or acrylic block attenuators, the rotating spoke test tool enables simulation of the movement of guide wires and radiopaque catheters, seen in angiography or cardiac catheterization patient procedures. The rotating spoke test pattern consists of a

Fig. 6.20 The rotating spoke test tool (Model L-629, Ludlum Medical Physics, USA). (Image courtesy of Ludlum)

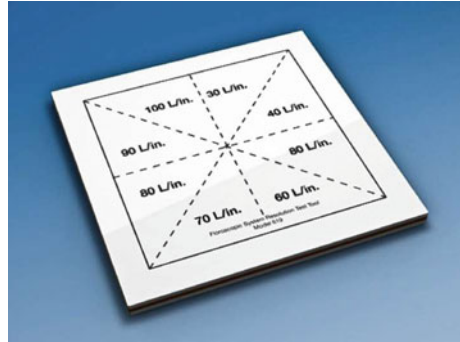


circular acrylic disk of 13.97 cm diameter with 12 steel wires arranged on its surface in 30-degree intervals. The wire diameters range from 0.508 to 0.127 mm. There are 2 wires of each size directly opposite to each other on the disk. There are 6 lead objects (labeled with number 1 to 6) on each half of the disk near the perimeter. The disk is mounted on a synchronous motor with a speed of 30 rotations per minute (RPM) to simulate movement of the wires (Fig. 6.20).

6.2.2.5 Ludlum Fluoroscopy Resolution Test Tool

The fluoroscopic resolution test tool (Model L-601, Ludlum Medical Physics, USA) is a square plastic plate ($19 \times 19 \times 0.3$ cm) containing eight groups of copper and brass mesh screening. The phantom is used for resolution checks of the fluoroscopic imaging systems. There are three models of test tools available, each with different resolutions for standard-, medium-, and high-resolution ranging from 16 to 60 lines per inch, 30 to 100 lines per inch, and 60 to 150 lines per inch. The screens are arranged in an irregular and non-sequential rotation to permit better visualization of the different resolution patterns. The phantom can also be used to optimize television system focus as well as mirror optics and image intensifier settings (Fig. 6.21).

Fig. 6.21 The fluoroscopic resolution test tool (Model L-601, Ludlum Medical Physics, USA). (Image courtesy of Ludlum)



6.3 Vendor-Specific QA Tools

6.3.1 Agfa Auto QC Tools

Auto QC² (Agfa Healthcare, USA) is a QA program for verifying that the Agfa CR systems are working optimally and consistently. Auto QC² can be used both for acceptance testing when setting up the CR systems, and for constancy testing for periodic QC. The Auto QC² program includes a special designed phantom (hafnium phantom), positioning template, automated analyzing software, a filter unit, and a light field indicator. This test requires only a single phantom exposure for both spatial and contrast tests. The utilization of a rare-earth hafnium step wedge element in the phantom significantly reduces the exposure control issues that can affect QC tools employing only copper or aluminum. The phantom complies with the AAPM [3], IEC 61267 [6], and IEC 62220-1-1 [7] recommendations.

Auto QC² can be used for five functional test groups:

1. Acceptance testing: used for the initial setup of the CR system and for establishing an operational baseline standard.
2. Periodic QC: a subset of the acceptance procedure, for monitoring the state of the CR system in routine use.
3. Plate inventory: provides individual and statistical performance data on all imaging plates.
4. Light field indicator: to check collimation accuracy of the X-ray exposure.
5. Monitor check: to check the performance of the monitor in viewing CR images (Fig. 6.22).

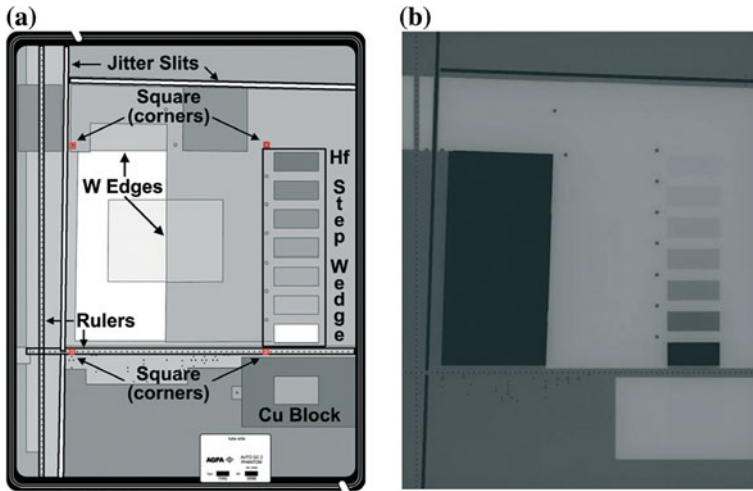


Fig. 6.22 The (a) internal construction and (b) X-ray image of the Hafnium phantom used in the Agfa Auto QC² QA program. (Image courtesy of Agfa Healthcare, USA)

6.3.2 Carestream DirectView Total Quality Tool for DR/CR System

The DirectView TQT (Carestream Health Inc, USA) phantom and software provide a method to measure image quality in order to verify that all Carestream DR or CR detectors within a facility are operating within the specified range. This QC system enables performance of objective image tests and QC measurements with the same interface used for examinations. The system is equipped with administrative analysis and reporting software to monitor the IEC exposure index, TQT data, reject rates, and collect and review other data for all Carestream CR, DR, and DRX systems within a healthcare facility. The TQT can also be used to measure and verify the performance of individual cassettes used in the DirectView CR/DR Systems (Fig. 6.23).

6.3.3 Fuji FCR 1 Shot Phantom

The Fuji FCR 1 Shot Phantom (Fujifilm, USA) enables a system-wide quality analysis by incorporating eight performance tests into a single exposure. The phantom provides valuable evaluation of the imaging plate, CR image reader, exposure room, hard copy printer, and imaging workstations (Fig. 6.24).

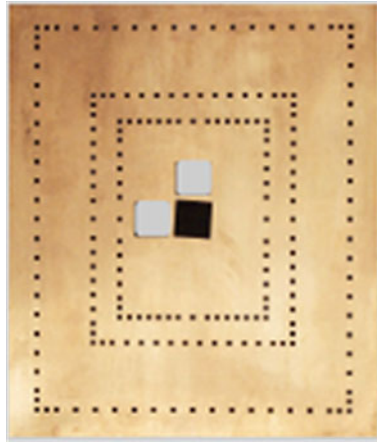


Fig. 6.23 The direct view TQT phantom (Carestream Health Inc, USA) used for QC tests for all Carestream DR or CR detectors. (Image courtesy of Carestream Health Inc, USA)

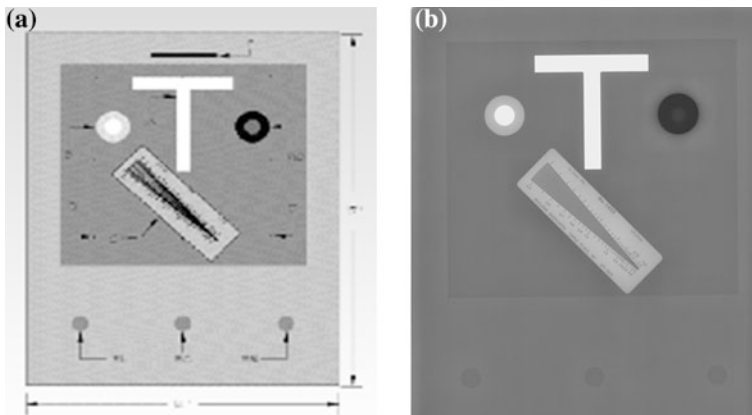


Fig. 6.24 **a** The FCR 1 Shot Phantom (Fujifilm, USA). **b** Example of the CR image of the FCR 1 Shot phantom. (Image courtesy of Fujifilm, USA)

6.3.4 *Fuji FCR 1 Shot Phantom Plus*

The Fuji FCR 1 Shot Phantom Plus (Fujifilm, USA) is an advanced QC program with automated tests, software, and reports specifically for use with Fujifilm CR and DR systems as well as the QC workstations. This phantom, made of acrylic, is a quality analysis system incorporating extensive test parameters into an automated program. Visual and automated calculations can be performed through the user interface.

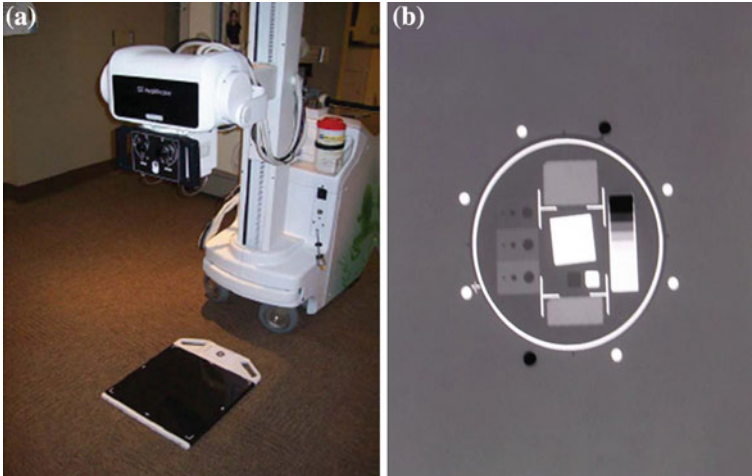


Fig. 6.25 **a** The QAP setup for a mobile DR system. The same setup can be used to assess both detector check and the full QAP tests. **b** The digital X-ray image of the flat-field phantom. (Images courtesy of GE Healthcare, UK)

6.3.5 GE Quality Assurance Process

GE QAP (GE Healthcare, UK) is a QA program used primarily to check the overall performance of the digital radiography systems. The QAP consists of a series of tests that should be performed on a scheduled (weekly) basis. Most of the analysis and reporting features are included in the software as automated program. There are two types of quality tests: detector check and a full QAP test that requires exposures to be done on a flat-field phantom (Fig. 6.25).

6.4 Future Development on Imaging Phantoms

The optimal imaging performance and appropriate radiation dose of X-ray equipment should be routinely tested. However, most of the existing phantoms were developed to test film/screen and image intensifier systems. Recently, the film/screen or image intensifier techniques are being increasingly replaced by flat-panel detectors (FPDs). Unfortunately, the phantoms for the evaluation of such systems are generally vendor-specific and are not comparable across the different system, and their validity cannot be confirmed. Therefore, it is imperative that simple QC phantom be available for easy evaluation of FPD image performance across a variety of different systems.

Chida et al. [8] has recently developed a QC phantom to evaluate the spatial resolution, low-contrast resolution, and dynamic range on single (one-shot) X-ray

exposures for FPD radiography and fluoroscopy. The phantom consists of three copper thicknesses (0.5, 1.5, and 3.0 mm), an aluminum step wedge (0.1 to 2.7 mm), and piano wire of various diameters (0.08 to 0.5 mm). The phantom is claimed to be simple, inexpensive, and useful for a routine QC of all FPD systems.

In addition, the use of vendor-specific QC program allows automatic processing and analysis of the radiographic images acquired, hence increases the objectivity of the system evaluation. In a QC program, the quality of the image is very useful to characterize the physical properties of the imaging chain. Therefore, specific phantoms that can be used to evaluate the images of CR or DR systems will be very useful. Mayo et al. [9] have developed a series of phantoms that can be used for this purpose. They have also developed specific software to analyze the phantom images obtained with digital processing techniques based on mathematical algorithms applied to the phantoms. The phantoms should include a wide range of image quality tests such as threshold contrast resolution, limiting spatial resolution, dynamic range, homogeneity zone, alignment accuracy, etc.

As the conventional QC tests are gradually being replaced by the vendor-specific QAP program, there is a need to develop an independent phantom or program to verify and compare across different QAP programs. Currently, there is no known standard protocol available to check the specification and performance of these vendor-specific QA programs. There is also no system capable of capturing QC data for comparison and monitoring across different QAP tools. Thus, it is imperative that an international guidelines or protocol needs to be developed to ensure proper implementation of the system.

There is an increased public awareness of radiation exposures, and therefore, there is a need for developing methods whereby all diagnostic imaging is properly performed in optimally maintained imaging equipment, and all patients' radiation exposure is monitored. Several phantoms (anthropomorphic as well as mathematical phantoms) have been developed to assess radiation dosimetry in routine clinical examinations. These phantoms associated with calculation software are well established for advanced imaging techniques such as CT, nuclear medicine procedures, etc. At the present, radiographic and fluoroscopic dose records, as well as QC dose report, are almost entirely hand-recorded into paper logbooks typically at the operator's control console or with DR systems manually retrieved from PACS [10]. However, fetching the whole series of such examinations from the PACS is time consuming, and more importantly, it is not possible to generate user or protocol-specific radiation dose reports. Therefore, there is a trend toward developing standardized toolkits to automatically capture and integrate radiation dose records, QA, and QC report in a timely fashion [11, 10]. Several commercial dose monitoring and management systems are available today.

Acknowledgments We thank the manufacturers and suppliers of the phantoms and test tools described in this chapter for providing us with the necessary information regarding their products.

A.1 6.5 Web Resources

Majority of the phantoms' description and specification were obtained from the manufacturers' or suppliers' official websites, as listed below:

Manufacturer/supplier	Official Website
Agfa Healthcare, USA	http://www.agfahealthcare.com
Carestream Health, Inc., USA	http://www.carestream.com
Computerized Imaging Reference System (CIRS), Inc., USA	http://www.cirsinc.com
Fluke Biomedical, USA	http://www.flukebiomedical.com
Fujifilm, USA	http://www.fujifilm.com
Gammex, Inc., USA	http://www.gammex.com
General Electric (GE) Healthcare, UK	http://www.gehealthcare.com
Kyoto Kagaku Co. Ltd, Japan	http://www.kyotokagaku.com
Leeds Test Objects Ltd, UK	http://www.leedstestobjects.com
Radiology Support Devices (RSD), Inc., USA	http://www.rsdphantoms.com
The Phantom Laboratory, USA	http://www.phantomlab.com

References

1. International Electrotechnical Commission. (1999). Evaluation and routine testing in medical imaging departments. Part 3-1: Acceptance tests—Imaging performance of X-ray equipment for radiographic and radioscopy systems. IEC 61223-3-1, International Electrotechnical Commission, Geneva, Switzerland.
2. Chotas, H. G., Floyd, C. E., Jr, Johnson, G. A., & Ravin, C. E. (1997). Quality control phantom for digital chest radiography. *Radiology*, 202, 111–116.
3. American Association of Physicists in Medicine. (1998). AAPM Report No. 60. Instrumentation requirements of diagnostic radiological physicist, AAPM.
4. American Association of Physicists in Medicine. (1990). AAPM Report No. 31. Standardized methods for measuring diagnostic X-ray exposures, AAPM.
5. National Electric Manufacturers Association. (2000). NEMA Standards Publication XR 21-2000: Characteristics of and test procedures for a phantom to benchmark cardiac fluoroscopic and fluorographic performance. In National Electric Manufacturers Association (Ed.), *XR 21-2000, National Electric Manufacturers Association*, Virginia, USA.
6. International Electrotechnical Commission. (2005). *Medical diagnostic X-ray equipment: Radiation conditions for use in the determination of characteristics, IEC 61267*. Geneva, Switzerland: International Electrotechnical Commission.
7. International Electrotechnical Commission. (2003). *Medical electric equipment: Characteristics of digital X-ray imaging devices—Part 1: Determination of the detective quantum efficiency, IEC 62220-1*. Geneva, Switzerland: International Electrotechnical Commission.
8. Chida, K., Kaga, Y., Haga, Y., Takeda, K., & Zuguchi, M. (2013). Quality control phantom for flat panel detector X-ray systems. *Health Physics*, 104, 97–101.

9. Mayo, P., Rodenas, F., Marin, B., Campayo, J., G. V. (2009). Analysis of digital radiographic equipments with development of specific phantoms and software. In J. Slotter, et al. (Eds.), *IFMBE Proceedings* (pp. 425–428) Berlin, Heidelberg: Springer.
10. Ng K. H. (2013). Ensuring safety when transitioning to digital radiography in practice. In *Proceedings of the international conference on radiation protection in medicine—Setting the scene for the next decade*. International Atomic Energy Agency (IAEA), Bonn, Germany, Dec 3–7, 2012.
11. Wang, S., Pavlicek, W., Roberts, C. C., Langer, S. G., Zhang, M., Hu, M., et al. (2011). An automated DICOM database capable of arbitrary data mining (including radiation dose indicators) for quality monitoring. *Journal of Digital Imaging*, 24, 223–233.
12. Conway, B. J., Butler, P. F., Duff, J. E., Fewell, T. R., Gross, R. E., Jennings, R. J., et al. (1984). Beam quality independent attenuation phantom for estimating patient exposure from x-ray automatic exposure controlled chest examinations. *Medical Physics*, 11, 827–832.

Chapter 7

Computer Tomography Phantom Applications

Paulo R. Costa

7.1 Historical Perspective

Computed tomography (CT) using X-rays was the first imaging modality used in Medicine associating computer processing with data obtained from patients' X-ray transmission. This innovative technique developed during the second half of the 1960s and available for clinical use in 1972 has brought a new vision about the contrast details of the patient's body. The architecture of CT machines associated with the wide-range sensitivity of the employed detectors becomes available a level of tissue differentiation not found before in any other imaging system. The powerful diagnostic capability, associated with the possibility of viewing slices of the body, recognized CT as one of the milestones on the development of clinical images in the last century [1].

Many visionary pioneers of the technical and conceptual development of CT scanners are reported in the literature, such as W. H. Oldendorf, D. E. Kuhl, R. Q. Edwards, and A. M. Cormack [2]. The introduction of this image modality to diagnostic Medicine was so accepted by the scientific community, that Sir Godfrey Hounsfield, who is recognized as the major contributor of the CT scanners development and who obtained the first patents of the CT apparatus in 1968 and 1972, was distinguished with the Nobel Prize in Physiology or Medicine in 1979. He shared this prize with the physicist Allan Cormack.

All these new possibilities of improving the diagnoses of known diseases and also recognizing new pathologies or early stages of pathological tissues were followed by the need of developing new methods for improving the image performance properties and the evaluation of doses in patients and staff. The drastic changes in the CT scanners architecture compared to other diagnostic X-ray machines presented as a new paradigm for Medical Physicists on determining dose

P. R. Costa (✉)

Department of Nuclear Physics, University of São Paulo, Rua do Matão, Travessa R, 187, São Paulo, SP 05508-090, Brazil

e-mail: pcosta@if.usp.br

characteristics thirty years ago. These architecture modifications included the change from plane-parallel to cylindrical geometry for example. The major challenge was in measurement for a cross section as opposed to a flat field. This new geometric aspect of the CT scanners, generating a narrow X-ray fan beam, which produced a radiation profile with axial symmetry inside the patient, required been adequately quantified by a dosimetric parameter or function unknown until that time. Later, a “dose index” for CT applications was introduced to cover this need.

After the first developments of quality assurance and dose assessment of early-generation CT scanners, it was clear for the professionals working on technical aspects of measurements adequacy for improving the safety of patients and the assurance of high image qualities that the evolution of the systems available in the market will be very fast [3]. The engineering teams of the CT vendors are constantly searching for better spatial resolution, thinner slices and faster image acquisitions and reconstruction algorithms. However, these factors also represent constant need for new measurement techniques and phantoms, corresponding to the crescent changes on the CT equipment capabilities. Since the end of the last century, Medical Physicists and Radiologists saw the emergence of new CT technologies, such as multi-slice, current-modulated, half-second rotation, dual-energy, dedicated breast, and 4D cone beam. Each one of them presents new diagnostic capabilities, but individually requires new studies in quality control and dosimetry. The development of phantoms followed the same process, and it shows to be of major importance on the qualification of the CT scanners in order to balance patient safety and diagnostic capabilities. During this time, radiation doses [3] and dose reduction techniques [4] have been a constant concern for the medical physicists and other professional involved with this kind of imaging technique.

Recently, an impressive growth has been observed in the use of new imaging technologies employing ionizing radiation, in special CT machines [5, 6]. A study conducted by Fazel et al. [7] demonstrated that around 75 % of the dose in the North American population during the years between of 2005 and 2007 was related to CT and Nuclear Medicine procedures in this period. However, these two techniques represented only 21 % of the imaging procedures conducted in that population. These numbers alerted the community for the need of systematic dose assessment in CT examinations and increasing the investments in education in all levels associated with the radiologic image chain (radiologist,technologist, physicists, nurses, engineers, administrators, etc.) to recognize the correct risks associated with these clinical protocols [8, 9].

7.2 Acceptance and Quality Control Testing

7.2.1 Phantoms for Accessing Dosimetry

During the second half of the 1970s, many papers appeared in the literature describing methodologies and devices for the dosimetric characterization of CT systems [10, 11]. These methods, however, were just organized in a consistent

manner with the introduction of the CT dose index (CTDI) by Shope et al. [12]. This index, which was (and is) frequently confounded with patient dose [13], formed the mathematical, conceptual, and experimental base for the dosimetric characterization of CT machines and protocols [14]. Nowadays, there are substantial improvements of the original CTDI definitions. These definitions can be found in the literature [15], and deeply exploring their concepts is out of the context of the present work. Moreover, with the recent changes on the architecture of the CT machines, these CT metrics are in progress of adaptation to be used (or not) when evaluating doses to wide-beam CT systems. Very comprehensive texts are available discussing the recent developments in CT dosimetry [16].

The CTDI definition considers the dose profile as composed of a superposition of a primary dose distribution, related to the portion of the X-ray beam modulated by the pre-patient collimator, which is used to produce the image, and a scatter profile, originated the interaction of the primary beam with a phantom material. The standardized phantom material chosen to be used in CTDI measurements was the polymethyl methacrylate (PMMA). The International Electrotechnical Commission adopted this CTDI measuring method for comply its dosimetric requirements for CT equipment [17].

Dose measurements can be performed in two ways: computing the CT dose profiles or integrating the average signal with an ionizing chamber [18], [19]. The dose profile methods were traditionally performed by using TLD's aligned in rows and positioned inside the dosimetric phantom [20]. More recently, this time-consuming method has been substituted by the use of OSL strips [21–23], Gafchromic films [24] or MOSFET detectors [25]. Using these kinds of approaches, it is possible to recognize not only the dosimetric properties, but also the geometric properties of the radiation profile, and to compare it with the sensitive CT profiles for different collimations [26].

The methodologies using position-sensitive devices above described are not practical for routine dosimetry of CT scanners. In these cases, the use of pencil-shaped ion chambers is preferred. The use of ion chambers specific for CT was introduced by Suzuki and Suzuki [27] and it is widely applied today. Similar to the re-evaluation of the applications of CTDI, considering the new scanner designs, the use of these pencil chambers has been discussed in the scientific community [28–30]. One of the proposed alternatives is the use of a farmer-type detector for dose evaluation purposes of wide-beam scanners [31].

Anyway, independently of the dosimetry methodology chosen, the traditional phantom design is composed of cylindrical blocks of massive PMMA with standardized diameters (16 and 32 cm) representing parts of the body (head or trunk/abdomen) for adult or pediatric dose assessment (Fig. 7.1). These plastic blocks have holes with diameters adequate for inserting the pencil ion chambers, the position-sensitive dosimeters, or farmer-type chambers [32].

The experience of using these cylindrical blocks, associated with the searching for more detailed dosimetric information, conducted the industry to develop some more sophisticated CTDI phantoms. Two examples of these different solutions are shown in Figs. 7.2 and 7.3. Figure 7.2 presents a stack of PMMA blocks forming a

Fig. 7.1 Head and body CT dosimetric phantom manufactured by Radcal Corporation. The phantoms are composed of cylindrical massive blocs of PMMA containing holes dimensioned for the exact introduction of pencil ion chambers



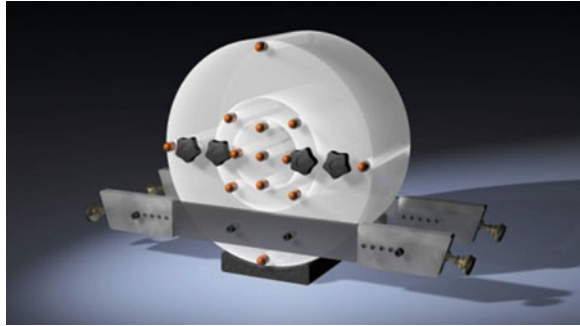
system which represents a human head. This phantom was designed for cone beam CT (CBCT) dose evaluations and can also be used for CT dose evaluations with TLD's, ionization chambers or Gafchromic films. On the other hand, Fig. 7.3 shows a new development of dosimetric phantom composed of nesting PMMA disks with standardized diameters for evaluating CTDI for pediatric and adult protocols. The phantom can be coupled to a support, which suspends the device over the equipment couch and aligns it along the central axis of the imaging system. It enables the use of the phantom in helical mode of operation of the CT equipment.

An important use of different size and shape acrylic phantoms for pediatric dose investigations in CT was conducted by Siegel et al. [33]. The study analyzed the dosimetric response of a multi-detector CT scanner when parameters such as applied voltage, AEC, and size and shape of the phantoms are associated with image noise and contrast. They found that the measured doses in an 8-cm-diameter phantom are superior to 50 and 100 % for applied voltages of 80 and 140 kV, respectively, when compared to the doses measured using a 32-cm-diameter phantom adopting a protocol-defined tube current value. However, when the tube current was adapted to the phantom size, the dose reduction for the 8-cm-diameter

Fig. 7.2 SedentexCT dose phantom composed of a stack of PMMA blocks forming a system which represents a human head (www.leadstestobjects.com)



Fig. 7.3 Dosimetric phantom composed of nesting PMMA disks with standardized diameters for evaluating CTDI for pediatric and adult protocols (www.cirsinc.com)



phantom was about 80 %. They also found that the reduction in the applied voltage can increase the image noise significantly. This kind of study using different size and shape of geometric phantoms generated many initiatives on optimizing pediatric CT imaging protocols [34].

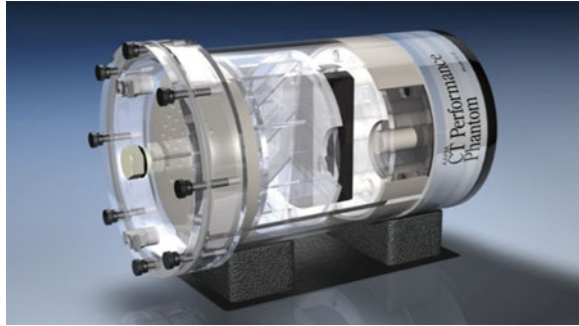
7.2.2 Phantoms for Accessing Image Quality

After the introduction of the commercial CT scanners by EMI in the early 1970s, the scientific community started to evaluate the capabilities and limitations of that new imaging device [35]. However, the previously known image quality evaluation techniques were not adapted to the geometric characteristics of the CT scanners neither to their physical and architectonic properties, such as voltage and current range and gantry geometry. This situation resulted in proposals for geometric apparatus intending to quantify the main image properties of the CT images, such as spatial resolution in low- and high-contrast background, image noise, slice thickness, and also some kind of artifacts (motion, beam hardening, uniformity).

A few years after the popularization of the CT device in the clinical environment, Edwin McCullough, from Mayo Clinic, published two papers showing the applications of a PMMA test object for the evaluation of the image quality of commercial scanners [36, 37]. The McCullough and colleagues' ideas have contributed to the AAPM Task Force on CT Scanner Phantoms, and their progresses were adopted on the first guide for quality control and dosimetry in CT published by AAPM [38], and which based the development of many posterior quality control programs [39]. The AAPM CT test phantom (Fig. 7.4) also included an insert for TLD measurements of the dose profile and alignment. This phantom was widely used around the world for at least 20 years for establishing quality control and acceptance testing programs for CT scanners.

The AAPM CT quality control phantom includes many interesting inserts for performance evaluation of the CT scanners in terms of its image quality, but it is

Fig. 7.4 CIRS Model 610 phantom which complies with the recommendations of the AAPM for a CT performance phantom [38]. The phantom measures ten distinct CT performance parameters



inconvenient because of the need to be filled with water. In order to develop more practical methods for evaluating image quality in CT, several solid phantoms were developed for this purpose. One of the most familiar solid quality assurance CT phantom was proposed based on the works of Goodenough and collaborators [40, 41] using a tissue-equivalent epoxy resin developed by White [42]. This phantom was improved during the last decades and received specific inserts and accessories for taking into account the different requirements for image quality evaluation resulting from technological development of the CT scanners (Fig. 7.5). The phantom is made from solid-cast materials, eliminating material absorption of water and leaks associated with water bath phantoms, as well as problems related to varied water sources.

Other kind of modular phantom for image quality assessment purpose is presented in Fig. 7.6. This phantom was developed in a modular design and in the body of the phantom are holes for inserting small disks which provide specific information about image quality parameters, such as spatial and contrast resolution, pixel intensity, beam hardening, geometric distortion, uniformity and noise.

There are many other phantoms for CT image quality which can be found in the specialized market. This text has not the intention to provide comprehensive information for all available phantom models neither to exclude any commercial product. The phantom option many times depends on the basic QA protocol

Fig. 7.5 Catphan[®] quality image solid phantom manufactured by The Phantom Laboratories [43]

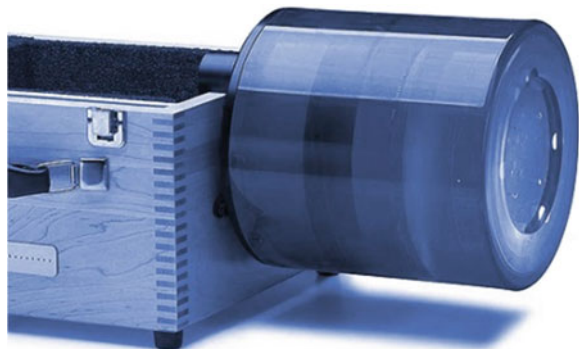


Fig. 7.6 Phantom developed in a modular design with holes for inserting small discs which provide image quality information (www.leedstestobjects.com)



adopted by the imaging facility [44, 45]. Other important kinds of solid phantom to be considered are related to accreditation programs for CT devices. These phantoms will receive a special topic in this chapter.

7.3 Use of Phantoms in the Accreditation Process

The definition of accurate criteria for quality assessment in CT systems was very closely connected to the development of specific phantoms. The AAPM Task Group number 2 was focused on acceptance tests of CT machines, and its report 39 [20] recommended the combined use of commercial phantoms to some generic objects designed specifically for the compliance to the document.

In 2000, the European Community expanded the concept of Quality Criteria Guidelines existing for other imaging modalities for CT [46]. In this document, guidance is adopted for establishing quality criteria and equipment performance associated with patient doses. The purpose was to provide an operational framework for radiation protection, correlating adequate technical parameters for generating images with good quality and the radiation safety of the patients.

The more contemporary and sophisticated concepts of quality assessment in medical imaging are included on the accreditation programs. The American College of Radiology (ACR) introduced a CT accreditation program ten years ago. The program involves the submission of information regarding the clinical protocols adopted in the facility, dose measurements, and the performance evaluation using clinical and phantom images [47]. The phantom designed for the image quality assessment required for the ACR accreditation program has the capability of providing information of positioning accuracy, accuracy of the CT No., slice

Fig. 7.7 ACR CT Phantom manufactured by Gammex, Inc. The phantom is designed to be an integral part of the American College of Radiology CT Accreditation Program



width, low contrast resolution, spatial resolution in high-contrast, CT number uniformity, and image noise [48].

The ACR CT accreditation phantom (Fig. 7.7) is composed of four modules constructed by water-equivalent material. The diameter of the phantom is 20 cm, and each module has 4 cm depth. They also have inserts which produces structures on the CT images for assessment of the characteristic quality parameters above described.

The ACR accreditation process also requires the submission of CTDI measurements. The context of these measurements are the same used in regular QC procedures, considering the adequate care to the alignment of the measuring setup. The phantoms used are the 16- and 32-cm-diameter PMMA blocks mentioned above, and the applicant must submit measurements resulting of the application of protocols for adults (head and abdomen) and pediatric (abdomen) examinations.

7.4 Anthropomorphic Phantoms for CT Applications

Anthropomorphic phantoms were introduced in radiation protection in Medicine with the aim of mimicking human tissue radiation absorption properties, and also its average anatomical characteristics such as electron density and effective atomic number variations. Alderson et al. [49] introduced the concepts of tissue-equivalent material [50] associated with a human-shaped phantom for applications in radiation therapy treatment plans (see Chap. 4). These dosimetric phantoms were constructed using a real human skeleton embedded in a material which mimics the human soft tissue. They also included a low density tissue for molding the shape of the lungs. This was called the “Alderson Phantom” and it is widely applied in diagnostic imaging dosimetry for varied applications [51], usually associated with the insertion of film or thermoluminescent dosimeters [52]. This kind of realistic phantom

has shown to be very useful for CT dosimetry since the beginning of the dose investigations of this technique [53].

The idea of using tissue-equivalent materials for CT evaluation purposes has been in place for at least 30 years [54]. Recently, anthropomorphic phantoms have been applied for dose estimation in CT in a wide assortment of applications using different kind of radiation detectors. The phantom exemplified in Fig. 7.8 is composed of a proprietary urethane formulation for mimic human soft tissue. This material has an effective atomic number and mass density which simulates muscle tissue with randomly distributed fat. The phantom also has lung material with the same effective atomic number as the soft tissue material, but with a density which simulates lungs in a median respiratory state, and a natural human skeleton [55].

Many authors have dedicated special attention to the high doses usually resulting from applying angiographic CT in Cardiology. For example, Nikolic et al. [56] associated a commercial phantom to semiconductor field-effect detectors in order to investigate the consequences of voltage and heart beats frequency on the absorption of radiation dose in radiosensitive organs. In 2006, Hurwitz et al. [57] published a study regarding female breast doses using a gender-specific phantom. A similar approach was adopted by Litmanovich et al. [58] on studying the effects of scanner parameters on breast, lung, and pelvic organs employing a female phantom. TLD evaluation using anthropomorphic phantoms and ionization chamber measurements with PMMA cylindrical phantoms can also be related to Monte Carlo simulations, providing very reliable information regarding 3D dose distributions resulted from CT imaging procedures [59]. These authors have considered important aspects of the protocols such as patient size, the use of tube current modulation, and the scanner architecture.

Researchers have also been motivated to use anthropomorphic phantoms for investigation of the sex-dependent tissue-weighting factors adopted by



Fig. 7.8 The RANDO[®] phantom manufactured by The Phantom Laboratory. The phantom is composed of a proprietary urethane formulation for mimicking human soft tissue [55]

International Commission on Radiation Protection publication 103 [60]. Monte Carlo simulations have been widely used for this purpose and also for evaluating age-specific dose characteristics.

One of the first results for the estimation of effective dose for pediatric CT examinations with Monte Carlo simulations was published by Huda et al. [61]. The authors adopted simple mathematical anthropomorphic age-specific phantoms for obtaining body region factors correlating effective doses and energy imparted during CT procedures. A more recent Monte Carlo simulation approach to this problem was published by Deak et al. [62] relating these factors to previously measured dose-length product (DLP) values. Different practical situations were investigated by these authors: four scanner voltages, five patient sizes/ages, and five body regions with dosimetric interest. Using these input parameters and the Oak Ridge National Laboratory phantom series [63], they calculated a series of conversion factors for calculation of the effective dose from measured values of DLP. They also compared their results when considering the recommendation of two different ICRP publications (60 and 103).

A complementary size-/age-specific Monte Carlo-based dosimetric approach was developed by Melo Lima et al. [64]. In this study, age- and posture-specific children mathematical phantoms were used. These phantoms are based on the technique developed by Kramer et al. [65] for adult male and female phantoms called MASH and FASH obtained from anatomical atlas using 3D modeling software [66]. Recently, these authors published results of skeleton dosimetry based on micro-CT images using the same anatomical models [67].

In general, in the last decades, the scientific community has promoted many efforts to consolidate special care in radiation protection in pediatric radiology. This special attention is clearly demonstrated by the Image Gently[®] campaign, an alliance focusing radiation safety in pediatric imaging, started in 2006 by the US Society of Pediatric Radiology, but which also involves many different segments of the society around the world. Dose evaluation and optimization in CT pediatric procedures have been adopted as one of the most studied issues of radiation dosimetry in the recent years [68], and the use of age-specific anthropomorphic phantoms has been adopted by the researchers for non-invasive determination of dose characteristics for these special procedures. A few years ago, stakeholders involved in this subject were stimulated by the Image Gently Alliance to work in partnership and define a vendor summit to bring the dose optimization in pediatric CT inside the clinical routine [69].

In the beginning of the last decade, a group from University of Texas elaborated strategies for conducting adequately CT procedures in pediatric patients [70]. They used commercial phantoms which simulate body proportions of children of 1, 5, and 10 years old and also an adult phantom and compared their superficial dose measurements with CTDI data, using the noise as an image quality parameter. They found that dose reductions in the range of 60–90 % are possible when the technical parameters are adequate to age-/size-specific patients. More recently, pediatric anthropomorphic phantoms were used in order to estimate organ doses

delivered by multi-detector CT scanners using or not an automatic exposure control system [71].

The popularization of the multi-detector CT scanners around the world brings many diagnostic advantages to the clinical area, but also resulted in a gap of knowledge about the dosimetric properties of these large-field CT machines and their effects in the human health. In 2007, Birnbaum et al. [72, 73] published a study using a customized abdominal anthropomorphic phantom constructed with tissue-equivalent materials and presented a cross-comparison of models and manufactures of CT machines. Their approaches were focused on the soft tissue contrast differentiation among commercial machines.

Other very important topics in terms of radiation protection that must be considered are doses in the fetus when a pregnant patient is submitted to CT procedures, especially in the cases of abdominal examinations. In such cases, careful considerations relating the fetal dose estimation and the associated risk must be conducted, taking into account the pregnancy stage and the characteristics of the CT procedure. These kinds of investigation are generally conducted using anthropomorphic phantoms.

Wagner et al. [74] presented a guide for orientation of the medical community when conducting X-ray examination on pregnant women. In a posterior publication, Wagner et al. [75] have treated the case of conceptus doses considering CT examinations. Osei and Falkner [76] studied fetal doses in general radiologic examinations and proposed an algorithm for estimating the fetal dose [77] and the associated risks [78]. Their studies were based on Monte Carlo simulations. Recently, CT evaluation doses were incorporated to the method [79] as well as the risk estimation [80].

Empirical CT fetal dose studies using anthropomorphic phantoms were introduced by Felmler et al. in 1990 [81] and more recently by Dietrich et al. [82], Hurwitz et al. [83], Jaffe et al. [84, 85], and finally by Gilet et al. [86]. These last authors used an anthropomorphic phantom and TLD's for determining fetal doses resulting from pulmonary CT angiograms and abdominal and pelvic CT procedures considering 4-, 16-, and 64-slice multi-detector scanners. Early pregnancy and gestational ages of 10, 18, and 38 weeks were considered. An Alderson anthropomorphic phantom was modified by adding soft tissue attenuation-equivalent material to simulate the different pregnancy stages considered in the study.

Other types of anthropomorphic phantoms are constructed using tissue-equivalent materials mimicking specific parts of the body. The differences on the radiation attenuation resulting from the anatomy of the body can also be evaluated using PMMA slabs filled with water. These kinds of devices and also a group of semi-anthropomorphic phantom were very recently used by Wang et al. [87]. These specific anthropomorphic or semi-anthropomorphic phantoms, filled with water or composed of tissue-equivalent materials, are practical and useful for investigating very specific dosimetric properties of the CT procedures or defined parts of the body. Birnbaum et al. [72, 73] have also developed specific tissue-equivalent materials for testing attenuation properties of CT protocols taking into

account different situations (scanner type, convolution kernel, and tube current). Tissue-equivalent materials were also developed by Peng [88] for a specific population.

7.5 Phantoms for Investigation of Specific Imaging and Dosimetry Issues

Currently, the CT becomes a general nomenclature for an image modality which has been reconfigured in more specialized sub-modalities. Specific system designs, image processing methods, accessories, or hardware improvements provide clinical capabilities and dose reduction which were not common in the CT facilities years ago. Examples of this new CT specialized and sub-modalities are the systems designed to cardiac or breast imaging, respectively, providing fast data collection and high contrast, with doses as low as possible. Dual-energy CT devices are other example of these new technologies.

The technological advances in CT systems are followed by the need of investigating specific characteristics in terms of image quality or dosimetry. Frequently, these investigations require the development and validation of phantoms to be applied focusing some specific capability of the CT device or the amount or radiation impinging the patient for make this clinical information available [89].

The effectiveness of current modulation on providing dose reduction when the radiation output is changed according to the patient body attenuation is one of the more intensively investigated property of modern CT systems. This operational characteristic is patient specific but must be implemented following an acceptable image noise standard, in order to produce images clinically acceptable. Since the current modulation depends on the attenuation, anthropomorphic, semi-anthropomorphic, or cylindrical dosimetry phantoms can be used for quantify the dose optimization resulting from its use. Duan et al. [90] used such phantoms for determining surface dose reduction using organ-based current modulation protocols. Incorrect operations of these systems were also investigated by Matsubara et al. [91] using commercial elliptical phantoms when the centralization of the patient is inappropriate.

Specifically designed phantoms are also proposed for determining the correct operation of current modulation systems. This approach was originally introduced by Kalender et al. [92] evaluating one of the first commercial equipment's providing current modulation option. The ImPACT program proposes the use of a conical PMMA block (Fig. 7.9) for testing the response of the modulation system when the patient size changes on the z-direction [93].

Dual-source CT equipment was introduced in the middle of the last decade. They offer an important contribution to cardiac CT images, providing better temporal resolution during ECG-controlled clinical procedures [94]. McCollough et al. [95] adopted the methodology described in IEC standard 60601-2-44 [17] for

Fig. 7.9 Conical PMMA block for testing AEC response of the system when the patient size changes on the z-direction [96]



determining the dose performance of a dual-source 64-slice system. This method adopts the widely used PMMA blocks with different diameters for measuring dose indexes.

The involuntary motions of the human body have also been focused by researchers looking for quality or dosimetric evaluations of CT protocols. One of the first studies considering these involuntary characteristics was conducted by Morehouse [97]. More recently, results of investigations which contribute to the development of flow and/or motion phantoms can be found in the literature [98, 99]. These devices can be designed for a domestic evaluation, or they can be produced focusing future validation and commercial use [100].

7.6 Perspectives on Phantom Developments for Image Quality and Dosimetry in CT

The development of phantoms occurred since the first generations of the CT machines until recently introduced large beam equipment was strongly related to the geometrical aspects of the systems, and to their image capabilities. Additionally, the development of CT technologies implicated the evolution of dose indicators and metrics, which consequently has influenced the design and validation of devices and measurement techniques for describing the dose aspects related to these imaging procedures. In the future, this compromise between technological developments and phantom designs will be maintained and, probably, consolidated.

An example of the strong relationship between new imaging technologies and the phantom design evolution is the assessment of image quality of dedicated breast CT equipment. In this kind of image, the sensitivity profile is one of the most important parameters to be evaluated, since it is related to the efficiency of the equipment on producing an image using the amount of radiation impinging in

considered slice of the patient body. Additionally, the breast tissue presents specific characteristic which must be taken into account in order to reproduce the response of the system when this kind of image is performed. These technical and anatomical constrains were recently considered by Nosratieh et al. [101]. These authors did an adaptation on a commercial adipose tissue phantom introducing circular brass disks into the phantom slabs, which were used for the slice-sensitive profile (SSP) evaluation. This example shows how new phantoms can be creatively designed in the future adopting as basis existing materials and simple, but effective, adaptations.

Other correlations that will probably influence the creation of new phantoms are the consideration of patient motion. Many efforts have been made for allocating the body involuntary motion as one of the variables to be considered on phantom designs. These considerations usually implicate on the introduction of mechanically induced motion with amplitude and frequency which mimic the natural motion of some part of the body. These kinds of considerations are especially important if the image sequence has the purpose to be used on cancer treatment procedures. Szegedi et al. [102] emphasizes the importance of the use of the four-dimensional CT as a tool for characterizing patient-specific organ/tumor motion. For this purpose, the authors developed a deformable liver phantom which can be moved simulating the displacement of this organ with the patient breath. The simulation of this movement is performed by a piston coupled to the liver phantom.

These works above mentioned are just two examples of many which can be found in the literature. The extension of number of published works reinforces the perspective of the future development of phantoms adapted of specifically designed for attending the need of image quality or dosimetric information on CT field. This is a very exciting research area which is following very closely the strong developments of new CT technologies.

A more specific development is been working by the AAPM Task Group 200. This TG is working out on the elaboration of practical measuring methods for accounting the metrics introduced at AAPM report 111 [16]. Their proposed measuring solution considers the use of a larger phantom to capture the scatter tails of the radiation profile and changes on the dosimetric CT protocols, considering not only with single axial scans but also with helical scans [103]. The proposed phantom is been designed as a cylinder constructed on high density polyethylene 30 cm in diameter and 60 cm in length, including some inserts and holes for the introduction of radiation detectors. This phantom is in validation phase and, after been incorporated as a regular-use tool for dosimetric assessment in CT scanners, will probably be a major change in the CT phantoms scenario used until today.

References

1. Keevil, S. F. (2011). Physics and medicine: A historical perspective. *Lancet*, 379, 1517–1524. (Published Online April 18 2012).
2. Webb, S. (1990). *From the watching of shadows—The origins of radiological tomography*. Bristol: Adam Hilger, ed.
3. Rothenberg, L. N., & Pentlow, K. S. (1992). Radiation dose in CT. *Radiographics*, 12, 1225–1243.
4. McCollough, C. H., Bruesewitz, M. R., & Kofler, J. M, Jr. (2006). CT dose reduction and dose management tools: Overview of available options. *RadioGraphics*, 26, 503–512.
5. Brenner, D. J., & Hall, E. J. (2007). Computed tomography: An increasing source of radiation exposure. *New England Journal of Medicine*, 357, 2277–2284.
6. Nickoloff, E. L., & Alderson, P. O. (2001). Radiation exposures to patients from CT: Reality, public perception, and policy. *American Journal of Roentgenology*, 177, 285–287.
7. Fazel, R., Krumholz, H. M., Wang, Y., Ross, J. S., Chen, J., Ting, H. H., Shah, N. D., Nasir, K., Einstein, A. J., and Nallamothu, B.K. (2009). Exposure to Low-Dose Ionizing Radiation from Medical Imaging Procedures. *N Engl J Med*, 361, 849–857. doi:10.1056/NEJMoa0901249.
8. Fayngersh, V., & Passero, M. (2009). Estimating radiation risk from computed tomography scanning. *Lung*, 187, 143–148.
9. Freudenberg, L. S., & Beyer, T. (2011). Subjective perception of radiation risk. *Journal of Nuclear Medicine*, 52(Suppl 2), 29S–35S.
10. International Commission on Radiological Protection. (2007b). *Managing patient dose in multi-detector computed tomography (MDCT)*. ICRP Publication 102. Annals of the ICRP 37(1). Elsevier ed.
11. Thomadsen, B. R., Paliwal, B. R., Laursen, J. F., Filamor, C. O., & van de Geijn, P. (1983). Some phantom designs for radiation dosimetry and CT applications. *Medical Physics*, 10, 886–888.
12. Shope, T. B., Gagne, R. M., and Johnson, G. C. (1981). A method for describing the doses delivered by transmission x-ray computed tomography. *Med Phys*, 8(4), 488–495.
13. McCollough, C. H., Leng, S., Yu, L., Cody, D. D., Boone, J. M., & McNitt-Gray, M. F. (2011). CT Dose Index and patient dose: They are not the same thing. *Radiology*, 259, 311–316.
14. McCullough, E. C., & Payne, J. T. (1978). Patient dosage in computed tomography. *Radiology*, 129, 457–463.
15. American Association of Physicists in Medicine. (2008). The measurement, reporting and management of radiation dose in CT. Report No. 96 of AAPM Task Group 23, Available in <http://www.aapm.org/pubs/reports/>.
16. American Association of Physicists in Medicine (2010). Comprehensive methodology for the evaluation of radiation dose in x-ray computed tomography. Report No. 111 of AAPM Task Group 111. Available in <http://www.aapm.org/pubs/reports/>.
17. International Electrotechnical Commission. (2009). *Medical electrical equipment: Part 2–44—Particular requirements for the safety of x-ray equipment for computed tomography*. Publication no. 60601-2-44. Ed. 3.: International Electrotechnical Commission, 1–36. Geneva, Switzerland.
18. Furlow, B. (2010). Radiation dose in computed tomography. *Radiologic Technology*, 81, 437–450.
19. Knox, H. H., & Gagne, R. M. (1996). Alternative methods of obtaining the computed tomography dose index. *Health Physics*, 71, 219–224.
20. Lin, P.-J. P., Beck, T.J., Borrás, C., Cohen, G., Jucius, R.A., Kriz, R.J., Nickoloff, E.L., Rothenberg, L.N., Strauss, K.J., Villafana, T. (1993). Specification and acceptance testing of computed tomography scanners. Report No. 39 of AAPM Task Group 2. Available in <http://www.aapm.org/pubs/reports/>.

21. Lavoie, L., Ghita, M., Brateman, L., & Arreola, M. (2011). Characterization of a commercially-available, optically-stimulated luminescent dosimetry system for use in computed tomography. *Health Phy*, *101*, 299–310.
22. Vrieze, T. J., Sturchio, G. M., & McCollough, C. H. (2012). Precision and accuracy of a commercially available CT optically stimulated luminescent dosimetry system for the measurement of CT dose index. *Medical Physics*, *39*, 6580–6584.
23. Yukihara, E. G., Ruan, C., Gasparian, P. B. R., Clouse, W. J., Kalavagunta, C., & Ahmad, S. (2009). An optically stimulated luminescence system to measure dose profiles in x-ray computed tomography. *Physics in Medicine & Biology*, *54*, 6337–6352.
24. Gorny, K. R., Leitzen, S. L., Bruesewitz, M. R., Kofler, J. M., Hangiandreou, N. J., & McCollough, C. H. (2005). The calibration of experimental self-developing Gafchromic® HXR film for the measurement of radiation dose in computed tomography. *Medical Physics*, *32*, 1010–1016.
25. Mukundan, S., Wang P. I., Frush, D. P., Yoshizumi, T., Marcus, J., Kloeblen, E., and Moore, M. (2007). MOSFET Dosimetry for Radiation Dose Assessment of Bismuth Shielding of the Eye in Children. *American Journal of Roentgenology*.*188*:1648–1650.
26. Gagne, R. M. (1989). Geometrical aspects of computed tomography: Sensitivity profile and exposure profile. *Medical Physics*, *16*, 29–37.
27. Suzuki, A., & Suzuki, M. N. (1978). Use of a pencil-shaped ionization chamber for measurement of exposure resulting from a computed tomography scan. *Medical Physics*, *5*, 536–539.
28. Boone, J. M. (2007). The trouble with CTD100. *Medical Physics*, *34*, 1364–1371.
29. Brenner, D. J., & McCollough, C. H. (2006). It is time to retire the computed tomography dose index (CTDI) for CT quality assurance and dose optimization. *Medical Physics*, *33*, 1189–1191.
30. Dixon, R. L. (2003). A new look at CT dose measurement: Beyond CTDI. *Medical Physics*, *30*, 1272–1280.
31. Dixon, R. L. et al. (2010). The future of CT dosimetry—Comprehensive methodology for the evaluation of radiation dose in x-ray computed tomography. Report of AAPM Task Group III.
32. International Atomic Energy Agency (IAEA). (2007). Dosimetry in diagnostic radiology: An international code of practice. Technical Reports Series No. 457 (IAEA).
33. Siegel, M. J., Schmidt, B., Bradley, D., Suess, C., & Hildebolt, C. (2004). Radiation dose and image quality in pediatric CT: Effect of technical factors and phantom size and shape. *Radiology*, *233*, 515–5221.
34. Ngaile, J. E., Msaki, P., & Kazema, R. (2012). Patient-size-dependent radiation dose optimisation technique for abdominal CT examinations. *Radiation Protection Dosimetry*, *148*, 189–201.
35. McCullough, E. C. (1980). Specifying and evaluating the performance of computed tomography (CT) scanners. *Medical Physics*, *7*, 291–296.
36. McCullough, E. C., Raker, H. I., Houser, O. W., & Reese, D. F. (1974). An evaluation of the quantitative and radiation features of a scanning x-ray transverse axial tomography: the EMI scanner. *Radiology*, *111*, 709–715.
37. McCullough, E. C., Payne, J. T., Baker, H. L., Hattery, R. R., Sheedv, P. P., Stephens, D. S., et al. (1976). Performance evaluation and quality assurance of computed tomography (CT) equipment with illustrative data for ACTA, delta and EMI scanners. *Radiology*, *120*, 173–188.
38. Judy P. F., Balter, S., Bassano, D., McCullough, E.C., Payne, J.T. & Rothenberg, L. (1977). *Phantoms for performance evaluation and quality assurance of CT scanners*. AAPM report nr. 1. American Association of Physicists in Medicine, Chicago.
39. Bellon, E. M., Miraldi, F. D., & Wiesen, E. J. (1979). Performance of evaluation of computed tomography scanners using a phantom model. *American Journal of Roentgenology*, *132*, 345–352.

40. Goodenough, D. J., Weaver, K. E., & Davis, D. O. (1977). Development of a phantom for evaluation and assurance of image quality in ct scanning. *Optical Engineering*, *16*, 52–65.
41. Goodenough, D. J., Levy, J. R., & Kasales, C. (1998). Development of phantoms for spiral CT. *Comput Med Imag Grap*, *22*, 247–255.
42. White, D. R., Martin, R., & Darlison, R. (1977). Epoxy resin based tissue substitutes. *British Journal of Radiology*, *50*, 814–821.
43. The Phantom Laboratory. (2012b). Catphan[®] 500 and 600 manual. Available on line in <http://www.phantomlab.com/library/pdf/catphan500-600manual.pdf>.
44. The Institute of Physics and Engineering in Medicine. (1997). Recommended standards for the routine performance testing of diagnostic x-ray imaging systems. *IPEM Report No 77*. Institute of Physics and Engineering in Medicine, New York.
45. The Institute of Physics and Engineering in Medicine. (2003). Measurement of the performance characteristics of diagnostic x-ray systems used in medicine. *IPEM Report No: 32 Part III: Computed tomography x-ray scanners* (2nd edition). York, Institute of Physics and Engineering in Medicine.
46. European Commission. (2000). European guidelines on quality criteria for computed tomography. EUR 16262 EN. Luxembourg, Office for Official Publications of the European Communities.
47. American College of Radiology. (2012). CT accreditation program requirements. Available in <http://www.acr.org/~/media/ACR/Documents/Accreditation/CT/Requirements.pdf>.
48. McCollough, C. H., Bruesewitz, M. R., McNitt-Gray, M. F., Bush, K., Ruckdeschel, T., Payne, J. T., et al. (2004). The phantom portion of the American College of Radiology (ACR) computed tomography (CT) accreditation program: Practical tips, artifact examples, and pitfalls to avoid. *Medical Physics*, *31*, 2423–2442.
49. Alderson, S. W., Lanzl, L. H., Rollins, M., & Spira, J. (1962). An instrumented phantom system for analog computation of treatment plans. *American Journal of Roentgenology*, *87*, 185–195.
50. White, D. R. (1978). Tissue substitutes in experimental radiation physics. *Medical Physics*, *5*, 467–479.
51. Archer, B. R., Glaze, S., North, L. B., & Bushong, S. C. (1977). Dosimeter placement in the rando phantom. *Medical Physics*, *4*, 315–318.
52. Vacirca, S. J., Pasternack, B. S., & Blatz, H. (1972). A film-thermoluminescent dosimetry method for predicting body doses due to diagnostic radiography. *Physics in Medicine & Biology*, *17*, 71–80.
53. Yalcintas, M. G., & Nalcioğlu, O. (1979). A method for dose determination in computerized tomography. *Health Physics*, *37*, 543–548.
54. Fullerton, G. D., & White, D. R. (1979). Anthropomorphic test objects for CT scanners. *Radiology*, *133*, 217–222.
55. The Phantom Laboratory. (2012a). RAN 100 and RAN 110 datasheet brochure. Available on line in http://www.phantomlab.com/library/pdf/rando_datasheet.pdf.
56. Nikolic, B., Khosa, F., Lin, P. J. P., Khan, A. N., Sarwar, S., Yam, C.-S., et al. (2010). Absorbed radiation dose in radiosensitive organs during coronary CT angiography using 320-MDCT: Effect of maximum tube voltage and heart rate variations. *American Journal of Roentgenology*, *195*, 1347–1354.
57. Hurwitz, L. M., Yoshizumi, T. T., Reiman, R. E., Paulson, E. K., Frush, D. P., Nguyen, G. T., et al. (2006). Radiation dose to the female breast from 16-MDCT body protocols. *American Journal of Roentgenology*, *186*, 1718–1722.
58. Litmanovich, D., Tack, D., Lin, P. J., Boiselle, P. M., Raptopoulos, V., Bankier A. A., (2011). Female breast, lung, and pelvic organ radiation from dose-reduced 64-MDCT thoracic examination protocols: a phantom study. *AJR Am J Roentgenol*. 197(4), 929–934. doi: 10.2214/AJR.10.6401.
59. Deak, P., van Straten, M., Shrimpton, P. C., Zankl, M., & Kalender, W. A. (2008). Validation of a Monte Carlo tool for patient-specific dose simulations in multi-slice computed tomography. *European Radiology*, *18*, 759–772.

60. International Commission on Radiological Protection. (2007a). *The 2007 recommendations of the international commission on radiological protection*. ICRP Publication 103. Elsevier ed.
61. Huda, W., Atherton, J. V., Ware, D. E., & Cumming, W. A. (1997). An approach for the estimation of effective radiation dose at CT in pediatric patients. *Radiology*, 203, 417–422.
62. Deak, P. D., Smal, Y., & Kalender, W. A. (2010). Sex- and age-specific conversion factors used to determine effective dose from Dose-Length product. *Radiology*, 257, 158–166.
63. Cristy, M. (1980). Mathematical phantoms representing children of various ages for use in estimates of internal dose. Report no. ORNL/NUREG/TM-367. Oak Ridge, Tenn: Oak Ridge National Laboratory.
64. Melo Lima, V. J., Cassola, V. F., Kramer, R., de Oliveira Lira, C. A. B., Khoury, H. J., & Vieira, J. W. (2011). Development of 5- and 10-year-old pediatric phantoms based on polygon mesh surfaces. *Medical Physics*, 38, 4723–4736.
65. Kramer, R., Vieira, J. W., Khoury, H. J., Lima, F. R. A., & Fuelle, D. (2003). All about MAX: A male adult voxel phantom for Monte Carlo calculations in radiation protection dosimetry. *Physics in Medicine & Biology*, 48, 1239–1262.
66. Cassola, V. F., de Melo Lima, V. J., Kramer, R., & Khoury, H. J. (2010). FASH and MASH: Female and male adult human phantoms based on polygon mesh surfaces. Part I: Development of the anatomy. *Physics in Medicine & Biology*, 55, 133–162.
67. Kramer, R., Cassola, V. F., Vieira, J. W., Khoury, H. J., de Oliveira Lira, C. A. B., & Brown, K. R. (2012). Skeletal dosimetry based on CT images of trabecular bone: update and comparisons. *Physics in Medicine & Biology*, 57, 3995–4021.
68. Boone, J. M., Geraghty, E. M., Seibert, J. A., & Wootton-Gorges, S. L. (2003). Dose reduction in pediatric CT: A rational approach. *Radiology*, 228, 352–360.
69. Strauss, K. J., Goske, M. J., Frush, D. P., Butler, P. F., & Morrison, G. (2009). Image Gently vendor summit: Working together for better estimates of pediatric radiation dose from CT. *American Journal of Roentgenology*, 192, 1169–1175.
70. Cody, D. D., Moxley, D. M., Krugh, K. T., O’Daniel, J. C., Wagner, L. K., & Eftekhari, F. (2004). Strategies for formulating appropriate MDCT techniques when imaging the chest, abdomen, and pelvis in pediatric patients. *American Journal Roentgenology*, 182, 849–859.
71. Brisse, H. J., Robilliard, M., Savignoni, A., Pierrat, N., Gaboriaud, G., De Rycke, Y., et al. (2009). Assessment of organ absorbed doses and estimation of effective doses from pediatric anthropomorphic phantom measurements for multi-detector row CT with and without automatic exposure control. *Health Physics*, 97, 303–314.
72. Birnbaum, B. A., Hindman, N., Lee, J., & Babb, J. S. (2007). Multi-detector row CT attenuation measurements: Assessment of intra- and interscanner variability with an anthropomorphic body CT phantom. *Radiology*, 242, 109–119.
73. Birnbaum, B. A., Hindman, N., Lee, J., & Babb, J. S. (2007). Influence of multidetector CT reconstruction algorithm and scanner type in phantom model. *Radiology*, 244, 767–775.
74. Wagner, L. K., Lester, R. G., & Saldana, L. R. (1985). *Exposure of the pregnant patient to diagnostic radiations: a guide to medical management*. Philadelphia: Lippincott.
75. Wagner, L. K., Archer, B. R., & Zeck, O. F. (1986). Conceptus dose from state-of-the-art CT scanners. *Radiology*, 159, 787–792.
76. Osei, E. K., & Faulkner, K. (1999). Fetal doses from radiological examinations. *British Journal of Radiology*, 72, 773–780.
77. Osei, E. K., Darko, J. B., Faulkner, K., & Kotre, C. J. (2003). Software for the estimation of fetal radiation dose to patients and staff in diagnostic radiology. *Journal of Radiological Protection*, 23, 183–194.
78. Osei, E. K., & Faulkner, K. (2000). Radiation risks from exposure to diagnostic x-rays during pregnancy. *Radiography*, 6, 131–144.
79. Osei, E. K., & Barnett, R. (2009). Software for the estimation of organ equivalent and effective doses from diagnostic radiology procedures. *Journal of Radiological Protection*, 29, 361–376.

80. Osei, E. K., & Darko, J. (2013). A survey of organ equivalent and effective doses from diagnostic radiology procedures. *ISRN Radiology*, 2013, 1–9.
81. Felmlee, J. P., Gray, J. E., Leetzow, M. L., & Price, J. C. (1990). Estimated fetal radiation dose from multislice CT studies. *American Journal of Roentgenology*, 154, 185–190.
82. Dietrich, M. F., Miller, K. L., & King, S. H. (2005). Determination of potential uterine (conceptus) doses from axial and helical CT scans. *Health Physics*, 88, S10–S13.
83. Hurwitz, L. M., Yoshizumi, T., Reiman, R. E., Goodman, P. C., Paulson, E. K., Frush, D. P., et al. (2006). Radiation dose to the fetus from body MDCT during early gestation. *American Journal of Roentgenology*, 186, 871–876.
84. Jaffe, T. A., Neville, A. M., Anderson-Evans, C., Long, S., Lowry, C., Yoshizumi, T. T., et al. (2009). Early first trimester fetal dose estimation method in a multivendor study of 16- and 64-mdct scanners and low-dose imaging protocols. *American Journal of Roentgenology*, 193, 1019–1024.
85. Jaffe, T. A., Yoshizumi, T. T., Toncheva, G. I., Nguyen, G., Hurwitz, L. M., & Nelson, R. C. (2008). Early first-trimester fetal radiation dose estimation in 16-MDCT without and with automated tube current modulation. *American Journal of Roentgenology*, 190, 860–864.
86. Gilet, A. G., Dunkin, J. M., Fernandez, T. J., Button, T. M., & Budorick, N. E. (2011). Fetal radiation dose during gestation estimated on an anthropomorphic phantom for three generations of CT scanners. *American Journal of Roentgenology*, 196, 1133–1137.
87. Wang, J., Christner, J. A., Duan, X., Leng, S., Yu, L., & McCollough, C. H. (2012). Attenuation-based estimation of patient size for the purpose of size specific dose estimation in CT. Part II. Implementation on abdomen and thorax phantoms using cross sectional CT images and scanned projection radiograph images. *Medical Physics*, 39, 6678–6772.
88. Peng, G., Zeng, Y., Luo, T., Zhao, F., Peng, S., You, R., et al. (2012). Organ dose evaluation for multi-slice spiral ct scans based on China Sichuan chest anthropomorphic phantom measurements. *Radiation Protection Dosimetry*, 150, 292–297.
89. McCollough, C.H. (2011). Translating protocols across patient size: Babies to bariatric. Lecture in the 2011 AAPM Summit on CT Dose. October 7–8 2011, Denver, CO.
90. Duan, X., Wang, J., Christner, J. A., Leng, S., Grant, K. L., & McCollough, C. H. (2011). Dose reduction to anterior surfaces with organ-based tube-current modulation: Evaluation of performance in a phantom study. *American Journal of Roentgenology*, 197, 689–695.
91. Matsubara, K., Koshida, K., Ichikawa, K., Suzuki, M., Takata, T., Yamamoto, T., et al. (2009). Misoperation of CT automatic tube current modulation systems with inappropriate patient centering: Phantom studies. *American Journal of Roentgenology*, 192, 862–865.
92. Kalender, W. A., Wolf, H., & Suess, C. (1999). Dose reduction in CT by anatomically adapted tube current modulation. II. Phantom measurements. *Medical Physics*, 26, 2248–2253.
93. Keat, N. (2005). *CT scanner automatic exposure control system*. ImPACT report 05016. MHRA reports, London.
94. Flohr, T. G., Bruder, H., Stierstorfer, K., Petersilka, M., Schmidt, B., & McCollough, C. H. (2008). Image reconstruction and image quality evaluation for a dual source CT scanner. *Medical Physics*, 35, 5882–5897.
95. McCollough, C. H., Primak, A. N., Saba, O., Bruder, H., Stierstorfer, K., Raupach, R., et al. (2007). Dose performance of a 64-channel dual-source CT scanner. *Radiology*, 243, 775–784.
96. Capeleti, F.F., Melo, C.S., Furquim, T.A.C., Nersissian, D.Y. (2011). Phantom development for quality control in automatic exposure control in computed tomography systems. *Poster Presented on 18th International Conference of Medical Physics*, April 17–20 2011, Porto Alegre, Brazil.
97. Morehouse, C. C., Brody, W. R., Guthaner, D. F., Breiman, R. S., & Harell, G. S. (1980). Gated cardiac computed tomography with a motion phantom. *Radiology*, 134, 213–217.
98. Boll, D. T., Merkle, E. M., Paulson, E. K., & Fleiter, T. R. (2008). Dual-Energy multidetector CT assessment in a pilot study with anthropomorphic phantom. *Radiology*, 247, 687–695.

99. Driscoll, B., Coolens, C., & Keller, H. (2011). Quantitative DCE-CT imaging quality assurance with a novel dynamic flow phantom. *Medical Physics*, *38*, 3874.
100. Horiguchi, J., Kiguchi, M., Fujioka, C., Shen, Y., Arie, R., Sunasaka, K., et al. (2008). Radiation dose, image quality, stenosis measurement, and CT densitometry using ECG-Triggered coronary 64-MDCT angiography: A phantom study. *American Journal of Roentgenology*, *190*, 315–320.
101. Nosratiéh, A., Yang, K., Aminololama-Shakeri, S., & Boone, J. M. (2012). Comprehensive assessment of the slice sensitivity profiles in breast tomosynthesis and breast CT. *Medical Physics*, *39*, 7254–7261.
102. Szegedi, M., Szegedi, P. R., Sarkar, V., Hinkle, J., Wang, B., Huang, Y., et al. (2012). Tissue characterization using a phantom to validate four-dimensional tissue deformation. *Medical Physics*, *39*, 6065–6070.
103. McNitt-Gray, M. (2013). CT dose measurements. Lecture presented at Hands-on Workshop for Physicists. MD Anderson Cancer Center, February 8–10, 2013.

Chapter 8

Mammography Phantoms

Alessandra Tomal

8.1 Introduction

Mammography is considered the preferred technique for early detection of the breast cancer. Due the similarity on the elemental composition of the normal and abnormal tissues that comprise the breast, and also due the small size of the breast nodules in the early stage, the optimization of IQ and dose in mammography is a critical factor [69].

Breast phantoms play an important role in the optimization process in mammography through the assessment of IQ and accurate determination of dose, quality control (QC), and quality assurance (QA) in mammography; optimization of specific imaging tasks, such as detection of masses and microcalcifications, dosimetry in mammography, and characterization of the performance of an imaging system [1, 22, 41, 56, 69]. Breast phantoms have also been used for comparison of the performance of different equipment and technologies. In addition, optimization of exposure techniques and study of new imaging technologies, such as dual-energy mammography, contrast-enhanced dual-energy mammography, digital breast tomosynthesis, and breast CT [5, 7, 49, 57, 58] involve a large application of mammographic phantoms.

The main requirement for a breast phantom is the composition with tissue-equivalent material, which reproduces the attenuation properties of the human breast tissues. The material needs to be stable over time and can be moldable [56, 68]. The most used tissue-equivalent materials are plastic (i.e., PMMA—polymethyl methacrylate) or epoxy resins [68], which represents breasts composed of different percentages of adipose and glandular tissues, based on breast composition presented in the literature [33, 40, 70]. Although the breast tissue-equivalent material can be manufactured using components which have similar composition and densities to

A. Tomal (✉)

Institute of Physics, Federal University of Goiás, Campus Samambaia, Caixa Postal 131Goiânia, Goiás 74001-970, Brazil

e-mail: alessandra_tomal@yahoo.com.br; atomal@if.ufg.br

the real breast tissues, studies point to the need for a careful analysis to choose the most adequate material to simulate the scattering properties of different breast compositions [42, 56].

The breast phantoms are also designed to be realistically shaped and molded to represent the real breast dimensions in simple uniform blocks or highly detailed design, containing embedded inserts that mimic clinically relevant features of the normal and pathological structures and background within the breast.

Since 1980s, the screen–film mammography was considered the gold technique for early detection of breast cancer. In this technique, the use of breast phantoms was essential for establishment of QC and QA programs for monitoring both IQ and radiation dose in the mammographic examination [1, 25, 38, 39]. Recently, digital mammography is gradually replacing the conventional film–screen mammography in most countries [26, 39, 49]. Consequently, it is in progress an important activity related to the development of QC protocols [39] and optimization of this digital technology [7, 18, 58, 67]. Moreover, novel breast imaging techniques, such as dual-energy mammography, contrast-enhanced dual-energy mammography, digital breast tomosynthesis, and breast CT, have justified the necessity for developing new breast phantoms containing specific features to be used for IQ and dose assessment of these contemporary technologies [12, 13, 57].

8.2 Phantoms for Imaging

8.2.1 Phantom for Quality Control and Accreditation Programs

High IQ is fundamental in mammographic screening programs, in order to improve the sensitivity of the exam for the early detection of breast pathologies. In this context, breast phantoms play a fundamental role to establish, assess, and optimize IQ in mammography. Breast phantoms are also used for accreditation of new mammography facilities for both screen–film and full-field digital mammography (FFDM) systems.

Breast test phantoms to evaluate IQ could contain embedded inserts that mimic the anatomical breast structures and/or artificial features such as low-contrast details, microcalcifications, fibers, high-contrast frequency patterns, and step wedges, which are used to evaluate high- and low-contrast object detection, spatial resolution, noise response, and detectability threshold [12, 22, 41, 44, 69].

In general, test phantom assessment criteria in accreditation programs for screening mammography are subjective [35], being based on IQ scores defined from detail visibility of different targets, such as microcalcifications and low-contrast masses and fibers [1, 14, 25]. The basic condition of the utilization of an IQ phantom is that a given dimension of group structures should be visualized in a

mammographic image, even if the phantom is imaged on different machines applying different procedures.

The main test phantoms available for the purpose of IQ assessment in mammography are described below. One of the first phantoms developed to contain insert structures mimicking those found in a clinical mammography was the Bart test phantom, which was described in 1980 by White and Tucker [69]. The Bart test phantom was originally designed to be used for assessing IQ in mammography and for comparison purposes of UK breast imaging practice by the Hospital Physicists' Association [29]. The phantom was formulated to be composed of epoxy resin BR12 [68], simulating the composition of an average breast tissue, representing a homogeneous mixture of 50 % adipose tissue and 50 % water. Inside the BR12 phantom, test inserts were included to evaluate different structures and materials on the IQ, being basically the following: adipose and water-like structures, calcifications, and skin step edge. The structures of interest present inside the phantom had different geometric shapes and dimension, and they were composed of epoxy resin-based substitutes, aluminum oxide, and silicon. The Bart phantom was designed to evaluate the performance of IQ in mammography combined in different ways, allowing assess to the contrast and resolution of mammographic devices. However, the use of this phantom for practical evaluation of several mammographic devices shows some difficulties, since it was never available commercially and it is also little sensitive to changes in tube potential and focal spot size [45].

Due to the importance of evaluating IQ in mammography using test objects, many efforts were done to develop a breast phantom that has greater sensitivity to changes in tube potential and better discrimination between different equipment and image receptor. In this context, several phantoms were produced and are described below.

In 1987, the test phantom Leeds TOR[MAX] was developed to implement routine QC procedures within the U.K. National Breast Cancer Screening Programme [16, 17]. TOR[MAX] comprises D-shaped PMMA plates, representing the average 50 % adipose–50 % glandular (50:50) breast. An additional TOR [MAX] test object includes different types of structures in a homogeneous background: high- and low-contrast bar patterns, low-contrast discs, and a step wedge [21, 28]. The test pattern and details included on the Leeds TOR[MAX] phantom provide quantitative information for IQ purposes, allowing the measurement of grayscale rendition, high-contrast spatial resolution, and both large- and small-area detail detectability [16]. In 1992, it was developed a supplementary test phantom TOR[MAM], which contains details that provides a radiological image with an appearance more closely to that achieved during a clinical mammographic examination [16]. TOR[MAM] phantom also comprises a D-shaped PMMA test object divided in two halves, which include different types of test details. One half of this phantom is designed for quantitative evaluation and contains groups of fibers, calcifications, and low-contrast discs composed of equivalent breast-tissue materials. The other half contains structures that mimic breast tissue with groups of microcalcifications, simulating a clinical mammographic image [74]. Such phantoms have been used in several studies

concerning the IQ performance of imaging system for screen–film, computed radiography, FFDM, and image processing of digital imaging [16, 21]. With the advent of novel 3D breast imaging techniques, as digital breast tomosynthesis, the use of such test phantom is also showed to be useful for evaluation of digital breast image reconstruction algorithms [9].

Kimme-Smith et al. [41] compared several mammography test objects (commercially available and prototype) with respect to their resolution and contrast targets and the dose. In this study, the authors observed a great variation on the quantities evaluated with the phantom and details compositions and also described the need for a reliable phantom for evaluating the IQ and dose in mammography.

Law [44] described the construction of the Du Pont mammographic test phantom, constituted by a PMMA block with 12×12 cm area and total thickness of 4 cm, simulating an average 50:50 breast. The phantom was developed to contain high-contrast bar patterns and different structures that mimic clinical mammographic features, such as microcalcifications, fibrous structures, and small spherical objects, which allow the assessment of minimum detail contrast and resolution score. The developed phantom has been found to have better sensitivity and discrimination, making it suitable for studying the IQ performance in mammography.

In the last decades, several national and international protocols for mammography QC program have pointed to the importance of using a mammographic accreditation phantom to perform the image QC of mammographic systems in the QC and QA programs [1, 25, 38, 39]. The American College of Radiology (ACR) introduced a standard accreditation phantom (ACR phantom) [6, 22, 34, 48] to access the image for QC purposes in the mammography accreditation program (MQA). The ACR phantom simulates a 50:50 breast of 4.5 cm thickness, and it consists of a PMMA block and a wax block containing the test structures of known size, shape, and density (Fig. 8.1). The structures included in the wax insert consist of nylon fibrils, groups of microcalcifications, and lens-shaped masses, representing different structures or malignancies similar to those found clinically when imaging a real breast. The visibility of these structures in the radiographic image ranges from visible to invisible, defining a visibility threshold and giving a global IQ score [24, 37, 48]. Performance of this imaging quality test is an important factor in the accreditation of a facility [14].

The ACR phantom has been used for assessing IQ in both film–screen mammography and FFDM; however, phantoms designed for screen/film mammography could show low sensitivity in FFDM [36, 37, 47, 62]. Huda et al. [37] showed that the ACR phantom is unsatisfactory for assessing IQ in FFDM and it requires modifications to have the appropriate range and sensitivity for current digital mammography imaging systems available [32]. Besides, there are several commercially available digital mammography accreditation phantoms (Gammex, Radiation Measurements Inc.; CIRS—Computerized Imaging Reference Systems Inc). The composition of the phantom and the included structures are the same as in the ACR phantom; however, the phantom thickness and the number of inserted objects are different, and they have smaller sizes. In addition, Song et al. [62]

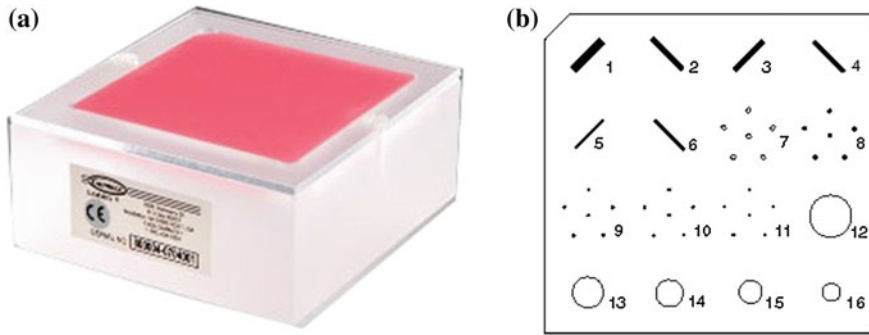


Fig. 8.1 **a** ACR phantom and **b** structures layout (Model 156, Gammex—RMI Radiation Measurements Inc., Middleton, WI) http://www.gammex.com/ace-files/Gammex_Catalog.pdf

compared the ACR phantom and digital mammography accreditation phantom in terms of the signal-to-noise ratio (SNR) and the visibility of the inserted objects for assessment of IQ on FFDM. The authors concluded that ACR accreditation phantom is superior, being satisfactory for assessing the IQ in FFDM, if appropriate voltage and current–time product settings are kept during phantom image acquisition.

Recently, many countries have developed their own mammography QC program, regulating the minimum IQ performance and doses related to a mammographic examination. In Brazil, for example, the Brazilian College of Radiology (CBR) and the National Agency for Health Surveillance (ANVISA) recommend standards of practice for mammography, in which the IQ assessment should be performed using a specific test object (CDM-phantom MAMA) developed for this purpose. The commercially available CDM-phantom MAMA was developed in Brazil, and it presents similarities to the ACR phantom, being composed of PMMA plates and a wax insert region, containing different detail objects: high-contrast bar pattern, microcalcifications, fibers, tumor-like masses, and low-contrast details. This phantom is widely used for mammographic QC in different facilities in Brazil and also for studies on IQ and dosimetry [53].

In addition to the standard plastic breast phantom, as the PPMA, other breast phantoms with different composition were proposed to evaluate the performance of mammographic systems in terms of IQ, based on the composition of breast tissues and breast geometry described by Hammerstein et al. [33]. The commercially available CIRS phantom models 010 and 011A (CIRS, Inc., Norfolk, VA) for IQ assessment are made of D-shaped epoxy resin-equivalent material, simulating breast of different thickness, and glandular content within an external shield layer of simulating adipose tissue. This phantom allows a detailed evaluation of a mammographic system for several normal and pathological breast structures, consisting of microcalcifications, high-contrast resolution pattern, low-contrast masses, line-pair test pattern, and a step wedge.

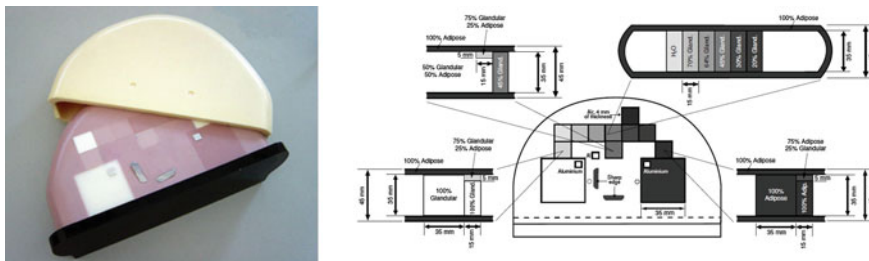


Fig. 8.2 Test phantom developed by Pachoud et al. [54]

In 2004, a new test phantom was also developed for IQ evaluation in digital and conventional mammography by Pachoud et al. [54]. The authors developed a prototype test phantom, composed of CIRS equivalent materials. A 35-mm layer of 50:50 glandular/adipose tissue equivalent is surrounded by a 5-mm-thick covering of 100 % adipose equivalent material, representing the breast model proposed by Hammerstein et al. [33]. The phantom comprises regions with different tissue compositions (100 % adipose, 50:50 mixture, and 100 % glandular) and includes structures which are used to evaluate several IQ features, such as low- and high-contrast resolution, spatial resolution, and image noise (Fig. 8.2). A step wedge with different glandular/adipose compositions is included within the central layer for signal output calibration. The test phantom also contains two areas composed of 100 % glandular- and 100 % adipose-equivalent breast tissue, which can be used for assessment of noise power spectra. Two holes are included on the phantom's top surface, at 60 mm from the chest wall, which can hold thermoluminescent dosimeters (TLD) for entrance skin dose measurements. The new test phantom proposed by Pachoud et al. [54] proved to be useful for assessments of several IQ parameters (contrast, dynamic range, spatial resolution, and noise) for conventional and digital mammography equipments, allowing to compare different image systems. Otherwise, this phantom should be used as complement to another phantom in assessment of IQ in mammography, since it does not contain structures for detections tasks.

8.2.2 Contrast–Detail Phantom

The success of a mammographic screening program is related with the production of high-quality images, which provides the maximum diagnostic information in order to distinguish tissue alterations within the breast with very low contrast and small size. Contrast–detail (CD) detection measurement is the technique most used for assessing the performance of an imaging system based on identification of small alterations [15, 66]. In the CD experiment, the observers record the small size of object that they perceive, at a given confidence level, on the image of

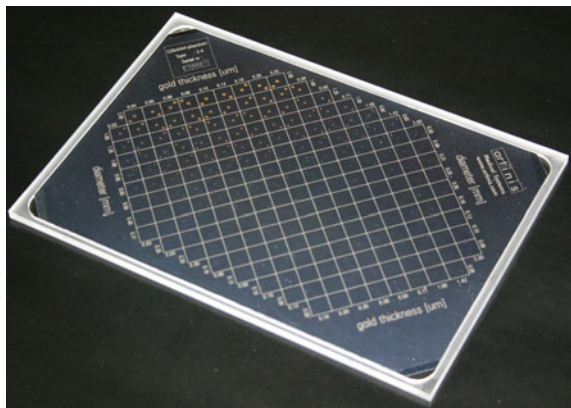
simple objects that vary both in diameter and contrast. Thompson and Faulkner [66] described a CD test phantom for screen–film mammography, containing series of discs of varying attenuation and diameter, which were chosen to simulate significant structures in a mammographic image, such as low-contrast tissue masses and higher-contrast small object such as microcalcifications.

The importance of CD measurements for assess the IQ performance of mammographic devices has been recognized, and this test has been included in several protocols. The European guidelines [26] for the QC in digital mammography define threshold contrast standards for digital mammography, based on CD measurements, in order to ensure that digital mammography systems have a performance at least as well as film–screen systems. This test is usually performed by using the commercially available Nijmegen CDMAM (Artinis Medical Systems) CD phantom, which consists of an aluminum base with gold discs of various thickness and diameter, attached to PMMA cover block (Fig. 8.3) [8].

The use of CD test phantom in screen–film and digital mammography has demonstrated a large potential in several applications. Robson et al. [59] used a CD phantom to establish optimal optical density values for two mammographic film–screen combinations, based on the signal-to-noise ratio (SNR). Berns et al. [7] have employed a CD test phantom to determine the optimal exposure technique in FFDM compared to screen–film mammography, including the comparison of the performance of different analog and digital mammography systems. With the advent of digital mammography systems, the CD test phantom plays a fundamental role for evaluating the effect of pixel size on the detection of simulated microcalcifications in digital mammography, as described by Suryanarayanan et al. [63], who used the CDMAM phantom.

Novel mammographic IQ test phantom design has been proposed as a cheaper alternative for image QA and evaluation of the CD score for the breast screening programs [43, 65]. The phantom developed by Kotre and Porter [43] was based on LaserJet printed test features on a Mylar projector transparency, on which the test features are composed of 50 % by weight of iron oxide present in the toner. The low-contrast test features are sandwiched between two PMMA blocks. Despite the

Fig. 8.3 Nijmegen CDMAM contrast–detail phantom (http://www.artinis.com/product/cdmam_34)



simplified manufacture process, this novel test phantom design is cheaper, more flexible, and offers a performance similar to other commercial mammographic CD phantoms in terms of image of low-contrast structures, being a good alternative way for producing test phantoms [43]. However, this phantom has disadvantages, since high-contrast resolution structures cannot be produced through the standard printing process.

8.3 Phantoms for Dosimetry

The knowledge of the absorbed dose to the breast during a mammographic examination is an important topic for QA programs, since it is related to carcinogenesis risk and allows comparisons between different imaging techniques and equipments. In this way, the assessment of the breast dose in a mammographic examination is essential in breast screening programs in which predominantly asymptomatic women are examined.

The mean glandular dose (MGD) is considered the most appropriate quantity for risk assessments associated with mammography, since the glandular tissue is the most vulnerable tissue in the breast [19, 71]. Therefore, the MGD has been recommended by several national and international protocols as the dosimetric parameter to be evaluated in mammography [1, 25, 38, 49].

A direct measurement of MGD is impossible for any individual breast, and in most practical situation, it is derived from the product of the measured entrance air kerma and appropriated conversion factors [49]. The conversion factors were initially measured using an appropriated test phantom [33] and also calculated using Monte Carlo simulation [10, 19, 71].

Breast phantoms are usually employed to estimate the MGD based on measurements of the entrance surface air kerma and half-value layer (HVL) [20, 23]. The entrance air kerma and HVL can be directly measured by placing the ionization chamber at the tube side of the phantom and level with its top surface, positioned to a distance between 4 and 6 cm from the chest wall, defined according the used protocol [1, 25, 50, 51]. The incident air kerma can also be measured using TLD dosimeters placed on the entrance surface of the phantom or breast [1, 25].

The standard breast phantom for dosimetry in mammography usually represents a typical breast composed of a 50:50 mixture of adipose and glandular tissues [20, 33]. Several national and international protocols recommended that the standardized phantom chosen for dose evaluation in mammography is constructed from PMMA, and its thickness ranges from 4 to 5 cm [20, 60, 61].

Although a PMMA standard phantom is widely used for dose measurements, it is a limited approach since it provides a quantitative dose evaluation for only a particular breast tissue composition and thickness. In practice, there is a significant variation in the average breast thickness and composition for a group of women in a given geographical region [20, 72], so that the MGD measured using phantoms is not representative of true breast doses [3]. In this way, the use of phantoms of

different thickness and composition is useful for estimating the MGD for realistic woman population.

Several phantoms have been developed to mimic the radiological properties of different breast tissue, allowing a detailed dose assessment in mammography [31, 68]. The most common phantom is BR12, commercially available originally from Nuclear Associates (Cleveland, OH), today Fluke Biomedical Corporation. This phantom is composed of resin epoxy tissue-equivalent, simulating a tissue composition of 50 % glandular tissue and 50 % adipose tissue and developed by White [68]. CIRS (Norfolk, VA) manufacturer also offers phantom materials of different thicknesses and compositions, simulating 100 % glandular breast to 100 % adipose breasts. These phantoms have been recommended by national and international protocols and have been employed in several countries for studying the MGD with QC purposes [1, 60].

In the last years, new phantoms were developed to provide a more accurate evaluation of MGD. Argo et al. [3] described the construction of breast tissue-equivalent series (BRTES) of phantoms composed of epoxy resin, simulating glandularities from 0 to 100 %. The authors observed that, in comparison with the BRTES phantom, the standard 4-cm-thickness ACR phantom and BR12 are likely to underestimate the MGD for most patients, being the variation dependent on local patient demographics. Almeida et al. [2] produced breast phantoms BTE, based on BRTES tissue-equivalent material, to simulate glandular and adipose tissues, in order to evaluate MGD in mammography. In their work, the authors concluded that BTE phantoms should be used instead of PMMA-based phantoms for appropriate estimate of MGD in mammography, since most of the women present breast grandularity lower than 50 % [31, Young et al. 75, 72].

8.4 Anthropomorphic Phantoms for Mammographic Imaging

Anthropomorphic phantoms were introduced in mammography to provide a more realistic task to the observer, since they mimic the composition and geometric structures of the breast, providing X-ray images similar to those present in a real breast [57]. The first anthropomorphic breast phantom introduced for IQ and dose assessment in mammography was constructed by embedding fixed tissues in plastic [27]. However, these types of phantoms change their characteristics with time, and they cannot be easily reproduced in identical copies. A new concept of anthropomorphic breast phantom was introduced by Caldwell and Yaffe [11] and Yaffe et al. [73], who have developed the “Rachel” phantom. This phantom consists of a breast tissue-equivalent base, simulating the tissue structures, combined with a mercury-enhanced mammogram, which simulates the fine details. The Rachel phantom is commercially available (Gammex RMI, Model 169, Gammex Inc., Middleton, WI), being widely used for mammography quality IQ

and dose studies [46], since it provides realistic breast images simulating the breast architecture and anatomical noise. However, the application of the Rachel phantom is limited to evaluation of 2D projection imaging systems, since this phantom does not mimic the real 3D breast anatomy [11, 12].

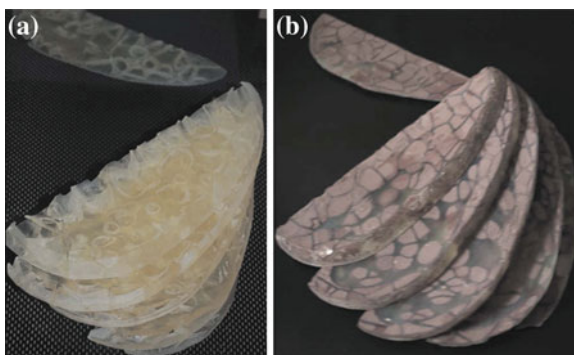
On other hand, several anthropomorphic phantoms are constructed by combining tissue-equivalent material spheres of different dimensions and compositions, embedded in a homogeneous background and contained inside a plastic box [4, 55, 64]. Although the image pattern achieved with these phantoms is not similar to a real breast image, the sphere phantom is very simple to construct and can easily produce different background realizations [30]. Sphere phantoms have been widely used for evaluating the IQ and doses in mammography, and also for optimizing the examination procedures of new mammographic techniques, such as dual-energy mammography, contrast-enhanced dual-energy mammography, and digital breast tomosynthesis [4, 55, 64].

The patient dose reduction in FFDM compared with conventional screen–film system has also been studied by analyzing the effect on the detectability of microcalcifications in an anthropomorphic breast phantom, as described by Obenauer et al. [52].

In the last years, CIRS slab phantom (model 020) became commercially available. This phantom is constructed with D-shaped slabs composed of a heterogeneous mixture of two breast-equivalent materials, allowing to create a large number of different backgrounds.

More recently, 3D anthropomorphic phantoms for IQ assessment of 2D and 3D breast X-ray imaging systems have been developed by Carton and coworkers [12,13], based on a computer model that generates breast voxel phantoms (Fig. 8.4). These phantoms are composed of tissue-equivalent materials of varying size, shape, glandularity, and internal composition [12, 13], and they show potential to be used for both qualitative and quantitative performance assessments for 2D and 3D breast X-ray imaging systems. Finally, Freed et al. [30] described an anthropomorphic phantom to be used for both X-ray and MRI breast imaging

Fig. 8.4 Anthropomorphical phantom developed by Carton et al. [12] **a** Phantom sections of the fibroglandular tissue, skin, and Cooper’s ligaments composed by tissue equivalent materia with 50% glandular equivalence **b** Phantom sections after filling the structures with epoxy resin with 100% adipose equivalence



modalities, composed of a mixture of lard and egg white. This phantom proved to be a useful tool for quantitative assessment of IQ in 2D and 3D mammographic techniques, for the purpose of detection and characterization.

8.5 Standard Phantom Use in the Future

The standard breast phantoms used nowadays in QC and QA programs for optimization and accreditation of mammographic equipments represent an average 50 % adipose–50 % glandular breast. However, Geise and Palchevsky [31] and Young et al. [75] have showed that effective glandular content that simulated in the average woman is 35 %. Besides, recently, Yaffe et al. [72] showed that approximately 95 % of the women presented breast glandular content <45 %, while the standard average breast composition is 20 % glandular. In this way, more realistic phantoms should be developed for accurate assessment of IQ and dose in mammography, considering the new standard breast composition.

The introduction of novel 3D X-ray breast imaging techniques, such as digital breast tomosynthesis and breast computed tomography (breast CT), also have significantly increased the need for 3D anthropomorphic breast phantom to properly simulate the breast anatomy [57]. A proper 3D anthropomorphic breast phantom would allow for the evaluation of IQ parameters, thereby optimizing new imaging techniques and reconstruction algorithms for 3D imaging techniques, and also allowing for comparisons to the performance of 2D and 3D imaging techniques [12].

References

1. ACR. (1999). *Mammography quality control manual*. Reston: American College of Radiology.
2. Almeida, C. D., Coutinho, C. M. C., Dantas, B. M., Peixoto, J. E., & Koch, H. A. (2012). A new mammography dosimetric phantom. *Radiation Protection Dosimetry*, *151*, 196–198.
3. Argo, W. P., Hintenlang, K., & Hintenlang, A. D. E. (2004). A tissue-equivalent phantom series for mammography dosimetry. *Journal of Applied Clinical Medical Physics*, *5*, 112–119.
4. Baldelli, P., Bravin, A., Di Maggio, C., Gennaro, G., Sarnelli, A., Taibi, A., et al. (2006). Evaluation of the minimum iodine concentration for contrast-enhanced subtraction mammography. *Physics in Medicine and Biology*, *51*, 4233–4251.
5. Baldelli, P., Phelan, N., & Egan, G. (2010). Investigation of the effect of anode/filter materials on the dose and image quality of a digital mammography system based on an amorphous selenium flat panel detector. *British Journal of Radiology*, *83*, 290–295.
6. Barnes, G. T., & Hendrick, R. E. (1994). Mammography accreditation and equipment performance. *Radiographics*, *14*, 129–138.
7. Berns, E. A., Hendrick, R. E., & Cutter, G. R. (2003). Optimization of technique factors for a silicon diode array full-field digital mammography system and comparison to screen-film mammography with matched average glandular dose. *Medical Physics*, *30*, 334–340.

8. Bijkerk, K. R., Lindeijer, J. M., & Thijssen, M. A. O. P. (1993). The CDMAM phantom: A contrast-detail phantom specifically for mammography. *Radiology*, *185*, 395–399.
9. Bliznakova, K., Kolitsi, Z., Speller, R. D., Horrocks, J. A., Tromba, G., & Pallikarakis, N. (2010). Evaluation of digital breast tomosynthesis reconstruction algorithms using synchrotron radiation in standard geometry. *Medical Physics*, *37*, 1893–1903.
10. Boone, J. M. (1999). Glandular breast dose for monoenergetic and high-energy x-ray beams: Monte Carlo assessment. *Radiology*, *213*, 23–37.
11. Caldwell, C. B., & Yaffe, M. J. (1990). Development of an anthropomorphic breast phantom. *Medical Physics*, *17*, 273–280.
12. Carton, A. K., Bakic, P., Ullberg, C., Derand, H., & Maidment, A. D. A. (2011). Development of a physical 3D anthropomorphic breast phantom. *Medical Physics*, *38*, 891–896.
13. Carton, A. K., Gavenonis, S. C., Currivan, J. A., Conant, E. F., Schnall, M. D., & Maidment, A. D. A. (2010). Dual-energy contrast-enhanced digital breast tomosynthesis—a feasibility study. *British Journal of Radiology*, *83*, 344–350.
14. Chakraborty, D. P., & Eckert, M. P. (1995). Quantitative versus subjective evaluation of mammography accreditation phantom images. *Medical Physics*, *22*, 133–143.
15. Cohen, G., McDaniel, D. L., & Wagner, L. K. (1984). Analysis of variations in contrast-detail experiments. *Medical Physics*, *11*, 469–473.
16. Cowen, A. R., Brettell, D. S., Coleman, N. J., & Parkin, G. J. S. (1992). A preliminary investigation of the imaging performance of photostimulable phosphor computed radiography using a new design of mammographic quality-control test object. *British Journal of Radiology*, *65*, 528–535.
17. Cowen, A. R., & Coleman, N. J. (1991). Physics in diagnostic radiology. Design of test objects and phantoms for quality control in mammographic screening. York, UK, IPEM. IPEM Report 61.
18. Cunha, D. M., Tomal, A., & Poletti, M. E. (2012). Optimization of x-ray spectra in digital mammography through Monte Carlo simulations. *Physics in Medicine and Biology*, *57*, 1919–1935.
19. Dance, D. R. (1990). Monte Carlo calculation of conversion factors for the estimation of mean glandular breast dose. *Physics in Medicine and Biology*, *35*, 1211–1219.
20. Dance, D. R., Skinner, C. L., & Carlsson, G. A. (1999). Breast dosimetry. *Applied Radiation and Isotopes*, *50*, 185–203.
21. Darabara, D. G., Taibi, A., & Speller, R. D. (2002). Image-quality performance of an a-Si: H-based X-ray imaging system for digital mammography. *Nuclear Instruments and Methods in Physical Research Section A*, *477*, 521–526.
22. DeWerd, L. A., Wochos, J., & Cameron, J. (1979). ACR phantom based upon a random phantom “Wisconsin mammography phantoms”. In W. Logan & E. P. Muntz (Eds.), *Reduced dose mammography*. New York: Masson.
23. DeWerd, L. A., Micka, J. A., Laird, R. W., Pearson, D. W., O’Brien, M., & Lamperti, P. (2002). The effect of spectra on calibration and measurement with mammographic ionization chambers. *Medical Physics*, *29*, 2649–2654.
24. Dougherty, G. (1998). Computerized evaluation of mammographic image quality using phantom images. *Computerized Medical Imaging and Graphics*, *22*, 365–373.
25. EC (1996). *European guidelines on quality criteria for diagnostic radiographic images*. EUR 16260. Luxembourg: European Commission.
26. EC (2006). *European Guidelines for Quality Assurance in Mammography Screening*. Report EUR 14821. Luxembourg: European Commission.
27. Egan, R. L., & Fenn, J. O. (1968). Phantoms for evaluating mammography techniques and roentgenographic detail. *American Journal of Roentgenology*, *102*, 936–939.
28. Faulkner, K., & Law, J. (1994). A comparison of mammographic phantoms. *Brit J Radiol*, *67*, 174–180.
29. Fitzgerald, M., White, D. R., White, E., & Young, J. (1981). Mammographic practice and dosimetry in Britain. *British Journal of Radiology*, *54*, 212–220.

30. Freed, M., Badal, A., Jennings, R. J., de las Heras, H., Myers, K. J., & Badano, A. (2011). X-ray properties of an anthropomorphic breast phantom for MRI and x-ray imaging. *Phys Med Biol*, *56*, 3513–3533.
31. Geise, R. A., & Palchevsky, A. (1996). Composition of mammographic phantom materials. *Radiology*, *198*, 347–350.
32. Gennaro, G., Ferro, F., Contento, G., Fornasin, F., & di Maggio, C. (2007). Automated analysis of phantom images for the evaluation of long-term reproducibility in digital mammography. *Physics in Medicine and Biology*, *52*, 1387–1407.
33. Hammerstein, G. R., Miller, D. W., White, D. R., Masterson, M. E., Woodard, H. Q., & Laughlin, J. S. (1979). Absorbed radiation-dose in mammography. *Radiology*, *130*, 485–491.
34. Hendrick, R. E. (1992). Quality assurance in mammography—accreditation, legislation, and compliance with quality assurance standards. *Radiologic Clinics of North America*, *30*, 243–255.
35. Hessler, C., Depeursinge, C., Grecescu, M., Pochon, Y., Raimondi, S., & Valley, J. F. (1985). Objective assessment of mammography systems: 1. Method. *Radiology*, *156*, 215–219.
36. Huda, W., Qu, G. Y., Jing, Z. X., Steinbach, B. G., & Honeyman, J. C. (2000). How does observer training affect imaging performance in digital mammography? In E. A. Krupinski (Ed.), *Medical imaging 2000: Image perception and performance* (Vol. 1, pp. 259–266).
37. Huda, W., Sajewicz, A. M., Ogden, K. M., Scalzetti, E. M., & Dance, D. R. (2002). How good is the ACR accreditation phantom for assessing image quality in digital mammography? *Academic Radiology*, *9*, 764–772.
38. IAEA (2007). Dosimetry in diagnostic radiology: An international code of practice, technical reports series No. 457. *International Atomic Energy Agency*. Vienna, Austria, International Atomic Energy Agency.
39. IAEA (2011). *Quality assurance programme for digital mammography*. IAEA human health series No 17. Vienna: International Atomic Energy Agency.
40. ICRU. (1989). *Tissue substitutes in radiation dosimetry and measurement*. Bethesda: International Commission on Radiation Units and Measurements.
41. Kimme-Smith, C., Bassett, L. W., & Gold, R. H. (1989). A review of mammography test objects for the calibration of resolution, contrast, and exposure. *Medical Physics*, *16*, 758–765.
42. Kosanetzky, J., Knoerr, B., Harding, G., & Neitzel, U. (1987). X-ray diffraction measurements of some plastic materials and body tissues. *Medical Physics*, *14*, 526–532.
43. Kotre, C. J., & Porter, D. J. T. (2005). A printed image quality test phantom for mammography. *British Journal of Radiology*, *78*, 746–748.
44. Law, J. (1991). A new phantom for mammography. *British Journal of Radiology*, *64*, 116–120.
45. Law, J., Faulkner, K., & Smith, S. (1989). Variation of image quality with x-ray tube potential in mammography. *British Journal of Radiology*, *62*, 192–192.
46. Liu, X., Lai, C.-J., Whitman, G. J., Geiser, W. R., Shen, Y., Yi, Y., et al. (2011). Effects of exposure equalization on image signal-to-noise ratios in digital mammography: A simulation study with an anthropomorphic breast phantom. *Medical Physics*, *38*, 6489–6501.
47. McLean, D., Eckert, M., Heard, R., & Chan, W. (1997). Review of the first 50 cases completed by the RACR mammography QA programme: Phantom image quality, processor control and dose considerations. *Australasian Radiology*, *41*, 387–391.
48. McLelland, R., Hendrick, R. E., Zininger, M. D., & Wilcox, P. A. (1991). The American-college of radiology mammography accreditation program. *American Journal of Roentgenology*, *157*, 473–479.
49. NCRP (2004). *A Guide to Mammography and Other Breast Imaging Procedures*, NCRP Report 149. Bethesda: National Council on Radiation Protection and Measurements.
50. Ng, K. H., DeWerd, L. A., & Schmidt, R. C. (2000). Mammographic image quality and exposure in South East Asia. *Australasian Physical and Engineering Sciences*, *23*, 135–137.

51. Ng, K. H., Aus, R. J., DeWerd, L. A., & Vetter, J. R. (1997). Entrance skin exposure and mean glandular dose: Effect of scatter and field gradient at mammography. *Radiology*, *205*, 395–398.
52. Obenaus, S., Hermann, K. P., & Grabbe, E. (2003). Dose reduction in full-field digital mammography: An anthropomorphic breast phantom study. *British Journal of Radiology*, *76*, 478–482.
53. Oliveira, M., Nogueira, M. S., Guedes, E., Andrade, M. C., Peixoto, J. E., Joana, G. S., et al. (2007). Average glandular dose and phantom image quality in mammography. *Nuclear Instruments and Methods in Physical Research Section A*, *580*, 574–577.
54. Pachoud, M., Lepori, D., Valley, J. F., & Verdun, F. R. (2004). A new test phantom with different breast tissue compositions for image quality assessment in conventional and digital mammography. *Physics in Medicine and Biology*, *49*, 5267–5281.
55. Park, S., Liu, H., Jennings, R., Leimbach, R., Kyprianou, I., Badanoa, A., et al. (2009). A task-based evaluation method for x-ray breast imaging systems using variable-background phantoms. *Proceedings of SPIE*, *7258*, L1–L9.
56. Poletti, M. E., Gonçalves, O. D., & Mazzaro, I. (2002). X-ray scattering from human breast tissues and breast-equivalent materials. *Physics in Medicine and Biology*, *47*, 47–63.
57. Prionas, N. D., Burkett, G. W., McKenney, S. E., Chen, L., Stern, R. L., & Boone, J. M. (2012). Development of a patient-specific two-compartment anthropomorphic breast phantom. *Physics in Medicine and Biology*, *57*, 4293–4307.
58. Ranger, N. T., Lo, J. Y., & Samei, E. (2010). A technique optimization protocol and the potential for dose reduction in digital mammography. *Medical Physics*, *37*, 962–969.
59. Robson, K. J., Kotre, C. J., & Faulkner, K. (1995). The use of a contrast-detail test object in the optimization of optical-density in mammography. *British Journal of Radiology*, *68*, 277–282.
60. Sharma, R., Sharma, S. D., & Mayya, Y. S. (2012). A survey on performance status of mammography machines: Image quality and dosimetry studies using a standard mammography imaging phantom. *Radiation Protection Dosimetry*, *150*, 325–333.
61. Sharma, R., Sharma, S. D., Mayya, Y. S., & Chourasiya, G. (2012). Mammography dosimetry using an in-house developed polymethyl methacrylate phantom. *Radiation Protection Dosimetry*, *151*, 379–385.
62. Song, S. E., Seo, B. K., Yie, A., Ku, B. K., Kim, H.-Y., Cho, K. R., et al. (2012). Which phantom is better for assessing the image quality in full-field digital mammography? American college of radiology accreditation phantom versus digital mammography accreditation phantom. *Korean Journal of Radiology*, *13*, 776–783.
63. Suryanarayanan, S., Karellas, A., Vedantham, S., Sechopoulos, I., & D’Orsi, C. J. (2007). Detection of simulated microcalcifications in a phantom with digital mammography: Effect of pixel size. *Radiology*, *244*, 130–137.
64. Taibi, A., Fabbri, S., Baldelli, P., di Maggio, C., Gennaro, G., Marziani, M., et al. (2003). Dual-energy imaging in full-field digital mammography: A phantom study. *Physics in Medicine and Biology*, *48*, 1945–1956.
65. Theodorakou, C., Horrocks, J. A., Marshall, N. W., & Speller, R. D. (2004). A novel method for producing x-ray test objects and phantoms. *Physics in Medicine and Biology*, *49*, 1423–1438.
66. Thompson, S. R., & Faulkner, K. (1991). A phantom for the measurement of contrast detail performance in film-screen mammography. *British Journal of Radiology*, *64*, 1049–1055.
67. Tomal, A., Cunha, D. M., & Poletti, M. E. (2013). Optimal x-ray spectra selection in digital mammography: A semi-analytical study. *IEEE Transactions on Nuclear Science*, *60*, 728–734.
68. White, D. R. (1977). Formulation of tissue substitute materials using basic interaction data. *Physics in Medicine and Biology*, *22*, 889–899.
69. White, D. R., & Tucker, A. K. (1980). A test object for assessing image quality in mammography. *British Journal of Radiology*, *53*, 331–335.

70. Woodard, H. Q., & White, D. R. (1986). The composition of body-tissues. *British Journal of Radiology*, *59*, 1209–1219.
71. Wu, X., Barnes, G. T., & Tucker, D. M. (1991). Spectral dependence of glandular tissue dose in screen-film mammography. *Radiology*, *176*, 143–148.
72. Yaffe, M. J., Boone, J. M., Packard, N., Alonzo-Proulx, O., Huang, S.-Y., Peressotti, C. L., et al. (2009). The myth of the 50-50 breast. *Medical Physics*, *36*, 5437–5443.
73. Yaffe, M. J., Byng, J. W., Caldwell, C. B., & Bennett, N. R. (1993). Anthropomorphic radiological phantoms for mammography. *Medical Progress Through Technology*, *19*, 23–30.
74. Young, K. C., & Ramsdale, M. L. (1993). Evaluation of mammography image quality phantoms. *Radiation Protection Dosimetry*, *49*, 171–173.
75. Young, K. C., Ramsdale, M. L., Bignell, F. (1998). Review of dosimetric methods for mammography in the UK breast screening programme. *Radiation Protection Dosimetry*, *80*, 183–186.

Chapter 9

Phantoms for Ultrasound

Experimentation and Quality Control

Evan J. Boote

9.1 Background

Phantoms used in ultrasound were born out of a need for models of human anatomy and tissue characteristics. Initial ultrasound phantom construction was based on containers filled with water and would be constructed with metal rods at specific locations in order to provide a distance calibration. As ultrasound equipment became more sophisticated and advanced, it was recognized that a better material was needed to provide a medium for transmission of sound at the correct speed, to have reflectors that cause an echo to be returned to the transducer, while providing an attenuation of sound that is similar to that of experienced by sound waves in tissue. Hence, as is the case with many imaging modalities, the development of ultrasound phantoms has been driven by the progressively improved specifications of ultrasound imaging equipment [1].

Various materials, such as urethane polymers or soft plastics, were initially analyzed as possible media for phantom construction; however, these materials were deficient in one more of the physical parameters of ultrasound. The earliest report of materials designed to mimic tissue characteristics was published by a group at the University of Wisconsin–Madison [2, 3]. The methods of tissue-mimicking gel production developed from this work has served as the basis for many subsequent ultrasound phantoms. In the remainder of this chapter, the term “tissue mimicking” will be abbreviated by the initials “TM.”

Ultrasound phantom design and construction was also a part of the UW ultrasound group’s early work, always with application toward ultrasound quality control [4], but also, to provide an experimental platform for a better understanding of ultrasound physics and how imaging performance is related to the propagation of ultrasound in tissues [5, 6]. Anthropomorphic phantoms have been

E. J. Boote (✉)
Spectrum Health, Grand Rapids, MI, USA
e-mail: Evan.Boote@spectrumhealth.org

constructed and applied as part of a quality assurance program for a large, multi-center breast ultrasound study [7].

Contributions to ultrasound phantom development have also come from a number of ultrasound research laboratories, including the FDA [8], and research groups in Great Britain [9], the Netherlands [10], France [11, 12], Germany [13, 14], and Canada [15, 16]. While many of these have been built to provide a means to analyze the performance of imaging systems, a number of other phantoms are constructed for experiments to measure attenuation [17], backscatter [18–20], ultrasound exposimetry [21], and more recently, bulk material characteristics [22]. The latter types serve as “gold standards” to verify that the ultrasound techniques being used to measure tissue properties are indeed valid.

In addition to the laboratory development, a number of commercial vendors manufacture and market ultrasound phantoms for ultrasound quality control and training. With the worldwide market for ultrasound equipment is approaching \$5 billion per year with about a 5 % growth rate [23], these vendors have a large and growing market for a wide variety of quality assurance phantoms. Some designs are based on or developed from standards developed by national and international committees concerning ultrasound image quality. For example, the Technical Standards Committee of the American Institute of Ultrasound in Medicine has published descriptions of phantoms that have been produced by commercial vendors. In particular, the International Electrotechnical Commission, Group 87 has produced documents that describe phantoms and testing procedures for diagnostic ultrasound equipment [24, 25]. However, most of the commercial phantoms available today are built with unique designs made by a vendor based upon some common elements required for ultrasound quality control; these include a scanning/acoustic window, regularly spaced reflectors, and a background with a given sound speed and attenuation properties. Figure 9.1 shows images from several commercial vendors.

In addition to these, various methods have been published to fabricate “in-house” phantoms for various teaching and position equipment verifications. These range from a mixture of water and cornstarch [26], to mixtures of store-bought gelatin and psyllium hydrophilic mucilloid fiber [27]. The advantage of these phantoms is the low cost and ease of acquisition [28], albeit without absolute verification of the acoustic properties.

The objective of this chapter is to provide the reader with some basic parameters that are required for ultrasound phantoms, both for quality control of ultrasound as well as physical measurement standards. In addition, the design features of a basic ultrasound image quality control phantom will be considered as well as some specialized applications and the manner in which phantom design changes to accommodate these requirements. Lastly, the ongoing development and future trends in ultrasound phantoms will be discussed.

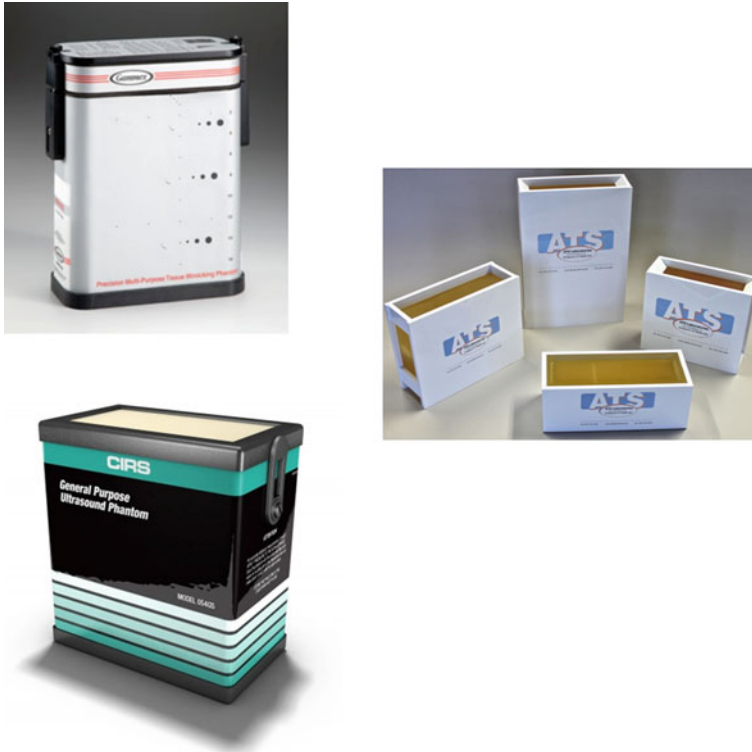


Fig. 9.1 Examples of commercially available ultrasound phantoms

9.2 Physical Parameters Required for Ultrasound Phantoms

The fact that the physical basis for ultrasound imaging is rather complex (compared to radiographic imaging) leads to the necessity of accurate physical parameters in ultrasound phantoms used for image quality measurements. Three key parameters are necessary for a proper ultrasound phantom, (1) sound speed, (2) attenuation and the frequency dependence of attenuation and (3) scattering. Other physical parameters, such as the density, non-linear parameter (B/A), are of some importance, but not always regarded as critical to a successful tissue mimic [28]. For obvious reasons, these parameters become more critical when the phantom is to be used as a standards model in an acoustics experiment. In some cases, e.g., for TM blood, the non-Newtonian fluid characteristics of human blood are impossible to mimic and therefore blood flow patterns are not precisely reproduced in Doppler phantoms vessels [29].

These physical properties should be applicable over the frequency range of most clinical diagnostic ultrasound systems (2–15 MHz). In response to the development

Table 9.1 Acoustic parameters for various tissues (several sources)

Tissue/Material	Velocity (m s ⁻¹)	Attenuation (dB cm ⁻¹ MHz ⁻¹)	Density (kg m ⁻³)	Acoustic impedance (MRayl)	Backscatter coefficient (10 ⁻⁴ cm ⁻¹ sr ⁻¹)
Air	330		1.2	0.0004	
Water	1,480	0.0022	1,000	1.48	
Soft tissue (average)	1,540	0.3–0.8	1,043	1.63	
Muscle	1,547–1,600	0.2–0.6	1,050	1.62	
Blood	1,560–1,584	0.2	1,060	1.68	0.1–1
Breast	1,510	0.75	1,020	1.54	
Liver	1,555–1,595	0.4–0.7	1,060	1.69	1–25
Cardiac	1,576	0.52	1,060	1.67	
Fat	1,450–1,480	0.5–1.8	950	1.40	

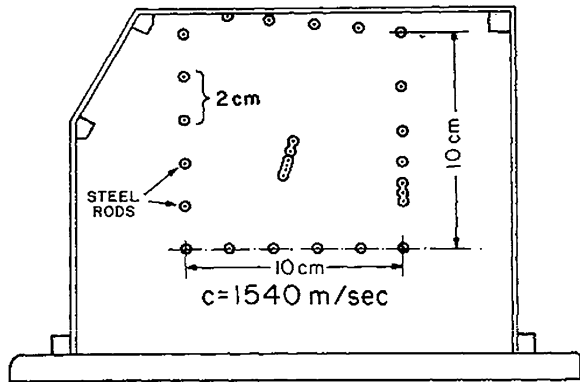
of higher-frequency probes for higher resolution imaging (preclinical at 20 MHz and above) have resulted in characterization of agar-based ultrasound phantoms at these frequencies [30–32].

Table 9.1 provides a range of typical compressional sound speed, density, and acoustic attenuation for a set of tissues. Sound speed and attenuation are the easiest parameters to verify and control and thus are regarded to be well-controlled in commercially available phantoms. Acoustic scattering, quantified by the backscatter coefficient (differential scattering cross section per unit volume) is a more difficult parameter to measure. Desirable characteristics for ultrasound phantom materials not only include these acoustic parameters, but also stability (thermal and temporal), low cost, and ease of manufacture.

9.2.1 Sound Speed (Density and Acoustic Impedance)

As mentioned at the beginning of this chapter, early ultrasound phantoms were typically built as plexiglass containers that were filled with water to provide a transmission medium for sound. As water is the simplest tissue substitute, this was an inexpensive alternative. One of the earliest of these types was the AIUM-type 100 ultrasound phantom (Fig. 9.2) [33]. Reflectors placed at fixed “depths” in the phantom produced echoes that would be registered on the ultrasound images and evaluated to determine correct distance calibration. This was important for early ultrasound units, which commonly required adjustment to insure that the depth calibration based on round trip time was correct. The reflectors were placed at depths that were adjusted so that the phantoms were built to “mimic” the sound speed of tissue ($c = 1.54\text{mm}/\mu\text{s}$) even though the sound speed of water is about 4 % slower ($1.48\text{mm}/\mu\text{s}$). Later phantoms were built with reflectors placed at the proper depths, and the sound speed of the fluid medium was increased by adding alcohol to water. The addition of 7.4 % ethanol to water increases the sound speed to $1,540\text{m s}^{-1}$.

Fig. 9.2 The AIUM 100 mm ultrasound test object



One of the disadvantages of water-based phantoms is there is a strong temperature dependence of the sound speed in water. Lubbers [34] provides a simple equation for the compressional sound speed in water over an interval of 15°–35° C:

$$c = 1404.3 + 4.7 T - 0.04 T^2 \tag{9.1}$$

Though it is a simple, easily obtained acoustic medium, water is insufficient for ultrasound phantoms requiring accurate sound speeds. Soft tissue substitutes having more accurate and stable sound speeds are desirable for use with imaging systems. Other tissue substitutes are typically based on gelatins, agarose, or other materials based on organic hydrocarbon-based chains. Some commercially marketed phantoms are constructed from urethane rubber; these offer stability in sound speed, but have a lower density and sound speed than soft tissue. Targets in these urethane phantoms are adjusted to “mimic” a phantom having a sound speed of 1,540 m s⁻¹.

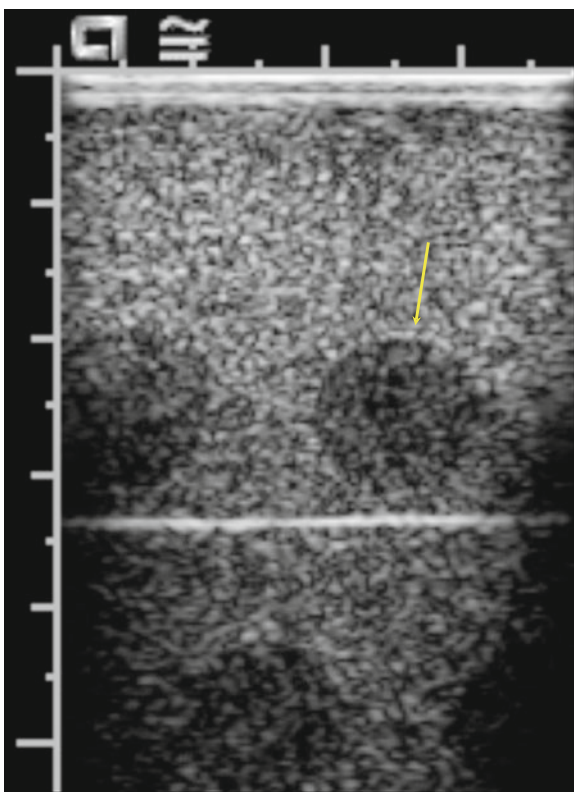
Many TM-gel-based phantoms are made from gelatin or agarose and are formulated to have a sound speed that is within 2 % of the sound speed of soft tissue (1,540 m s⁻¹). This can be accomplished by the addition of n-propanol alcohol [2], evaporated milk [35], or glycerol [36]. Reproducible and stable sound speed and density at room temperatures have been achieved through the use of these materials. Longevity is another issue with gelatin phantoms; this has been mitigated by adding antimicrobial agents into the gel and sealing the phantom well to prevent desiccation.

Layers of subcutaneous fat are often encountered in the transmit–receive ultrasound paradigm, and in some cases, the simulation of these fat layers are important to mimic the “true” conditions encountered by the beam as it passes through these layers [37]. In order to evaluate the effect of these sound speed, acoustic impedance boundaries, and varying attenuation layers on the performance of multi-element transducers, layers (sometimes with varying thicknesses) of fat simulating material are interposed between the scanning surface and the parenchyma mimic. Safflower oil is typically used as a substitute for subcutaneous fat [38]. Methods to incorporate these fat substitutes in oil-dispersed gelatin molds have been described, resulting in materials with sound speeds (1,491 m s⁻¹) and attenuation and scattering characteristics similar to that of human fat.

The importance of proper control of sound speed and density in gel-based phantoms must be emphasized here, especially in phantoms built to provide low-contrast imaging targets. Because acoustic reflection at an interface is related to the acoustic impedance ($Z = \text{velocity} \times \text{density}$), any small differences at an interface will produce an echo that is registered in the ultrasound image. Having such a readily visible interface defeats the purpose of placing low-contrast objects within a background as the targets are quite easily discerned by this bright echo that appears on the ultrasound image. Commercial vendors strive to make these acoustic impedance differences as small as possible. Figure 9.3 is an example of a low-contrast test object with a slight impedance mismatch; this shows up as a bright echo at the perpendicular interface between the acoustic beam and the border between the background and the object.

With the widespread adoption of harmonic imaging, the non-linearity parameter (B/A) has become of somewhat greater importance [39]. B/A is a non-dimensional value that expresses the degree to which the density (and hence sound speed) changes in a material with respect to the pressure amplitude. These pressure-dependent changes thus produce increasing propagation in compression and decreasing propagation speed in rarefaction, converting sine wave into sawtooth

Fig. 9.3 The arrow points to a very slight acoustic impedance mismatch between the background of the phantom and the low-contrast (*lower echogenicity*) object. This may lead to a false impression of the presence of an object



and resulting in the generation of harmonics. In harmonic imaging mode, an ultrasound system using a broad-frequency response transducer sends pulses at a lower frequency, but “tunes” to receive echoes centered at two times this frequency. A phantom with a tissue-like B/A (reported to be equal to around 7 for soft tissues) will demonstrate and test harmonic imaging reliably.

Gelatin-based phantoms have another advantage over liquid-based media in that the incorporation of other particles and materials to achieve tissue-like attenuation and scattering within the phantom.

9.3 Attenuation

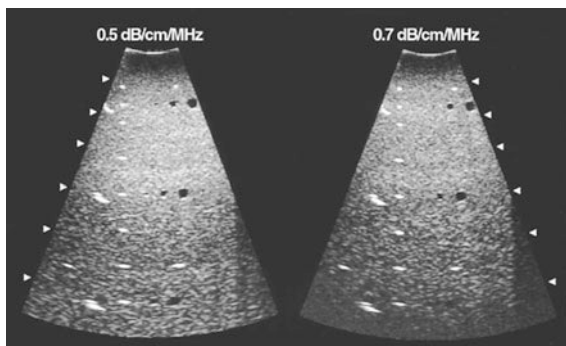
Attenuation is a very important property for phantoms used to evaluate the performance of ultrasound imaging systems. This is due to the fact that the attenuation of the sound energy in the pulse–echo mode is compensated for by time-gain compensation (TGC). Furthermore, the formation of the ultrasound image in a state-of-the-art ultrasound system is a complex process that at times involves multiple transmit beams and image reconstruction and sophisticated image processing that takes into account the expected attenuation that occurs during anatomical imaging. Acoustic attenuation increases roughly linearly with frequency, which means that (a) different frequency probes will result in widely varying attenuation, and (b) systems designed to achieve broad-band frequency response will exhibit different results if the ultrasound phantom does not have tissue-like attenuation properties.

As seen in Table 9.1, the attenuation of soft tissue varies widely, but is usually approximated as being linear with frequency. Attenuation is expressed in decibels per unit length (typically cm) and normalized by frequency. For example, if the attenuation is 3 dB cm^{-1} and the frequency is 5 MHz, then the attenuation is $0.6 \text{ dB cm}^{-1} \text{ MHz}^{-1}$. For soft tissue mimics, the target attenuation is between 0.5 and $0.7 \text{ dB cm}^{-1} \text{ MHz}^{-1}$. A non-linear attenuation response (f^n , $n > 1$) will result in higher attenuation at higher frequencies than what would be encountered in soft tissues. This may produce test results that show degraded performance for higher-frequency transducers [37].

Acoustic attenuation is achieved in gel-based phantom materials through the introduction of graphite powder [2], evaporated milk [35], Al_2O_3 [40], and by PMMA microsphere [41]. For the microspheres, the dominant mechanism contributing to attenuation is scattering. However, soft tissues are a weakly scattering medium, e.g., attenuation is not dominated by scattering. In addition, scattering is not linear with frequency, due to Rayleigh and Mie scattering, depending upon the ultrasound frequency. Therefore, the high number density microsphere approach is not as desirable to produce attenuation coefficients that scale linearly with frequency.

Most of the commercially available phantoms are constructed to have either 0.5 or $0.7 \text{ dB cm}^{-1} \text{ MHz}^{-1}$. In some cases, the higher attenuation value is used to provide a more strenuous test of system sensitivity, particularly at the lower

Fig. 9.4 An example of the effect of attenuation. These images are acquired with the same ultrasound configuration; the phantom on the left has lower attenuation. The brighter appearance beyond 8 cm depth is due to less signal loss at depth



frequencies. This reduces the required size and weight of a phantom, yet still provides the ability to determine a maximum depth of penetration around 2.5 MHz. Another approach taken is to have two sections of the phantom, one with $0.5 \text{ dB cm}^{-1} \text{ MHz}^{-1}$ and one with $0.7 \text{ dB cm}^{-1} \text{ MHz}^{-1}$ (Fig. 9.4).

9.4 Scattering

Acoustic scattering in ultrasound is the result of small-scale (size of the wavelength and smaller) inclusions of varying acoustic impedance [42]. Scattering is dependent upon the acoustic impedance, the size and shape of the scattering object, and the frequency of the sound [43]. For a volume of scatterers, one typically refers to the “backscatter coefficient,” which is the degree of scattering per unit volume. This value will vary according to the differential scattering cross section per “scatterer” and the density of scatterers (N per cm^3). The backscatter coefficient expressed in dimensions of $\text{cm}^{-1} \text{ sr}^{-1}$ and for soft tissues is in the range of 10^{-3} – 10^{-4} and between 10^{-4} and 10^{-5} for blood.

Many of current commercial phantoms incorporate 20–80 micron diameter glass beads at appropriate concentrations to achieve a backscatter coefficient that approximates liver tissue [20]. While the acoustic impedance difference of glass beads and the background gels is considerably more significant than tissue acoustic impedance differences, the number of scatterers per unit volume is adjusted accordingly. Similarly, objects of varying contrast can be made by changing the concentration of scatterers. This is typically done on the decibel scale, e.g., -6 or $+3$ dB.

Because the statistics of scattering are affected by the scatterer density [44], the diameter of the scatterers must be small enough and number density of scatterers must be large enough to provide sufficient statistical variation to demonstrate ultrasound speckle. As is the case with backscatter coefficient, many TM phantom materials aim to mimic liver tissue in this regard.

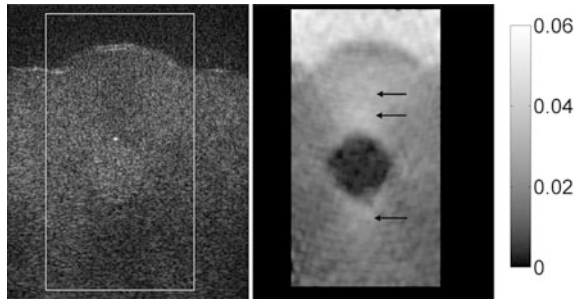


Fig. 9.5 An example of a phantom with an inclusion simulating a fibroadenoma. A standard B-mode image is on the left; the right side is an elastogram. For the image on the right, the bright region at the top of the image corresponds to softer TM fat while the harder TM fibroadenoma is the dark region in the center of the image

9.5 Mechanical Properties

More recently, the mechanical (viscoelastic) properties of ultrasound phantoms must be considered. These have become important since the introduction of methods which analyze ultrasound echo signals to under varying degrees of compression [45, 46], or, alternatively through the use of acoustic radiation force [47, 48]. Phantoms serve as useful means by which these methods are tested, both in the laboratory as the algorithms are developed as well as a way to check the contrast display performance for elastography applications on clinical equipment. Oil-in-gelatin-based phantoms have been developed to mimic this property of tissue, with a Young's modulus value of between 6 and 12 kPa. Harder (more stiffness) objects are typically present as inclusions in the background, with the same sound speed, attenuation, and scattering; these are used to evaluate the effectiveness of the algorithm by providing a comparison of the backscatter image alongside the elastography image (see Fig. 9.5). The challenge is to maintain all of the other acoustic characteristics as constant while varying the Young's modulus.

9.6 Multi-Modality Phantoms Based on TM Gels

From the earliest days of CT and ultrasound as complimentary modalities, individuals have attempted to utilize phantoms that could be applied to both [49] modalities. Acoustic tissue models based on organic materials offer similar X-ray attenuation characteristics as soft tissues. It is not difficult to incorporate other (higher atomic number) structures into the gel phantoms. In addition, it is also possible to dope the same aqueous gels used for ultrasound phantoms with paramagnetic salts to obtain tissue-like magnetic resonance properties (T1 and T2) [50]. This eventually resulted in the construction of a prostate mimic that could be

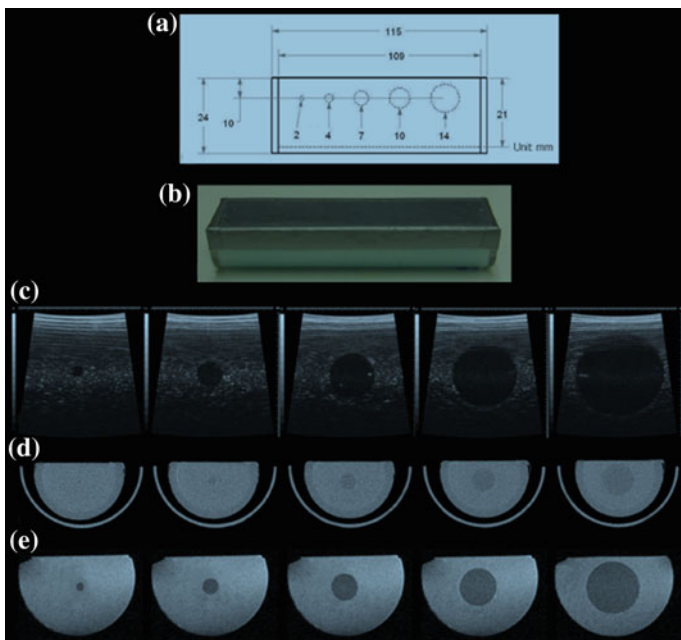


Fig. 9.6 An example of a multimodality phantom with ultrasound (*top row*), computed tomography (*middle row*) and magnetic resonance imaging (*bottom row*) systems used for preclinical imaging (need permission from Lee, Fullerton, etc., UTHSA)

used for ultrasound, CT, and MRI [51]. Another set of phantoms has been produced by a collaboration between a commercial vendor and a university laboratory [52]. These phantoms are designed to determine the accuracy of volume measurements for preclinical imaging systems and are compatible with US, CT, and MRI.

Other phantoms have been constructed for determination of proper safety checks for therapeutic applications of ultrasound. These have been used in high-intensity-focused ultrasound (HIFU) therapy applications under guidance by MRI [53]. Another “liver” ultrasound phantom has been applied to identify spatial errors in surgical navigation systems [54]. As ultrasound imaging continues to evolve into an imaging and therapeutic modality, many more phantom configurations and applications could result (Fig. 9.6).

9.7 Applications of Phantoms in Ultrasound

Ultrasound phantoms constructed as test tool measurement standards are often custom-built with the measurement device requirements in mind. Most common methods for sound speed, attenuation, and backscatter measurements involve

immersion in water baths to control temperature and to provide a coupling medium to acoustic transducers. If produced using gelatin-based recipes, the phantoms are typically cast inside a box or cylinder of plexiglass, then are covered with a thin layer of plastic [55]. The immersion experiment is conducted with a parallel beam interface to the acoustic beam. With two parallel acoustic “windows,” the phantom may be used for through transmission (sound speed and attenuation) and for pulse–echo (backscatter) measurements.

The additional parameters (non-linearity, mechanical stiffness) become more important when the objective of the phantom is to become a standard test object for validation of measurement methods and algorithms.

Another manner in which ultrasound phantoms are used for teaching and training. Ultrasonographers are required to understand and know the underlying anatomy and its appearance as they perform studies. Anthropomorphic phantoms are intended to provide a reusable and repeatable, if not quite realistic, way to provide the trainee with the experience of placing the ultrasound probe on the correct part of the body, locating the anatomy of interest and then to optimize and capture the images required for the study. In some instances, these phantoms are recognizable in the mannequin-like appearance; other types are only small portions of the body or are (for endocavitary transducers) enclosed within a box with an opening for insertion of the transducer [56]. Another type models the fetus at different stages of development (Fig. 9.7).

Additionally, training phantoms are useful when an operator is training to perform needle-based biopsy procedures where ultrasound imaging is used for guidance. The development of operator hand-eye coordination and muscle memory is the objective of these phantoms. One of the more common of these types are cast in the shape of a breast and have “cysts” and “lesions” embedded within as targets for drainage or

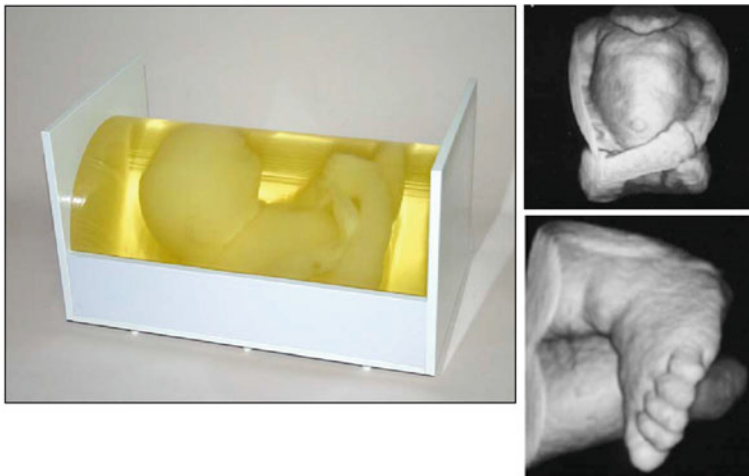


Fig. 9.7 An example of an anthropomorphic phantom; simulating an in-utero fetus

biopsy, respectively. Another category of these phantoms are used for training physicians to perform peripheral nerve blocks under ultrasound guidance. These phantoms include a TM background, artery and vein (collapsible) simulated by tubing, TM bone, TM muscle, and hyper- and hypo-echoic TM nerve bundles.

With ultrasound use proliferating beyond the radiology department (and other “traditional” ultrasound users such as obstetrics, vascular, and cardiac), the demand for these teaching and training phantoms can only increase. While ultrasound has typically relied upon human volunteers for teaching and training, the more invasive procedures preclude the use of volunteers.

Finally, the most common application for ultrasound phantoms is for verification of imaging system performance. In addition, verification of Doppler ultrasound system performance is also useful with specially designed ultrasound phantoms. These aspects will be considered in more detail in the following sections.

9.8 Image Quality Control

As stated at the beginning of the chapter, ultrasound phantom development has been driven by the need to evaluate the performance of ultrasound imaging equipment. While it seems rather obvious, it needs to be stated that phantom design and construction is dictated by the types of tests that are to be performed [57].

For ultrasound imaging, the development of new technology has outpaced the development of phantoms; imaging system vendors are in a competitive race to bring to market the best spatial and contrast resolution possible. At times, these systems have exceeded the characteristics of the phantom. Ultrasound imaging, while on the surface seemingly simple, is in reality a very complex process; consider the formation of a beam by a set of transducer elements, over a wide band of frequencies at a single depth or multiple depths. The acoustic energy is attenuated and scattered—the received echoes are “focused” again by a set of delays on the transducer elements and the signal is amplified (time-dependent to correct for attenuation) and processed by another complex set of algorithms that threshold, logarithmically transform, and envelope detect. If operating in harmonic mode, the RF signal is filtered to remove the fundamental frequency and retain only the first harmonic. Images are reconstructed from a set of acoustic lines that are recorded differently for transducer types, for example, linear versus curvilinear arrays. Add to this complexity the possibility of multi-dimensional (1.25x, 1.5x, and 2x transducer arrays) and multiple shapes and frequencies of transducers. The image that is formed by a set of acoustic lines also undergoes image processing to establish the gray scale and reduce speckle.

This leads to a wide variety of phantom designs and applications, aimed at testing differing aspects of imaging system performance; it is beyond the scope of this text to report on all of these, so the focus here will be on basic imaging system quality control. The principle tests that are usually expected in the course of ultrasound imaging QC are distance calibration, sensitivity, uniformity, and resolution (spatial and contrast) [58].

Distance calibration determination is achieved by placed fixed targets at specific depths within the TM material. These are typically narrow nylon fibers which are imaged in cross section (the image plane perpendicular to the direction of the fiber run). Cursors are placed on the image and a comparison is made between the known distance and the measured distance. In most cases, an accuracy determination is made in both the axial (beam direction) as well as the lateral direction. An extension of this test would be to determine the accuracy of the area determination for a single slice or, in the case of a three-dimensional ultrasound imaging protocol, the volume measurement accuracy.

Sensitivity is a measure of the ability of the ultrasound instrument to detect and display images based on subtle echo signals without excessive noise present. Modern ultrasound systems have very sensitive transducers with a wide dynamic range. Of course, attenuation increases with range and this means that the ability to image deeper structures in the body is limited by the system sensitivity. This depth range may be affected by damage to the transducer, either to the elements themselves or to the matching layer that is the interface between the acoustic element and the body. Damage to the insulation surrounding the transducer cable may affect sensitivity due to the increased RF noise that is detected and amplified by the scanner electronics.

Phantoms are used to assess the sensitivity of the system by determining the maximum depth of penetration. An quasi-objective visual test is possible, where the observer uses the calipers to place a point at which the noise overcomes the echo signals. A more objective method is to use a computer to analyze the statistical properties of the image data and determine a merit factor that relates to signal versus noise [59].

Image uniformity is important for accurate diagnostic review by physicians. Non-uniformities in the image might be mistaken for pathology or artifacts related to pathology. Imaging of a known material, e.g., phantom with a uniform background, allows the end user to have confidence in the performance of the instrument. A uniform appearance across the lateral direction indicates that all elements of the transducer are performing nominally. Non-uniformity in the axial direction may be the result of an incorrect reconstruction with multiple transmit focus, defective time-gain amplification or errors in the transmit and receive focusing of the beam.

For a state-of-the-art ultrasound scanner, image uniformity is most likely to be caused by transducer damage or malfunction in a group of elements. A recent report cites image uniformity as the most likely issue to be discovered by routine quality control testing [60]. As a result, these authors recommended quarterly inspections of ultrasound units and transducers for image uniformity.

Ultrasound resolution, like the imaging systems, is complex. Spatial resolution can be thought of in terms of three dimensions, which are not isotropic and varying with the depth in the acoustic field (figure of ultrasound planes). Resolution in ultrasound imaging is closely related to frequency; generally, higher frequencies improve the spatial resolution. Contrast resolution could improve (in part because of changes in speckle), but higher attenuation usually defeats this improvement when deeper penetration is required. Multi-element transducers offer the potential to

improve spatial resolution through the use of wide apertures and time-delay focusing [61]. Early ultrasound phantoms presented a set of targets (nylon strings) to testing the axial and lateral spatial resolution only. Even then, the actual resolution measurement was neither truly all axial nor truly lateral, but rather a combination.

A group at the FDA introduced the concept of contrast and detail, after the same fashion used for computed tomography [8]. This phantom used targets of varying backscatter in the shape of cones to present different size “lesions” of varying contrast levels. An observer was to determine the minimum dimension and contrast that could be detected against the background. However, this arrangement assumes that the targets encountered by an ultrasound system are essentially two-dimensional. Further complicating matters is the use of various image scaling and interpolation algorithms, applied to real-time image display. This, combined with adjustable gain, makes evaluation of spatial resolution a difficult proposition [62].

The introduction of multi-row transducers made possible focusing of the beam in the elevational plane. This improves spatial resolution and, due to the lessening of partial volume artifact, improves contrast resolution. Madsen and Rownd proposed a phantom to test spatial resolution based on the ability to visualize spherical objects with no scattering against a background with identical sound speed and attenuation [63]. This phantom, in combination with a computer assisted analysis, provides an objective means by which spatial resolution could be determined [64–66].

9.9 Doppler Phantoms

Doppler ultrasound applications have existed as long as ultrasound imaging. Beginning with continuous wave Doppler, the introduction of duplex Doppler and color flow imaging in the 1980s and 1990s has led to the development of phantoms to assess performance and quantitative accuracy [13, 67–69].

Doppler phantoms are either built with a mechanical device for presenting motion to the ultrasound beam or are built with a pump system and simulated vessels in a TM background (vessel-based phantoms which shall be referred to as VB phantoms). The advantage of the former is that calibration of velocity is simple and accurate. These types of phantoms do not, however, challenge the signal to noise limits of the Doppler ultrasound system. The VB phantoms, while not provided a precisely calibrated velocity, provide a more realistic test of the Duplex and color flow systems. As previously discussed, the echogenicity of blood is low compared to soft tissues. Blood-mimicking fluids have been the topic of a number of publications; however, one physical aspect of blood that is very difficult to reproduce is the non-Newtonian property of blood. This affects the flow profile in both normal and stenotic vessels.

The pulsatile flow of blood as a result of normal cardiac contraction has been modeled in phantoms. This is a goal that developers have tried to achieve due in part to the importance of waveform peak and minimum velocities on the computation of flow indices [70]. Simple pumping systems can only provide simple

flow patterns (constant or on/off). Various types of pumps have been proposed and built; these range in sophistication from a gravity flow system to typical pumping systems as well as a pump system specially built to mimic cardiac flow [71]. Collaboration between groups involved in CT and MRI may also prove useful to developing more realistic pulsatile flow patterns.

VB phantoms range from simple arrangements of tubes to sophisticated models of pathology. The latter are often modeled after mild to severe stenoses [72–74] of the common carotid artery including the branch into the internal and external carotid arteries [74, 75]. In addition, some phantoms have been built to demonstrate low flow rate in very small bundles, as a means to evaluate the ability to detect perfusion with power Doppler systems [76, 77].

9.9.1 Current/Future Developments

Current ultrasound phantoms designed for quality control testing are evolving in response to more recent developments in ultrasound technology. Maintaining good contact and acoustic coupling is one problem encountered during the testing of curvilinear transducers. Working groups within the American Association of Physicists in Medicine [78], the International Electrotechnical Commission [79], and the American Institute of Ultrasound in Medicine [80] continue to work on modifications to the phantom design to accommodate these and other probes. A similar type of issue is encountered with the introduction of full two-dimensional arrays. In this situation, the acoustic window of the phantom needs to be of the proper size to have the transducer fit. Along with the efforts to develop these phantoms, a number of various groups are working on computer programs designed to work with one or more ultrasound phantoms to provide objective performance measurements.

Efforts to develop a standard ultrasound accreditation phantom have been difficult; however, there is ongoing work at the American College of Radiology to develop a required set of tests and performance measures for both the Ultrasound Accreditation Program and the Breast Ultrasound Accreditation Program. While not currently in the plans, an accreditation phantom standard would be of benefit to make testing procedures uniform and allow performance measures to be used in a manner similar to that for mammography, CT, and MRI accreditation programs.

Another area of development has been the electronic based “phantoms.” In these, there is no tissue-mimicking material involved. Rather, electronic transducers couple to the ultrasound scanner probe and “respond” to the pulsing by the scanner by “returning” controlled echo signals. One system involves a test of only the transducer, using compatible connector and a water tank to perform a pulse-receive test on each element of the probe (Fig. 9.8). This procedure allows one to detect individual elements which are in full or partial failure. This device is promoted as a tool to allow individual consultants or institutions to screen probes for proper functioning [81, 82]. This same concept (testing individual elements) is



Fig. 9.8 Example of an electronic ultrasound test device—the ultrasound transducer is mounted on the stand to the right and placed in a water tank. The probe is connected to the box on the left which is controlled by a computer. Individual “pings” of elements of the transducer produce echoes which bounce back from the reflector (this is configured for a curvilinear probe) and processed to determine which elements are operational

applied in a simpler device, which pings back when a pulse is detected. During the operation of this tool, the monitor of the ultrasound system is reviewed to visualize the response. If there is some dropout due to failed or malfunctioning elements, it would be visualized on the image. A similar approach has been implemented for at least one major ultrasound vendor through internal software available via a service interface.

Another form of electronic test phantom has been developed to test Doppler instruments [83]. Programming these electronic phantoms is considerably complex; however, once accomplished, there is a considerable flexibility to change the responding signal, for example, Doppler-shifted frequencies, additive noise, and varying levels of attenuation and speckle. Descriptions of these types of phantoms include an interface to a MATLAB program to allow for custom programming of the response to the transducer.

9.10 Summary

Ultrasound phantoms vary widely by application. The majority of phantoms constructed for sale are used in the quality control application whereas many of the in-house phantoms are fabricated by research groups to meet the experimental and development needs. In both cases, TM materials are most likely to be based on gelatin materials, from recipes that have been empirically found to control sound speed, attenuation, and backscatter.

Future phantom developments will most likely be required to match improvements in ultrasound system technology; ideally, these would include acoustic parameters of quantitative interest, both as a means of verifying proper machine operation as well as providing confidence in measurements made by the ultrasound system. As sophistication of ultrasound equipment increases, the demands for acoustically realistic materials and phantoms will likely also increase.

References

1. Carson, P. L., & Fenster, A. (2009). Anniversary paper: Evolution of ultrasound physics and the role of medical physicists and the AAPM and its journal in that evolution. *Medical Physics*, *36*, 411–428.
2. Madsen, E. L., Zagzebski, J. A., Banjavic, R. A., & Jutila, R. E. (1978). Tissue mimicking materials for ultrasound phantoms. *Medical Physics*, *5*, 391–394.
3. Burlew, M. M., Madsen, E. L., Zagzebski, J. A., Banjavic, R. A., & Sum, S. W. (1980). A new ultrasound tissue-equivalent material. *Radiology*, *134*, 517–520.
4. Carson, P., & Zagzebski, J. A. (1980). *Pulse echo ultrasound imaging systems: Performance tests and criteria* (pp. 1–79). College Park, MD: AAPM.
5. Banjavic, R. A., & Zagzebski, J. A. (1981). Ultrasonic pulse-echo beam width and axial response approximations for clinical broadband focused transducers. *Ultrasound in Medicine and Biology*, *7*, 63–71.
6. Zagzebski, J. A., Banjavic, R. A., Madsen, E. L., & Schwabe, M. (1982). Focused transducer beams in tissue-mimicking material. *Journal of Clinical Ultrasound*, *10*, 159–166.
7. Madsen, E. L., Zagzebski, J. A., & Frank, G. R. (1982). An anthropomorphic ultrasound breast phantom containing intermediate-sized scatterers. *Ultrasound in Medicine and Biology*, *8*, 381–392.
8. Smith, S. W., & Lopez, H. (1982). A contrast-detail analysis of diagnostic ultrasound imaging. *Medical Physics*, *9*, 4–12.
9. Sheppard, J., & Duck, F. A. (1982). Ultrasonic tissue-equivalent materials using inorganic gel mixtures. *British Journal of Radiology*, *55*, 667–669.
10. van Wijk, M. C., & Thijssen, J. M. (2002). Performance testing of medical ultrasound equipment: fundamental vs. harmonic mode. *Ultrasonics*, *40*, 585–591.
11. Oudry, J., Bastard, C., Miette, V., Willinger, R., & Sandrin, L. (2009). Copolymer-in-oil phantom materials for elastography. *Ultrasound Medical Biology*, *35*, 1185–1197 (2009). [pii]:S0301-5629(09)00053-2, doi:[10.1016/j.ultrasmedbio.2009.01.012](https://doi.org/10.1016/j.ultrasmedbio.2009.01.012).
12. Bridal, S. L., Roberjot, V., Laugier, P. & Berger, G. (1996). Attenuation and backscatter coefficient measurements from 2 to 60 MHz using backscattered RF signals from a tissue-mimicking phantom. In *Proceedings of the IEEE Ultrasonics Symposium 2*, (pp. 1151–1154).
13. Kollmann, C., Bezemer, R. A., Fredfeldt, K. E., Schaarschmidt, U. G. & Teirlinck, C. J. in *Ultraschall in der Medizin* (Stuttgart, Germany: 1980) Vol. 20, (pp. 248–257, 1999).
14. Kollmann, C. in *Ultraschall in der Medizin* (Stuttgart, Germany : 1980) Vol. 28, (pp. 438–439, 2007).
15. Nadkarni, S. K., Austin, H., Mills, G., Boughner, D., & Fenster, A. (2003). A pulsating coronary vessel phantom for two-and three-dimensional intravascular ultrasound studies. *Ultrasound in Medicine and Biology*, *29*(4), 621–628.
16. Rickey, D. W. & Fenster, A. A. (1996). Doppler ultrasound clutter phantom. *Ultrasound in Medicine and Biology*, *22*, 747–766 (1996). [pii]:0301562996000452.
17. Insana, M., Zagzebski, J., & Madsen, E. (1983). Improvements in the spectral difference method for measuring ultrasonic attenuation. *Ultrasonic Imaging*, *5*, 331–345.

18. Insana, M. F., Madsen, E. L., Hall, T. J., & Zagzebski, J. A. (1986). Tests of the accuracy of a data reduction method for determination of acoustic backscatter coefficients. *Journal of the Acoustical Society of America*, 79, 1230–1236.
19. Hall, T. J., Madsen, E. L., Zagzebski, J. A., & Boote, E. J. (1989). Accurate depth-independent determination of acoustic backscatter coefficients with focused transducers. *Journal of the Acoustical Society of America*, 85, 2410–2416.
20. Wear, K. A. et al. (2005). Interlaboratory comparison of ultrasonic backscatter coefficient measurements from 2 to 9 MHz. *Journal of Ultrasound in Medicine*, 24, 1235–1250 (2005). [pii]:24/9/1235.
21. Stiles, T. A., Madsen, E. L., Frank, G. R., Diehl, T. & Lucey, J. A. Tissue-mimicking liquid for use in exosimetry. *Journal of Ultrasound in Medicine*, 24, 501–516 (2005). [pii]:24/4/501.
22. Insana, M. F., Hall, T. J., Chaturvedi, P., & Kargel, C. (2001). Ultrasonic properties of random media under uniaxial loading. *Journal of the Acoustical Society of America*, 110, 3243–3251.
23. Auntminnie. (2012). Study: Global ultrasound market to grow at 5% rate. <http://www.auntminnie.com/index.aspx?sec=ser&sub=def&pag=dis&ItemID=98757>.
24. IEC-Technical-Committee-87. (2011). Ultrasonics—Real-time pulse-echo scanners—Phantom with cylindrical, artificial cysts in tissue-mimicking material and method for evaluation and periodic testing of 3D-distributions of void-detectability ratio (VDR). <http://webstore.iec.ch/webstore/webstore.nsf/artnum/044952!opendocument>.
25. IEC-Technical-Committee-87. (1986). Methods of measuring the performance of ultrasonic pulse-echo diagnostic equipment. <http://webstore.iec.ch/webstore/webstore.nsf/artnum/017421!opendocument>.
26. King, D. M., Hangiandreou, N. J., Tradup, D. J. & Stekel, S. F. (2010). Evaluation of a low-cost liquid ultrasound test object for detection of transducer artefacts. *Physics in Medicine and Biology*, 55, N557–N570 (2010). [pii]:S0031-9155(10)59794-X, doi:10.1088/0031-9155/55/23/N01.
27. Lo, M. D., Ackley, S. H. & Solari, P. (2012). Homemade ultrasound phantom for teaching identification of superficial soft tissue abscess. *Emergency Medicine Journal*, 29, 738–741 (2012). [pii]:emermed-2011-200264, doi:10.1136/emermed-2011-200264.
28. Browne, J. E., Ramnarine, K. V., Watson, A. J. & Hoskins, P. R. Assessment of the acoustic properties of common tissue-mimicking test phantoms. *Ultrasound in Medicine and Biology*, 29, 1053–1060 (2003). [pii]:S030156290300053X.
29. Hoskins, P. R. (2008). Simulation and validation of arterial ultrasound imaging and blood flow. *Ultrasound in Medicine and Biology*, 34, 693–717 (2008). [pii]:S0301-5629(07)00549-2, doi:10.1016/j.ultrasmedbio.2007.10.017.
30. Cannon, L. M., Fagan, A. J. & Browne, J. E. (2011). Novel tissue mimicking materials for high frequency breast ultrasound phantoms. *Ultrasound in Medicine and Biology*, 37, 122–135 (2011). [pii]:S0301-5629(10)00537-5, doi:10.1016/j.ultrasmedbio.2010.10.005.
31. Culjat, M. O., Goldenberg, D., Tewari, P. & Singh, R. S. (2010). A review of tissue substitutes for ultrasound imaging. *Ultrasound in Medicine and Biology*, 36, 861–873 (2010). [pii]:S0301-5629(10)00075-X, doi:10.1016/j.ultrasmedbio.2010.02.012.
32. Brewin, M. P., Pike, L. C., Rowland, D. E. & Birch, M. J. (2008). The acoustic properties, centered on 20 MHz, of an IEC agar-based tissue-mimicking material and its temperature, frequency and age dependence. *Ultrasound in Medicine and Biology*, 34, 1292–1306 (2008). [pii]:S0301-5629(07)00661-8, doi:10.1016/j.ultrasmedbio.2007.12.017.
33. AIUM. (1975). The AIUM 100 mm test object and recommended procedures for its use. *Reflections*, 1, 74–91.
34. Lubbers, J. (1998). *Ultrasound in Medicine and Biology*.
35. Madsen, E. L., Frank, G. R. & Dong, F. Liquid or solid ultrasonically tissue-mimicking materials with very low scatter. *Ultrasound in Medicine and Biology*, 24, 535–542 (1998). [pii]:S0301-5629(98)00013-1.

36. Ramnarine, K. V., Nassiri, D. K., & Hoskins, P. R. (1998). Validation of a new blood-mimicking fluid for use in Doppler flow test objects. *Ultrasound in Medicine and Biology*, *24*, 451–459.
37. Browne, J. E., Watson, A. J., Hoskins, P. R., & Elliott, A. T. (2005). Investigation of the effect of subcutaneous fat on image quality performance of 2D conventional imaging and tissue harmonic imaging. *Ultrasound in Medicine and Biology*, *31*, 957–964.
38. Madsen, E. L., et al. (2006). Anthropomorphic breast phantoms for testing elastography systems. *Ultrasound in Medicine and Biology*, *32*, 857–874.
39. Parker, K. J., Dooley, M. M. & Rubens, D. J. (2011). Imaging the elastic properties of tissue: the 20 year perspective. *Physics in Medicine and Biology*, *56*, R1–R29 (2011). [pii]:S0031-9155(11)64279-0, doi:[10.1088/0031-9155/56/1/R01](https://doi.org/10.1088/0031-9155/56/1/R01).
40. Teirlinck, C. J., et al. (1998). Development of an example flow test object and comparison of five of these test objects, constructed in various laboratories. *Ultrasonics*, *36*, 653–660.
41. Kondo, T., & Kitatuji, M. (2005). New tissue mimicking materials for ultrasound phantoms. *Ultrasonics Symposium*, *3*, 1664–1667.
42. Nicholas, D. (1982). Evaluation of backscattering coefficients for ex- cised human tissues: Results interpretation and associated measurements. *Ultrasound in Medicine and Biology*, *8*, 17–28.
43. Bamber, J. C., & Hill, C. R. (1981). Acoustic properties of normal and cancerous human liver—I. dependence on pathological condition. *Ultrasound in Medicine and Biology*, *7*, 121–133.
44. Sleefe, G. E., & Lele, P. P. (1988). Tissue characterization based on scatterer number density estimation. *IEEE Transactions on Ultrasonics, Ferroelectrics and Frequency, Control*, *35*, 749–757. doi:[10.1109/58.9332](https://doi.org/10.1109/58.9332).
45. Ophir, J., Céspedes, I., Ponnekanti, H., Yazdi, Y., & Li, X. (1991). Elastography: A quantitative method for imaging the elasticity of biological tissues. *Ultrasonic Imaging*, *13*, 111–134.
46. Hall, T. J. (2003). AAPM/RSNA physics tutorial for residents: topics in US: Beyond the basics: Elasticity imaging with US. *Radiographics*, *23*, 1657–1671 (2003). [pii]:23/6/1657, doi:[10.1148/rg.236035163](https://doi.org/10.1148/rg.236035163).
47. Walker, W. F., Fernandez, F. J., & Negron, L. A. (2000). A method of imaging viscoelastic parameters with acoustic radiation force. *Physics in Medicine and Biology*, *45*, 1437–1447.
48. Nightingale, K. R., Palmeri, M. L., Nightingale, R. W., & Trahey, G. E. (2001). On the feasibility of remote palpation using acoustic radiation force. *Journal of the Acoustical Society of America*, *110*, 625–634.
49. Sommer, F. G., Filly, R. A., Edmonds, P. D., Reyes, Z., & Comas, M. E. (1980). A phantom for imaging biological fluids by ultrasound and CT scanning. *Ultrasound in Medicine and Biology*, *6*, 135–140.
50. Blechinger, J. C., Madsen, E. L., & Frank, G. R. (1988). Tissue-mimicking gelatin-agar gels for use in magnetic resonance imaging phantoms. *Medical Physics*, *15*, 629–636.
51. D’Souza, W. D., et al. (2001). Tissue mimicking materials for a multi-imaging modality prostate phantom. *Medical Physics*, *28*, 688–700.
52. Lee, Y. C., Fullerton, G. D., Baiu, C., Lescrenier, M. G., & Goins, B. A. (2011). Preclinical multimodality phantom design for quality assurance of tumor size measurement. *BMC Medical Physics*, *11*, 1.
53. Hipp, E., Partanen, A., Karczmar, G. S., & Fan, X. (2012). Safety limitations of MR-HIFU treatment near interfaces: A phantom validation. *Journal of Applied Clinical Medical Physics*, *13*, 3739.
54. Shevchenko, N., Schwaiger, J., Markert, M., Flatz, W. & Lueth, T. C. Evaluation of a resectable ultrasound liver phantom for testing of surgical navigation systems. In *IEEE Annual International Conference of the Engineering in Medicine and Biology Society 2011*, (pp. 916–919). doi:[10.1109/IEMBS.2011.6090205](https://doi.org/10.1109/IEMBS.2011.6090205).
55. Anon. Saran (plastic). [http://en.wikipedia.org/wiki/Saran_\(plastic\)](http://en.wikipedia.org/wiki/Saran_(plastic)).

56. Xu, D., Abbas, S. & Chan, V. W. (2005). Ultrasound phantom for hands-on practice. *Regional Anesthesia and Pain Medicine*, 30, 593–594 (2005). [pii]:S1098-7339(05)00539-0, doi:10.1016/j.rapm.2005.08.007.
57. McCarty, K., & Stewart, W. (1983). Aspects of the design of performance measuring test objects. *Ultrasound in Medicine and Biology*, Suppl 2, 185–189.
58. Goodsitt, M. M., Carson, P. L., Witt, S., Hykes, D. L., & Kofler, J. M., Jr. (1998). Real-time B-mode ultrasound quality control test procedures. Report of AAPM Ultrasound Task Group No. 1. *Medical Physics*, 25, 1385–1406.
59. Thijssen, J. M., Weijers, G., & de Korte, C. L. (2007). Objective performance testing and quality assurance of medical ultrasound equipment. *Ultrasound in Medicine and Biology*, 33, 460–471.
60. Hangiandreou, N. J., Stekel, S. F., Tradup, D. J., Gorny, K. R. & King, D. M. (2011). Four-year experience with a clinical ultrasound quality control program. *Ultrasound in Medicine and Biology*, 37, 1350–1357 (2011). [pii]:S0301-5629(11)00250-X, doi:10.1016/j.ultrasmedbio.2011.05.007.
61. Thomenius, K. (1996). Evolution of ultrasound beamformers. In *Proceedings of IEEE Ultrasonics Symposium*, Vol. 2, (pp. 1615–1622).
62. Kanal, K. M., Kofler, J. M., & Groth, D. S. (1998). Comparison of selected ultrasound performance tests with varying overall receiver gain and dynamic range, using conventional and magnified field of view. *Medical Physics*, 25, 642–647.
63. Rownd, J. J., Madsen, E. L., Zagzebski, J. A., Frank, G. R. & Dong, F. (1997). Phantoms and automated system for testing the resolution of ultrasound scanners. *Ultrasound in Medicine and Biology*, 23, 245–260 (1997). [pii]:S0301562996002050.
64. Kofler, J. M., Jr. & Madsen, E. L. (2001). Improved method for determining resolution zones in ultrasound phantoms with spherical simulated lesions. *Ultrasound in Medicine and Biology*, 27, 1667–1676 (2001). [pii]:S0301562901004732.
65. Kofler, J. M., Lindstrom, M. J., Kelcz, F., & Madsen, E. L. (2005). Association of automated and human observer lesion detecting ability using phantoms. *Ultrasound in Medicine and Biology*, 31, 351–359.
66. Kofler, J. M., & Madsen, E. L. (2002). Improved method for determining resolution zones in ultrasound phantoms with spherical simulated lesions. *Ultrasound in Medicine and Biology*, 27, 1667–1676.
67. Hoskins, P. R., Anderson, T., & McDicken, W. N. (1989). A computer controlled flow phantom for generation of physiological Doppler waveforms. *Physics in Medicine and Biology*, 34, 1709–1717.
68. Stewart, S. F. (2001). Effects of transducer, velocity, Doppler angle, and instrument settings on the accuracy of color Doppler ultrasound. *Ultrasound in Medicine and Biology*, 27, 551–564.
69. Boote, E. J., & Zagzebski, J. A. (1988). Performance tests of Doppler ultrasound equipment with a tissue and blood-mimicking phantom. *Journal of Ultrasound in Medicine*, 7, 137–147.
70. Thompson, R. S., Trudinger, B. J., & Cook, C. M. (1988). Doppler ultrasound waveform indices: A/B ratio, pulsatility index and Pourcelot ratio. *British Journal of Obstetrics and Gynaecology*, 95, 581–588.
71. Rickey, D. W., Rankin, R., & Fenster, A. (1992). A velocity evaluation phantom for colour and pulsed Doppler instruments. *Ultrasound in Medicine and Biology*, 18, 479–494.
72. Rickey, D. W., Picot, P. A., Christopher, D. A. & Fenster, A. (1995). A wall-less vessel phantom for Doppler ultrasound studies. *Ultrasound in Medicine and Biology*, 21, 1163–1176 (1995). [pii]:0301562995000445.
73. Guo, Z. & Fenster, A. (1996). Three-dimensional power Doppler imaging: a phantom study to quantify vessel stenosis. *Ultrasound in Medicine and Biology*, 22, 1059–1069 (1996). [pii]:S0301562996001251.
74. Grant, E. G. et al. (2003). Carotid artery stenosis: Gray-scale and Doppler US diagnosis—society of radiologists in ultrasound consensus conference. *Radiology*, 229, 340–346 (2003). [pii]:2292030516, doi:10.1148/radiol.2292030516.

75. King, D. M., Ring, M., Moran, C. M., & Browne, J. E. (2010). Development of a range of anatomically realistic renal artery flow phantoms. *Ultrasound in Medicine and Biology*, *36*, 1135–1144. (Elsevier Ltd, 2010).
76. Gessner, R. C., Kothadia, R., Feingold, S. & Dayton, P. A. (2011). 3-D microvessel-mimicking ultrasound phantoms produced with a scanning motion system. *Ultrasound in Medicine and Biology*, *37*, 827–833 (2011). doi:S0301-5629(10)00676-9 [pii] [10.1016/j.ultrasmedbio.2010.12.013](https://doi.org/10.1016/j.ultrasmedbio.2010.12.013).
77. Hindle, A. J., & Perkins, A. C. (1994). A perfusion phantom for the evaluation of ultrasound contrast agents. *Ultrasound in Medicine and Biology*, *20*, 309–314.
78. American Association of Physicists in Medicine. www.aapm.org.
79. International Electrotechnical Commission.
80. American Institute of Ultrasound in Medicine.
81. Weigang, B., Moore, G., Gessert, J., & Phillips, W. (2003). The methods and effects of transducer degradation on image quality and the clinical efficacy of diagnostic sonography. *Journal of Diagnostic Medical Sonography*, *19*, 3–13.
82. Mårtensson, M., Olsson, M., & Brodin, L. Å. (2010). Ultrasound transducer function: annual testing is not sufficient. *European Journal of Echocardiography*, *11*(9), 801–805.
83. Gittins, J. & Martin, K. (2010). The Leicester Doppler phantom—a digital electronic phantom for ultrasound pulsed Doppler system testing. *Ultrasound in Medicine and Biology*, *36*, 647–655 (2010). doi:10.1016/j.ultrasmedbio.2010.01.003.

Chapter 10

Phantoms for Magnetic Resonance Imaging

Reed Selwyn

10.1 Introduction

Magnetic resonance imaging (MRI) provides exceptional soft tissue contrast and is capable of generating quantitative maps to demonstrate blood flow, water diffusion, temperature distribution, and tissue relaxation properties. MRI also has widely known drawbacks such as high cost and long acquisition times. To help mitigate these factors, several fast and ultra-fast MRI protocols such as fast spin-echo (FSE) and echo-planar imaging (EPI) have been developed to reduce acquisition time while attempting to maintain image quality as measured by spatial resolution, signal-to-noise ratio (SNR), and contrast-to-noise ratio (CNR). Fast imaging protocols tend to increase image distortion and ghosting, yet they also help minimize motion and flow artifacts. Attentive and routine quality assurance tests and calibrations using MRI-specific phantoms can reduce these artifacts.

In addition to fast imaging protocols, several quantitative MRI protocols such as relaxometry, magnetization transfer, spectroscopy, diffusion, perfusion, and blood oxygen level-dependent (BOLD) imaging are used in clinics and academic centers throughout the world. Quantitative techniques strive to produce parametric maps that are then overlaid on anatomical images such as T1 or T2-weighted images. The precision and accuracy of quantitative MRI depend on factors such as magnetic field stability and uniformity, gradient field instabilities, eddy currents, RF pulse profiles, and environmental conditions. Sequence-specific phantoms are

The views expressed are those of the author and do not reflect the official policy or position of the Uniformed Services University of the Health Sciences, the Department of Defense, or the United States Government.

R. Selwyn (✉)

Department of Radiology, Uniformed Services University, Bethesda, Maryland 20814, USA
e-mail: reed.selwyn@usuhs.edu

R. Selwyn

Department of Medical Physics, University of Wisconsin, Madison, Wisconsin 53705, USA

required to calibrate, normalize, and successfully interpret across multiple MRI platforms and field strengths. However, there are only a few standard MR phantoms that are routinely used for quality assurance testing or for normalizing scanner response for supporting multicenter clinical trials. It should be noted that researchers, academic centers, and vendors have constructed unique phantoms for a singular or limited purpose.

10.2 General MRI Phantom Construction

In general, MRI phantoms are fluid-filled objects that mimic body shapes and dimensions such as the head or abdomen—most are cylindrical or spherical in shape. Phantoms can be constructed with structures to evaluate image contrast, SNR, image uniformity, spatial resolution, slice thickness, and geometric accuracy. It is important to select materials that are free from susceptibility effects or signal disruption. For example, in the brain, the magnetic susceptibility in soft tissue is -9.05×10^{-6} and in air is 0.4×10^{-6} , and these differences result in a magnetic field inhomogeneity, which is especially problematic in the orbitofrontal cortex [1]. Materials such as Perspex, acrylic, nylon, or polystyrene produce minimal susceptibility effects at water/phantom junctions and are commonly utilized. For example, acrylic introduces a 0.003 parts per million (ppm) phase shift, whereas Teflon results in a 0.03 ppm shift measured at 3T [2]. Both materials are considered acceptable for MR field measurements. The filling fluid can be doped with a solution such as copper sulfate to modify the relaxation times for expediency and to minimize temperature dependence of relaxation times. For example, the American College of Radiology (ACR) has produced a standard MRI phantom that is filled with a solution of 10 mM nickel chloride and 75 mM sodium chloride [3]. This phantom will be discussed in more detail. Vendors also provide body-specific phantoms that mimic conductivities found in the human body and electrical loading of the coil. These loading phantoms are designed to fit specific body coils and are used during acceptance testing and annual physics testing to evaluate image uniformity, ghosting, and SNR. Figure 10.1 provides a photograph of typical loading phantoms.

Fig. 10.1 A photograph showing several MRI loading phantoms provided with the General Electric Healthcare (Waukesha, WI) MRI system. Each vendor provides coil-specific loading phantoms



10.3 American College of Radiology Accreditation Phantom

MR provides exceptional soft tissue contrast with high spatial resolution (<1 mm) or ultra-high-resolution (<0.5 mm) imaging. Spatial resolution is an important parameter to evaluate, and it depends on several factors such as the field of view (FOV), the number of frequency/readout and phase encode steps, and slice thickness based on transmit bandwidth and gradient strength. Other important parameters are low-contrast detectability, geometric distortion, image uniformity, slice thickness accuracy, and signal-to-noise ratio. To evaluate these essential system parameters, a standard protocol and phantom should be used for reproducibility. For MRI accreditation, the American College of Radiology (ACR) has established a protocol comprised of a standardized T1-weighted and T2-weighted protocols and a cylindrical MRI phantom. Ihalainen et al. [4] compared 11 different MRI systems operating at field strengths of 1.0T, 1.5T, and 3.0T using the ACR accreditation head phantom. In general, the ACR protocol was simple to follow and easy to perform and allows clinicians to link quality assurance results to image quality. However, the choice of some parameters such as receiver bandwidth was not provided, and the ACR protocol does not support quality assurance testing for advanced imaging techniques such as fat saturation or spectroscopy. Commercially available ACR accreditation phantoms for head (large phantom) and knee (small phantom) are shown in Figs. 10.2 and 10.3.

The ACR generated a head phantom that is a short, hollow cylinder made from acrylic and measures 148 mm (length) and 190 mm (diameter), the same size as a typical head, and a knee phantom that is 100 mm long by 100 mm in diameter. The head phantom is filled with a solution of 10 mM NiCl and 75 mM NaCl, and the knee phantom is filled with 10 mM NiCl and 0.45 % by weight aqueous NaCl to mimic the T1 and T2 of soft tissue (ACR MRI Quality Control Manual). Several quantitative tests can be made using the structures found inside each phantom. These tests are described in detail in the *Phantom Test Guidance for the ACR MRI*

Fig. 10.2 ACR large head phantom, 148 mm (length) \times 190 mm (diameter)

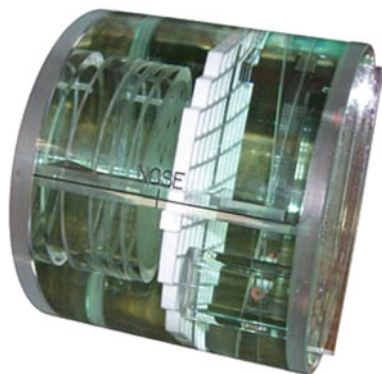
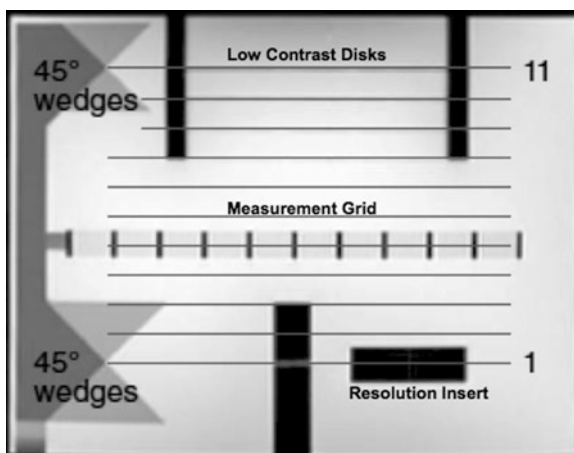


Fig. 10.3 ACR small knee phantom, 100 mm (length) \times 100 mm (diameter)



Fig. 10.4 A sagittal localizer of the phantom is displayed and shows two 45° wedges, 11 axial slice locations that intersect wedges at slices 1 and 11, four low-contrast disks (slices 8–11), a resolution insert (slice 1), and measurement grid (slice 5)



Accreditation Program (www.acr.org), and this section will only present the tests in general and will focus on phantom structures.

1. **Geometric Accuracy**—Geometric accuracy describes the degree of geometric distortion and refers to either displacement or scaling errors. The scaling error is determined by measuring the length (148 mm) and diameter (190 mm) on a localizer. A sagittal localizer of the phantom is displayed in Fig. 10.4 and shows two 45° wedges, 11 axial slice locations, low-contrast disks, the resolution insert, and measurement grid at slice 5. The wedges are 2 cm in length, crossing at 1 cm, and are separated by 100 mm. Length and diameter measurements are also obtained at slice 1. Figure 10.5 shows an image of the measurement grid that consists of a 10 \times 10 array of squares that is useful for measuring the diagonal lengths (190 mm).
2. **High-Contrast Spatial Resolution**—A spatial resolution insert is located in slice 1 and consists of small holes filled with water. This insert evaluates the ability of the MRI scanner to resolve small objects with sufficient contrast. Figure 10.6a shows an image of the resolution insert with three pairs of holes that includes an upper array and a lower array, not square but skewed. The arrays share a

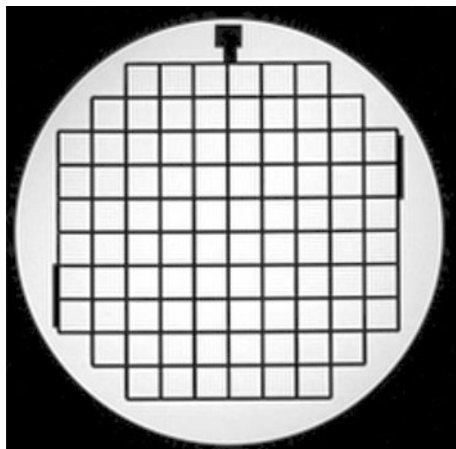


Fig. 10.5 An image of the 10 × 10 array comprising the measurement grid located in axial slice 5

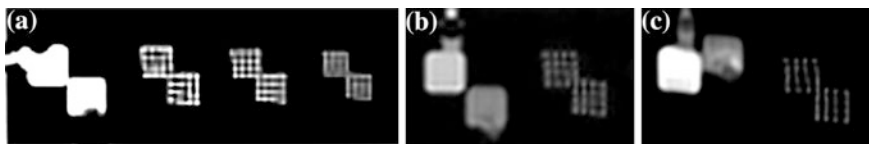


Fig. 10.6 **a** Resolution insert located in slice 1 of the ACR head phantom. **b** Chemical shift module with image acquired at BW = 32 kHz. The module is located to the *left* of the resolution insert. **c** Chemical shift insert with image acquired at BW = 2 kHz. The shift of the fat square in the A/P direction is clearly demonstrated

common hole located at the corner. The hole diameter reduces from 1.1 mm on the left pair to 0.9 mm on the right pair. The upper array has 4 rows of 4 holes that are separated by a length that is twice the hole diameter and is used to evaluate the left–right resolution. The lower array has 4 columns of 4 holes that are separated like the upper array but is used to evaluate the anterior–posterior resolution.

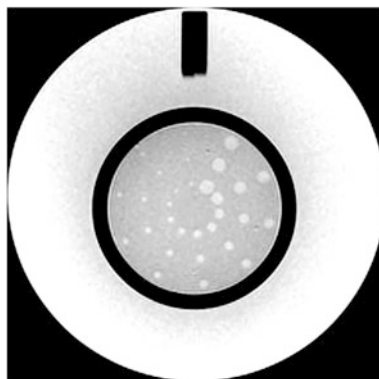
The two squares located on the left side of the resolution insert comprise a chemical shift module and provide a method to assess chemical shift and to estimate the receiver bandwidth (BW) setting. The upper square is filled with water and the lower square represents fat. Modifying the receiver BW will result in a shift in the frequency encode direction as shown in Fig. 10.6.

3. **Slice Thickness Accuracy**—There is a slice thickness insert located in slice 1 that contains 2 ramps that cross with a slope of 10:1 with respect to the plane of the slice. Therefore, the angle between the axial slice and the ramp is about 5.71°, $\tan^{-1}(1/10)$ and results in a signal that appears 10 times the thickness of the prescribed slice. The ramps are 1-mm-wide slots etched into a plastic block



Fig. 10.7 **a** Slice thickness accuracy displayed in slice 1, located directly above resolution insert. **b** Slice position accuracy is evaluated by measuring the difference in the vertical bar lengths at the *top* of the phantom

Fig. 10.8 Low-contrast detectability is evaluated by counting visible spokes in slices 8–11. Slice 11 is displayed with all spokes clearly visible



that are filled with the phantom solution since the slots are open to the phantom. Right to left tilt will be visible in the ramp signal and can help identify alignment issues (Fig. 10.7a).

4. Slice Position Accuracy—The 45° wedges shown in Fig. 10.7 are observed on slices 1 and 11 and are used to determine the slice position accuracy. Well-positioned slices will cross the wedges at the 45° intersection and will result in equally sized bars located at the top of slices 1 and 11 (Fig. 10.7b).
5. Low-Contrast Detectability—The ACR phantom has four low-contrast disks or plastic membranes located in slices 8 through 11. Each disk has a different thickness and, for the same slice thickness, a different partial volume effect. More or less volume averaging leads to a change in contrast. The contrast varies from 1.4 %, 2.5 %, 3.6 %, and 5.1 % from slice 8 to slice 11. Each disk consists of 10 spokes with 3 small holes per spoke—a total of 30 holes per slice (Fig. 10.8, slice 11). All holes in the same spoke have the same diameter but the diameter decreases, moving clockwise, from 7 to 1.5 mm.

Overall, the ACR MR phantom enables basic daily/routine QA testing by technologists and more advanced testing by medical physicists. Routine testing of the MR system provides the clinicians with important feedback and assurances of reproducibility. In addition, the ACR phantom is a useful troubleshooting tool for physicists, which also enables multiplatform, multivendor comparisons.

10.4 Alzheimer's Disease Neuroimaging Initiative Phantom

The Alzheimer's Disease Neuroimaging Initiative (ADNI) is a multicenter, multivendor MRI study focused on developing standard methods for acquiring and processing MRI data to reduce measurement uncertainty. An MRI phantom was designed to track and correct scanner performance such as post-processing gradient warping correction [5]. This imaging phantom was constructed by The Phantom Laboratory (Salem, NY) and is used to measure SNR, CNR or image contrast, and spatial distortion. The phantom, Magphan[®] Quantitative Imaging Phantom, consists of 165 spherical objects inside a 20-cm diameter, water-filled clear urethane shell. The spherical objects are 1.4-mm-thick polycarbonate shells filled with various concentrations of copper sulfate. For assessing spatial distortion, there are 158 fiducial spheres at 1.0 cm and two at 1.5-cm inner diameter (ID) filled with 0.82 g of copper sulfate pentahydrate per liter. A single 6-cm sphere filled with 0.82 g of copper sulfate pentahydrate per liter solution is used for testing SNR, and four 3-cm spheres with copper sulfate pentahydrate solutions ranging from 0.22 to 0.59 g/l are used for testing CNR or image contrast. For the 3-cm CNR spheres, the target T1 ranges from 900 to 450 ms (Magphan[®] EMR051 manual). Figure 10.9 shows the internal components of the ADNI phantom, and Fig. 10.10 provides an example of a typical distortion plot generated by the Image Owl (Salem, NY) MR Distortion Service. The photographs were provided by The Phantom Laboratory (Salem, NY).

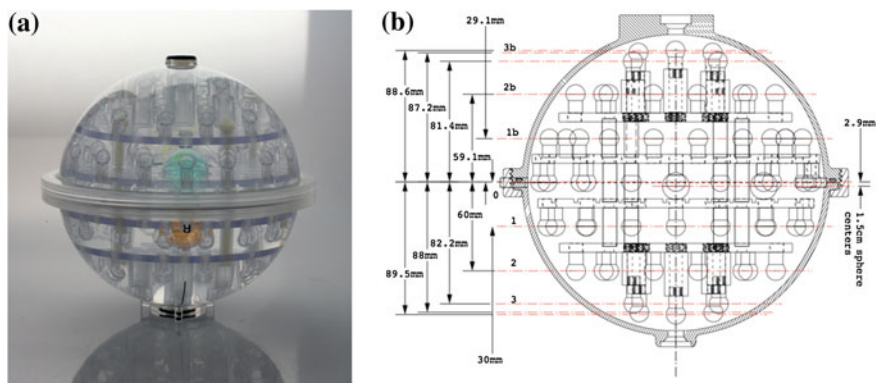


Fig. 10.9 *Left* A photograph of the Magphan[®] Quantitative Imaging Phantom. *Right* Design specifications for the imaging phantom. Photographs provided by the Phantom Laboratory (Salem, NY)



Fig. 10.10 An image distortion plot generated using Image Owl (Salem, NY) MR Distortion Service. The Magphan[®] Quantitative Imaging Phantom is scanned, and the DICOM image set is uploaded for processing. Actual and imaged sphere positions are evaluated to provide fourth-order distortion measurements

10.5 National Institute of Standards and Technology Phantom

The National Institute of Standards and Technology (NIST) has developed the first MRI phantom that is traceable to national standards [6]. The phantom shown in Fig. 10.11 is designed after the ADNI MRI phantom and ACR phantom and is nicknamed ‘Phannie’ [5]. Similar to the ADNI phantom, the NIST phantom was designed to mimic the human head and is a 20-cm water-filled spherical polycarbonate shell. There are five polyphenylene sulfide (PPS) plates connected with PPS rods. PPS was chosen due to its low water absorption and thermal expansion. The five coronal plates support 57 fiducial spheres, three arrays consisting of 14 elements each to assess T1/T2/proton density, and a resolution insert and slice profile wedges similar to the ACR phantom. The fiducial spheres are 1 cm in diameter and are located on a 4-cm three-dimensional grid. The fiducials are distributed on plates, located anterior to posterior, in groups of 5, 13, 26, 13, and 5. The T1/T2/proton density arrays are designed to be NIST traceable. The T1 array (green) is doped with various concentrations of NiCl₂ to provide a wide range of T1 values for a given field strength and temperature ($B = 1.5T$, $temp = 20\text{ }^{\circ}C$, $T1 = 22\text{--}2,000\text{ ms}$). Russek et al. [6] have evaluated the influence of inversion

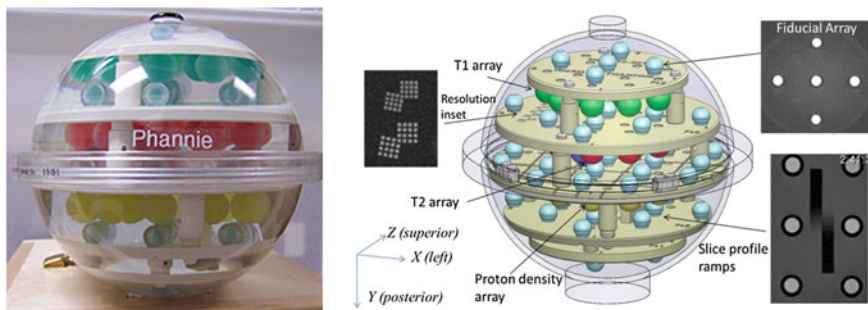


Fig. 10.11 *Left* Photograph of NIST Phannie phantom. *Right* A picture depicting the internal structure of the phantom, resolution insert, fiducial array, slice profile ramps, and location of relaxometry arrays (reproduced with permission) [6]

time, repetition time, and flip angle on measured T1 values. The T2 array (red) is doped with various concentrations of MnCl_2 to provide a wide range of T2 values for a given magnetic field strength and temperature ($B = 1.5\text{T}$, $\text{temp} = 20^\circ\text{C}$, $T_2 = 8\text{--}725\text{ ms}$). The proton density array (yellow) consists of various concentrations of deuterium and water. Eye decals are placed on the phantom shell to aid in phantom alignment in the scanner.

10.6 Magnetic Field Homogeneity Phantom

Magnetic field homogeneity throughout the field of view (FOV) is essential for high-quality, quantitative imaging. Suboptimal field homogeneity can result in poor fat and water saturation, geometric distortion, and signal loss. These effects are even more prevalent in ultra-fast imaging protocols, which are experiencing a surge in clinical applications. Initially, upon installation, the MRI is passively shimmed to eliminate field inhomogeneity introduced during shipment or from the local environment such as large iron structures near the MRI. Field homogeneity is generally described in terms of the variation in the Larmor frequency or magnetic field strength throughout the desired FOV and is expressed in ppm of the field-specific Larmor frequency or field strength. The shimming process typically results in field homogeneity of less than 0.5 ppm over a 30-cm diameter of spherical volume (DSV). Moreover, MRI vendors provide an active shim coil technique for adjusting the field homogeneity prior to each scan. Overall, field homogeneity phantoms should not perturb the field and should evaluate a clinically acceptable FOV.

Three methods for testing field homogeneity are currently supported. The ACR Magnetic Resonance Imaging Quality Control Manual, Medical Physicist's section, describes two methods: spectral peak and phase difference map. Both techniques require that a uniform, spherical phantom be placed at the isocenter of the magnet.

Fig. 10.12 A photograph of the magnetic field homogeneity phantom issued by General Electric Healthcare (Waukesha, WI) during installation of the MRI system



The manufacturer specifies the homogeneity over a DSV, and the phantom should at least cover the same DSV. The DSV may be specified up to 50 cm DSV, which can be problematic for phantom construction. This sizable, uniform phantom is typically provided by the vendor and is stored in multiple parts. Figure 10.12 shows a three-part uniformity phantom provided by General Electric (GE) that weighs over 120 lbs when fully assembled. Commercial vendors such as the Phantom Laboratory offer spherical phantoms to cover different DSVs. However, these phantoms do not include a filling solution. The homogeneity phantom is typically stored in the MRI room in order to reach thermal equilibrium. It should be noted that the two techniques referenced in the ACR manual are not always available on clinical MRI systems and vendor-specific techniques are generally used.

A third method described by Chen et al. [2] uses a bandwidth-difference technique to assess field homogeneity that is widely available. A two-piece spherical phantom was assembled using acrylic domes (25.4-cm outer diameter) and filled with distilled water doped with 0.01 mM copper sulfate to modify T1 and T2. An antibacterial agent, NaN_3 , was also added. Three acrylic plates, consisting of 108 holes (1.5 mm) drilled in each plate, were installed in the phantom. Each plate has six rows of six holes that cross at a 45° angle at the center, and the positional shift between holes is determined in two different bandwidth images. Chen et al. [2] demonstrated the difficulty in obtaining data from the spectral peak and phase shift methods.

10.7 Proton Relaxation Phantoms

MRI is widely appreciated for high-resolution, soft tissue imaging, but MRI is also quantitative and can measure several tissue-specific characteristics such as proton density and relaxation time. It should be noted that this information is not easily

converted to electron density for use with radiation treatment planning or attenuation correction for positron emission tomography imaging. Tissue-specific longitudinal relaxation time (T1) and transverse relaxation time (T2) depend on molecular motion and the local microenvironment. Therefore, tissue relaxation times that differ from normal or baseline levels may indicate inflammation, edema, microhemorrhage, or biological dysfunction. Relaxation times depend on field strength, temperature, and MRI sequence parameters. A typical sequence for measuring T1 is a 2D gradient recalled echo or spin-echo inversion recovery (GRE-IR or SE-IR) with 4 inversion times (TI) of 50, 400, 1,100, and 2,500 ms; repetition time (TR) of 2,550 ms; and echo time (TE) of 7–14 ms [7]. Measurement of T2 depends on TR settings, and Cheung et al. [8] recommends a fast radio-frequency enforced steady state (FRESS) spin echo for mapping T2 without TR effects. An optimized gold standard sequence for T2 mapping presented by Pell et al. [9] is a single spin echo, six echoes with TE between 30 and 230 ms, TR of 10 s, with a refocusing slice selection width equal to three times the excitation slice selection width. Table 10.1 shows typical T1 and T2 values for common tissues imaged at 1.5 and 3.0T measured in vitro immediately after excision [10]. It should be noted that these values are different from values published by others such as Akber et al. [11]. The reader is referred to work by Akber [11], Stanisz et al. [10], and Kato et al. [12] for recent reviews of tissue relaxation times. Overall, significant differences in measured T1 or T2 values can be expected due to differences in pulse sequence utilized.

For accurate and precise measurements of human T1 and T2 values, standardized pulse sequences are essential. Phantoms for quantifying T1 and T2 values should have relaxation times and dielectric properties that are representative of human tissues and are homogeneously distributed throughout the phantom. Phantoms have been constructed using aqueous solutions doped with paramagnetic ions such as $GdCl_3$, $MnCl_2$, $CuSO_4$, or $NiCl_2$. These phantoms provide a homogeneous solution in a rigid container but generally suffer from flow or motion artifacts. The ACR head phantom, for example, is filled with a solution of 10 mM NiCl and 75 mM NaCl and mimics general tissue relaxation times. Gelatin phantoms are also doped with paramagnetic ions but do not suffer from flow artifacts and are typically based on polyacrylamide, polyvinyl alcohol, gelatin, agarose, or agar. Recently, carrageenan was used as a gelling agent to stabilize the

Table 10.1 Typical T1 and T2 values for various tissues measured at 1.5 and 3T

Tissue	T1 values (ms)		T2 values (ms)	
	3T	1.5T	3T	1.5T
Blood	1,932 ± 85	1,441 ± 120	275 ± 50	290 ± 30
White matter	1,084 ± 45	884 ± 50	69 ± 3	72 ± 4
Gray matter	1,820 ± 114	1,124 ± 50	99 ± 7	95 ± 8
Muscle	1,412 ± 13	1,008 ± 20	50 ± 4	44 ± 6
Liver	812 ± 64	576 ± 30	42 ± 3	46 ± 6

phantom without influencing T1 or T2 values [12]. The proposed phantom also contains NaCl to modify conductivity, GdCl_3 to modify T1, agarose to modify T2, NaN_3 as an antiseptic, and distilled water. The proposed NIST phantom will also provide a traceable measurement of T1 and T2 values as discussed in earlier.

10.8 Diffusion Phantoms

Diffusion-weighted MRI provides a quantitative method to measure tissue-specific diffusion characteristics such as apparent diffusion coefficient (ADC), mean diffusivity (MD), and fractional anisotropy (FA) that can help clinicians and scientists better understand underlying brain architecture and microstructure. Diffusion tensor imaging (DTI) was introduced in the mid-1990s and provides a mathematical framework for detecting directional diffusion, both isotropic and anisotropic diffusion, for visualizing motion along tracts [13]. Diffusion techniques have been used extensively for imaging neurological dysfunction and disease such as inflammation, multiple sclerosis, traumatic axonal injury, cellular infiltration/activation, and connectivity studies [14–17].

Like other tissue-specific measurements, obtaining reliable and reproducible data is challenging and depends on several acquisition parameters such as field strength, field homogeneity, eddy current compensation, SNR, b-values, TR, TE, gradient-encoding scheme, and pulse sequence. Zhu et al. [18] conducted a multicenter study comparing DTI results and variability using a diffusion phantom and a single travelling human volunteer. A novel isotropic diffusion phantom was developed based on work by Tofts et al. [19] using three cyclic alkanes—cyclohexane, cycloheptane, and cyclooctane—contained in cylindrical polycarbonate containers to mimic white and gray matter [19]. Phantom and human data show significant inter-site differences in accuracy and precision of FA and MD values due to eddy current, gradient nonlinearity, and magnetic field inhomogeneity effects. It should also be noted that this study used the same vendor, MRI system, hardware, and software at each site. Currently, there is no gold standard technique to accurately compare measured diffusion parameters across platforms. Wang et al. [20] proposes to use the ACR head phantom with a standard spin-echo DTI, a single shot EPI readout, and a standard 30 direction gradient-encoding scheme for conducting quality assurance testing for diffusion imaging [20]. The ACR phantom is widely available, has internal structures to help minimize fluid motion, and is already used for routine QC. However, the ACR phantom does not have structured anisotropy and does not match diffusivities typically observed in human neuroimaging. These limitations could be overcome by developing a head phantom consisting of internal structures with varying diffusivities and anisotropy. In order to calibrate diffusion studies, as previously mentioned, Tofts et al. [19] proposed using alkanes for developing a phantom to mimic human tissue. However, Pierpaoli et al. [21] proposes a less toxic, less flammable solution of polyvinylpyrrolidone (PVP) as a potential isotropic phantom to assess diffusion MRI. The measured average diffusivity was independent

of diffusion time, a linear function of PVP concentration up to 50 %, and had a 2 % coefficient of variation for repeated measurements over a 15-month period. Overall, PVP has desirable properties for producing calibration phantoms to assess diffusion protocols across various platforms.

Mimicking biological anisotropic diffusion is not a simple achievement since physiological diffusion depends on cell infiltration, tract density and direction, fiber diameter, and background homogeneity. Several studies have developed and tested anisotropic diffusion phantoms, which have generally depended on embedding fibers in a homogeneous background [22–27]. These fibers vary in thickness, group density, direction, and diffusion characteristics. Phantoms were developed out of Micro-Dyneema[®] filled with saline doped with Gd, polyamide fibers wrapped around acrylic glass and glass capillaries filled with water [22, 24, 27]. Lorenz et al. [23] used a standard DW EPI sequence with 61 diffusion encoding directions and b-factors of 0 and 1,000 s/mm² to compare four different fibers with various thicknesses and fiber packing density: hemp (H), rayon (R), linen (L), and Dyneema[®] (Dy). Dy fibers provided higher FA (0.68), improved homogeneity, and minimal susceptibility artifacts. Ebrahimi et al. [26] presented a new phantom that utilized microfabrication lithography to generate channels to match neuronal structure. The phantom made of polydimethylsiloxane (PDMS), a silicon-based polymer, consisted of eight layers comprised of 100 channels 50 μm wide by 250 μm deep. The channels are filled with water to simulate fibers. However, only a few channels were tracked fully along the phantom axis due to various undesirable effects. In similar fashion, Samuel et al. constructed a 1.5 \times 1.5 cm \times 0.3 mm PDMS phantom comprised of thirty 10- μm -thick spin-casted layers with curved and straight microchannels measuring 5 μm in width and 8.7 μm (curved) or 3.6 μm (straight) spacing [28]. The water-filled MRI phantom was imaged on a Bruker Biospec 7T MRI (Bruker, Inc., Billerica, MA) using a standard 3D diffusion-weighted SE sequence with b-value of 800 s/mm². DTI showed less anisotropic diffusion than expected and quantitative results were not provided.

Unlike white matter, gray matter is comprised of randomly aligned axons and dendrites and has multiple cell types. Even though axons demonstrate anisotropic diffusion, the random alignment of axons in gray matter result in voxel mixing and isotropic diffusion measured on a macroscopic level. A double-pulsed gradient spin-echo (d-PGSE) sequence presented by Komlosh et al. [29] and Shemesh et al. [30] has the ability to measure net displacements of spins during multiple diffusion periods, which may convey details of small structures, below the voxel resolution. Komlosh et al. [31] evaluated this d-PGSE sequence with a novel gray matter phantom that is macroscopically isotropic but microscopically anisotropic. The gray matter phantom is a collection of randomly oriented 0.5 mm long fused silica glass tubes with an ID = 20 μm and OD = 90 μm (Polymicro Technologies). The glass tubes were filled with pure water by condensation of water vapor. The d-PGSE accurately measured diffusion coefficients for free diffusion approximated by Gaussian displacements, using short diffusion times (Δ), but do not accurately measure restricted diffusion. Komlosh et al. [27] describe another novel water-filled phantom consisting of two lead glass capillary array (GCA) wafers (13 mm OD

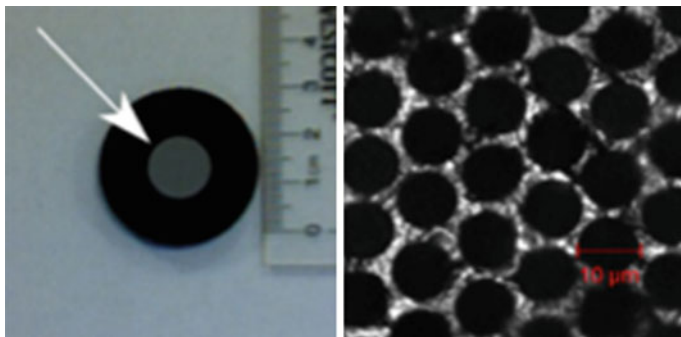


Fig. 10.13 *Left* A photograph of the 13-mm glass capillary array phantom proposed by Komlosh et al. *Right* A confocal transmission image of the microcapillaries

each) with microcapillaries of 10 μm pore diameter and 500 μm thickness. Unlike the gray matter phantom, this phantom is coherently organized and the GCA wafers are macroscopically homogeneous. Figure 10.13 shows a photograph of the 13-mm disk and confocal transmission image of the microcapillaries. Measurements of the pore diameter using the d-PGSE sequence were within 5 % of expected diameter [29, 30]. These results are partially due to the phantom having closely packed fiber arrays, 12 μm center-to-center, which provides increased pore volume and, as a result, high MR signal that is essential for diffusion MRI measurements. The GCA wafers are available in various pore sizes and diameters and can be stacked together to form a more heterogeneous diffusion phantom. The GCA phantom can be used to calibrate and validate MRI measurements of pore diameter and diameter distribution.

Overall, to improve the quality of multicenter, multivendor, or multisystem diffusion MRI studies, it is essential to develop and widely distribute a gold standard diffusion phantom that can calibrate measurements associated with free and restrained diffusion as well as small pore diameter measurements.

10.9 Temperature Considerations

The temperature of the sample directly influences the parameters measured from proton-weighted, T1-weighted, T2-weighted, diffusion and spectroscopy protocols. This temperature dependence can negatively affect quantitative measurements but can also provide useful clinical information regarding tissue temperature. Several thermal energy deposition techniques such as laser-induced thermotherapy, high-intensity focused ultrasound, and radiofrequency (RF) ablation or microwave heating can be used to noninvasively sensitize or ablate tumors [32]. The ability to accurately deliver a known temperature and to confirm delivery of desired treatment is paramount for clinical effectiveness. MRI is a useful tool

for noninvasively guiding thermal treatments by producing near real-time temperature maps or thermometry imaging [33]. Three methods for MR thermometry have been widely studied: T1 mapping, Brownian motion and diffusion, and chemical shift (CS) or proton resonance frequency (PRF) [34].

Since magnetic susceptibility is inversely proportional to temperature and the equilibrium magnetization is proportional to susceptibility, the signal obtained in a proton-weighted MR sequence decreases as the temperature increases if properly controlled for perfusion effects in vivo [34, 35]. This temperature dependence is small, approximately $0.3 \text{ \%}/^\circ\text{C}$ and, as a result, proton-weighted MR thermometry requires high SNR and long repetition times. For T1-weighted imaging, the spin–lattice interaction prolongs the relaxation time, or recovery of longitudinal magnetization, as temperature increases. Since the spin–lattice interaction varies by tissue, the temperature dependence also varies by tissue. For example, the temperature dependence in the liver is approximately $1\text{--}2 \text{ \%}/^\circ\text{C}$ and $0.97 \text{ \%}/^\circ\text{C}$ for fat [36–39]. This is an important consideration for quantitative T1 mapping for MR thermometry. Overall, the T1-weighted signal decreases as temperature increases due to the previously discussed reduction in equilibrium magnetization and increased T1 times. Kraft et al. [40] investigated the temperature dependence of T1 on phantoms comprised of gel doped with paramagnetic copper (Cu^{+2}), manganese (Mn^{+2}), and nickel (Ni^{+2}) ions. The T1 values at 100 MHz for Ni^{+2} -doped agar gels demonstrated insignificant temperature dependence, whereas Cu^{+2} - and Mn^{+2} -doped gels showed a significant temperature dependence ($10 \text{ ms}/^\circ\text{C}$) that also varied with ion concentration levels [40, 41]. This is an important factor when selecting a phantom filling solution such as NiCl. Unlike T1 measurements, T2 values determined using a T2-weighted protocol show little temperature dependence or dependence on ion concentration. This is beneficial information for phantom construction, but it is also indicates that T2 mapping is not a viable technique for MR thermometry.

Water diffusion can also serve as a thermal indicator. Molecular diffusion is based on thermal Brownian motion, and there is a direct relationship between diffusion coefficients and temperature based on the Stokes–Einstein relationship [42]. An initial study by Delannoy et al. [43] shows that the diffusion coefficient increases $2.4 \text{ \%}/^\circ\text{C}$ for a polyacrylamide gel phantom doped with 5 mM of copper sulfate using a 1.5T MRI, whereas Le Bihan et al. [44] measured $2.8 \text{ \%}/^\circ\text{C}$ at 0.5T. Results in phantom show good accuracy, subcentimeter resolution, and relatively fast acquisition times [45]. In vivo diffusion measurements clearly show an increase in contrast related signal between heated and unheated tissue as temperature increased in New Zealand rabbit brains [46]. In order to identify appropriate phantom filling solutions for diffusion imaging, Tofts et al. [19] obtained diffusion coefficients for 15 liquids, alkanes, over a temperature range of $15\text{--}30 \text{ }^\circ\text{C}$. Results indicated that n-tridecane has a diffusion coefficient similar to normal white matter with reasonable T1 and T2 values. Overall, diffusion techniques are more sensitive to temperature effects when compared to relaxometry but diffusion-related signal variations are difficult to interpret due to competing physiological factors such as tissue coagulation as temperature increases.

Due to the complexities associated with diffusion-based thermometry, researchers have evaluated the proton chemical shift or resonant frequency drift, which depends on temperature. The temperature dependence of the proton resonance frequency (PRF) is a function of the screening constant and the magnetic susceptibility constant [47, 48]. The fraction and state of hydrogen bonds in water vary as a function of temperature. As a result, there is less effective molecular screening, a drift in the local magnetic field, and a related shift in the PRF. In addition, as previously discussed, the equilibrium magnetization is proportional to the local magnetic susceptibility, which is inversely proportional to temperature. In attempt to characterize these two factors, using pure water in gel and porcine muscle and fat tissue, De [49] showed that susceptibility effects were negligible for muscle but dominate for fat tissue and that the screening constant is the same for water and muscle tissue. Similarly, Ishihara et al. [50] showed that the water proton chemical shift for pure water (-0.01 ppm/ $^{\circ}\text{C}$) is similar to the shift for different tissues measured in vitro, thereby eliminating the requirement for individual tissue calibration curves. Bertsch et al. [41] compared temperature maps generated based on chemical shift and T1 relaxation for homogeneous gel and heterogeneous muscle phantoms. The chemical shift method proved to be more accurate for homogeneous media but less accurate for fat containing media. In general, susceptibility effects can be ignored in muscle tissue but will lead to errors and reduce measurement accuracy in fat tissue. This is an important consideration for thermometry measurements and calibration using dedicated tissue-specific phantoms. Olsrud et al. [51] investigated the PRF shift using interstitial laser thermotherapy in several tissue-like phantoms such as 2 % agarose gel, pure water, porcine liver, and white of eggs. A mostly linear relationship was identified for PRF shift and temperature change in agarose gel. The reported temperature dependence for agarose gel was 0.0085 ppm/ $^{\circ}\text{C}$, which is slightly less than pure water dependence of 0.01 ppm/ $^{\circ}\text{C}$. However, successful calibration ensured that gel and water provided the same results. This phantom is applicable over a wide temperature range and can be configured in several geometries. Because PRF provides accurate temperature measurements over a wide temperature range, varies linearly with temperature, and is independent of tissue changes, PRF is a highly suitable technique for thermometry.

References

1. Yoder, D. A., et al. (2004). MRI simulator with object-specific field map calculations. *Magnetic Resonance Imaging*, 22(3), 315–328.
2. Chen, H.-H., et al. (2006). Routine testing of magnetic field homogeneity on clinical MRI systems. *Medical Physics*, 33(11), 4299–4306.
3. Jackson, E. et al. (2010). *Acceptance testing and quality assurance procedures for magnetic resonance imaging facilities*. In M. J. Bronskill et al. (Eds.), College park: American association of physicists in medicine.

4. Ihalainen, T.M. et al. (2011). MRI quality assurance using the ACR phantom in a multi-unit imaging center. *Acta oncologica*, 50(6), pp. 966–972, (Stockholm, Sweden).
5. Gunter, J. L., et al. (2009). Measurement of MRI scanner performance with the ADNI phantom. *Medical Physics*, 36(6), 2193–2205.
6. Russek, S. et al. (2012). Characterization of NIST/ISMRM MRI system phantom. *Proc. Intl. Soc. Mag. Reson. Med.*, p. 2456.
7. Barral, J. K., et al. (2010). A robust methodology for in vivo T1 mapping. *Magnetic resonance in medicine : Official Journal of the Society of Magnetic Resonance in Medicine/ Society of Magnetic Resonance in Medicine*, 64(4), 1057–1067.
8. Cheung, J. S., et al. (2012). Fast radio-frequency enforced steady state (FRESS) spin echo MRI for quantitative T2 mapping: Minimizing the apparent repetition time (TR) dependence for fast T2 measurement. *NMR in Biomedicine*, 25(2), 189–194.
9. Pell, G. S., et al. (2006). Optimized clinical T2 relaxometry with a standard CPMG sequence. *Journal of Magnetic Resonance Imaging : JMRI*, 23(2), 248–252.
10. Stanisiz, G. J., et al. (2005). T1, T2 relaxation and magnetization transfer in tissue at 3T. *Magnetic Resonance in Medicine : Official journal of the Society of Magnetic Resonance in Medicine/Society of Magnetic Resonance in Medicine*, 54(3), 507–512.
11. Akber, S. F. (2008). Water proton relaxation times of pathological tissues. *Physiological Chemistry and Physics and Medical NMR*, 40, 1–42.
12. Kato, H. et al. (2005). Composition of MRI phantom equivalent to human tissues. *Medical Physics*, 32(10), pp. 3199–3208. Available at: <http://eutils.ncbi.nlm.nih.gov/entrez/eutils/elink.fcgi?dbfrom=pubmed&id=16279073&retmode=ref&cmd=prlinks&holding=uwisclib&otool=uwisclib>.
13. Basser, P. J., Mattiello, J., & LeBihan, D. (1994). MR diffusion tensor spectroscopy and imaging. *Biophysical Journal*, 66(1), 259–267.
14. Sundgren, P. C., et al. (2004). Diffusion tensor imaging of the brain: Review of clinical applications. *Neuroradiology*, 46(5), 339–350. Springer.
15. Le Bihan, D. (2003). Looking into the functional architecture of the brain with diffusion MRI. *Nature Reviews Neuroscience*, 4(6), 469–480.
16. Beaulieu, C. (2002). The basis of anisotropic water diffusion in the nervous system—a technical review. *NMR in Biomedicine*, 15(7–8), 435–455.
17. Van Boven, R. W., et al. (2009). Advances in neuroimaging of traumatic brain injury and posttraumatic stress disorder. *The Journal of Rehabilitation Research and Development*, 46(6), 717.
18. Zhu, T., et al. (2011). Quantification of accuracy and precision of multi-center DTI measurements: a diffusion phantom and human brain study. *NeuroImage*, 56(3), 1398–1411.
19. Tofts, P. S., et al. (2000). Test liquids for quantitative MRI measurements of self-diffusion coefficient in vivo. *Magnetic Resonance in Medicine : Official journal of the Society of Magnetic Resonance in Medicine/Society of Magnetic Resonance in Medicine*, 43(3), 368–374.
20. Wang, Z. J., et al. (2011). A quality assurance protocol for diffusion tensor imaging using the head phantom from American college of radiology. *Medical Physics*, 38(7), 4415–4421.
21. Pierpaoli, C. et al. (2009). Polyvinylpyrrolidone (PVP) water solutions as isotropic phantoms for diffusion MRI studies. In *ISMRM 17th Annual Meeting and Exhibition, Honolulu, Hawai'i*. April 18–24, p. 1414.
22. Fieremans, E. et al. (2005). A flexible hardware phantom for validation of diffusion imaging sequences. In *Proc. Intl. Soc. Mag. Reson. Med.* 13, p. 1301.
23. Lorenz, R., Kreher, B.W. & Hennig, J. (2006). Anisotropic Fiber Phantom for DTI validation on a clinical scanner. *Proceedings of ISMRM 14th Scientific Meeting. Seattle, USA*.
24. Laun, F.B. et al. (2007). Investigation of a DTI-phantom with properties similar to in vivo neuronal tissue. *Proc Intl Mag Reson Med Berlin*, 15, p.1526.
25. Sadleir, R. J., et al. (2009). A controllably anisotropic conductivity or diffusion phantom constructed from isotropic layers. *Annals of Biomedical Engineering*, 37(12), 2522–2531.

26. Ebrahimi, B. et al., (2010). A microfabricated phantom for diffusion tensor imaging. *SPIE Medical*, pp.76261Q–76261Q–8.
27. Komlosh, M. E., et al. (2011). Pore diameter mapping using double pulsed-field gradient MRI and its validation using a novel glass capillary array phantom. *Journal of Magnetic Resonance*, 208(1), 128–135.
28. Samuel, R., et al. (2011). Microfluidic laminate-based phantom for diffusion tensor-magnetic resonance imaging (DT-MRI). *Journal of Micromechanics and Microengineering: Structures, Devices, and Systems*, 21(9), 950271–9502711.
29. Komlosh, M. E., et al. (2008). Observation of microscopic diffusion anisotropy in the spinal cord using double-pulsed gradient spin echo MRI. *Magnetic Resonance in Medicine : Official journal of the Society of Magnetic Resonance in Medicine/Society of Magnetic Resonance in Medicine*, 59(4), 803–809.
30. Shemesh, N., et al. (2010). From single-pulsed field gradient to double-pulsed field gradient MR: Gleaning new microstructural information and developing new forms of contrast in MRI. *NMR in Biomedicine*, 23(7), 757–780.
31. Komlosh, M. E., et al. (2007). Detection of microscopic anisotropy in gray matter and in a novel tissue phantom using double Pulsed Gradient Spin Echo MR. *Journal of magnetic resonance*, 189(1), 38–45. (San Diego, Calif.: 1997).
32. Bozzini, G., et al. (2013). Focal therapy of prostate cancer: Energies and procedures. *Urologic oncology*, 31(2), 155–167.
33. Turner, R. & Streicher, M. (2012). Measuring temperature using MRI: a powerful and versatile technique. *New York: Magma*, 25(1), pp. 1–3.
34. Rieke, V., & Butts Pauly, K. (2008). MR thermometry. *Journal of Magnetic Resonance Imaging*, 27(2), 376–390.
35. Young, I. R., et al. (1994). Further observations on the measurement of tissue T1 to monitor temperature in vivo by MRI. *Magnetic Resonance in Medicine*, 31(3), 342–345.
36. Bottomley, P. A. (1984). A review of normal tissue hydrogen NMR relaxation times and relaxation mechanisms from 1 to 100 MHz: Dependence on tissue type, NMR frequency, temperature, species, excision, and age. *Medical Physics*, 11(4), 425.
37. Bottomley, P. A. (1987). A review of 1H nuclear magnetic resonance relaxation in pathology: Are T1 and T2 diagnostic? *Medical Physics*, 14(1), 1.
38. Matsumoto, R., et al. (1994). Tissue temperature monitoring for thermal interventional therapy: Comparison of T1-weighted MR sequences. *Journal of Magnetic Resonance Imaging*, 4(1), 65–70.
39. Hynynen, K., et al. (2000). Temperature monitoring in fat with MRI. *Magnetic Resonance in Medicine : Official Journal of the Society of Magnetic Resonance in Medicine/Society of Magnetic Resonance in Medicine*, 43(6), 901–904.
40. Kraft, K. A., et al. (1987). An MRI phantom material for quantitative relaxometry. *Magnetic Resonance in Medicine*, 5(6), 555–562.
41. Bertsch, F., et al. (1998). Non-invasive temperature mapping using MRI: Comparison of two methods based on chemical shift and T1-relaxation. *Magnetic Resonance Imaging*, 16(4), 393–403.
42. Einstein, A. (1905). On the movement of small particles suspended in stationary liquids required by the molecular-kinetic theory of heat. *Annalen der Physik*, 17, 549.
43. Delannoy, J., et al. (1991). Noninvasive temperature imaging using diffusion MRI. *Magnetic Resonance in Medicine*, 19(2), 333–339.
44. Le Bihan, D., Delannoy, J., & Levin, R. L. (1989). Temperature mapping with MR imaging of molecular diffusion: application to hyperthermia. *Radiology*, 171(3), 853–857.
45. Zhang, Y., et al. (1992). On the accuracy of noninvasive thermometry using molecular diffusion magnetic resonance imaging. *International journal of hyperthermia*, 8(2), 263–274.
46. Bleier, A. R., et al. (1991). Real-time magnetic resonance imaging of laser heat deposition in tissue. *Magnetic Resonance in Medicine : Official journal of the Society of Magnetic Resonance in Medicine/Society of Magnetic Resonance in Medicine*, 21(1), 132–137.

47. Schneider, W. G., Bernstein, H. J., & Pople, J. A. (1958). Proton magnetic resonance chemical shift of free (gaseous) and associated (liquid) hydride molecules. *The Journal of Chemical Physics*, 28(4), 601.
48. Hindman, J. C. (1966). Proton resonance shift of water in the gas and liquid states. *The Journal of Chemical Physics*, 44(12), 4582–4592.
49. Poorter, J. D. (1995). Noninvasive MRI thermometry with the proton resonance frequency method: Study of susceptibility effects. *Magnetic Resonance in Medicine*, 34(3), 359–367.
50. Ishihara, Y., et al. (1995). A precise and fast temperature mapping using water proton chemical shift. *Magnetic Resonance in Medicine*, 34(6), 814–823.
51. Olsrud, J., et al. (1999). MRI thermometry in phantoms by use of the proton resonance frequency shift method: Application to interstitial laser thermotherapy. *Physics in Medicine and Biology*, 43(9), 2597–2613.
52. American College of Radiology. *Site Scanning Instructions for Use of the MR Phantom for the ACR*, Reston: The American College of Radiology. Available at: <http://www.acr.org>.

Chapter 11

Nuclear Medicine and PET Phantoms

Mark T. Madsen and John J. Sunderland

11.1 Introduction

Nuclear medicine is a medical field where radioactive materials are administered to patients to either obtain diagnostic information or deliver a therapeutic radiation dose. Although the therapeutic application of nuclear medicine is primarily limited to the treatment for hyperthyroid conditions and several cancers (e.g., thyroid cancer, lymphoma, and bone metastases palliation), there are diagnostic nuclear medicine procedures for virtually every tissue and organ system of the body. Table 11.1 summarizes common nuclear medicine procedures.

The diagnostic information obtained from a nuclear medicine procedure is contained in the images of the distribution of radiolabeled compounds (radiopharmaceuticals) that emit gamma rays or other high-energy photons (such as annihilation radiation) that are transmitted through body tissues and externally detected. For some procedures such as thyroid uptake determination, imaging is not required, but most nuclear medicine studies generate images of the internal distribution of the radiopharmaceuticals. These images may be planar projections acquired with a gamma camera or tomographic images from either single-photon emission computed tomography (SPECT) or positron emission tomography (PET) systems. Tomographic images require images from multiple projection angles and a mathematical algorithm that operates on the projections to generate transverse tomographic slices. SPECT projections are typically acquired from one or more gamma cameras that collect images as they rotate around the patient. With PET imaging, only radionuclides that decay by positron emission and generate annihilation radiation are used. The simultaneous detection of the annihilation photons

M. T. Madsen (✉) · J. J. Sunderland
Department of Radiology, The University of Iowa, Iowa, US
e-mail: mark-madsen@uiowa.edu

Table 11.1 Example nuclear medicine procedures

Procedures	Indication	Radiopharmaceutical
Brain perfusion	Stroke and epilepsy	Tc-99 m HMPAO, Tc-99 m ECD, F-18 FDG*(PET)
Thyroid scan	Graves disease, thyroid cancer	I-123 NaI, Tc-99 m pertechnetate
Bone scintigraphy	Metastatic cancer, hairline fractures	Tc-99 m MDP
Myocardial perfusion	Coronary artery disease	Tc-99 m sestamibi, Tc- 99 m tetrofosmin, Tl- 201 chloride, Rb-82 chloride (PET)
Lung ventilation/perfusion	Pulmonary embolism	Tc-99 m DTPA aerosol, Tc-99 m MAAA
Hepatobiliary function	Acute cholecystitis, common bile duct obstruction	Tc-99 m mebrofenin
Renal function	Renal obstruction, acute tubular necrosis	Tc-99 m MAG3, Tc- 99 m DTPA
GI bleeding	Identify sites of active bleeding	Tc-99 m labeled red blood cells
Gastric emptying	Gastroparesis, gastroesophageal reflux	Tc-99 m sulfur colloid
Lymphoscintigraphy	Sentinel node location for melanoma and breast cancer	Tc-99 m sulfur colloid
PET whole-body Imaging	Lung, colon, breast, thyroid cancer	F-18 FDG* *(fluorodeoxyglucose)

in opposed detectors provides an elegant and (compared to gamma cameras) highly sensitive way to collect projection data.

Compared with other imaging modalities, nuclear medicine studies have higher statistical fluctuations (image noise) and poorer spatial resolution. Ultimately, this is the result of relatively low flux of gamma rays emanating from the patient and the difficulty in creating projection images with the high-energy photons associated with gamma rays. Because nuclear medicine studies require the administration of radioactive materials to patients (most often by intravenous injection), the patients are irradiated until all the radioactivities are decayed and cleared from the body. This along with other constraints set by the imaging instrumentation limit how much radioactivity can be administered and the statistical quality of the resulting images. To optimize the image quality, a great deal of effort has been devoted to using all the available gamma rays efficiently and to make sure that the imaging systems are in proper working order. These actions require a way of simulating a variety of radionuclide distributions. This is accomplished by using phantoms. Phantoms may be physical devices that contain radioactive solutions that are imaged with the nuclear medicine or PET instruments or they may be computer based models that generate image data that can be processed as if it came from actual imaging devices.

Phantoms are used for many applications in nuclear medicine. The common applications include the performance evaluation of imaging and detecting systems, the investigation of reconstruction algorithms, and the estimation of radiation dose from internally distributed radionuclides. A wide variety of physical and mathematical phantoms have been used and these will be discussed in detail in the following sections.

11.2 Mathematical Phantoms

Although physical phantoms play an important role in nuclear medicine and PET imaging, they are not especially useful for simulating radioactivity concentrations of complicated, realistic distributions. In many situations, the most useful information is gained from computer simulations where a more or less realistic anthropomorphic distribution is generated and used to either estimate radiation dose or to model the imaging process for evaluating reconstruction algorithms or other image processing techniques. Mathematical phantoms of increasing complexity have been developed for a number of nuclear medicine applications.

11.2.1 *Internal Radiation Dosimetry*

The first application of mathematical phantoms in nuclear medicine was for internal radiation dosimetry. The radiation dose from an internally distributed radionuclide depends on the size and geometry of the distribution. Although energetic charged particles such as electrons or positrons are absorbed within a relatively short range (~ 5 mm/MeV), gamma rays are more penetrating. The absorbed fraction characterizes how much of the gamma ray energy is locally absorbed and initial attempts at internal dosimetry began with the determination of absorbed fractions of gamma rays as a function of energy for different sized spheres and ellipsoids [1]. It was realized early on that this information had limited use in predicting organ doses where the actual geometry of tissues and organs was not well modeled by this simplistic assumption. Work began within the Society of Nuclear Medicine's Medical Internal Radiation Dose Committee (MIRD) to construct a stylized (equation-based) mathematical phantom of the entire body where a wider range of geometric shapes were used to simulate internal organs [2, 3]. Because the location of each of these geometric organs could accurately be defined, Monte Carlo calculations of absorbed fractions within and between organs of the MIRD phantom could be made leading to a rational and consistent approach for estimating internal radiation doses. A cross-sectional image of the MIRD phantom is shown in Fig. 11.1. The MIRD phantom has also been used by other investigators for estimating the dose from CT exposures.

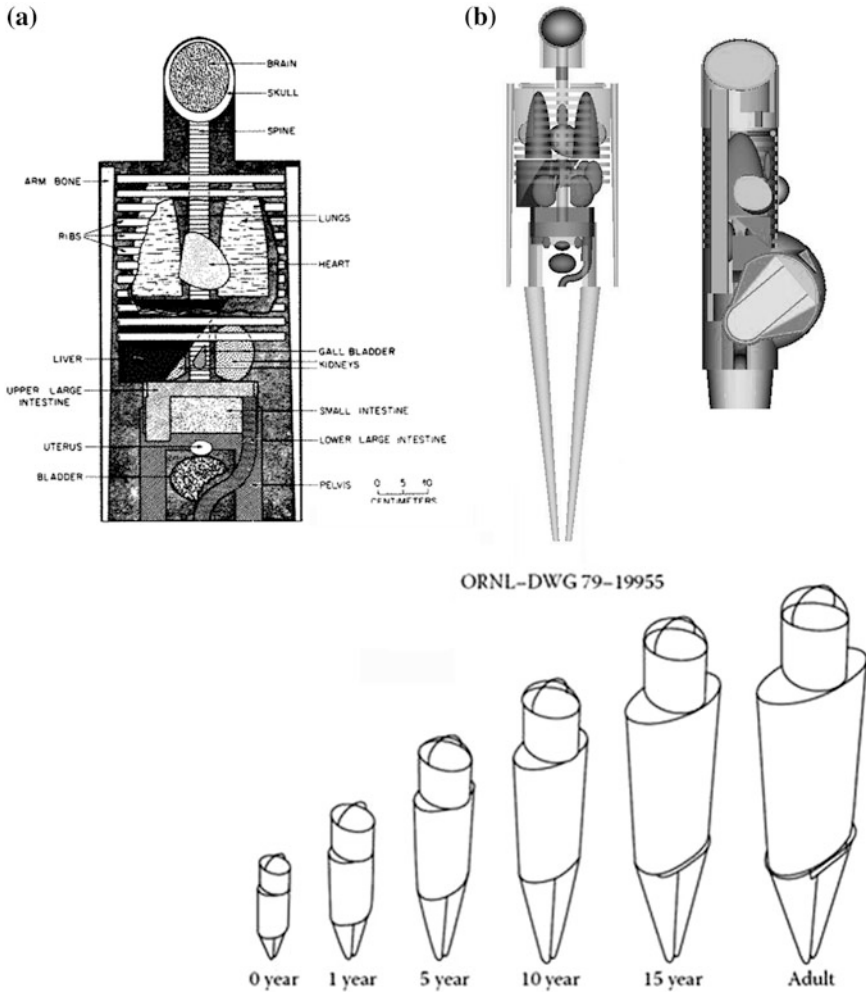


Fig. 11.1 Stylized mathematical phantom. Body and organs are represented by geometric shapes for ease in calculations. **a** MIRD phantom. **b** Oak Ridge Laboratory mathematical phantoms for internal dosimetry of children, females, and pregnant females

One shortcoming associated with the MIRD phantom is that it represents a standard-sized 70 kg male although both male and female gonads were included. Additional phantoms using the same geometric approach (and retaining both male and female organs) were introduced in 1987 with representations for newborn, 1, 5, 10, and 15 years old (Fig. 11.1) [4]. Another addition to this family of phantoms was made in 1995 with the inclusion of 4 adult female representations comprised of 1 standard female and 3 pregnant females at different gestational stages [5]. A number of specific modifications to the MIRD phantom have been made which include customized head and brain models, major airways, the peritoneal cavity,

the prostate gland, and the gastrointestinal and genitouretal tracts. There is a commercial product (Body Builder, White Rock Science) that allows the user to construct a mathematical phantom of any age by interpolating between the age models of Cristy and Eckerman.

Each of the phantom models discussed above are equation based. Another approach uses voxelized information from a whole-body CT or MRI scan where there have been expert segmentation and identification of each of the tissues and organs [6]. The ICRP has adopted this approach for its reference dose phantoms. The reference phantoms were constructed by modifying GOLEM and LAURA which are male and female voxel models. The organ masses of both models were adjusted to match the ICRP adult reference male and reference female without sacrificing the realism.

11.2.2 Image Reconstruction and Processing

The phantoms used for internal radiation dosimetry have the appropriate design for estimating approximate radiation doses for nuclear medicine procedures. Because of the wide variation in individual organ sizes and shapes as well as the specific pharmacokinetics, and the resulting uncertainties, little is to be gained by striving for more realistic representation. However, when it comes to simulating internal distributions for evaluation of reconstruction algorithms or other image processing techniques, more realism is a necessity. The sharp boundaries associated with the geometric organ representations do not reflect reality and would adversely affect attempts to optimize algorithms. This is a limitation associated with many physical phantoms as well.

There is a need to have mathematical phantoms where a realistic radiopharmaceutical distribution is accurately known so that the efficacy of different reconstruction, correction, or analysis algorithms can be objectively evaluated. Simple stylized phantom representations like the checkerboard and Shepp–Logan phantom have been used for emission tomography evaluations, but those have been primarily used to demonstrate feasibility of an approach. Since any accurate simulation of emission tomography requires a co-registered attenuation map in addition to the radiopharmaceutical distribution, tissue attenuation must be included in any truly mathematical phantom used for nuclear medicine applications. Thus, anthropomorphic phantoms designed for the purpose of simulating realistic imaging situations must be capable of generating both emission and transmission data sets.

The first software package that provided the dual emission and transmission capability was the mathematical cardiac torso (MCAT) phantom [7]. The MCAT phantom was a more sophisticated version of the MIRD phantom where basic geometric primitives were used to construct the anatomy of the thorax. These building block objects were overlapped and intersected to provide improved realism while maintaining the mathematical capability to assign radioactivity concentrations and attenuation factors to the geometric organs (Fig. 11.2). The

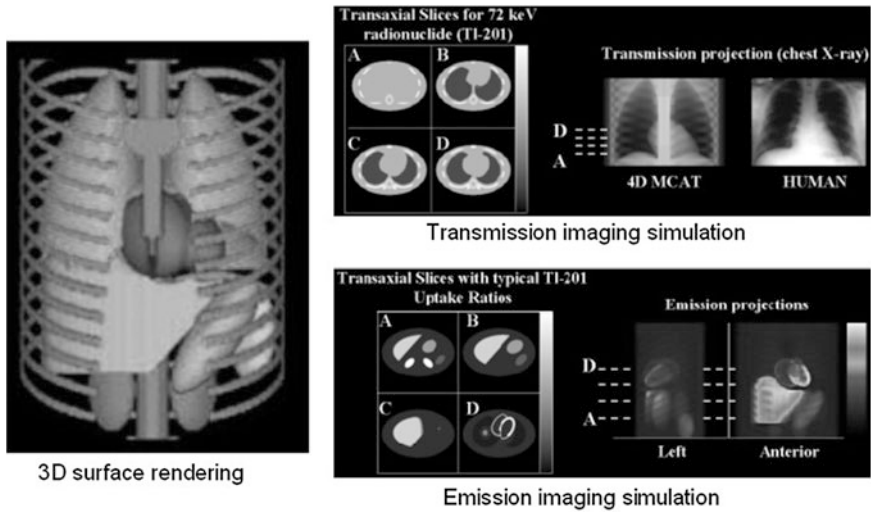


Fig. 11.2 The MCAT phantom developed at the University of North Carolina provides more realistic organ geometry while retaining the equation-based approach

flexibility of the phantom was further extended by adding cardiac and respiratory motion functionality.

Although the MCAT phantom was used in many investigations to improve reconstruction algorithms for myocardial perfusion imaging, the reliance on geometric shapes limited the realism with which human anatomy was portrayed. A new approach replaced the geometric primitives with non-uniform rational B-splines (NURBS), which are routinely used in computer animation graphics [8]. NURBS have a large amount of flexibility that not only can accommodate a wide variety of shapes, but also allow those shapes to be easily altered through the manipulation of a small number of control points. To obtain a realistic organ shape, a three-dimensional NURBS surface is fitted to the manually segmented CT image of the desired organ. This has been accomplished for all the major organs in the body to yield the NCAT phantom, which is limited to the thorax, and the extended NCAT phantom which represents the full body. The NCAT phantom has also improved capability of simulating cardiac and respiratory motion because of the flexibility of NURBS (Fig. 11.3).

The NCAT phantom is sufficient for most of the applications that would be associated with nuclear medicine imaging, but it does not offer the spatial resolution required for simulating CT and MRI. To accommodate more demanding imaging situations, the XCAT phantom was developed which uses subdivision surfaces along with NURBS to achieve more realism [9]. Although NURBS have a lot of flexibility, there are certain structures like the cerebral cortex or internal anatomy of the breast where that approach is not practical. Subdivision surfaces, which are based on a polygonal mesh that can be iteratively subdivided and

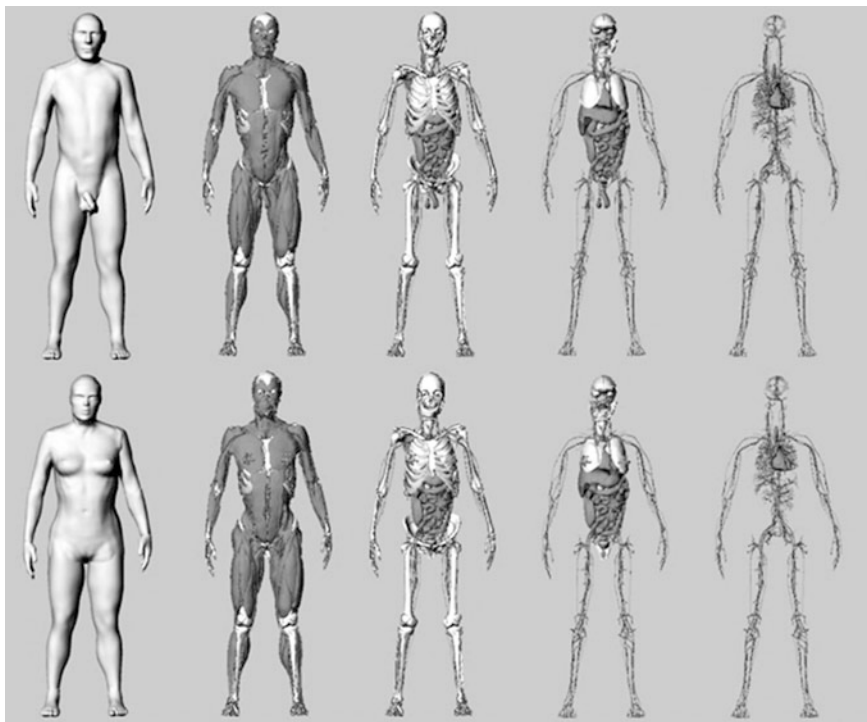


Fig. 11.3 The NCAT phantom uses NURBS fitting of voxelized CT scans to obtain realistic organ shapes that can easily be controlled for simulating organ motion. Figure courtesy of Paul Segars, Carl E. Ravin Advanced Imaging Laboratories

smoothed, are much more effective for modeling these tissues. More than 9,000 structures now comprise the adult XCAT phantom. In addition to improving the cardiac and respiratory motions, age-based whole-body phantoms have also been generated that include children of 2 and 16 months along with 4, 6, 8, 10, and 12 years old. The work has also been extended to mouse and rat phantoms as described in the preclinical imaging section below.

11.3 Physical Phantoms

Although mathematical models and phantoms are a necessary component of internal dosimetry and the development of image reconstruction and processing algorithms, the evaluation and calibration of imaging instrumentation require a real object with a known radioactive distribution of material, i.e., a physical phantom. The physical phantoms used in nuclear medicine and PET are typically more or less complicated hollow chambers with access ports allowing them to be

filled with water (or perhaps other liquids) and radioactive materials that can be uniformly mixed. Physical phantoms have primarily been used for the calibration, quality assurance, and acceptance testing of clinical devices, calibrations, validation standards for simulations and in the development of new imaging instrumentation.

11.3.1 Calibrations

Nuclear medicine (including) PET often seeks to be quantitative in either a relative or an absolute sense. An example of relative quantitation is left ventricular ejection fraction where the fraction of blood pumped from the left ventricle with each beat is estimated from the relative change in radioactivity between end systole and end diastole. An example of absolute quantitation is when the radioactivity concentration can be directly measured based on the detected count values in a SPECT or PET image. Phantoms often play an integral part in performing these tests.

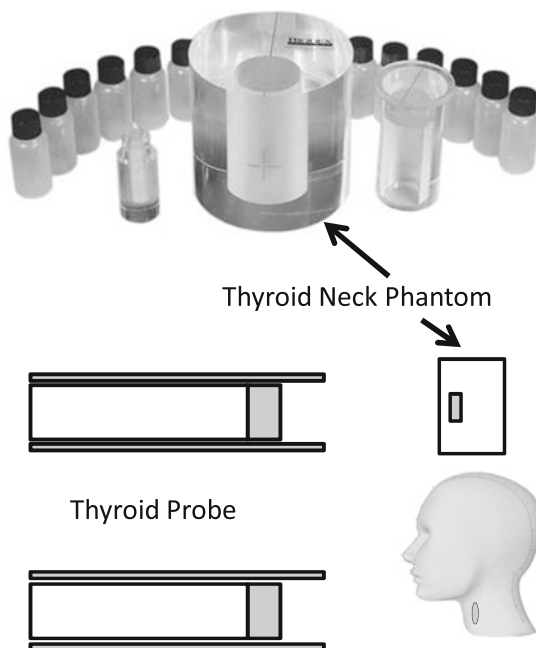
11.3.2 Thyroid Uptake Scans

Diagnostic information about thyroid function can be obtained by measuring the fraction of ingested iodine that is accumulated in the thyroid gland over a 24-h period. Since radioactive isotopes of iodine are handled by the thyroid gland in the same way as stable iodine, thyroid uptake fractions can be determined by comparing the count rate from patient's thyroid one day after the administration of a radioiodine capsule with the count rate obtained from the radioiodine capsule prior to the administration. In order for this comparison to be meaningful, the initial counting of the radioiodine capsule should have a similar geometry and attenuation factors as the radioactivity distributed in the thyroid. This is accomplished by placing the radioiodine capsule in a neck phantom during the count assay (Fig. 11.4). The neck phantom is a cylinder of plastic material with an off-center cavity that is similar to the typical depth within the neck where the thyroid is located.

11.3.3 Standardized Uptake Value Calibration

In PET tumor imaging with F-18 FDG, a semiquantitative parameter known as the standardized uptake value (SUV) is used to characterize potentially malignant lesions. The SUV compares the concentration of radioactivity within an area of interest (usually an abnormality) with the expected average radioactivity concentration of F-18 FDG assuming uniform mixing of the radiotracer throughout the entire body. In order to calculate SUVs, the PET imaging system must be calibrated

Fig. 11.4 The thyroid neck phantom is used to approximate the tissue attenuation of the neck so that an accurate assessment of thyroid radioiodine uptake can be determined



by imaging a known activity concentration. This is accomplished by accurately measuring a source of F-18 and mixing in a water-filled cylindrical phantom of known volume. The concentration is calculated as the radioactivity (with corrections for decay) divided by the phantom volume. Images of the phantom are acquired on the PET scanner using a calibration protocol. Regions of interest are drawn on the reconstructed images at several locations, and a calibration factor is determined between the PET measured concentration in the regions and the known radioactivity concentration derived from the dose calibrator.

11.4 Quality Assurance and Acceptance Testing

The primary use of physical phantoms has been for the quality assurance and testing of radionuclide imaging devices including gamma cameras and SPECT and PET systems.

11.4.1 Gamma Camera QC

Field uniformity: When a gamma camera is exposed to a uniform flux of gamma rays (referred to as a flood field), it is expected that the associated image will also be uniform. The monitoring of gamma camera uniformity is a daily requirement,

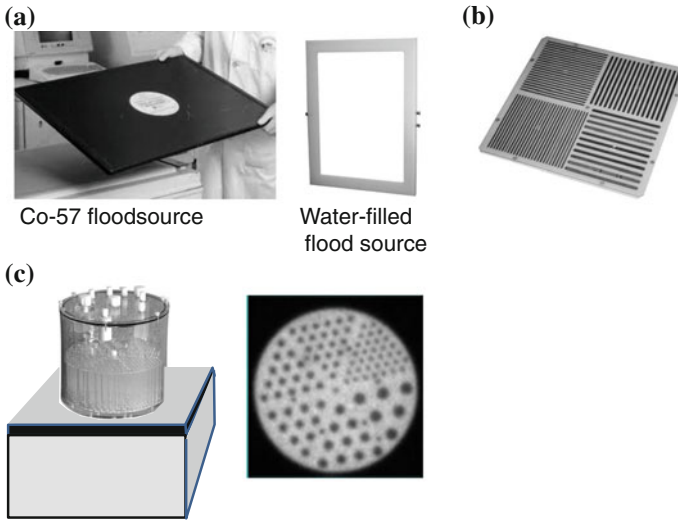


Fig. 11.5 Phantoms used for gamma camera quality control. **a** Co-57 and water-filled flood sources. **b** Quadrant bar phantom. **c** SPECT phantom on collimated gamma camera along with associated image

and it can be performed either intrinsically or extrinsically. Intrinsic field uniformity is measured by using a distance point source of radioactivity (usually Tc-99 m) to illuminate the uncollimated detector. Extrinsic field uniformity uses a large, uniformly distributed (flood) source positioned on the collimator. Most often a Co-57 flood source is used, but flood source phantoms are commercially available. As shown in Fig. 11.5a, the flood source phantom is a large, thin rectangular water-filled container into which Tc-99 m or other radionuclide is injected.

Spatial resolution: Spatial resolution is a measure of the amount of blurring that the system imparts during the generation of an image. Often there are many components that contribute to the final system resolution such as intrinsic spatial resolution, collimation, source location, and image smoothing to name a few. The complete characterization of spatial resolution requires that point or line source functions are known. These are obtained from line profiles through images of point or line sources. However, for much of nuclear imaging when there is no scattered radiation involved, the point and line source functions are well approximated by Gaussian functions, and a single parameter such as the full width at half maximum (FWHM) is sufficient. Another approach to characterizing spatial resolution is through identification of the smallest resolution bar pattern that can be resolved.

Intrinsic spatial resolution: The National Electrical Manufacturers Association (NEMA) describes a series of standards for characterizing the performance of radionuclide imaging systems [10]. For the intrinsic spatial resolution of a gamma camera, the standard requires the determination of the FWHM and full width at tenth maximum (FWTM) of line spread functions. The line spread functions are

generated by exposing a series of 1-mm slits located in a 3-mm-thick lead plate positioned directly on the detector (NEMA slit phantom). The slits are separated by 30 mm and should be long enough to cover the useful field of view of the gamma camera. A point source of Tc-99m (or other radionuclide of interest) is centered over the slit phantom and positioned approximately 2 m away. (NEMA recommends a distance of 5 times the largest camera field of view dimension, but that is not necessary to achieve accurate results). Static images of the slit projections are acquired with a pixel size of approximately 0.7 mm, and the line spread functions are generated from 30-mm-wide profiles taken perpendicular to the lines. A common way of characterizing the line spread functions is by its width at 50 % of the maximum value referred to as the FWHM and also by the similarly defined FWTM.

Quadrant bar phantom: A more common approach to assessing intrinsic spatial resolution is with the quadrant bar phantom consisting of 4 sets of lead bars (Fig. 11.5b). In each quadrant, the bars all have the same width and the separation between bars is the same as the bar width. The sizes of the bars are typically 3.5, 3.0, 2.5, and 2.0 mm, and each set is perpendicular as shown in Fig. 11.5b. The quadrant bar phantom is placed on the uncollimated detector, and a projection image is acquired from a distant, centered point source (~ 2 m). The acquisition matrix is typically 512×512 with some magnification to achieve pixels size less than 1 mm. Resolution is determined by the smallest size bar pattern that can be resolved. Many gamma cameras are capable of resolving the 2-mm bar sector.

Extrinsic spatial resolution: Extrinsic resolution characterizes how the gamma camera system performs with the collimators in place and reflects the clinical system performance.

Line source: The line spread function generated from the image of a line source positioned 10 cm above a collimated gamma camera is used to quantify extrinsic spatial resolution. The line source is typically a thin-walled tube of plastic or aluminum with an inner diameter that is less than 2 mm. The tube is filled with a Tc-99m compound in solution. Because the extrinsic spatial resolution is worse than the intrinsic, the pixel size can be smaller and a 256×256 acquisition matrix with some magnification is usually adequate. As with the intrinsic line spread functions, the resolution is usually expressed in terms of the FWHM and FWTM.

Quadrant bar phantom: For low-energy collimation, the quadrant bar phantom can be used to assess extrinsic resolution. The quadrant bar phantom is placed directly on the collimator, and a flood field source, usually a solid Co-57 source, is placed on the top of the phantom. As with the line source, a 256×256 acquisition matrix with some magnification is used to acquire a projection image of the bars. For a low-energy high-resolution collimator, the 2.5–3-mm bar sectors should be resolved on most gamma cameras. The quadrant bar phantom may generate artifacts if used with medium or high-energy collimation. Moire patterns occur when the size of the bars is comparable to the collimator hole size. This can be avoided by using quadrant bar phantoms designed for extrinsic testing that have larger bar sizes.

SPECT phantom: Another way of monitoring extrinsic spatial resolution is with a SPECT phantom. Images of an activity loaded SPECT phantom are acquired with the phantom sitting directly on the collimator as shown in Fig. 11.5c. Resolution is assessed in terms of the smallest rod pattern that is resolvable.

11.4.2 SPECT QC

The performance of SPECT imaging systems is most commonly assessed by cylindrical phantoms with rod and sphere inserts [11, 12]. There are 3 commercial phantoms (shown in Fig. 11.6) that are available with similar design features, the Carlson phantom, the ECTphan phantom, and the Jaszczak phantom (also referred

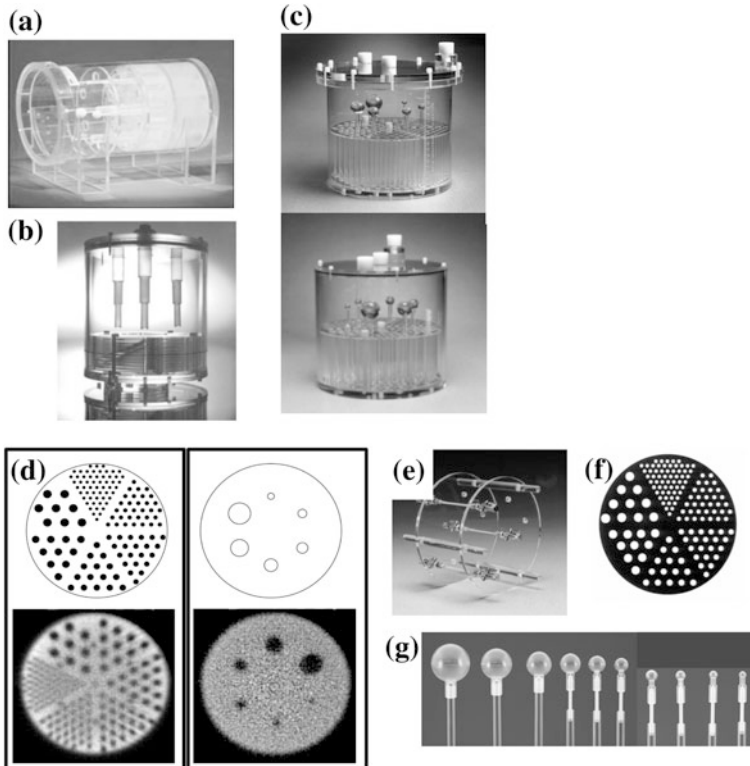


Fig. 11.6 SPECT phantoms used for quality control. **a** Carlson phantom. **b** ECTphan. **c** Jaszczak phantom and ACR flangeless SPECT phantom. **d** Cold rod and sphere inserts. **e** Line source insert. **f** Hot rod insert. **g** Fillable spheres

to as the ACR phantom). These phantoms can also be used to evaluate PET imaging systems.

Carlson SPECT phantom: The Carlson SPECT phantom is shown in Fig. 11.6a. It is plastic-walled cylinder that is 12 inches long with an 8 inch inside diameter. For measuring spatial resolution, it has an insert consisting of 7 plastic rods ranging in size from 5.9 to 22.3 mm. There are also 7 solid plastic spheres with the same diameters as the rods for assessing scatter and contrast. Additional optional inserts are available that display hot rods instead of the cold rods described above and a crossed grid for assessing spatial linearity.

ECTphan: The ECTphan (also referred to as Specphan) is also plastic-walled cylinder that has four main imaging sections for determining slice width and pixel sizing, spatial resolution, uniformity and noise, and contrast (Fig. 11.6b). Slice width is determined from imaging a ramp object and pixel size is obtained from 4 “hot” calibration hole sources separated by 120 mm. A set of four bars ranging from 2 to 8 mm provides spatial resolution information. There are three low-fillable contrast inserts that are 40 mm long with diameters of 10, 15, 20 mm.

Jaszczak phantom: The Jaszczak phantom is shown in Fig. 11.6c. It is a plastic-walled cylinder with an inside diameter of 21.6 cm and an inside height of 18.6 cm. The ACR SPECT accreditation phantom is identical to the Jaszczak phantom with the exception that it does not have a flange that extends beyond the cylinder walls (Fig. 11.6c). The bottom section is used for assessing spatial resolution and has 6 rod sectors with rod diameters ranging from 4.8 to 12.7 mm in the most commonly available model (Fig. 11.6d). Mounted above the rods are 6 solid spheres that range in size from 9.5 to 31.8 mm that are used for assessing scatter and contrast. Other rod and sphere sets are available that can be used in the same vessel with either finer or coarser rods and spheres. Other quality control inserts are available as options for the Jaszczak phantom as shown in Fig. 11.6e–11.6g. The 3 line source phantoms (Fig. 11.6e) is used to quantify spatial resolution, while the “hot” source sector phantom (Fig. 11.6f) provides spatial resolution information in terms of the smallest detectable sector. Figure 11.6g shows a set of fillable hollow spheres ranging in volume from 31 μ l to 16 ml.

11.4.3 PET Phantoms

The nature of PET is different enough that it requires a different set of phantoms for acceptance testing and quality assurance. In the next sections, these phantoms will be discussed along with their applications.

PET acceptance testing: The acceptance testing of new PET scanning systems primarily requires the verification of the NEMA instrument specifications [13]. The PET NEMA tests include spatial resolution, count sensitivity, and scatter fraction (Fig. 11.7).

PET scatter fraction: The scatter fraction is defined as the ratio of scatter events to the total events (true coincidences and scattered radiation). The first

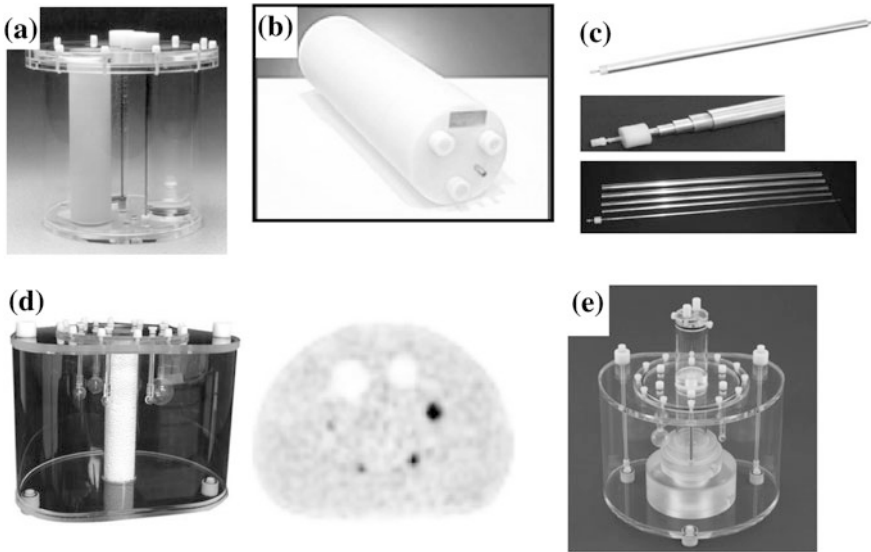


Fig. 11.7 PET QC phantoms. **a** Original NEMA NU-2 1994 PET phantom. **b** NEMA scatter phantom. **c** NEMA sensitivity phantom. **d** NEMA IEC image quality phantom. **e** PET/CT phantom with 6 internal structures used for validating PET and CT alignment

NEMA PET phantom (Fig. 11.7a) fits within the axial field of view of most PET tomographs. Because it was recognized that scattered radiation (and random coincidences) can also originate from radioactivity outside to the axial field of view, a large cylindrical polyethylene phantom was designed (Fig. 11.7b). The phantom dimensions are 20 cm in diameter with a length of 70 cm, and it has a 6.4-mm hole that is offset 4.5 cm from the central axis that runs the entire length of the phantom to receive a fillable line source. The scatter fraction is determined with a low activity source by comparing the scattered events from an acquired sinogram to the total events. This phantom is also used to evaluate the count rate capability of the PET tomograph.

PET sensitivity: The count sensitivity is assessed from a line source filled with F-18. However, the plastic material used for the source does not sufficiently absorb all the emitted positrons causing an underestimation of the system sensitivity. To address that issue, an aluminum sleeve is used to cover the line source (Fig. 11.7c). Although this improves the absorption of the positrons, it also causes some attenuation of the annihilation radiation. To compensate for that issue, 5 additional concentric sleeves of aluminum are stepwise added to the source with a count acquisition occurring with each additional sleeve. This increased absorption with increasing sleeves is used to extrapolate what the count rate would be with no aluminum attenuation.

PET image quality and corrections: PET image quality is assessed with the IEC body phantom shown in Fig. 11.7d. The phantom is configured with 6 fillable

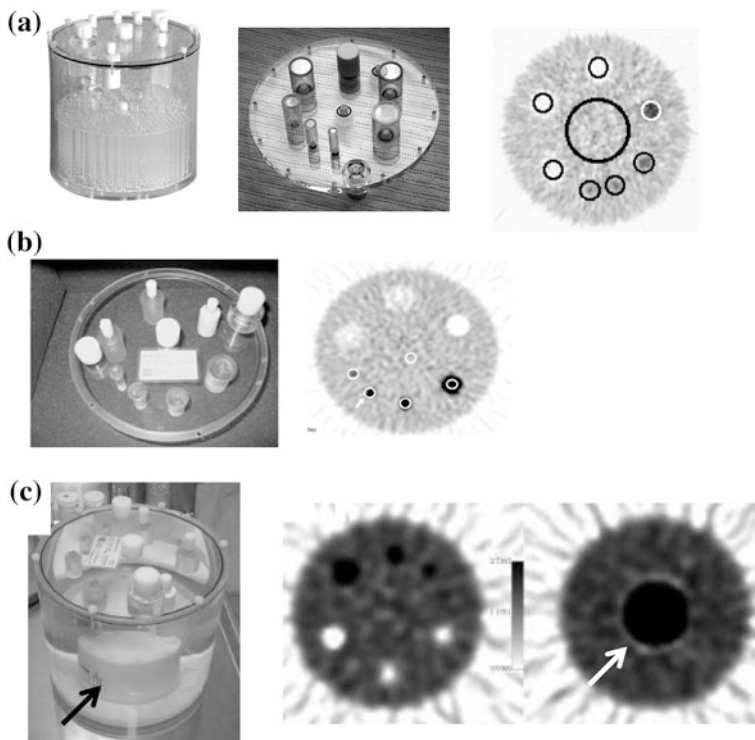


Fig. 11.8 ACR PET QC phantoms. **a** ACR PET phantom with faceplate. **b** Modified faceplate with Ge-68 sources (*arrows*). **c** Modified ACR PET phantom with addition large Ge-68 source (*arrows*)

spheres, the four smallest of which are filled with a uniform concentration of F-18, while the largest two are filled water. The large cylindrical insert is filled with a low-density material to simulate lung tissue attenuation. The rest of the phantom is filled with water with sufficient F-18 activity to achieve a hot sphere-to-background ratio of 4:1. Images of the phantom are acquired on the PET scanner with appropriate corrections for scattered radiation, random coincidences, and attenuation. Regions of interests are placed over each of the spheres and 12 other locations in the background. Figure 11.7e shows a PET/CT phantom designed to validate PET and CT alignment.

PET accreditation: The American College of Radiology is one of three organizations that provides accreditation for PET imaging systems and is the only organization that requires the submission of phantom images as part of the accreditation process. The phantom used for PET system evaluations is the ACR flangeless phantom with the spheres removed and a modified faceplate as shown in Fig. 11.8a. The faceplate has 4 fillable cylinders ranging from 8 to 25 mm in diameter) along with a Teflon cylinder and two additional 25-mm-diameter cylinders, one of which is air filled and the other with non-radioactive water. The four

hot cylinders are filled with a F-18 solution so that they all have the same concentration, and F-18 radioactivity is added to the primary phantom chamber to achieve a 2.5:1 concentration ratio. Images of the phantom are acquired on the PET scanner with appropriate corrections for scattered radiation, random coincidences, and attenuation. One large region of interest is drawn in the center of the phantom and 7 additional regions (1 for each cylinder) large enough to encompass the inside of the 25-mm hot cylinder are positioned over the each of the faceplate cylinders. SUVs calculated from the region measurements are reported.

PET phantoms used in multicenter trials. Many multicenter trials evaluating the use of quantitative PET for monitoring the response to therapy have been initiated. For such trials, it is important to be able to estimate the system and clinic-based variability associated with standardized uptake values [14–16]. Some of these trials have just used uniform concentrations of tracers either by mixing F-18 radioactivity into the water compartment or with solid phantoms with a uniform distribution of Ge-68 in a resin. Several different phantoms have been used in these trials. One based on the ACR phantom is shown in Fig. 11.8b with the 4 hot spheres filled with Ge-68 in epoxy. For another study, the phantom was further modified by removing the rod sector insert and replacing it with a larger Ge-68 source as shown in Fig. 11.8c. Another phantom that has been used is the NEMA IEC image quality phantom filled with a uniform Ge-68 resin in the primary cavity of the phantom and a higher concentration of the Ge-68 resin in the spheres to achieve a 4:1 ratio.

11.5 Anthropomorphic Physical Phantoms

Through the years, a number of nuclear medicine phantoms have been designed that more realistically simulate the geometry and the expected clinical distribution of radiopharmaceuticals. These phantoms have been useful for providing qualitative measures of instrumentation performance and for validating mathematical models and Monte Carlo simulations.

The first commercially available nuclear medicine organ phantom is the thyroid phantom as shown in Fig. 11.9a. The chambers for the thyroid lobes have different volumes so that the apparent radioactivity concentration in the left lobe is twice that of the right lobe. Each lobe has 2 circular nodules, 3 of which are solid so that no radioactivity distributes in those locations. The 4 nodules, located in the right lobe, have the same water depth as the left lobe and show up as a “hot” (increased radioactivity) nodule.

Early PET research focused on brain metabolic imaging and the group at UCLA developed several phantoms that simulated the cortical and white matter structures of the brain along with the ventricles. The first phantom represented a single slice of the brain. It was constructed in a manner similar to the thyroid phantom where the different depths of the chambers resulted in an apparent 4 to 1 gray to white matter concentration while the regions corresponding to the ventricles was solid

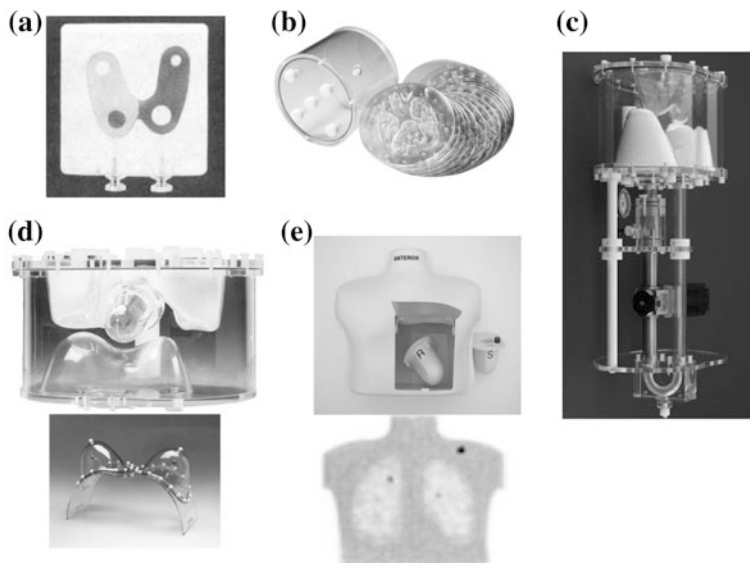


Fig. 11.9 Organ phantoms. **a** Thyroid. **b** Hoffman 3D brain. **c** Dynamic heart phantom. **d** Thorax and abdomen with lung, heart, and liver components and breast option. **e** courtesy of Paul Christian, University of Utah

with no radioactivity accumulation. A three-dimensional version of this phantom was produced consisting of 19 inserts that encompassed the entire brain (Fig. 11.9b). Within each of the 19 inserts are 5 thinner slices that maintain the appropriate apparent radioactivity tissue concentrations. Other fillable commercial brain phantoms with a variety of inserts are available.

Because of the importance of myocardial perfusion imaging, phantoms simulating the distribution of radioactivity in the heart wall have been developed that can be positioned within phantoms that simulate the thorax. Figure 11.9c and d shows examples of commercially available heart phantoms simulating myocardial perfusion imaging. The phantoms have separate chambers for the myocardium and ventricular cavities and also have inserts that simulate perfusion defects. The cardiac phantom shown in Fig. 11.9c simulates the beating heart and can be used to test the effects of motion and gated acquisition.

The SPECT and PET phantoms used for quality control are cylindrical and as such do not approximate a human contour very well. Elliptical phantoms became available with a variety of inserts of both QC-related objects (rods and spheres) and simulated organs such as the spine, heart, and lungs. This ultimately has led to the generation of a trunk phantom (thorax and abdomen) which also accommodates the lung and heart inserts (Fig. 11.9d and e). The trunk phantom has a separate liver compartment and by judiciously adjusting the administered activity to the compartments can produce quite realist images. Additional options for the trunk phantom include larger contour rings and a separate fillable breast compartment that is positioned on the anterior (Fig. 11.9d).

Patient simulator phantoms: The Society of Nuclear and Molecular Imaging has a quality assurance program for comprehensive evaluation of clinical procedures that include myocardial perfusion (Fig. 11.9e), gastric emptying, and PET tumor imaging (Fig. 11.9e). These realistic phantoms allow the assessment of acquisition, processing, and interpretation of these important nuclear medicine imaging procedures.

11.6 Preclinical Imaging Phantoms

Over the past decade, there has been an increasing focus on the development of small animal imaging with SPECT and PET. Serial imaging sessions on mice and rats are necessary for the development of new radiopharmaceuticals and treatment regimes. Commercial small animal PET and SPECT systems are available that are capable of submillimeter spatial resolution, and as a result, custom phantoms are required for the evaluation and quality assurance of these devices [17–19]. Figure 11.10 shows an array of phantoms designed for small animal imaging systems. Some of these phantoms are available in two sizes consistent with rat and mouse imaging. A miniature version of the SPECT phantom with a cold rod resolution insert shown in Fig. 11.10a along with additional inserts such as the

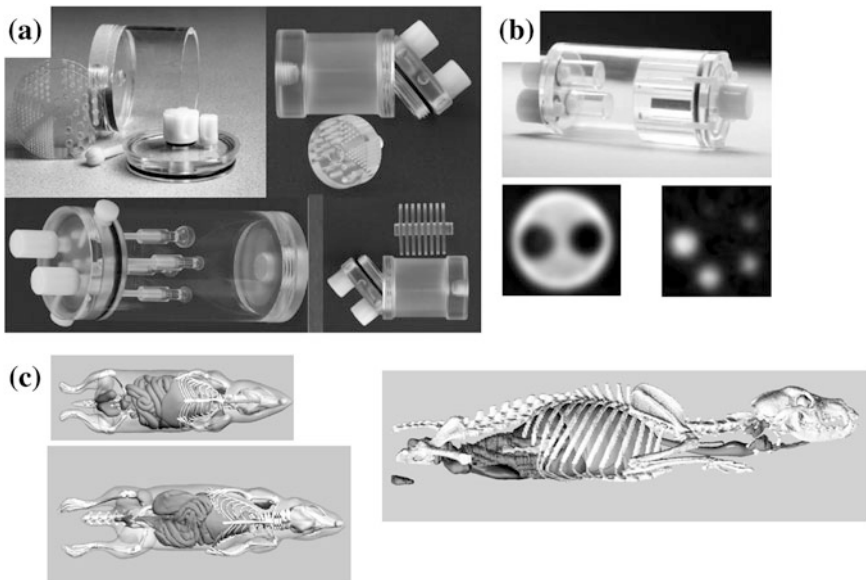


Fig. 11.10 Preclinical phantoms. **a** Commercial small animal QC phantoms with cold rods, hot rods, microspheres, and DeFrise inserts. **b** NEMA NU 4 small animal PET phantom with images taken through the large chambers and the hot rod sections. **c** courtesy of Paul Segars, Carl E. Ravin Advanced Imaging Laboratories

“hot” source resolution pattern (also referred to as a Derenzo phantom), hollow, fillable spheres and a micro-Defrise phantom. The Defrise phantom yields a set of uniform disks of radioactivity that is sensitive to artifacts from incomplete 3D sampling. The NEMA NU-4 small animal PET phantom is shown in Fig. 11.10b [19]. The two large chambers can be filled with radioactivity at desired concentrations, but are meant to have one filled with air and the other with plain water. The five hot rods have a length of 20 mm with diameters of 1, 2, 3, 4, and 5 mm.

11.7 Other Approaches to Physical Phantoms

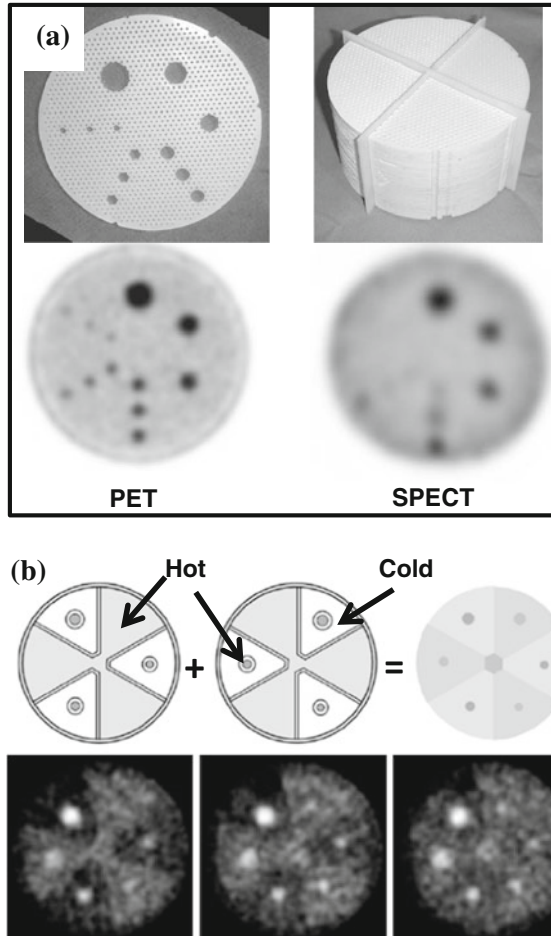
Depending on how the phantom information will be used, there can be issues with fillable spheres used in physical phantoms. This is because the wall surrounding the sphere cavity has a finite thickness which can enhance the detection of the sphere. This is especially a problem with small spheres where the volume of the spherical shell can be a substantial fraction of the cavity volume. Also, it can be challenging to fill small cavities with liquid completely without bubbles. There have been several approaches used to overcome this problem.

One way to avoid the shell effect is to use solid sources that do not need to be contained in a cavity. Sources can be uniformly distributed in epoxy or a resin and shaped as spheres or any arbitrary shape. These can then be positioned in radioactive background solutions before they set up. The disadvantage to this approach is that the phantom cannot be replenished so unless an appropriate long-lived source is available, it can be expensive. Fortunately, there are several possible alternatives to overcome this problem.

One clever approach for making complicated radioactive distributions is to use radioactive ink with a computer-connected printer. There is a fairly linear relationship between the gray scale and the density of ink dots laid down on the paper so that the printed image corresponds to a fairly accurate radioactivity distribution. Volumetric phantoms can be obtained by printing multiple planes that are appropriately adjusted to the desired distribution thickness. The downside to this approach is primarily the time it takes to print the many sheets that are required for a large volume and the potential radiation cleanup that may be required.

Still another approach for making physical phantoms that avoids problems with the shell effect is the porous core phantom as shown in Fig. 11.11a. The phantom consists of a stack of individually die-stamped perforated disks with an array of holes (pores) that are 2.4 mm in diameter and separated by a center-to-center distance of 4.8 mm [21]. This arrangement produces a uniform appearance with either a SPECT or a PET system with a spatial resolution greater than 4 mm as shown by the images in Fig. 11.11a. Larger-sized holes can be stamped in the disks, and different contrast levels can be generated by presence or absence of interspersing disks. The stack of disks are axially aligned in a cylindrical phantom that is filled with a radioactive solution. This approach is effective in producing circular and spherical patterns without the shell effect. There are limits, however,

Fig. 11.11 Wall-less object phantoms. **a** Reprinted with permission from Medical Physics from ref. [20]. **b** Reprinted with permission from Physics in Medicine and Biology from ref. [21]



to the size of the objects that can be produced this way because of issues with filling the phantom.

There are situations where lesion detection studies using physical phantoms are useful. That can be a particular challenge for small animal imaging systems where the spatial resolution requires millimeter or smaller-sized objects without the shell effect. One approach to creating images for evaluation is based on the superpositioning of separately acquired images of a background distribution and an object distribution (like a fillable) sphere (Fig. 11.10b). For SPECT or PET imaging, separate sinograms of the background and object distributions can be acquired at a high count density and subsampled to simulate a range of count densities. The subsampled sinograms can be added together and reconstructed to generate the object within the background at any desired contrast or noise level [21].

11.8 Summary

The nature of PET and SPECT imaging lends itself to the use of both physical and mathematical phantoms for internal dosimetry, quality assurance, and image processing research. Phantoms will continue to play a major role as nuclear medicine imaging continues to evolve.

References

1. Snyder, W. S., Fisher, H. L., Jr, Ford, M. R., & Warner, G. G. (1969). Estimates of absorbed fractions for monoenergetic photon sources uniformly distributed in various organs of a heterogeneous phantom. *Journal of Nuclear Medicine, (Suppl 3)*, 7–52.
2. Loevinger, R., & Berman, M. (1968). A schema for absorbed-dose calculations for biologically-distributed radionuclides. *Journal of Nuclear Medicine, (Suppl 1)*, 9–14.
3. Stabin, M. G., Xu, X. G., Emmons, M. A., Segars, W. P., Shi, C., & Fernald, M. J. (2012). RADAR reference adult, pediatric, and pregnant female phantom series for internal and external dosimetry. *Journal of Nuclear Medicine, 53*, 1807–1813.
4. Cristy, M. & Eckerman, K. (1987). Specific absorbed fractions of energy at various ages from internal photon sources. *Report ORNL/TM 8381*.
5. Stabin, M., Watson, E., Cristy, M., Ryman, J., Eckerman, K., Davis, J., Marshall, D. & Gehlen, M. (1995). Mathematical models and specific absorbed fractions of photon energy in the nonpregnant adult female and at the end of each trimester of pregnancy. *Oak Ridge National Laboratory Report*.
6. Zaidi, H., & Xu, X. G. (2007). Computational anthropomorphic models of the human anatomy: the path to realistic Monte Carlo modeling in radiological sciences. *Annual Review of Biomedical Engineering, 9*, 471–500.
7. LaCroix, K. J., Tsui, B. M., & Hasegawa, B. H. (1998). A comparison of 180 degrees and 360 degrees acquisition for attenuation-compensated thallium-201 SPECT images. *Journal of Nuclear Medicine, 39*, 562–574.
8. Segars, W. P., Tsui, B. M., Frey, E. C., Johnson, G. A., & Berr, S. S. (2004). Development of a 4-D digital mouse phantom for molecular imaging research. *Molecular Imaging Biology, 6*, 149–159.
9. Segars, W. P., Sturgeon, G., Mendonca, S., Grimes, J., & Tsui, B. M. (2010). 4D XCAT phantom for multimodality imaging research. *Medical Physics, 37*, 4902–4915.
10. Hines, H., Kayayan, R., Colsher, J., Hashimoto, D., Schubert, R., Fernando, J., et al. (2000). National electrical manufacturers association recommendations for implementing SPECT instrumentation quality control. *Journal of Nuclear Medicine, 41*, 383–389.
11. Graham, L. S. (1995). Quality control for SPECT systems. *Radiographics, 15*, 1471–1481.
12. Graham, L. S., Fahey, F. H., Madsen, M. T., van Aswegen, A., & Yester, M. V. (1995). Quantitation of SPECT performance: Report of task group 4, nuclear medicine committee. *Medical Physics, 22*, 401–409.
13. National Electrical Manufacturers Association. (2007). *Performance Measurement of Positron Emission Tomographs*. Rosslyn: National Electrical Manufacturers Association.
14. Kadmas, D. J., & Christian, P. E. (2002). Comparative evaluation of lesion detectability for 6 PET imaging platforms using a highly reproducible whole-body phantom with (22)Na lesions and localization ROC analysis. *Journal of Nuclear Medicine, 43*, 1545–1554.
15. Doot, R. K., Scheuermann, J. S., Christian, P. E., Karp, J. S., & Kinahan, P. E. (2010). Instrumentation factors affecting variance and bias of quantifying tracer uptake with PET/CT. *Medical Physics, 37*, 6035–6046.

16. Beyer, T., Czernin, J., & Freudenberg, L. S. (2011). Variations in clinical PET/CT operations: results of an international survey of active PET/CT users. *Journal of Nuclear Medicine*, *52*, 303–310.
17. Larsson, E., Strand, S. E., Ljungberg, M., & Jonsson, B. A. (2007). Mouse S-factors based on Monte Carlo simulations in the anatomical realistic Moby phantom for internal dosimetry. *Cancer Biother Radiopharm*, *22*, 438–442.
18. Keenan, M. A., Stabin, M. G., Segars, W. P., & Fernald, M. J. (2010). RADAR realistic animal model series for dose assessment. *Journal of Nuclear Medicine*, *51*, 471–476.
19. Goertzen, A. L., Bao, Q., Bergeron, M., Blankemeyer, E., Blinder, S., Canadas, M., et al. (2012). NEMA NU 4-2008 comparison of preclinical PET imaging systems. *Journal of Nuclear Medicine*, *53*, 1300–1309.
20. DiFilippo, F. P., Price, J. P., Kelsch, D. N., & Muzic, R. F., Jr. (2004). Porous phantoms for PET and SPECT performance evaluation and quality assurance. *Med. Physics*, *31*, 1183–1194.
21. DiFilippo, F. P., Gallo, S. L., Klatte, R. S., & Patel, S. (2010). A fillable micro-hollow sphere lesion detection phantom using superposition. *Physics in Medicine and Biology*, *55*, 5363–5381.

Part III
Computational Phantoms

Chapter 12

Computational Phantoms for Organ Dose Calculations in Radiation Protection and Imaging

X. George Xu

12.1 Introduction

Dosimetry for ionizing radiation has to do with the determination of amount and distribution pattern of the energy deposited in a part or parts of the human body from internal or external radiation sources. To protect against occupational exposures, dose limits for radiosensitive organs are recommended by international organizations and are adopted as national regulations. In both diagnostic radiology and nuclear medicine, X-ray photons and gamma rays traverse through body tissues to form images of the anatomy, depositing radiation energy in organs along the pathway via secondary electrons. Accurate radiation dosimetry is essential but also quite challenging for three reasons: (1) there are many diverse exposure scenarios resulting in unique spatial and temporal relationships between the source and human body; (2) an exposure can involve multiple radiation types, each of which is governed by different radiation physics principles, such as photons (X-ray photons, gamma rays, and positrons), electrons, alpha particles, neutrons, and protons; (3) the human body consists of a large number of anatomical structures of diverse shape, composition and density, leading to complex radiation interaction patterns. Since it is inconvenient to place a dosimeter inside the human body, organ dose estimates have been obtained mostly using a physical phantom or a computational phantom that mimics the interior and exterior anatomical features of the human body.

Historically, the term *phantom* was used in most radiological science literature to mean a physical model of the human body. In the radiation protection community, however, the term has also been used to refer to a mathematically defined *anatomical model* that is distinctly different from a physiologically based model such as that related to respiration or blood flow. In this chapter, the phrases, “computational phantom” and “physical phantom,” are used to avoid confusion.

X. George Xu (✉)

Nuclear Engineering Program, Rensselaer Polytechnic Institute, Troy, NY, USA
e-mail: xug2@rpi.edu

As discussed extensively in this book, a physical phantom is made of solid materials equivalent to bones and soft tissues that can be molded to resemble the human anatomy and then cut into slices that contain cavities for tiny radiation dosimeters. The approach of using such physical phantoms was known to be expensive and time-consuming due to tedious experimental and radiation safety procedures. Luckily, the advent of the first generation of computers and Monte Carlo simulation methods for nuclear weapons research in the 1940s made it gradually possible to calculate organ doses using a computational phantom. A computational phantom must define the exterior features of the entire human body as well as selected internal organs in terms of volume, mass, and shape. Coupled with information on tissue density and chemical composition, a computational phantom allows for a researcher to use the well-established Monte Carlo methods to calculate radiation interactions and energy deposition in the body [1–3]. Monte Carlo methods, which are based on statistical simulations, have a long history, but the real application to radiation transport simulations and the associated software development arose from nuclear weapons research at Los Alamos National Laboratory during World War II [235]. Although additional work is needed to specify a radiation source and the irradiation geometry, the computational approach has advantageous in comparison with the physical approach in versatility, efficiency, precision, and safety. There are situations, such as internally distributed radiation sources, where the computational approach is the only option. Since the 1960s, the development and application of computational human phantoms became a specialized field of research that intimately associated with radiation protection, imaging, and radiotherapy. Physical phantoms are used to perform benchmark for computational results when needed.

Computational phantoms existed for more than 60 years. The early users were from national laboratories who had access to powerful computers. A focused research group on computational phantoms was not formed until early 1990s when personal computers became a common research tool. Several workshops were held on computational phantoms. In 1996, Dimbylow from National Board of Radiological Protection, UK, organized the first workshop on voxelized computational phantoms [4]. In 2000, Eckerman organized a similar workshop at Oak Ridge National Laboratory, US [244]. By then, there was a widespread interest from the international community about the voxelized computational phantoms. To foster collaboration, I worked with many colleagues to form the Consortium of Computational Human Phantoms (CCHP) in 2005 during the American Nuclear Society Monte Carlo 2005 Topical Meeting in Chattanooga, TN, USA, from April 17–21, 2005 (<http://www.virtualphantoms.org>). Under the umbrella of CCHP, I later served as the co-editor with Dr. Keith Eckerman, Oak Ridge National Laboratory, for “Handbook of Anatomical Models for Radiation Dosimetry” which was published in 2009 involving 64 authors from 13 countries [245]. In 2011, I organized with Professor Junli Li, the 3rd International Workshop on Computational Phantoms for Radiation Protection, Imaging, and Radiotherapy at Tsinghua University, Beijing, China (<http://www.virtualphantoms.org/3rdWorkshopInBeijing.html>). The Beijing Workshop was the first time to use this workshop

title and to engage researchers from the non-ionizing radiation dosimetry community. The 4th workshop is being planned for May 20–22, 2013 in Zurich, Switzerland. These workshops have shown to be important in disseminating research ideas, facilitating collaboration, and developing a roadmap for the future.

According to Xu [5], approximately 121 computational phantoms, plus 27 physical phantoms, had been reported in the literature for studies involving ionizing and non-ionizing radiation by the end of 2009. A significant portion of the literature on radiation protection dosimetry is related to the development and application of these phantoms. The organs and body surfaces of computational phantoms have been defined in terms of a variety of solid geometry modeling techniques. Each of these techniques was adopted at specific times in the last 60 years, exhibiting an interesting scientific journey that reflects the advances in computer and medical imaging technologies. Like other research fields, non-technical considerations also had their share in shaping the world of computational phantoms that we know today. As the evolution continues, particularly at the accelerated computing power witnessed in the past decade, it is vitally important to know where we are going. There are many interesting questions facing researchers today. Why did the computational phantoms evolve the way they did? What will be the future directions in this research field? The answers to these questions and many others require an understanding and evaluation of the rationales and processes responsible for some of the most widely used phantoms. The different modeling techniques are defined, and a summary of historical milestones in the development of computational phantoms for ionizing and non-ionizing radiation applications is provided.

12.2 Computational Geometries Used for Phantoms

Computational phantoms are solid geometry models that depict exterior and interior anatomical features of a human body. For radiation dosimetry, a phantom must define the surface of an organ in which radiation interactions and energy depositions are to be calculated by tracing individual particles. Clearly, the construction of such phantoms must consider multiple factors such as anatomy, radiosensitivity, computational efficiency, and geometrical compatibility with a Monte Carlo code.

The computer graphics community has dealt extensively with solid geometry modeling for computer-aided design (CAD). Two general methods of solid geometry modeling have been widely developed: constructive solid geometry (CSG) and boundary representation (BREP) [6–9]. The topology—spatial location and relationship of the surfaces—is fundamentally different for these two methods. CSG allows a modeler to create a solid object using Boolean operators (or the equivalent) to combine very simple objects called primitives. Examples of these primitives include cuboids, cylinders, prisms, pyramids, spheres, cones, and ellipsoids—surfaces that are easily described by quadric equations. CSG

representations are easy to adopt and can yield good results when the objects are relatively simple in shape.

Modern CAD software systems, however, are based on the more powerful BREP methods. There are two types of information in the BREP: topological and geometric. Topological information provides the relationships among vertices, edges, and faces. In addition to connectivity, topological information also includes orientation of edges and faces. In advanced BREP-based CAD, the exterior of an object are defined as NURBS, which afford very smooth surfaces. The faces can alternatively be represented as polygons whose vertices are defined by a set of coordinate values x , y , and z . A polygon mesh or unstructured grid is a collection of vertices and polygons that define the geometric shape of a polyhedral object in CAD. In principle, NURBS and polygonal meshes are interchangeable BREP data structures; however, unlike the CSG representation, BREP is much more flexible because a richer set of operation tools are available (e.g., extrusion, chamfering, blending, drafting, shelling, and tweaking). These features allow BREP-based phantoms to include very complex anatomical features. Furthermore, the BREP technique is ideally suited for surface deformation—an operation necessary for the adjustment of organ size and for organ motion simulations as described later. These surface equations are computationally efficient and are accepted by nearly all Monte Carlo codes. However, even with complicated and carefully designed Boolean operations like this, phantoms based on quadric surfaces are not anatomically realistic in terms of their geometry. When using a Monte Carlo code, the geometry of the left lung is often further simplified by replacing the ellipsoid B with several planes. This type of phantoms is commonly referred to as “stylized” or “mathematical” phantoms.

Voxels, as a CSG modeling technique, define the left lung as an assembly of 3D cuboids. Medical image data can be converted to voxel geometry that provides a direct way to realistically describe the human anatomy. The geometry of a voxel is very simple for existing Monte Carlo codes to handle, although the large number of voxels may require the use of enhanced computer hardware or special Monte Carlo software preparation. On the other hand, each tomographic image slice needs to be treated by a “segmentation” process, which assigns each pixel to an organ or tissue of interest such as the lung, bone, or skin using a unique identification number. It can take a significant amount of time to prepare a voxel-based phantom, because there is no automatic segmentation algorithm that works on all organs. Furthermore, a voxel phantom is based on images for one subject, therefore lacking the anatomical variability associated with organ size, shape, and location that are important in the current paradigm for radiation protection dosimetry. Finally, the boundary of the lung in a voxel phantom is defined by uneven steps instead of a smooth surface. As a result, the anatomical fidelity depends on the voxel size, especially for thin and small tissues such as the skin, eye lens, ribs, and bone marrow. An adjustment to the organ shape will likely involve all underlying voxels, which is computationally inefficient. These types of computational human body models are commonly referred to as “voxel” or “tomographic” phantoms.

An organ can also be defined by the advanced BREP modeling techniques involving NURBS or polygon mesh surfaces. The most common technique to create a BREP-based phantom involves the surface contour extraction of each organ from a tomographic image data set using a commercial software package, followed by the integration of individual organs into a whole-body assembly. In essence, the contours convert the voxels into NURBS or mesh surfaces that are smooth and anatomically realistic. These phantoms are commonly referred to as “NURBS,” “mesh,” or “BREP” phantoms.

12.3 The Evolution of Computational Phantoms

The historical development of computational phantoms has been reviewed previously, mostly focusing on a certain time period or a particular type of phantoms [10, 11]. These reviews did not explicitly classify phantom modeling techniques, and since the time of their publication, a number of phantoms have been developed using the new BREP methods. Xu [5] was the first to officially group computational phantoms into three generations basing on chronological and technical information in the literature: (1) The first-generation phantoms developed and widely used until 1990s: *stylized* phantoms whose organs are delineated by a combination of simple surface equations, (2) The second-generation phantoms first emerged in late 1980s and then rapidly adopted by many groups in the 1990s: *voxel* or *tomographic* phantoms that are directly based on segmented and labeled medical images of real people, and (3) The third-generation phantoms developed by a relative small group of advanced researchers in the mid-2000s: *BREP* (or mistakenly the *hybrid*) phantoms using B-Splines, NURBS, or polygon meshes.

12.3.1 First-Generation Stylized Phantoms (Prior to the 1990s)

The first-generation computational phantoms were developed for the purpose of assessing organ doses from internally deposited radioactive materials for workers and patients [12, 13–18]. Some of the earliest dose assessment techniques were developed in the first-third of the twentieth century primarily for use with interstitial radiation sources such as radium. With the increase in the size and speed of computers, some progress occurred during the late 1950s and through the 1960s and eventually the efforts led to stylized anthropomorphic phantoms—those resemble the human anatomy.

Stylized phantoms originated from work performed at Oak Ridge National Laboratory (ORNL). The first attempts at developing a computational anthropomorphic phantom were reported by Fisher and Snyder at ORNL in the 1960s [19, 20].

Using CSG modeling techniques involving shapes such as elliptical cylinders and cones, they developed the so-called Fisher-Snyder adult phantom. The adult phantom was assumed to be standing erect with the arms at the sides of the body. Three specific regions were defined; the head and neck, the trunk including the arms, and the legs. The head and neck were represented by a 14×20 cm elliptical cylinder with a height of 24 cm. The trunk and arms were modeled as a larger elliptical cylinder, 20×40 cm with a height of 70 cm. The legs below the buttocks were modeled as a truncated elliptical cone with a height of 80 cm. Regions of little dosimetric importance were not included, e.g., the hands, feet, ears, and nose. The composition of the phantom was assumed to be tissue distributed homogeneously throughout. No attempt was made to model the lungs or skeleton or to define the locations of specific organs in the phantom. Approximately 120 sub-regions were defined in the phantom, which were used to assign approximate values of the absorbed doses to organs located within specific regions. In some cases, absorbed dose estimates for large organs required the evaluation of the doses deposited in several of these regions. Even though the original phantom was designed for use with internally deposited radionuclides, Snyder saw many other applications. In addition, in 1967, he used the phantom to study the distribution of dose in the body from external, point sources of gamma rays [21]. He studied four photon energies (0.07, 0.15, 0.5, and 1.0 MeV) and four different source locations at distances of one and two meters from the center of the phantom.

Fisher and Snyder also developed the “similitude” children phantoms which were scaled-down versions of the adult with added assumption that the entire body was a homogenous tissue (i.e., the lungs and skeleton were ignored). These phantoms represented children with ages of 0 (newborn), one, five, ten, and fifteen years of age. These early designs were assumed to have outer dimensions that represented the average height, surface area, and body mass of a child of the particular age. These phantoms became known as the “similitude phantoms” because of their resemblance to children. This approach had its limitations because children are generally not just “little adults.” However, these phantoms were the first developed to answer a real need in the nuclear medicine community [22].

In 1969, Snyder and his colleagues reported the first heterogeneous phantom that became known as the “MIRD-5 Phantom,” a name derived from the Medical Internal Radiation Dosimetry (MIRD) Committee of the Society of Nuclear Medicine which adopted the phantom [23]. This phantom was composed of a skeleton, a pair of lungs, and the remainder (soft tissue). The representation of internal organs in this mathematical phantom was crude, as the simple equations captured only the most general description of the position and geometry of each organ. The original model was intended to represent a healthy “average” adult male, the Reference Man, as defined by the International Commission on Radiological Protection (ICRP) from an extensive review of medical and other scientific literature on the European and North American populations [246]. The Reference Man was a 20- to 30-year-old Caucasian, 70 kg in weight and 170 cm in height (the height was later changed to 174 cm). In 1978, Snyder et al. published an elaborative set of specific absorbed fractions using an improved version of their

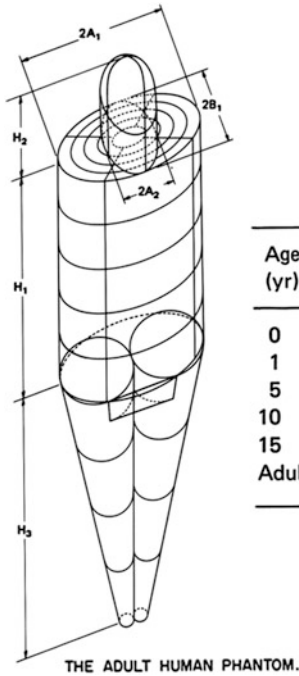
heterogeneous phantom which contained more than 20 organs and more detailed anatomical features [24].

The limitations associated with the approach of applying a set of scaling factors to the adult phantom to create age-dependent similitude phantoms were clear. Significant efforts were undertaken at ORNL during the mid-1970s to develop individual pediatric phantoms based upon a careful review of the existing literature for each particular age. This effort produced the next generation of mathematical phantoms that, although they appeared to be modeled after the adult, were designed independently. Three “individual phantoms” were designed by Hwang et al [25]. This set consisted of the newborn, the one-year, and five-year-old models. A separate effort was undertaken by Jones et al [25] for the 15 years old, and Deus and Poston [26] undertook the design of a 10 years old after the other four designs were complete. The development of the 10 years old was significantly different from those for the other four ages. In fact, this design was intended to point the way to the next generation of more realistic phantoms. Even though the design was completed and used for a limited number of dose calculations, it was not popular because of the very complex geometry and other approaches to the development of phantoms were followed.

12.3.2 Evolution of Stylized Phantoms

Building upon previous work, Cristy reported the development of a new series of stylized phantoms in 1980 and then with Eckerman in 1987 in ORNL/TM-8381 [27, 28]. This series or “family” of phantoms consisted of an adult male, a newborn, and individuals of ages 1, 5, 10, and 15 (also representing an adult female with additional anatomical features). Each phantom is composed of three tissue types with distinct densities: bone, soft tissue, and lung. They were analytically defined in three principal geometric sections as illustrated in Fig. 12.1—an elliptical cylinder representing the arms, torso, and hips; a truncated elliptical cone representing the legs and feet; and an elliptical cylinder representing the head and neck.

In 1995, Stabin and his colleagues at ORNL adapted the adult female phantom in this family to represent a pregnant woman at the end of each trimester of pregnancy [248]. This set of three stylized pregnant female phantoms was used for various internal nuclear medicine applications. Since the 1980s, a number of revised MIRD-5 phantoms were reported which incrementally improved upon the original Fisher-Snyder and Cristy-Eckerman phantoms using the same stylized modeling techniques; however, they are not explicitly listed in Table 1 (i.e., Bouchet et al. on a revised head and brain model [29]). With the availability of general-purpose Monte Carlo codes and affordable computers in the 1980s, this latest series of phantoms, referred to as the “Cristy-Eckerman Phantoms,” were quickly adopted by many users for a wide variety of internal dosimetry applications. Later, this set of phantoms was also used for external and internal dosimetry studies [30, 31].



ORNL-DWG. 74-9373

PHANTOM DIMENSIONS AND DOSE REGIONS

Age (yr)	Weight (kg)	H ₁ (cm)	H ₂ (cm)	H ₃ (cm)	A ₁ (cm)	B ₁ (cm)	A ₂ (cm)
0	3.148	23	13	16	5.5	5	4.5
1	9.112	33	16	28.8	8	7	6.5
5	18.12	45	20	46	11	7.5	6.5
10	30.57	54	22	64	14	8	6.5
15	53.95	65	23	78	18	9	7
Adult	69.88	70	24	80	20	10	7

Fig. 12.1 Stylized phantoms

In parallel with the efforts at ORNL by Cristy and Eckerman to revise the MIRD-5 Phantom, Kramer et al. from the GSF, Germany used the anatomical descriptions of the hermaphrodite MIRD-5 phantom to develop a pair of gender-specific adult phantoms known as the ADAM and EVA for external dosimetry studies [32]. The EVA phantom was derived by shrinking all relevant volumes of the MIRD-5 phantom with the total whole-body mass ratio of 0.83 that was revealed from the analysis of ICRP reference organ masses. Then, the female organ masses were modified to create space for neighboring organs. Finally, sex-specific organ such as testes, ovaries, uterus, and breasts were introduced into the appropriate phantom to yield ADAM and EVA, respectively. The chin was introduced by removing a section of the neck to create a more realistic external irradiation geometry for the thyroid. The female breasts were represented by two ellipsoid sections attached to the trunk of EVA. There are a number of minor anatomical differences, such as breast sizes, from those reported by Cristy and Eckerman [28, 32].

The stylized modeling technique was also adopted by one group for medical applications. The mathematical cardiac-torso (MCAT) phantom, which includes the major thoracic structures and organs, was developed by a research group led by Tsui (currently with Johns Hopkins University) at the University of North Carolina for use in nuclear medicine imaging research, specifically single-photon emission computed tomography (SPECT) and positron emission tomography (PET) [33–35].

The same group later developed the first NURBS-based motion-simulating phantom.

The Computational Anatomical Man (CAM) phantom developed by Billings and Yucker in 1973 for the National Aeronautics and Space Administration (NASA) demonstrated a very different and aggressive approach in stylized modeling because the phantom reportedly consisted of 1,100 unique geometric surfaces and 2,450 solid regions [36]. According to the authors, internal body geometries such as organs, voids, bones, and bone marrow were explicitly modeled using CSG modeling techniques. A computer program called CAMERA was also developed for performing analyses with the CAM phantom. The authors state that “extremely detailed geometrical model of the human anatomy, the most detailed yet prepared, has been developed for use in investigations dealing with exposure of astronauts to the natural space radiation environment. The model is equally applicable to investigations dealing with exposure of humans to radiation associated with nuclear weapon and nuclear power system environments as well as medical applications such as radiotherapy and radiography [36]. Indeed the surface geometry was so detailed that one may wonder how this was possible in the 1970s with much less capable computers. Unfortunately, the CAM phantom was never adopted for applications outside the aerospace industry and very little information about the work was accessible by the phantom research community (Tom Jordan, a contracted phantom developer and user, recently released some CAM phantom images at <http://cmpwg.ans.org/phantoms.html>).

In the early 1990s, it was clear that the research community no longer favored stylized phantom modeling methods. However, several groups continued to develop stylized phantoms for particular methods. Two groups developed computational phantoms of an embryo and fetus for space radiation dosimetry [249] and an adult representing the Korean population [37]. A group at the Nagoya Institute of Technology developed two new stylized phantoms for a 9-month Japanese infants in 2008 [38]. Researchers at the Key Laboratory of Particle & Radiation Imaging in Beijing created a new mathematical phantom named the Chinese mathematical phantom (CMP) in 2008 based on values obtained from the Reference Asian Man and the Chinese Reference Man [39]. A new MIRD phantom based on reference data for the standard Korean male was developed at the Catholic University of Pusan, Bugok [40]. The phantom was used to model a patient implanted with Iridium-192 for brachytherapy of prostate cancer. Bento et al. [41] at the Nuclear and Technological Institute (ITN) of Portugal developed a new mathematical phantom to simulate the reference male BOMAB phantom. The phantom was used to simulate the detection of internal sources of radiation with a whole-body counter (WBC). A series of four mathematical phantoms were developed at the Bhabha Atomic Research Centre to simulate the calibration of whole-body monitoring systems for internal radionuclide contamination using BOMAB phantoms [42].

For 40 years since the first anthropomorphic phantom was reported, these anatomically simplified phantoms have been used as the *de facto* “standard” representations of the ICRP “Reference Man” methodology which is based on “population-average” 50th

percentile anatomical parameters [246, 247]. Applications of stylized phantoms have eventually included many aspects of radiation protection, radionuclide therapy, and medical imaging [43]. In addition, national and international bodies have adopted organ dose estimates derived from these stylized phantoms in guidelines and regulations related to industrial and medical uses of ionizing radiation.

Although stylized phantoms made it possible to carry out Monte Carlo computations during times when computers were much less powerful, the original developers recognized the obvious shortcomings. Human anatomy is too complex to be realistically modeled with a limited set of surface equations. Many anatomical details in these models were compromised that sometimes led to inaccurate results. For example, when such phantoms were applied to nuclear medicine procedures where precise dosimetry is necessary, the calculated average organ and marrow doses did not produced strong correlations with observed marrow toxicity. Most nuclear medicine physicians consequently tend to administer lower-than-optimal amounts of radioactivity to avoid toxicity. For CT dose reporting, all existing commercial software systems are based on the stylized patient models that are known to cause very large errors for low-energy X-rays [44]. Similar stylized models have also been used to derive dose–response relationships for Japanese atomic bomb survivors and for medical patients in epidemiological studies. In the external-beam radiotherapy community, an early stylized homogenous phantom was used by the Radiation Epidemiology Branch of the National Cancer Institute (NCI) for nearly 30 years in studies related to organ doses of therapeutically irradiated patients [45]. By the 1980s, a few groups of researchers began to seek new ways to develop anatomically realistic phantoms.

12.3.3 Second-Generation Voxel Phantoms (from late 1980 to Early 2000s)

The development of anatomically realistic models was desirable but impossible until early 1980s when powerful computer and tomographic imaging technologies became available. With the advent of CT and MR imaging techniques, researchers could for the first time visualize the internal structures of the body in three dimensions (3D) and store the images in versatile digital formats. These advantages brought about the exciting and prolific era of the so-called voxel or tomographic phantoms . Xu [5] summarizes a total of 84 phantoms that were constructed from three types of tomographic images: CT and MR images from live subjects, as well as cross sectional photographs of cadavers. In two earlier review articles, the number of voxel phantoms was reported to be 21 by Caon [10] and 38 by Zaidi and Xu [11]. The increase in phantom number reported by Xu [5] was due to a more exhaustive literature search, recent developments, and the inclusion of phantoms developed for use solely in non-ionizing radiation applications.

In terms of solid geometry modeling techniques, a voxel—one of the basic CSG primitives—is simply a 3D representation of a pixel; however, compared with the medical applications such as radiation treatment planning, the task of developing reference human phantoms presented some unique and intractable challenges: (1) to construct a whole-body phantom, image slices should ideally cover the entire body—a process not normally carried out in routine medical examinations because of *X*-ray exposures or the lengthy time required for MR procedures; (2) a large amount of internal organs/tissues must be identified and segmented for organ dose calculations, whereas, in radiotherapy, only the tumor volume and adjacent regions are routinely outlined; (3) the image data size of a whole-body model, especially when high-resolution images are used, can be potentially too great for a computer to handle; and (4) a standardized patient phantom is often used to study diverse radiation types such as photons, electrons, neutrons, and protons, thus requiring considerable Monte Carlo simulation capabilities.

In terms of the developmental process, voxel phantoms are fundamentally different from the stylized ones. A tomographic image data set is composed of many slices, each displaying a 2-dimensional (2D) pixel map of the anatomy. The 3D volume of a voxel is measured by multiplying the pixel size by the thickness of an image slice. Unlike stylized phantoms, which are based on quadric surface equations, a voxel phantom contains a huge number of tiny cubes grouped to represent various anatomical structures. However, both quadric surface equations and voxels (cuboids) belong to the same class of CGS geometries

The creation of a tomographic phantom involves four general steps: (1) acquire a set of tomographic images (e.g., CT, MR, or anatomical photography) that cover the entire volume of the body; (2) identify organs or tissues of interest (e.g., lungs, liver, skin) from the original image slice by assigning every pixel with an identification number; (3) specify the density (e.g., soft tissue, hard bone, air) and chemical composition of organs or tissues; and (4) register the segmented image slices into a 3D volume that can be used for 3D visualization (for checking anatomical structures) and for Monte Carlo calculations. Figure 12.2 illustrates

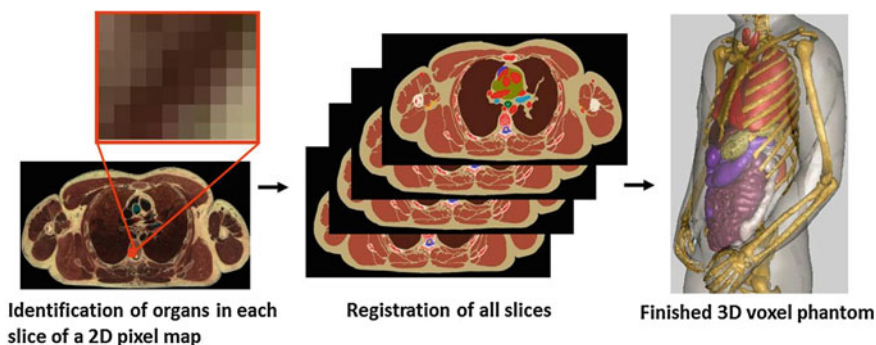


Fig. 12.2 Steps to create a voxel phantom illustrated using the Visible Human cadaver image data set [46]

these steps reported by Xu et al. [46] using the National Library of Medicine's Visible Human image data set.

The earliest effort to create image-based phantoms for radiation protection dosimetry is believed to have been reported by the late Professor S. Julian Gibbs of Vanderbilt University [47–49]. In these pioneering studies, Gibbs and her co-workers explored the use of 2D X-ray images as the basis to form an anatomically realistic model of the patient. They used this information in Monte Carlo calculations to assess the doses received by patients who underwent from medical and dental radiological procedures.

Zankl and her colleagues at GSF—National Research Center for Environment and Health in Germany (Now known as HZM—the German Research Center for Environmental Health) decided in the late 1980s to use CT imaging on healthy volunteers to develop what eventually became a family of 12 voxel phantoms: BABY, CHILD, DONNA, FRANK, HELGA, IRENE, GOLEM, GODWIN, VISIBLE HUMAN, LAURA, KLARA, and KATJA [50, 51], Petoussi-Henss 2002, [52–55]. The adult male phantoms were developed first, followed by the adult female, pediatric, and pregnant woman phantoms. The GOLEM and LAURA phantoms have recently undergone significant revision, to yield the REGINA and REX phantoms, which were released to the public as the ICRP Reference Computational Phantoms [56, 57]. Several processes were considered at the time when this set of reference phantoms were developed: (1) CT image data sets of individuals close to the Reference Man and Reference Woman (height and weight) were needed, (2) the data sets were segmented, (3) the body heights were adjusted to reference values by scaling the voxels, (4) the skeletal masses were adjusted to the reference values, and (5) individual organs were adjusted to reference values by adding and subtracting voxels.

In 1994, Zubal et al. [58] from Yale University published a head-torso model named VoxelMan, which was developed from CT images. The original phantom was used for optimizing nuclear medicine imaging. Improvements to the original phantom were made with an MRI scan data of a human brain. Users who are allowed to freely download the original data by using the Internet commonly refer to this phantom as the “Zubal phantom.” Two early users later revised the original data to report what are known as the MANTISSUE3-6 and VOXTISS8 phantoms by attaching arms and legs in two different positions to the original torso phantom [59, 60]. Adopting this publically available data, Kramer et al. from Brazil developed an adult male phantom named MAX (Male Adult voXel) in 2003 [61] and later an adult female phantom named FAX in 2004 [62], both adjusted in accordance with ICRP-89 reference body heights and organ masses. Kramer et al. revised the skeletons (cortical bone, spongiosa, medullary yellow bone marrow, and cartilage) of MAX and FAX in 2006 to improve their compatibility with the latest ICRP-103 recommendations. These revised phantoms are known as MAX06 and FAX06. The work by Kramer et al. is one of the earliest efforts to create ICRP-89 compatible voxel phantoms.

In 1996, Dimbylow from the National Radiological Protection Board (NRPB) (now known as the Health Protection Agency) in the United Kingdom reported the

development of an adult male phantom known as NORMAN from MR images [4]. NORMAN, which has a body height similar to the ICRP Reference Man, was first used by Dimbylow in a finite-element simulation code to determine the specific energy absorption rate from exposures to non-ionizing electromagnetic fields [63]. In 1997, his colleague Jones adopted NORMAN to estimate organ doses from external and internal photon sources [64]. In 2005, Dimbylow developed an adult female phantom, NAOMI, also from MRI scans [65, 66]. The phantom was rescaled to a height of 1.63 m and a mass of 60 kg, the dimensions of the ICRP Reference Woman. However, to date, the NAOMI phantom has been used only in non-ionizing radiation calculations. In 2005, a revised version of the NORMAN phantom, called NORMAN-5, was created by Ferrari & Gualdrini from ENEA-ION Istituto di Radioprotezione in Italy to derive external photon dose data [67]. One year later, Dimbylow merged the NAOMI with the stylized fetal phantoms developed by Chen to create a series of hybrid phantoms for pregnant women [68]. The process of adjusting two types of geometrical information was reported to be cumbersome.

In 1999, Caon et al. from Flinders University in Australia reported a torso phantom named ADELAIDE created from CT images of a 14-year-old girl [69, 70]. This phantom was interesting because, for some time, it was the only set of data for a teenage girl, and their studies provided CT dose estimates for this patient group. Caon later summarized his and other researchers' experience on voxel phantoms [10].

Realizing the need for additional phantoms representing children of various ages, Bolch and colleagues from the University of Florida (UF) developed a series of pediatric voxel phantoms that appeared between 2002 and 2006, representing children with ages ranging from newborn to 15 years old [71–73]. This approach was later extended to two groups (Groups A and B) of phantoms. Group A is composed of male and female voxel phantoms of a newborn, 1, 5, 10, and 15 years old for whom the phantom stature, total weight, and individual organ masses are targeted to within 1 % of ICRP Publication 89 reference values. Group B phantoms are constructed by scaling the Group A phantoms up and down to yield phantom at each 1-year-age interval, from newborn to 15 years old. The intent of the UF pediatric series was to provide a reference library of phantoms that could be matched to individual patients for age-specific organ dose assessment.

The VIP-Man voxel phantom was reported in 2000 by Xu and two of his students at Rensselaer Polytechnic Institute (RPI) in the United States [46]. VIP-Man was the first phantom that was based on cross-sectional color photographic images of a cadaver. The original photographs were of a 39-year-old male which were made available through the National Library of Medicine's famous Visible Human Project (VHP). VIP-Man is unique because the digitally captured color transversal photos a 0.33×0.33 mm pixel resolution, which was the best resolution at the time, and each photograph was taken after the removal (by shaving) of each successive 1-mm layer by a cryomacrotome [46]. The VIP-Man phantom consists of more than 3.7 billion voxels, and the original images were segmented to yield more than 1,400 organs and tissues, although only approximately 80 organs

and tissues were ultimately adopted for radiation dosimetry purposes. With ultra-fine and color images, attempts were made to segment and label a number of small and radiosensitive tissues including the stomach mucosa, skin, and red bone marrow. The finalized VIP-Man phantom had a heavy body mass of 103 kg, which served as an interesting variation from the ICRP reference value. The VIP-Man was used for a large number of studies in health and medical physics. Later, this group extended the 3D phantom into 4D using the NURBS technique. Several other groups also used the VHP images, but they primarily considered the CT data set without the arms. In 2004, Shi and Xu from RPI also reported the pregnant woman phantom, which was developed from rare partial-body CT images of an eight-month pregnant patient [74]. As of May 15, 2012, this paper on VIP-Man phantom by Xu et al. [46] had been cited 266 times and, according to Google Scholar, making it the most cited paper in “computational dosimetry phantoms.”

Two Japanese groups reported their independent efforts to develop voxel phantoms since 2001. Saito et al. [75] from the Japanese Atomic Energy Research Institute (JAERI) developed an adult male model named Otoko (the first Asian phantom) and an adult female phantom named Onago. More recently, Saito et al. has developed the JM, JM2, and JF phantoms which have a refined vertical slice thickness [76–78]. These phantoms were used mainly for radiation dosimetry applications in Japan. The work of Saito et al. was influenced by earlier projects at the GSF. The other group, Nagaoka et al., from the National Institute of Information and Communications Technology (NICT) in Japan reported an adult male model, named TARO, and an adult female model, named HANAKO, developed from MR images for radiofrequency electromagnetic-field studies [79]. Later, Nagaoka et al. would use a free-form deformation (FFD) to change the exterior features of the adult male phantom to develop Deformed Children phantoms of 3, 5 and 7 years old [78]. The authors reported that it was difficult to develop these phantoms with the FFD algorithm and the internal organs are not adjusted to age-dependent values. The Otoko phantom was recently used in a study to calculate dose conversion coefficients for the Japanese population [80].

Several Korean phantoms have been developed by researchers at Hanyang University in Korea from various image sources: Korean Man (KORMAN), Korean Typical MAN-1 (KTMAN-1), Korean Typical Man-2 (KTMAN-2), High-Definition Reference Korean (HDRK), and Korean WOMAN (KORWOMAN). The HDRK phantom was based on sectioned color photographs of an adult male cadaver that has high image resolution [81, 82]. The early work on these phantoms was carried out by the two Lee brothers, who moved in the early 2000s to the University of Florida, where they gradually published work on the Korean phantoms and also made important contributions to the NURBS-based phantoms. Kim spent several years in the US to complete his PhD. from Texas A&M University and then to serve as a research professor at RPI before returning to Hanyang University as a faculty member in the early 2000s. Their separate involvements in the area of voxel phantom development clearly originated from their experiences in the US. The KTMAN-2 phantoms have been used by Lee et al. [83] to measure the effects of selective collimation in cephalography.

Kim et al. [40] from the Korea Atomic Energy Institute have developed a series of voxel phantoms of different body shapes in order to calculate counting efficiencies for whole-body counters. The phantoms are meant to replace a physical BOMAB phantom, which will not yield proper results for the counting efficiencies in some patients due to differences in body shape, such as from obesity.

Three voxel phantoms representing an adult Chinese male have been reported since 2007: CNMAN produced from color photographs of a cadaver by the China Institute for Radiation Protection [85], VCH produced from a different set of cadaver color photographs by the Huazhong University of Science and Technology [86–88], and CVP produced from MR images by Tsinghua University [89, 51]. The Chinese government undertook the Chinese version of the Visible Human Project that resulted in multiple cadaver image data sets, some with slice thickness as fine as 0.2 mm. The lead developer of the CNMAN phantom, B Zhang, served as a research associate at RPI in 2007–2008. Another new Chinese phantom was developed by Li et al. [89] at the Key Laboratory of Particle and Radiation Imaging in Beijing. The phantom was named the Chinese voxel phantom (CVP) and was used to determine conversion coefficients for the Chinese populace. The phantom was produced from MR images of a young Chinese male and was segmented into 23 different tissues and organs.

Researchers at the French National Institute of Health and Medical Research (INSERM) reported a series of virtual whole-body patient models (WBPM) from CT images [90]. The phantoms accommodate different radiotherapy treatment positions, genders, and age groups. Alzier et al. developed a software tool to take patient data and adjust the phantom's anatomy in order to match the patient's anatomy.

In 2009, the ICRP released its Publication 110 which describes the development and intended use of the so-called ICRP computational phantoms of the Reference Male and Reference Female [56]. This pair of phantoms is based on medical image data of real people, yet is consistent with the data given in Publication 89 [247] on the reference anatomical and physiological parameters for both male and female subjects. The reference phantoms are constructed after modifying the voxel models (Golem and Laura) of two individuals whose body height and mass resembled the reference data. The organ masses of both models were adjusted to the ICRP data on the adult Reference Male and Reference Female, without compromising their anatomical realism. ICRP-110 is big step forward in standardization. However, the techniques used to develop such voxel phantoms were quickly out favor and were replaced by newer techniques.

A voxel phantom named NUDEL (NUmerical moDEL) was developed by Ferrari [91] for use in radiation protection. The phantom was constructed from CT data of the plastic AMOS (Anthropomorphic MODEL for dosimetric Studies) phantom. Dose calculations for several types of nuclide exposure were run in MCNPX code and were compared to values obtained from other voxel phantoms.

Patni et al. [92] of the Bhabha Atomic Research Centre in India published dose conversion coefficients obtained from the ICRP adult voxel phantoms. The study

adapted the phantoms for use in the Monte Carlo code FLUKA and calculated dose conversion coefficients for 9 different organs.

A radiological accident that occurred in South America in 2009 prompted the construction of a personalized voxel phantom to numerically calculate the dose the victim received. Courageot et al. [93] of the Institute for Radiological Protection and Nuclear Safety (IRSN) converted CT scans into a voxel phantom using the Simulation of External Source Accident with Medical Images (SESAME) tool. The dose distribution was calculated using MCNPX code and was used in the treatment of the victim. Courageot et al. [94] reported the Simulation of External Source Accident with Medical Images (SESAME) tool that allows the use of NURBS to model a victim's morphology and posture.

Tung et al. [95] from the Chang Gung University of Taiwan developed a voxel phantom of the Reference Taiwanese Adult. CT images from thirty Taiwanese adults were analyzed by hand and in the software environment 3D-Doctor and compared to reference values to construct the phantom.

Project members of MATSIM (MATROSHKA Simulation) at the Austrian Institute of Technology coordinated research to numerically simulate the effects of irradiation under reference radiation fields in outer space [96]. They created a two-part voxel phantom using the FLUKA Monte Carlo code and CT images from a physical RANDO phantom. The voxel phantom was split into the MATSIM torso and head. The results of the simulations were within one standard deviation of experimental values.

ORNL has not been actively involved in the development of voxel phantoms, although Eckerman was instrumental in the work at GSF related to the ICRP reference computational phantoms and a number of voxel phantom projects at several universities in the US. The only reported effort from ORNL was that of Akkurt et al. [97] on a hybrid of voxel and stylized geometries.

In 2011, the University of Florida (UF) published the results of a study on electron dosimetry using the UF adult male hybrid phantom [250]. Monoenergetic electron emissions, ranging in energy from 10-keV to 10-MeV, were simulated with particular interest on the active bone marrow and total shallow marrow. The skeletal tissues were imposed through whole-body CT images at 1-mm resolution. The results of the study were found to be compatible with the averaged skeletal values of the absorbed fraction given in ICRP 110, but incompatible with the internal dosimetry software used currently.

Recently, a team of scientists from Iran and Japan collaborated to develop a race-specified voxelized organ, specifically a Japanese male liver [98]. The purpose of this development was to have race-specific organ modeling for nuclear medicine and internal dosimetry purposes. The liver was constructed using the digital Zubal phantom and 35 CT scan images for male individuals of Japanese descent. The detailed process for this development included using a point-drift maximum likelihood alignment algorithm. The technique used allowed for the retainment of anatomical realism and provides nuclear medicine dosimetry with statistical parameters.

12.3.4 BREP Phantoms from 2000s to Present

Ten groups reported a total of 183 BREP-based phantoms. Segars's PhD. thesis at the University of North Carolina was the first publication that systematically described the NURBS-based modeling techniques [99]. The cardiac-torso (NCAT) phantom was developed from the Visible Human CT image data set and the 3D anatomy was later extended into the 4th dimension to model cardiac and respiratory motions. The beating heart model of the 4D NCAT was based on 4D tagged MRI data from a real patient. The 4D NCAT phantom offers a vast improvement over the stylized MCAT phantom, with more realistic models of the anatomy and the cardiac system, and the respiratory motions. The 4D NCAT has gained a widespread use particularly in nuclear medicine imaging research for evaluating and improving myocardial SPECT imaging. The conceptual design of the NCAT phantom also served as basis for the development of a 4D digital mouse phantom named MOBY [100, 101]. Segars et al. [102] released an update to the NCAT phantom in the form of a 4D NURBS-based cardiac phantom. The cardiac phantom was constructed from a series of tagged MRI images in the SURFdriver program. The cardiac phantom performs normal cardiac motion in simulations, but Segars released an application that can modify the heart's motion to account for some defects in the same study. The 4D extended cardiac-torso (XCAT) phantom family was recently developed as the next version of the 4D NCAT. It includes more detailed and realistic anatomy and physiology, suitable for use in higher-resolution imaging applications. The XCAT phantom family includes whole-body male and female anatomies based on the high-resolution Visible Male and Female anatomical data sets [103]. In addition to the basic anatomy, the cardiac and respiratory motions were also updated in the XCAT phantom. The series includes 47 phantoms based on of the XCAT phantom. The XCAT phantom was mapped to patient CT data to produce the series. Segars ran simulations of PET, SPECT, and CT to demonstrate the applicability of the phantoms. The NCAT and XCAT phantoms have been used by several research groups to simulate radiation dose from radiography [104, 105] and radiotherapy [237, 106]. A research group constructed a version of the XCAT heart to enhance the range of cardiac disorders that can be studied using the phantom [107]. Tward et al. [108] from John Hopkins University developed a series of pediatric phantoms from a base adult XCAT phantom. They used a MATLAB-based implementation of large deformation diffeomorphic metric mapping (LDDMM) to adjust the XCAT phantom to match pediatric reference data. The implementation used multi-channel LDDMM to treat each organ as a separate image unified by a common background. An algorithm to modify the XCAT phantom was developed and used to generate 24 male pediatric patients with 8 organs each.

In 2005, the research group led by Xu at RPI used the VIP-Man phantom to simulate respiratory motions by adopting the gated respiratory motion data of the NCAT phantom [251]. The 4D VIP-Man Chest phantom was used to study external-beam treatment planning for a lung cancer patient [233]. The group later

decided to apply the BREP techniques to a more challenging problem and, in 2007, reported the development of a series of phantoms representing a pregnant woman and her fetus at the end of 3-, 6-, and 9-month gestations [109]. These phantoms, referred to as the RPI pregnant females, were defined by polygonal meshes which were derived from separate anatomical information of a non-pregnant female, a 7-month pregnant woman CT data set, and a mesh model of the fetus. The organ volumes were adjusted in the mesh format using a commercial software package. The paper by Xu et al. was rated one of the 10 best papers in 2007 by Physics in Medicine and Biology. Continuing their triangular mesh approach, this group reported in 2008 the development of a pair of adult male and female phantoms, the so-called RPI Adult Male and Female [110, 111, 112]. This pair of adult phantoms was carefully adjusted to match the ICRP-89 reference values for more than 70 organs and 45 bones (including cortical bone, spongiosa, and cavities) as well as muscles. Several software algorithms were systematically developed to automate the deformation and organ overlap detection that were based entirely on about 126 sets of triangle meshes. The RPI Adult Male and Female phantoms are mesh-based BREP phantoms [112]. As an application, the female phantom was recently used to create phantoms of female workers with different breast sizes for the purpose of studying the effect of this parameter on the lung counting of internally deposited radionuclides [110]. The mesh models had to be converted to voxels to work with Monte Carlo codes that only handle CSG shapes. In a second application, Ding et al. [113] modified the RPI Adult Male and Female phantoms and produced 10 obese phantoms for the purpose of optimizing image quality and dose in obese patients. The initial study used the obese phantoms in dose calculations, and it was found that calculated dose for obese patients differed significantly from the dose calculated for normal weight phantoms. Taranenko and Xu [225] used the RPI-P phantom series to calculate conversion coefficients for fetuses from whole-body irradiation with monoenergetic proton beams. The simulation was run in MCNPX for 12 different source energies ranging from 100 MeV to 100 GeV, and for 6 different configurations. Gu et al. [114] used the RPI Pregnant Female phantoms to run dose calculations for multi-detector CT (MDCT) scans. The MDCT scanner and the phantoms were implemented in MCNPX code. The dose profiles showed that there was little risk to the patient or the fetus from the MDCT scans.

In 2007 and 2008, the UF group led by Bolch reported their work on the so-called “hybrid” male and female phantoms of newborn and 15-year-old patients [115, 116]. They created the BREP phantom series, called UFH-NURBS phantoms using the following steps. First, they segmented patient-specific CT image data from which they then generated polygonal meshes. These meshes were then converted to the NURBS format using commercial software. In this last process, they extracted several contours from the polygonal meshes and then generated the NURBS surfaces by a software tool called “lofting.” It was then in the NURBS geometrical domain they carried out organ adjustment to match the ICRP-89 reference. Therefore, their phantoms are in fact NURBS-based BREP phantoms, like those developed by Segars et al. [99]. In the final step, the NURBS-

based phantoms were voxelized so that they could be implemented in Monte Carlo calculations. However, in order to voxelize the smooth NURBS models, they transferred the NURBS surfaces back the polygonal meshes. The paper by Lee et al. [51] was also rated one of the 10 best papers in 2007 by Physics in Medicine and Biology. In 2011, Maynard et al. [117] from the UF produced a family of NURBS-based fetal phantoms. The phantoms were based on CT and MR images from fetal specimens of various ages between 10 and 30 weeks and were modified to conform to reference values. Tissues and organs were segmented using the modeling software 3D-Doctor and turned into polygon mesh surfaces. The models were then imported into Rhinoceros 3D to incorporate NURBS surfaces and correctly orient the models. The UF phantoms family has seen wide use. The UF hybrid adult male phantom was used in a study by Johnson et al. [118] to calculate the effects of patient size on dose conversion coefficients. A model of electron dosimetry on infants based on the UF hybrid newborn phantom and an earlier developed skeleton tissue model [119] was released by Pafundi et al. [120] from the University of Florida. Hough et al. [121] released a model for skeletal-based electron dosimetry in the ICRP reference male. CT scans of a cadaver were implemented in Rhinoceros 3D to modify the UF hybrid male reference phantom to include segmented skeletal tissue. Dimbylow et al. [122] published a study that used the University of Florida's newborn NURBS-based voxel phantom to calculate SAR for exposure to electromagnetic fields in the 20-MHz to 6-GHz region. Bahadori et al. [123] from the University of Florida released a publication studying dose estimates from space radiation on astronauts. They modeled the astronauts by adapting the UF family of hybrid phantoms to the 5th, 50th, and 95th percentiles for 40-year-old American males and 40-year-old Japanese females.

In 2008, the Vanderbilt group led by Stabin, in collaboration with Segars from Duke University, reported a "family" of adult and pediatric phantoms by adapting the NURBS-based NCAT adult male and female phantoms [124, 125]. ICRP-89 reference body and organ values were used to adjust NURBS surfaces. The authors state several advantages of this approach: (1) NURBS-based phantoms can be developed much more quickly than working with voxels and manually segmenting individual patient image data sets; (2) The phantoms have a higher level of internal consistency; and (3) The phantoms are complete from head to toe, thus avoiding the problem of missing organs in some of the medical images. It is noted that the groups at RPI, UF, and Vanderbilt (and Duke) developed these BREP phantoms as part of the joint Virtual Patients Project funded by the National Cancer Institute as well as other individual projects.

Cassola et al. (2010) at the Federal University of Pernambuco (UFPE) have constructed two phantoms based on polygon mesh surfaces. The phantoms, FASH (Female Adult meSH) and MASH (Male Adult meSH), were constructed using software, including Blender, ImageJ, Binvox, and MakeHuman. The researchers based their phantoms on anatomical models and atlases and showed that whole-body CT scans are unnecessary for phantom design. The organ masses were based on the values recommended for the male and female reference adult in report 89 from the ICRP. Cassola compared FASH and MASH to the RPI-AF and RPI-AM phantoms

and noted significant differences in anatomy. The UFPE group [238] made a series of calculations on the FASH and MASH phantoms. Large differences were observed compared to calculations done on the RPI-AM and RPI -AF mesh phantoms.

In 2010, four phantoms collectively named The Virtual Family were developed for electromagnetic exposure calculations by Christ et al. [126] at the Foundation for Research on Information Technologies in Society (IT'IS). The Virtual Family consists of a 34-year-old adult male, 26-year-old adult female, 11-year-old girl, and a 6-year-old boy. MR images from volunteers were analyzed and segmented into 80 different tissues and organs using the imaging processing software iSEG. The boundaries between the tissues and organs were then remodeled using the software tool Amira. The Virtual Family is a part of the larger Virtual Population project at IT'IS. The Virtual Population project has developed 6 additional anatomical models using the same methods that were used with the Virtual Family [127]. The additional models consist of the Virtual Classroom, a series of four child models, and two individually developed models: an obese 37-year-old male model, and an aged 84-year-old male model.

Cassola et al. [177] continued the work on the FASH and MASH phantoms and published a library of 18 phantoms in 2011. The phantoms were adjusted based on reference values for the 10th, 50th, and 90th height and mass percentiles for Caucasian members of each gender. The reference values were obtained from the PeopleSize software package, which obtained the values from over 100 publications in North America, Asia, Australia, and Europe. In 2011, the group published 5- and 10-year-old pediatric phantoms based on the same methodology that created FASH and MASH [128]. The phantoms were developed with polygon mesh surfaces in the modeling programs Blender and MakeHuman and were edited in the programs DIP (Digital Imaging Processing) and QtVoxel. The researchers used ICRP data for the 5- and 10-year-old reference children. They did not use medical images to construct the phantoms and instead relied on anatomical atlases and modeling software.

The group at IRSN developed a series of female torso phantoms in the Rhinoceros-3D modeling environment [183]. A base thoracic torso phantom was produced from mesh surfaces and NURBS and was based on the reference data from the ICRP adult female reference computational phantom. A series of 34 phantoms of differing girth, cup size, breast tissue composition, and internal organ volumes were created from the base phantom. They used the phantoms to ascertain the morphological dependence of counting efficiency curves from in vivo lung monitoring of workers [129]. In 2011, they released a thoracic male phantom and a mesh equivalent to the physical Livermore phantom for the purposes of simulating in vivo measurements [129]. The phantoms were modeled with mesh and NURBS geometries. Data from CT and MRI scans were analyzed in Isogray to delineate organs. The data were then imported to Rhinoceros 3D, where it was assembled into the two phantoms. Simulations of the two phantoms yielded comparable data to those done with voxel phantoms. The phantoms will be the basis for a new library of phantoms in a future study.

A separate project at the IRSN produced a library of 25 whole-body male phantoms in 2011 [130]. The phantoms were produced from data in the CAESAR

database, a compilation of male and female 3D models constructed from full-body optical imaging. A total of 22 male Caucasian optical models were used as the basis for the phantoms. The phantom's organs were constructed from ICRP reference data and added to the optical models. The phantoms possess a total of 109 segmented organs. The phantoms occupy a range of different body types, organ masses, and organ volumes.

Current permutations of hybrid phantoms must be voxelized so that they may be used in Monte Carlo dose calculations. Voxelizing a hybrid phantom reintroduces the majority of the limitations of the voxel phantoms. Researchers at Hanyang University in Korea have converted the voxel phantom VKH-Man into a polygon surface phantom using 3D-Doctor and directly implemented the phantom into Geant4 in order to circumvent this limitation [131]. Calculations on their new phantom, PSRK-Man (Polygon Surface Reference Korean Man) has been compared to the HDRK-Man phantom, which was also based on VKH-Man. The PSRK-Man phantom has overcome many of the limitations of a voxel phantom; however, the calculation speed for the phantom is 70–150 times slower than for its voxel counterpart HDRK-Man.

12.4 Applications of Computational Phantoms at RPI

Computational phantoms have been used extensively at RPI for diverse health physics and medical physics applications, including external photon beams from 10 keV to 10 MeV [132, 133], external electron beams [134, 135], external neutron beam in low energies (10^{-9} –20 MeV) and in high energy (20–10,000 MeV) [134, 136], external proton beams [137], photon dose to the red bone marrow [174], internal electron dosimetry [138, 139], SPECT and PET brain imaging [140], X-ray radiographs [141], X-ray image quality ROC/AUC analysis [142], interventional cardiological examinations [143], adjoint Monte Carlo algorithm for external-beam prostate radiation treatment planning [231], non-target organ doses from proton radiation treatments [145], respiration management in IGRT [233], imaging doses in IGRT [44], kV CBCT and MDCT [146], and time-resolved proton range telescope [147]. More information can be found at the website for Rensselaer Radiation Dosimetry and Measurement Group (<http://rrmdg.rpi.edu>).

12.5 Monte Carlo Methods and Computer Codes

There are a few comprehensive reviews or introductory articles about the Monte Carlo methods for applications in health physics and medical physics [148–150]. Several public-domain and popular Monte Carlo code systems include MCNP (X-5 Monte Carlo Team 2003), MCNPX [151], EGS [152], Geant4 [6, 7, 153], PENELOPE [154–156], and Fluka [157, 158].

12.6 Non-ionizing Radiation Applications

People who have been interested in non-ionizing radiation applications form a different group of voxel phantom developers. Most of this work was neglected in the previous review articles by Caon [10] and by Zaidi and Xu [11]. Interestingly, the phantoms used for studies of temperature rise in the human body from the interactions of radiofrequency energy were constructed through nearly identical steps and some of these phantoms, such as the NORMAN phantom, have been used for both ionizing and non-ionizing radiation applications. However, the majority of voxel phantoms were developed with only one application in mind. Some phantoms have been used for non-ionizing applications: the Visible Man from the VHP color photographs by the Brooks Air Force (Mason et al. 2000), [159], the DAM adult male phantom from MR images by a group in Italy [160], the SILVY 30-week pregnant woman phantom from hybrid CT (originally obtained by RPI) and MR images by the Graz University of Technology, Austria [161, 162], the MEET Man from VHP color photographs by University of Karlsruhe, Germany [163, 164], and the anatomically based model from MR images by University of Utah [165]. The redundancy in developing voxel phantoms from similar image sets such as the VHP is obvious.

Findlay and Dimbylow [166] from the Health Protection Agency in the UK published a study of the specific absorption rate (SAR) for exposure to electromagnetic fields using the NORMAN phantom. Findlay and Dimbylow [167] continued their work on SAR measurements and conducted a study of SAR in children due to Wi-Fi. He rescaled the sitting posture NORMAN phantom so that it matched ICRP reference values for a 10-year-old child. The effects of electromagnetic fields from Wi-Fi devices operating at 2.4 and 5 GHz were modeled using a FDTD method.

Uusitupa et al. (2010) published a study measuring SAR in the 300- to 5000-MHz region utilizing 15 voxel phantoms, including NORMAN, the Japan Male/Female, the VHP Male, and the VF series. The simulations were run with FDTD code on a HP supercluster at the Helsinki University of Technology in Finland. The study modeled the effects of different postures, human body models, and incoming direction of the electromagnetic field.

A series of 9 phantoms representing a pregnant female in each gestational month developed by a group from the University of Houston and the US Food Drug Administration (FDA) for studying the effects of radiofrequencies emitted from various electronic devices [168]. These phantoms only include a limited number of organs such as the body, placenta, embryonic fluid, bladder, bone, fetus, and the uterus. They used patient-specific MR images and CAD software to model the organ shapes.

12.7 Discussion and Conclusion

Computational phantoms have come a remarkably long way. Mathematical formulations of organs and tissues of the body used in the dosimetry of internally distributed radionuclides existed as early as the 1940s, although the first anthropomorphic phantom was not reported until the 1960s. In the 1970s and 1980s, the sophistication of these stylized phantoms was increased significantly. This evolution began with the specification of a single organ mass, followed by the use of simple shapes to simulate organs or the entire body of an adult human. The desire to model the entire body of a “Reference Man” and to specify the location, shape, volume, and mass of organs in the body as realistically as possible has remained the same to this day. The climax for stylized phantoms was reached in the 1980s when the gender- and age-specific family phantoms were systematically documented and widely adopted for various studies in internal and external radiation dosimetry, as well as in medical imaging and radiotherapy. By that time, Monte Carlo codes and personal computers had become accessible to a large number of researchers. The research on stylized human models carried out at ORNL up to the 1980s played an essential role in the history of computational phantoms. The sex-specific adult phantoms at GSF in the early 1980s were revisions of the MIRD-5 phantom originally developed at ORNL. Major extensions in the 1990s, on the pregnant women and brain/head models, were also closely tied to the earlier work at ORNL. The direct involvement of ORNL’s scientists in the SNM’s MIRD Committee facilitated the necessary standardization process. It is clear that close collaborations between leading developers were a key factor contributing to the success of these first-generation computational phantoms. Not all phantoms of this generation enjoyed the same recognition in the history. In fact, a few phantoms such as the CAM have been practically unknown by the mainstream radiation protection dosimetry community. The late 1980s would go into history as the beginning of an exciting new era of voxel phantoms. Collaboration in the information age would soon require new approaches, and as the history would show, no single developer was to dominate the new research agenda as ORNL once did.

The shift from stylized phantoms to voxel phantoms in the late 1980s was motivated by the desire to improve upon anatomical realism. The advent of modern computers and medical imaging fueled the research efforts by many researchers. For a long period of time in the 1990s and early 2000s, however, it was unclear to the research community what roles voxel phantoms would play. If voxel phantoms were to replace stylized phantoms, how much improvement in dose estimates should be expected? There were strong indications already that the approach of developing and applying the voxel phantoms was not perfect. For example, the of original images into organs and tissues required a very laborious and tedious manual process (there is only a limited number of organs such as the skeleton which can be processed automatically and semi-automatically), often taking months or years to complete. The earlier phantoms developed at GSF had relatively poor image slice thickness (from 4 to 8 mm), thus inevitably

compromising the anatomical accuracy. Even today, there is no consensus as to what constitutes a true segmentation because the process often involves some level of user-specific assumption about the anatomy during the image analysis. Certain organs such as the GI tract have poor image contrast, and the segmentation is nearly impossible in CT without enhancement. A typical image data set at more than $2\text{ mm} \times 2\text{ mm}$ pixel resolution is not fine enough to delineate many small radiosensitive organs. As a result, the skin of most existing voxel phantoms is defined artificially as the outermost layer of voxels. The segmentation of the red bone marrow is also challenging. Consequently, its dose is nearly always calculated empirically because it is not easy to model it directly in the phantom. When the developers of the VIP-Man phantoms reported that the red bone marrow was segmented from color pixels of $0.33 \times 0.33\text{ mm}$ resolution, the work was scrutinized by others partially due to the lack of consensus about the segmentation process. The lack of standardized procedures contributed to the current situation that although many phantoms and dosimetry data are reported, the accuracy may be impossible to evaluate.

Original voxel phantoms were realistic in depicting the anatomy, but they are person specific. The anatomical differences between two equally realistic voxel phantoms surprised many developers who were used to the idea that a radiation protection phantom must represent the average population. Realizing that there would be likely only one set of such “reference” phantoms, many developers later rushed to revise the original voxel phantoms by adjusting the organ sizes in the original image data to match with the ICRP recommended anatomical data. Others mixed anatomical sources from different subjects. In doing so, these phantoms lost the anatomical realism, which was the original motivation to abandon the stylized phantoms.

The history of computational phantom development has shown that it is the need for application, not the need for policy-making, which determines the course of technological advancement.

To date, the history of phantom development has been centered on the “Reference Man” paradigm which mandates a computational phantom to match approximately the 50th percentile values in terms of body height and weight for a specific gender and age group. Given the anatomical specificity in any voxel phantom, the Reference Man concept works against the original wish to improve the dose estimate in a population of workers who are obviously different from the anatomy depicted by the one voxel phantom. In contrast, the BREP phantoms may have demonstrated the feasibility to develop new-generation phantoms that represent a much broader range of individuals in terms of body height and weight, as well as organ topology. These features were impossible even 10 years ago, but the technology and collective experience of the research community seems to support that idea that we should and can move beyond the “Reference Man” paradigm.

Xu et al. [46] predicted that the advantages afforded by both the BREP type of surface geometries and anatomically realistic voxels would be eventually combined: “For the purposes of setting radiation protection standards, it may be possible to eventually bridge these two types of models, leading to a new generation

of hybrid ‘standard’ model(s) that will be acceptable to the radiation protection community. Such a new generation of models for radiation protection should be realistic enough to accurately represent major radiosensitive tissues and organs, and flexible enough to represent different populations by scaling. Computers are going to be so powerful that very complex models can be handled without a problem.” Impressively, the BREP phantoms were realized in only several years later.

Looking forward, in the next 10 years, advances in computational phantom research will be mostly driven by the power of new-generation Monte Carlo code and associated applications. There will be, of course, important dosimetry needs that should and can be addresses in the near future: (1) a fundamental change in the Reference-Man-based paradigm, (2) physics-based methods for deformation modeling, (3) posture-specific phantoms using motion capture, (4) phantoms and associated methods that report dose uncertainties, (5) multi-scale phantoms (whole-body phantom to eye phantom) (6) direct Monte Carlo simulations with advanced geometries such as NURBS and meshes, (7) near “real-time” Monte Carlo dose calculation using graphics processing units (GPUs) and other accelerators, (8) Increasingly person-specific whole-body computational phantoms, and (9) virtual-reality enabled computational phantom for treatment planning and training. The 60-year history shows that coordinated and cooperative efforts among radiological engineers, computer scientists, biologists, and clinicians are the key to the success of future research endeavors in computational phantoms.

Acknowledgments Helpful discussions in the past decade with many colleagues, especially K Eckerman, W Bolch, M Stabin, A Brill, WP Segars, B Tsui, H Paganetti, IG Zubal, M Zankl, N Petoussi-Henss, R Kramer, Q Liu, J Li, CH Kim, and K Sato through the Consortium of Computation Human Phantoms (CCHP). This review article is based on several chapters of the “Handbook of Anatomical Models for Radiation Dosimetry” published in 2009. M Pinkert and Ashley Rhodes, undergraduate students at RPI, helped compile the recent literature information. Research at RPI, which is highlighted in this article, involved the following former PhD students: Bozkurt et al. [134, 132, 236], Winslow et al. [169, 144, 239] Bednarz (2008), [240–242], Han et al. [147], Ding et al. [113, 243]. These research projects at RPI were supported by the following grants: National Science Foundation (BES-9875532), National Library of Medicine (R03LM007964, R01LM009362, and R01LM009362-03S1), National Cancer Institute (R01CA116743 and R42CA115122), National Institute of Biomedical Imaging and Bioengineering (R42EB010404), and National Institute of Standards and Technology (70NANB9H9198).

References

1. Attix, F. H. (1986). *Introduction to radiological physics and radiation dosimetry* (Vol. 14). London: Wiley.
2. Hubbell, J. H. (1969). Photon cross sections, attenuation coefficients and energy absorption coefficients from 10 keV to 100 GeV. *NSRDS-NBS 29*.
3. Storm, L., & Israel, H. (1970). Photon cross sections from 1 keV to 100 MeV for elements $Z=1$ to $Z=100$. *Atomic Data and Nuclear Data Tables*, 7, 565–681.
4. Dimbylow, P. J. (1996). The development of realistic voxel phantoms for electromagnetic field dosimetry. In *Proceedings Workshop on Voxel Phantom Development*, Chilton, UK.

5. Xu, X. G. (2009). Chapter 1. Computational phantoms for radiation dosimetry: A 40-year history of evolution. In *Handbook of anatomical models for radiation dosimetry*. Taylor & Francis, 2009.
6. Agostinelli, S., et al. (2003). Geant4 a simulation toolkit. *Nuclear instruments and methods in physics research section A*, 506, 250–303.
7. Geant4 Team. (2013). Geant4 user's guide for application developers <http://geant4.web.cern.ch/geant4/G4UsersDocuments/UsersGuides/ForApplicationDeveloper/html>, Last Accessed Oct 2013.
8. Leyton, M. (2001). *A generative theory of shape*. Berlin: Springer.
9. Stroud, I. (2006). *Boundary representation modeling techniques*. London: Springer. ISBN: 978-1-84628-312-3.
10. Caon, M. (2004). Voxel-based computational models of real human anatomy: A review. *Radiation and Environmental Biophysics*, 42, 229–235.
11. Zaidi, H., & Xu, X. G. (2007). Computational anthropomorphic models of the human anatomy: The path to realistic Monte Carlo modeling in radiological sciences. *Annual Review of Biomedical Engineering*, 9, 471–500.
12. Marinelli, L. D. (1942). Dosage determination with radioactive isotopes. *American Journal of Roentgenology*, 47, 210.
13. ICRP. (1959). Report of committee II on permissible dose for internal radiation. Oxford, UK: Pergamon Press.
14. Loevinger, R., Japha, E. M., & Brownell, G. L. (1965a). Discrete radioisotope sources. In Hine G. J. & Brownell G. L. (Eds.) *Radiation dosimetry*. New York: Academic Press.
15. Loevinger, R., Hiolt, J. G., & Hine, G. J. (1965b). Internally administered radionuclides. In Hine G. J. & Brownell G. L. (Eds.) *Radiation dosimetry*. New York: Academic Press.
16. Loevinger, R. (1969). Distributed radionuclide sources. In Attix F. H., & Tochilin (Eds.) *Radiation dosimetry* (2nd ed., Vol. 3). New York: Academic Press
17. Marinelli, L. D., Quimby, E. H., & Hine, G. J. (1948). Dosage determination with radioactive isotopes II. Practical considerations in therapy and protection. *American Journal of Roentgenology*, 59, 260.
18. Quimby, E. H. (1970). The development of radiation dosimetry in nuclear medicine. *Medical Radionuclides: Radiation Dose and Effects*, AEC Symposium Series 20.
19. Fisher, H. L. J., & Snyder, W. S. (1966). Variation of dose delivered by ¹³⁷Cs as a function of body size from infancy to adulthood. *ORNL-4007*.
20. Fisher, H. L. J., & Snyder, W. S. (1967). Distribution of dose in the body from a source of gamma rays distributed uniformly in an organ. *ORNL-4168*.
21. Snyder, W. S. (1968). *Variation of dose in man from exposure to a point source of gamma rays of Congres International sur la Radioprotection dans l'Utilisation Industrielle des Radioelements* (pp. 7–11), Paris, 13–15 Decembre 1965. Paris, Service Centra de Protection Contre les Rayonnements Io.
22. Kereiakes, J. G., Seltzer, R. A., Blackburn, B., & Saenger, E. L. (1965). Radionuclide doses to infants and children: A plea for a standard child. *Health Physics*, 11, 999–1004.
23. Snyder, W. S., Fisher, H. L., Ford, M. R., & Warner, G. G. (1969). Estimates of absorbed fractions for monoenergetic photon sources uniformly distributed in various organs of a heterogeneous phantom. *Journal of Nuclear Medicine*, 3(Suppl), 7–52.
24. Snyder, W. S., Ford, M. R., & Warner, G. G. (1978). Estimates of specific absorbed fractions for monoenergetic photon sources uniformly distributed in various organs of a heterogeneous phantom. *MIRD Pamphlet*, 5, Revised.
25. Jones, R. M. et al. (1976) The development and use of a fifteen-year-old equivalent mathematical phantom for internal dose calculations. *ORNL/TM-5278*.
26. Deus, S. F., & Poston, J. W. (1976). The development of a mathematical phantom representing a 10-year-old for use in internal dose calculations. In *Proceedings of the Symposium on Radiopharmaceutical Dosimetry HEW Publication (FDA) 76-8044*, Oak Ridge, TN.

27. Cristy, M. (1980). *Mathematical phantoms representing children of various ages for use in estimates of internal dose.*
28. Cristy, M. & Eckerman, K.F. (1987). Specific absorbed fractions of energy at various ages from internal photon sources I: Methods, *ORNL/TM-8381/V1.*
29. Bouchet, L. G., Bolch, W. E., Weber, D. A., Atkins, H. L., & Poston, J. W. (1999). MIRD Pamphlet No. 15: Radionuclide S values in a revised dosimetric model of the adult head and brain. Medical internal radiation dose. *Journal of Nuclear Medicine, 40*, 62S–101S.
30. Markovic, V. M., Krstic, D., & Nikezic, D. (2009). Gamma and beta doses in human organs due to radon progeny in human lung. *Radiation Protection Dosimetry, 135*, 197–202.
31. Takahashi, F., Shigemori, Y., & Seki, A. (2009). Accurate dose assessment system for an exposed person utilising radiation transport calculation codes in emergency response to a radiological accident. *Radiation Protection Dosimetry, 133*, 35–43.
32. Kramer, R. et al. (1982). The calculation of dose from external photon exposures using reference human phantoms and Monte Carlo methods: Part I. The male (ADAM) and female (EVA) adult mathematical phantoms. *GSF-Report S-885.*
33. Pretorius, P. H., Xia, W., King, M. A., Tsui, B. M., Pan, T. S., & Villegas, B. J. (1997). Evaluation of right and left ventricular volume and ejection fraction using a mathematical cardiac torso phantom. *Journal of nuclear medicine official publication Society of Nuclear Medicine, 38*, 1528–1535.
34. Tsui, B. M. W., Zhao, X. D., Gregoriou, G. K., Lalush, D. S., Frey, E. C., Johnston, R. E., et al. (1994). Quantitative cardiac SPECT reconstruction with reduced image degradation due to patient anatomy. *Nuclear Science, IEEE Transactions on, 41*, 2838–2844.
35. Tsui, B. M., Terry, J. A., & Gullberg, G. T. (1993). Evaluation of cardiac cone-beam single photon emission computed tomography using observer performance experiments and receiver operating characteristic analysis. *Investigative Radiology, 28*, 1101–1112.
36. Billings, M. P., & Yucker, W. R. (1973). *The Computerized Anatomical Man CAM Model, NASA CR-134043.* Washington, DC: Government Printing Office.
37. Park, S., Lee, J. K., & Lee, C. (2006). Development of a Korean adult male computational phantom for internal dosimetry calculation. *Radiation Protection Dosimetry, 121*, 257–264.
38. Hirata, A., Ito, N., Osamu, Fujiwara, Nagaoka, T., & Watanabe, S. (2008). Conservative estimation of whole-body-averaged SARs in infants with a homogeneous and simple-shaped phantom in the GHz region. *Physics in Medicine & Biology, 53*, 7215–7223.
39. Qiu, R., Li, J., Zhang, Z., Wu, Z., Zeng, Z., & Fan, J. (2008). Photon SAF calculation based on the Chinese mathematical phantom and comparison with the ORNL phantoms. *Health Physics, 95*, 716–724.
40. Kim, J. S., Ha, W. H., Jeong, J. H., Cho, K.-W., & Ki, Lee Jai. (2010). Use of photographic images to construct voxel phantoms for use in whole-body counting. *Radiation Protection Dosimetry, 138*, 119–122.
41. Bento, J., Barros, S., Teles, P., Neves, M., Gonçalves, I., Corisco, J., & Vaz, P. (2011). Monte carlo simulation of the movement and detection efficiency of a whole-body counting system using a BOMAB phantom. *Radiation Protection Dosimetry, 1–11.*
42. Bhati, S., Patni, H. K., Ghare, V. P., Singh, I. S., & Nadar, M. Y. (2011). Monte carlo calculations for efficiency calibration of a whole-body monitor using BOMAB phantoms of different sizes. *Radiation Protection Dosimetry, 1–6.*
43. ICRU. (1992). *Phantoms and computational models in therapy, diagnosis and protection. ICRU Report 48.* Bethesda: International Commission on Radiation Units and Measurements.
44. Gu, J. W., Bednarz, B., Xu, X. G., & Jiang, S. (2008). Assessment of patient organ doses and effective doses using the VIP-Man adult male phantom for selected cone-beam CT imaging procedures during image guided radiation therapy. *Radiation Protection Dosimetry, 131*, 431–443.
45. Stovall, M., Smith, S. A., & Rosenstein, M. (1988). Tissue doses from radiotherapy of cancer of the uterine cervix. *Medical Physics, 16*, 726–733.

46. Xu, X. G., Chao, T. C., & Bozkurt, A. (2000). VIP-Man: An image-based whole-body adult male model constructed from color photographs of the visible human project for multi-particle Monte Carlo calculations. *Health Physics*, 78, 476–486.
47. Gibbs, S., & Pujol, J. (1982). A Monte Carlo method for patient dosimetry from diagnostic x-ray. *Dentomaxillofac Radiol*, 11, 25.
48. Gibbs, S. J., Pujol, A., Chen, T. S., Malcolm, A. W., & James, A. E. (1984). Patient risk from interproximal radiography. *Oral Surgery, Oral Medicine, Oral Pathology*, 58, 347–354.
49. Gibbs, S. et al. (1987). Radiation doses to sensitive organs from intraoral dental radiography. *Dentomaxillofac Radiol*, 16.
50. Fill, U. A., Zankl, M., Petoussi-Hens, N., Siebert, M., & Regulla, D. (2004). Adult female voxel models of different stature and photon conversion coefficients for radiation protection. *Health Physics*, 86, 253–272.
51. Zeng, Z., et al. (2007). Dose assessment for space radiation using a proton differential dose spectrum. *Journal of Tsinghua University (Science and Technology)*, 46, 374.
52. Williams, G., Zankl, M., Abmayr, W., Veit, R., & Drexler, G. (1986). The calculation of dose from external photon exposures using reference and realistic human phantoms and Monte Carlo methods. *Physics in Medicine & Biology*, 31, 449–452.
53. Zankl, M., Veit, R., Williams, G., Schneider, K., Fendel, H., Petoussi, N., et al. (1988). The construction of computer tomographic phantoms and their application in radiology and radiation protection. *Radiation and Environmental Biophysics*, 27, 153–164.
54. Zankl, M., Fill, U., Petoussi-Hens, N., & Regulla, D. (2002). Organ dose conversion coefficients for external photon irradiation of male and female voxel models. *Physics in Medicine & Biology*, 47, 2367–2385.
55. Zankl, M. et al. (2005). GSF male and female adult voxel models representing ICRP Reference Man—the present status. In *Proceedings of The Monte Carlo Method: Versatility Unbounded in a Dynamic Computing World*, Chattanooga, TN, American Nuclear Society, A Grange Park, USA.
56. ICRP. (2009). Adult reference computational phantoms. *ICRP publication, 110*. Pergamon Press, Oxford, UK: Pergamon Press.
57. Schlattl, H., Zankl, M., & Petoussi-Hens, N. (2007). Organ dose conversion coefficients for voxel models of the reference male and female from idealized photon exposures. *Physics in Medicine & Biology*, 52, 2123–2145.
58. Zubal, I. G., Harrell, C. R., Smith, E. O., Rattner, Z., Gindi, G., & Hoffer, P. B. (1994). Computerized three-dimensional segmented human anatomy. *Medical Physics*, 21, 299–302.
59. Dawson, T. W., Caputa, K., & Stuchly, M. A. (1997). A comparison of 60 Hz uniform magnetic and electric induction in the human body. *Physics in Medicine & Biology*, 42, 2319–2329.
60. Sjögreen, K., Ljungberg, M., Wingårdh, K., Erlandsson, K., & Strand, S. E. (2001). Registration of emission and transmission whole-body scintillation-camera images. *Journal of Nuclear Medicine*, 42, 1563–1570.
61. Kramer, R., Vieira, J. W., Khoury, H. J., Lima, F. R. A., & Fuelle, D. (2003). All about MAX: A male adult voxel phantom for Monte Carlo calculations in radiation protection dosimetry. *Physics in Medicine & Biology*, 48, 1239–1262.
62. Kramer, R., Khoury, H. J., Vieira, J. W., Loureiro, E. C. M., Lima, V. J. M., Lima, F. R. A., et al. (2004). All about FAX: A Female Adult voXel phantom for Monte Carlo calculation in radiation protection dosimetry. *Physics in Medicine & Biology*, 49, 5203–5216.
63. Dimbylow, P. J. (1997). FDTD calculations of the whole-body averaged SAR in an anatomically realistic voxel model of the human body from 1 MHz to 1 GHz. *Physics in Medicine & Biology*, 42, 479–490.
64. Jones, D. G. (1997). A realistic anthropomorphic phantom for calculating organ doses arising from external photon irradiation. *Radiat Prot Dosimetry*, 72, 21–29.

65. Dimbylow, P. (2005). Development of the female voxel phantom, NAOMI, and its application to calculations of induced current densities and electric fields from applied low frequency magnetic and electric fields. *Physics in Medicine & Biology*, *50*, 1047–1070.
66. Dimbylow, P. (2005). Resonance behaviour of whole-body averaged specific energy absorption rate (SAR) in the female voxel model, NAOMI. *Physics in Medicine & Biology*, *50*, 4053–4063.
67. Ferrari, P., & Gualdrini, G. (2005). An improved MCNP version of the NORMAN voxel phantom for dosimetry studies. *Physics in Medicine & Biology*, *50*, 4299–4316.
68. Dimbylow, P. (2006). Development of pregnant female, hybrid voxel-mathematical models and their application to the dosimetry of applied magnetic and electric fields at 50 Hz. *Physics in Medicine & Biology*, *51*, 2383–2394.
69. Caon, M., Bibbo, G., & Pattison, J. (2000). Monte carlo calculated effective dose to teenage girls from computed tomography examinations. *Radiation Protection Dosimetry*, *90*, 445–448.
70. Caon, M., Bibbo, G., & Pattison, J. (1999). An EGS4-ready tomographic computational model of a 14-year-old female torso for calculating organ doses from CT examinations. *Physics in Medicine & Biology*, *44*, 2213–2225.
71. Lee, C., Nagaoka, T., & LEE, J. K. (2006). Implementation of Japanese male and female tomographic phantoms to multi-particle Monte Carlo code for ionizing radiation dosimetry. *Journal of Nuclear Science and Technology*, *43*, 937–945.
72. Nipper, J. C., Williams, J. L., & Bolch, W. E. (2002). Creation of two tomographic voxel models of paediatric patients in the first year of life. *Physics in Medicine & Biology*, *47*, 3143–3164.
73. Lee, C., Williams, J. L., Lee, C., & Bolch, W. E. (2005). The UF series of tomographic computational phantoms of pediatric patients. *Medical Physics*, *32*, 3537–3548.
74. Shi, C., & Xu, X. G. (2004). Development of a 30-week-pregnant female tomographic model from computed tomography (CT) images for Monte Carlo organ dose calculations. *Medical Physics*, *31*, 2491–2497.
75. Saito, K., Wittmann, A., Koga, S., Ida, Y., Kamei, T., Funabiki, J., et al. (2001). Construction of a computed tomographic phantom for a Japanese male adult and dose calculation system. *Radiation and Environmental Biophysics*, *40*, 69–75.
76. Sato, K., Noguchi, H., Emoto, Y., Koga, S., & Saito, K. (2007). Japanese adult male voxel phantom constructed on the basis of CT images. *Radiation Protection Dosimetry*, *123*, 337–344.
77. Sato, K., Noguchi, H., Endo, A., Emoto, Y., Koga, S., & Saito, K. (2007). Development of a voxel phantom of Japanese adult male in upright posture. *Radiation Protection Dosimetry*, *127*, 205–208.
78. Saito, K. et al. (2008). Construction of a voxel phantom based on CT data for a Japanese female adult and its use for calculation of organ doses from external electrons, Japanese. *Journal of Health Physics*, *43*(2), 122–130.
79. Nagaoka, T., Watanabe, S., Sakurai, K., Kunieda, E., Watanabe, S., Taki, M., et al. (2004). Development of realistic high-resolution whole-body voxel models of Japanese adult males and females of average height and weight, and application of models to radio-frequency electromagnetic-field dosimetry. *Physics in Medicine & Biology*, *49*, 1–15.
80. Takahashi, M., Kinase, S., & Kramer, R. (2011). Evaluation of counting efficiencies of a whole-body counter using Monte Carlo simulation with voxel phantoms. *Radiation Protection Dosimetry*, *144*, 407–410.
81. Choi, S. H. et al. (2006). Construction of a high-definition ‘Reference Korean’ voxel phantom for organ and tissue radiation dose calculation. In *World Congress on Medical Physics and Biomedical Engineering*, Seoul, Korea
82. Kim, C. H., Choi, S. H., Jeong, J. H., Choonsik, Lee, & Chung, M. S. (2008). HDRK-Man: A whole-body voxel model based on high-resolution color slice images of a Korean adult male cadaver. *Physics in Medicine & Biology*, *53*, 4093–4106.

83. Lee, B., Shin, G., Kang, S., Shin, B., Back, I., Park, H., Park, C., Lee, Jeongwoo., Lee, W., Choi, J., Park, R., Kim, Y. (2011). Dose evaluation of selective collimation effect in cephalography by measurement and Monte Carlo simulation. *Radiation Protection Dosimetry*, 1–7.
85. Zhang, B., Ma, J., Liu, L., & Cheng, J. (2007). CNMAN: A Chinese adult male voxel phantom constructed from color photographs of a visible anatomical data set. *Radiation Protection Dosimetry*, 124, 130–136.
86. Zhang, G., Liu, Q., & Luo, Q. (2007). Monte Carlo simulations for external neutron dosimetry based on the visible Chinese human phantom. *Physics in Medicine & Biology*, 52, 7367–7383.
87. Zhang, G., Liu, Q., Zeng, S., & Luo, Q. (2008). Organ dose calculations by Monte Carlo modeling of the updated VCH adult male phantom against idealized external proton exposure. *Physics in Medicine & Biology*, 53, 3697–3722.
88. Zhang, G., Luo, Q., Zeng, S., & Liu, Q. (2008). The development and application of the visible Chinese human model for Monte Carlo dose calculations. *Health Physics*, 94, 118–125.
89. Li, J.L., Qiu, R., Zhang, Z., Liu, L.Y., Zeng, Z., Bi, L., & Li, W.Q. (2009). Organ dose conversion coefficients for external photon irradiation using the Chinese voxel phantom (CVP). *Radiation Protection Dosimetry*, 135, 33–42.
90. Alziar, I., Bonniaud, G., Couanet, D., Ruaud, J. B., Vicente, C., Giordana, G., et al. (2009). Individual radiation therapy patient whole-body phantoms for peripheral dose evaluations: Method and specific software. *Physics in Medicine & Biology*, 54, N375–N383.
91. Ferrari, P. (2010). Development of an integrated couple of anthropomorphic models for dosimetric studies. *Radiation Protection Dosimetry*, 142, 191–200.
92. Patni, H. K., Nadar, M. Y., Akar, D. K., Bhati, S., & Sarkar, P. K. (2010). Selected organ dose conversion coefficients for external photons calculated using Icrp adult voxel phantoms and Monte Carlo code fluka. *Radiation Protection Dosimetry*, 1–11.
93. Courageot, E., Huet, C., Clairand, I., Bottollier-Depois, J. F., & Gourmelon, P. (2011). Numerical dosimetric reconstruction of a radiological accident in South America in April 2009. *Radiation Protection Dosimetry*, 144, 540–542.
94. Courageot, E., Sayah, R., & Huet, C. (2010). Development of modified voxel phantoms for the numerical dosimetric reconstruction of radiological accidents involving external sources: Implementation in SESAME tool. *Physics in Medicine & Biology*, 55, N231–N241.
95. Tung, C. J., Tsai, S. F., Tsai, H. Y., & Chen, I. J. (2011). Determination of voxel phantom for reference Taiwanese adult from CT image analyses. *Radiation Protection Dosimetry*, 146, 186–190.
96. Beck, P., Zechner, A., Rollet, S., Berger, T., Bergmann, R., Hajek, M., et al. (2011). *MATSIM : Development of a voxel model of the MATROSHKA astronaut dosimetric phantom*, 58, 1921–1926.
97. Akkurt H., Bekar K. B., & Eckerman K. F. (2008). VOXMAT: Phantom model with combination of voxel and mathematical geometry, *53rd Annual Health Physics Society Meeting*, Pittsburgh, PA, July 13–17.
98. Mofrad, F. B., Zoroofi, R. A., Tehrani-Fard, A. A., Akhlahpoor, S., Hori, M., Chen, Y. W., et al. (2010). Statistical construction of a Japanese male liver phantom for internal radionuclide dosimetry. *Radiation Protection Dosimetry*, 141, 140–148.
99. Segars, W. P. (2001). Ph.D thesis, University of North Carolina at Chapel Hill, pp. 243.
100. Segars, W. P., Tsui Benjamin, M. W., Frey Eric, C., Johnson, G. A., & Berr, S. S. (2004). Development of a 4-D digital mouse phantom for molecular imaging research. *Molecular Imaging and Biology MIB the Official Publication of the Academy of Molecular Imaging*, 6, 149–159.
101. Segars, W., & Tsui, B. (2007). 4D MOBY and NCAT phantoms for medical imaging simulation of mice and men. *Society of Nuclear Medicine Annual Meeting Abstracts*, 48, 203.

102. Segars Paul, W., Lalush David, S., Frey Eric, C., Manocha, D., King, Ma., & Tsui Benjamin, M. W. (2009). Improved dynamic cardiac phantom based on 4D NURBS and tagged MRI. *IEEE Transactions on Nuclear Science*, 56, 2728–2738.
103. Segars, W. P., Sturgeon, G. M., Ward, D. J., Ratnanather, J. T., Miller, M. I., & Tsui, B.M. W. (2010). The New XCAT Series of Digital Phantoms for Multi-Modality Imaging. *Journal of the Acoustical Society of America*, 2392–2395.
104. Tabary, J., Marache-Francisco, S., Valette, S., Segars, W.P., & Lartzien, C. (2009). Realistic X-ray CT simulation of the XCAT phantom with SINDBAD. In *2009 IEEE Nuclear Science Symposium Conference Record (NSS/MIC)* (pp. 3980–3983).
105. Niu, X., Yang, Y., Jin, M., Wernick, M. N., & King, Ma. (2010). Regularized Fully 5D Reconstruction of Cardiac Gated Dynamic SPECT Images. *IEEE Transactions on Nuclear Science*, 57, 1085–1095.
106. Peroni, M., Spadea, M. F., Riboldi, M., Baroni, G., Chen, G. T. Y., Sharp, G. C., Medicine, C., & Magna, S. (2009). *Validation of an automatic contour propagation method for lung cancer 4D adaptive radiation therapy*. Boston, MA: Department of Radiation Oncology, Massachusetts General Hospital, 4 Harvard Medical Methods, pp. 1071–1074
107. Veress, A. I., Segars, W. P., Tsui Benjamin, B. M., & Gullberg, G. T. (2011). Incorporation of a left ventricle finite element model defining infarction into the XCAT imaging phantom. *IEEE Transactions on Medical Imaging*, 30, 915–927.
108. Tward, D. J., Ceritoglu, C., Sturgeon, G., Segars, W. P., Miller, M. I., & Ratnanather, J. T. (2011). Generating patient-specific dosimetry phantoms with whole-body diffeomorphic image registration. In *Bioengineering Conference (NEBEC), 2011 IEEE 37th Annual Northeast* (pp. 1–2). IEEE.
109. Xu, X. G., Taranenko, V., Zhang, J., & Shi, C. (2007). A boundary-representation method for designing whole-body radiation dosimetry models: Pregnant females at the ends of three gestational periods—RPI-P3, -P6 and -P9. *Physics in Medicine & Biology*, 52, 7023–7044.
110. Hegenbart, L., Na, Y. H., Zhang, J. Y., Urban, M., & Xu, X. G. (2008). A Monte Carlo study of lung counting efficiency for female workers of different breast sizes using deformable phantoms. *Physics in Medicine & Biology*, 53, 5527–5538.
111. Xu, X. G., Zhang, J. Y., & Na, Y. H. (2008). Preliminary data for mesh-based deformable phantom development: Is it possible to design person-specific phantoms on-demand. *The International Conference on Radiation Shielding-11*.
112. Na, Y. H., Zhang, B., Zhang, J., Caracappa, P. F., & Xu, X. G. (2010). Deformable adult human phantoms for radiation protection dosimetry: Anthropometric data representing size distributions of adult worker populations and software algorithms. *Physics in Medicine & Biology*, 55, 3789–3811.
113. Ding, A., Mille, M. M., Liu, T., Caracappa, P. F., & Xu, X. G. (2012). Extension of RPI-adult male and female computational phantoms to obese patients and a monte carlo study on the effects on CT imaging dose. *Physics in Medicine & Biology*, 57, 2441–2459.
114. Gu, J., Bednarz, B., Caracappa, P. F., & Xu, X. G. (2009). The development, validation and application of a multi-detector CT (MDCT) scanner model for assessing organ doses to the pregnant patient and the fetus using Monte Carlo simulations. *Physics in Medicine & Biology*, 54, 2699–2717.
115. Lee, C., Lodwick, D., Hasenauer, D., Williams, J. L., Lee, C., & Bolch, W. E. (2007). Hybrid computational phantoms of the male and female newborn patient: NURBS-based whole-body models. *Physics in Medicine & Biology*, 52, 3309–3333.
116. Lee, C., Lodwick, D., Williams, J. L., & Bolch, W. E. (2008). Hybrid computational phantoms of the 15-year male and female adolescent: Applications to CT organ dosimetry for patients of variable morphometry. *Medical Physics*, 35, 2366–2382.
117. Maynard, M. R., Geyer, J. W., Aris, J. P., Shifrin, R. Y., & Bolch, W. (2011). The UF family of hybrid phantoms of the developing human fetus for computational radiation dosimetry. *Physics in Medicine & Biology*, 56, 4839–4879.

118. Johnson, P., Choonsik, Lee, Johnson, K., Siragusa, D., & Bolch Wesley, E. (2009). The influence of patient size on dose conversion coefficients: A hybrid phantom study for adult cardiac catheterization. *Physics in Medicine & Biology*, *54*, 3613–3629.
119. Pafundi, D., Lee, C., Watchman, C., Bourke, V., Aris, J., Shagina, N., et al. (2009). An image-based skeletal tissue model for the ICRP reference newborn. *Physics in Medicine & Biology*, *54*, 4497–4531.
120. Pafundi, D., Rajon, D., Jokisch, D., Lee, Choonsik, & Bolch, W. (2010). An image-based skeletal dosimetry model for the ICRP reference newborn–internal electron sources. *Physics in Medicine & Biology*, *55*, 1785–1814.
121. Hough, M., Johnson, P., Rajon, D., Jokisch, D., Lee, C., & Bolch, W. (2011). An image-based skeletal dosimetry model for the ICRP reference adult male–internal electron sources. *Physics in Medicine & Biology*, *56*, 2309–2346.
122. Dimbylow, P., Bolch, W., & Lee, C. (2010). SAR calculations from 20 MHz to 6 GHz in the University of Florida newborn voxel phantom and their implications for dosimetry. *Physics in Medicine & Biology*, *55*, 1519–1530.
123. Bahadori, A. A., Van Baalen, M., Shavers, M. R., Dodge, C., Semones, E. J., & Bolch Wesley, E. (2011). The effect of anatomical modeling on space radiation dose estimates: A comparison of doses for NASA phantoms and the 5th, 50th, and 95th percentile male and female astronauts. *Physics in Medicine & Biology*, *56*, 1671–1694.
124. Stabin, M., Emmons, M. A., Segars, W. P., Fernald, M., & Brill, A. B. (2008). ICRP-89 based adult and pediatric phantom series. *Society of Nuclear Medicine Annual Meeting Abstracts*, *49*, 14.
125. Stabin, M. G., Xu, X. G., Emmons, M. A., Segars, W. P., Shi, C., & Fernald, M. J. (2012). RADAR reference adult, pediatric and pregnant female phantom series for internal and external dosimetry. *Journal of Nuclear Medicine*, *53*(11), 1807–1813.
126. Christ, A., Kainz, W., Hahn, E. G., Honegger, K., Zefferer, M., Neufeld, E., et al. (2010). The Virtual Family—development of surface-based anatomical models of two adults and two children for dosimetric simulations. *Physics in Medicine & Biology*, *55*, N23–N38.
127. IT²IS. (2013). The virtual population: High-resolution anatomical models <http://www.itis.ethz.ch/services/anatomical-models/virtual-population/> Last Accessed Dec 2013.
128. de Melo Lima, V. J., Cassola, V. F., Kramer, R., de Oliveira Lira, C. A. B., Khoury, H. J., & Vieira, J. W. (2011). Development of 5- and 10-year-old pediatric phantoms based on polygon mesh surfaces. *Medical Physics*, *38*, 4723.
129. Farah, J., Broggio, D., & Franck, D. (2011). Examples of Mesh and NURBS modelling for in vivo lung counting studies. *Radiation Protection Dosimetry*, *144*, 344–348.
130. Broggio, D., Beurrier, J., Bremaud, M., Desbrée, a, Farah, J., Huet, C., et al. (2011). Construction of an extended library of adult male 3D models: Rationale and results. *Physics in Medicine & Biology*, *56*, 7659–7692.
131. Kim, C. H., Jeong, J. H., Bolch Wesley, E., Cho, K.-W., & Hwang, S. B. (2011). A polygon-surface reference Korean male phantom (PSRK-Man) and its direct implementation in Geant4 Monte Carlo simulation. *Physics in Medicine & Biology*, *56*, 3137–3161.
132. Chao, T. C., Bozkurt, A., & Xu, X. G. (2001). Conversion coefficients based on the VIP-Man anatomical model and EGS4-VLSI code for external monoenergetic photons from 10 keV to 10 MeV. *Health Physics*, *81*, 163.
133. Chao, T. C., Bozkurt, A., & Xu, X. G. (2003). Correction to Conversion coefficients based on the VIP-Man anatomical model and EGS4-VLSI code for external monoenergetic photons from 10 keV to 10 MeV. *Health Physics*, *84*(3), 390.
134. Bozkurt, A., Chao, T. C., & Xu, X. G. (2000). Fluence-to-dose conversion coefficients below 20 MeV based on the VIP-Man anatomical model. *Physics in Medicine & Biology*, *45*, 3059.
135. Chao, T. C., Bozkurt, A., & Xu, X. G. (2001). Organ dose conversion coefficients for 0.1–10 MeV electrons calculated for the VIP-MAN tomographic model. *Health Physics*, *81*, 203.

136. Bozkurt, A., Chao, T. C., & Xu, X. G. (2001). Fluence-to-dose conversion coefficients based on the VIP-Man anatomical model and MCNPX code for monoenergetic neutrons above 20 MeV. *Health Physics*, *81*, 184.
137. Bozkurt, A., & Xu, X. G. (2004). Fluence-to-dose Conversion Coefficients for Monoenergetic Proton Beams Based on the VIP-Man Anatomical Model. *Radiation Protection Dosimetry*, *112*(2), 219.
138. Chao, T. C., & Xu, X. G. (2001). Specific absorbed fractions from the image-based VIP-Man body model and EGS4-VLSI Monte Carlo code: Internal electron emitters. *Physics in Medicine & Biology*, *46*, 901.
139. Xu, X. G., Chao, T. C., & Bozkurt, A. (2005). Comparison of effective doses from various monoenergetic particles based on the stylised and the VIP-Man tomographic models. *Radiation Protection Dosimetry*, *115*, 530.
140. Chao, T. C., & Xu, X. G. (2004). S-values calculated from a tomographic head/brain model for brain imaging. *Physics in Medicine & Biology*, *49*, 4971.
141. Winslow, M., Huda, W., Xu, X. G., Chao, T. C., Shi, C. Y., Ogden, K. M., et al. (2004). Use of the VIP-Man Model to Calculate Energy Impacted and Effective Dose for X-ray Examinations. *Health Physics*, *86*, 174.
142. Son, I. Y., Winslow, M., Yazici, B., & Xu, X. G. (2006). X-ray imaging optimization using virtual phantoms and computerized observer modelling. *Physics in Medicine & Biology*, *51*, 4289.
143. Bozkurt, A., & Bor, D. (2007). Simultaneous determination of equivalent dose to organs and tissues of the patient and of the physician in interventional radiology using the Monte Carlo method. *Physics in Medicine & Biology*, *52*, 317.
144. Wang, B., Xu, X. G., Goorley, J. T., & Bozkurt, A. (2005a). The use of MCNP code for an extremely large voxel model VIP-Man. The Monte Carlo method: Versatility unbounded. In *A dynamic computing world*. American Nuclear Society (ISBN: 0-89448-695-0).
145. Jiang, H., Wang, B., Xu, X. G., Suit, H. D., & Paganetti, H. (2005). Simulation of organ-specific patient effective dose due to secondary neutrons in proton radiation treatment. *Physics in Medicine & Biology*, *50*, 4337.
146. Ding, A., Gu, J., Trofimov, A. V., & Xu, X. G. (2010). Monte Carlo calculation of imaging doses from diagnostic multidetector CT and kilovoltage cone-beam CT as part of prostate treatment plans. *Medical Physics*, *37*, 6199–6204.
147. Han, B., Xu, X. G., & Chen, G. T. Y. (2011). Proton radiography and fluoroscopy of lung tumors: A Monte Carlo study using patient-specific 4DCT phantoms. *Medical Physics*, *38*(4), 1903–1911.
148. Andreo, P. (1991). Monte Carlo techniques in medical radiation physics. *Physics in Medicine & Biology*, *36*, 861–920.
149. Raeside, D. E. (1976). Monte Carlo principles and applications. *Physics in Medicine & Biology*, *21*, 181–197.
150. Turner, J. E., Wright, H. A., & Hamm, R. N. (1985). A Monte Carlo primer for health physicists. *Health Physics*, *48*, 717–733.
151. Pelowitz, D. B. (2005). MCNPX User's Manual Version 2.5.0, *Los Alamos National Laboratory report LA-CP-05-0369*.
152. NRC. (2013). EGSnrc <http://irs.inms.nrc.ca/software/egsnrc/> Last Accessed Dec 2013.
153. Allison, J., Amako, K., Apostolakis, J., Araujo, H., Arce Dubois, P., Asai, M., et al. (2006). Geant4 developments and applications. *IEEE Transactions on Nuclear Science*, *53*, 270–278.
154. NEA. (2013). Penelope2011, A code system for Monte-Carlo Simulation of Electron and Photon transport <http://www.oecd-nea.org/tools/abstract/detail/NEA-1525/> Last Accessed Dec 2013.
155. Salvat, F., Fernández-Varea, J. M., & Sempau, J. (2003). PENELOPE, a code system for Monte Carlo simulation of electron and photon transport. *Simulation*, *5*, 253.

156. Badal, A., Kyprianou, I., Banh, D. P., Badano, A., & Josep, Sempau. (2009). penMesh—Monte Carlo radiation transport simulation in a triangle mesh geometry. *IEEE Transactions on Medical Imaging*, 28, 1894–1901.
157. Battistoni, G., Cerutti, F., Fassò, A., Ferrari, A., Muraro, S., Ranft, J., et al. (2007). The FLUKA code: Description and benchmarking. *Aip Conference Proceedings*, 896, 31–49.
158. Fluka Team. (2013). FLUKA <http://www.fluka.org/fluka.php> Last Accessed Dec 2013.
159. Wang, B., Xu, X. G., & Kim, C. H. (2004). A Monte Carlo CT model of the rando phantom. *Transactions-American Nuclear Society*, 90, 473.
160. Mazzurana, M., Sandrini, L., Vaccari, A., Malacarne, C., Cristoforetti, L., & Pontalti, R. (2003). A semi-automatic method for developing an anthropomorphic numerical model of dielectric anatomy by MRI. *Physics in Medicine & Biology*, 48, 3157–3170.
161. Cech, R., Leitgeb, N., & Pediaditis, M. (2007). Fetal exposure to low frequency electric and magnetic fields. *Physics in Medicine & Biology*, 52, 879–888.
162. Cech, R., Leitgeb, N., & Pediaditis, M. (2008). Current densities in a pregnant woman model induced by simultaneous ELF electric and magnetic field exposure. *Physics in Medicine & Biology*, 53, 177–186.
163. Doerfel, H., & Heide, B. (2007). Calibration of a phoswich type partial body counter by Monte Carlo simulation of low-energy photon transport. *Radiation Protection Dosimetry*, 123, 464–472.
164. Sachse, F.B. et al. (1997). MEET man—Models for simulation of electromagnetic, elastomechanic and thermic behavior of man. Erstellung und technische Parameter, Institut für Biomedizinische Technik: *Universität Karlsruhe*.
165. Tinniswood, A. D., Furse, C. M., & Gandhi, O. P. (1998). Power deposition in the head and neck of an anatomically based human body model for plane wave exposures. *Physics in Medicine & Biology*, 43, 2361–2378.
166. Findlay, R. P., & Dimbylow, P. J. (2009). Spatial averaging of fields from half-wave dipole antennas and corresponding SAR calculations in the NORMAN human voxel model between 65 MHz and 2 GHz. *Physics in Medicine & Biology*, 54, 2437–2447.
167. Findlay, R. P., & Dimbylow, P. J. (2010). SAR in a child voxel phantom from exposure to wireless computer networks (Wi-Fi). *Physics in Medicine & Biology*, 55, N405–N411.
168. Wu, D., Shamsi, S., Chen, J., & Kainz, W. (2006). Evaluations of specific absorption rate and temperature increase within pregnant female models in magnetic resonance imaging birdcage coils. *IEEE Transactions on Microwave Theory and Techniques*, 54, 4472–4478.
169. Winslow, M., Xu, X. G., & Yazici, B. (2005). Development of a simulator for radiographic image optimization. *Computer Methods and Programs in Biomedicine*, 78(3), 179–190
170. Alderson, S. W., Lanzl, L. H., Rollins, M., & Spira, J. (1962). An instrumented phantom system for analog computation of treatment plans. *The American journal of roentgenology, radium therapy, and nuclear medicine*, 87, 185–195.
171. Anon. (1975). *Report of the task group on reference man* (Vol. 23). Ottawa: ICRP Publication.
172. Briesmeister, J. F. (2003). MCNP—A general monte carlo N-particle transport code *LAUR031987*.
173. Capello, K., Kedzior, S., & Kramer, G. H. (2012). Voxel phantoms: The new ICRP computational phantoms: how do they compare? *Health Physics*, 102(6), 626–630.
174. Caracappa, P. F., Chao, T. C. E., & Xu, X. G. (2009). A study of predicted bone marrow distribution on calculated marrow dose from external radiation exposures using two sets of image data for the same individual. *Health Physics*, 96, 661–674.
175. Carlo, M. (2010). Extension of the NCAT phantom for the investigation of intra-fraction respiratory motion in IMRT using 4D. *Lung*, 1475.
176. Cassola, V. F. (2010). FASH and MASH: Female and male adult human phantoms based on polygon mesh surfaces: I. Development of the anatomy. *Physics in Medicine & Biology*, 55(1), 133.

177. Cassola, V. F., Milian, F. M., Kramer, R., de Oliveira Lira, C., & Khoury, H. J. (2011). Standing adult human phantoms based on 10th, 50th and 90th mass and height percentiles of male and female Caucasian populations. *Physics in Medicine & Biology*, *56*, 3749–3772.
178. CCHP. (2005). “Tomographic models for radiation protection dosimetry” Session, Monte Carlo 2005 Topical Meeting: The Monte Carlo Method: Versatility Unbounded In A Dynamic Computing World., Chattanooga, TN, USA, April 17–21, 2005.
179. Cheung, A. A., Niu, T., Faber, T. L., Segars, W. P., Zhu, L., & Chen, J. (2010). Simulation of left ventricular dyssynchrony using the XCAT phantom. In *Nuclear Science Symposium Conference Record (NSS/MIC)*, 2010 IEEE (pp. 3187–3189).
180. CIRS. (2013). Tissue Simulation and Phantom Technology <http://www.cirsinc.com> Last Accessed Dec 2013.
181. Coulot, J. (2003). Therapeutic applications of monte carlo calculations in nuclear medicine. *Physics in Medicine & Biology*, *48*, 2575.
182. CMPWG. (2013). Phantoms <http://cmpwg.ans.org/phantoms/camera.pdf> Last Accessed July 2013.
183. Farah, J., Broggio, D., & Franck, D. (2010). Female workers and in vivo lung monitoring: A simple model for morphological dependence of counting efficiency curves. *Physics in Medicine & Biology*, *55*, 7377–7395.
184. Ferrari, A., Pelliccioni, M., & Pillon, M. (1997). Fluence to effective dose and effective dose equivalent conversion coefficients for electrons from 5 MeV to 10 GeV. *Radiation Protection Dosimetry*, *69*, 97.
185. Furler, M. (2007). *Methods of converting geometry*. In CAD To MCNP Code. M.S. thesis. Rensselaer Polytechnic Institute.
186. Geant4 Team. (2013). Working groups http://geant4.web.cern.ch/geant4/collaboration/working_groups.shtml#wg.RUN Last Accessed Dec 2013.
187. Gjonaj, E., Bartsch, M., Clemens, M., Schupp, S., & Weiland, T. (2002). High-resolution human anatomy models for advanced electromagnetic field computations. *IEEE Transactions on Magnetics*, *38*, 357–360.
188. Griffith, R., Dean, P., Anderson, A., & Fisher, J. (1978). *Fabrication of a tissue-equivalent torso phantom for intercalibration of in vivo transuranic-nuclide counting facilities*.
189. Gu, J., Dorgu, A., & Xu X. G. (2008). Comparison of main software packages for CT dose reporting. *Review Literature And Arts Of The Americas*.
190. Hwang, J. M. L., Shoup, R. L., & Poston, J. W. (1976). Mathematical description of a newborn human for use in dosimetry calculations *ORNL/TM-5453*.
191. ICRP. (1990). Recommendations of the international commission on radiological protection. *ICRP Publication 60*. Oxford, UK: Pergamon Press.
192. Jin, W., Lim, Y. J., Xu, X. G., Singh, T. P., & De, S. (2005). Improving the visual realism of virtual surgery. *Proceedings of Medicine Meets Virtual Reality* (Vol. 13) Long Beach CA, IOS Press. pp. 227.
193. Jones, A. K., Simon, T. A., Bolch, W. E., Holman, M. M., & Hintenlang, D. E. (2006). Tomographic physical phantom of the newborn child with real-time dosimetry I. Methods and techniques for construction. *Medical Physics*, *33*, 3274–3282.
194. Katagiri, M., Hikoji, M., Kitaichi, M., Sawamura, S., & Aoki, Y. (2000). Effective dose and organ doses per unit fluence calculated for monoenergetic 0.1 MeV to 100 MeV electrons by the MIRD-5 phantom. *Radiation Protection Dosimetry*, *90*(4), 393.
195. Kim, J. I., Choi, H., Lee, B. I., Lim, Y. K., Kim, C. S., Lee, J. K., et al. (2006). Physical phantom of typical Korean male for radiation protection purpose. *Radiation Protection Dosimetry*, *118*, 131–136.
196. Kramer, G. H., Burns, L., & Noel, L. (1991). The BRMD BOMAB phantom family. *Health Physics*, *61*, 895–902.
197. Kramer, R. (2010). FASH and MASH: Female and male adult human phantoms based on polygon mesh surfaces: II. Dosimetric calculations. *Physics in medicine & biology*, *55*(1), 163

198. Kramer, R., Khoury, H. J., Vieira, J. W., & Lima, V. J. M. (2006). MAX06 and FAX06: Update of two adult human phantoms for radiation protection dosimetry. *Physics in Medicine & Biology*, *51*, 3331–3346.
199. Kyoto Kagaku co., LTD. (2013). Hands-on for Health Care Professionals—Simulators, Training Models, and Phantoms <http://www.kyotokagaku.com/> Last Accessed Dec 2013.
200. Lee, C., Lee, C., Williams, J. L., & Bolch, W. E. (2006). Whole-body voxel phantoms of paediatric patients—UF Series B. *Physics in Medicine & Biology*, *51*, 4649–4661.
201. Lee, C., Lee, C., Park, S.-H., & Lee, J.-K. (2006). Development of the two Korean adult tomographic computational phantoms for organ dosimetry. *Medical Physics*, *33*, 380–390.
202. Lee, C., Lee, J., & Lee, C. (2004). Korean adult male voxel model KORMAN segmented from magnetic resonance images. *Medical Physics*, *31*, 1017–1022.
203. Lee, C., & Lee, J. (2005). Reference Korean human models: Past, present, and future, *The Monte Carlo Method: versatility unbounded in a dynamic computing world*, Chattanooga, Tennessee.
204. Liu, X. P., Luo, Y. T., & Tong, L. L. (2005). Development and application of MCNP auto-modeling tool: Mcam 3.0. *Fusion Engineering and Design*, *75*, 1275–1279.
205. Marzocchi, O., Breustedt, B., Mostacci, D., Zankl, M., & Urban, M. (2011). Theoretical assessment of whole body counting performances using numerical phantoms of different gender and sizes. *Radiation Protection Dosimetry*, *144*, 339–343.
206. Menzel, H.-G., Clement, C., & DeLuca, P. (2009). ICRP Publication 110. Realistic reference phantoms: An ICRP/ICRU joint effort. A report of adult reference computational phantoms. *Ann ICRP*, *39*, 1–164.
207. Nagaoka, T., Togashi, T., Saito, K., Takahashi, M., Ito, K., Ueda, T., et al. (2006). An anatomically realistic voxel model of the pregnant woman and numerical dosimetry for a whole-body exposure to RF electromagnetic fields. *International Conference of the IEEE, Engineering in Medicine & Biology Society*, *1*, 5463–5467.
208. Nagaoka, T., Kunieda, E., & Watanabe, S. (2008). Proportion-corrected scaled voxel models for Japanese children and their application to the numerical dosimetry of specific absorption rate for frequencies from 30 MHz to 3 GHz. *Physics in Medicine & Biology*, *53*, 6695–6711.
209. Nagaoka, T., Togashi, T., Saito, K., Takahashi, M., Ito, K., & Watanabe, S. (2007). An anatomically realistic whole-body pregnant-woman model and specific absorption rates for pregnant-woman exposure to electromagnetic plane waves from 10 MHz to 2 GHz. *Physics in Medicine & Biology*, *52*, 6731–6745.
210. NCRP. (1985). *The experimental basis for absorbed-dose calculations in medical uses of radionuclides*, NCRP Report No 83.
211. Niu, X., Yang, Y., & Wernick, M. N. (2011). Temporal regularization in fully 5D reconstruction of cardiac gated dynamic spect images, 1504–7.
212. Petoussi-Hens, N., Zankl, M., Fill, U., & Regulla, D. (2002). The GSF family of voxel phantoms. *Physics in Medicine & Biology*, *47*, 89–106.
213. Phantom Laboratory. (2013). RANDO Phantoms <http://www.phantomlab.com/rando.html> Last Accessed Dec 2013.
214. Qiu, R., Li, J., Zhang, Z., Liu, L., Bi, L., & Ren, L. (2009). Dose conversion coefficients based on the Chinese mathematical phantom and MCNP code for external photon irradiation. *Radiation Protection Dosimetry*, *134*, 3–12.
215. Reihel, W., Hammersley, J. M., & Handscomb, D. C. (1966) *Monte Carlo methods*. London: Methuen & Co., New York: Wiley, 1964. VII+178 S., Preis: 25s *Biom Z*, *8*, 209–209.
216. Sato, K., Noguchi, H., Emoto, Y., Koga, S., & Saito, K. (2009). Development of a Japanese adult female voxel phantom. *Journal of Nuclear Science and Technology*, *46*, 907–913.
217. Segars, W. P., Mahesh, M., Beck, T. J., Frey, E. C., & Tsui, B. M. W. (2008). Realistic CT simulation using the 4D XCAT phantom. *Medical Physics*, *35*, 3800.

218. Shypailo, R. J., & Ellis, K. J. (2011). Whole body counter calibration using Monte Carlo modeling with an array of phantom sizes based on national anthropometric reference data. *Physics in Medicine & Biology*, *56*, 2979–2997.
219. Smans, K., Tapiovaara, M., Cannie, M., Struelens, L., Vanhavere, F., Smet, M., et al. (2008). Calculation of organ doses in x-ray examinations of premature babies. *Medical Physics*, *35*, 556–568.
220. Smith, T. J., Petoussi, N., & Zankl, M. (2000). Comparison of internal radiation doses estimated by MIRD and voxel techniques for a “family” of phantoms. *European Journal of Nuclear Medicine*, *27*, 1387.
221. Snyder, W. S., Ford, M. R., Warner, G. G., & Fisher, Jr H. L. (1969). Estimates of Absorbed Fractions for Monoenergetic Photon Sources Uniformly Distributed in Various Organs of a Heterogeneous Phantom. *Journal of Nuclear Medicine*, *10*.
222. Stabin, M. G., Sharkey, R. M., & Siegel, J. A. (2011). RADAR commentary: Evolution and current status of dosimetry in nuclear medicine. *Journal of Nuclear Medicine*, *52*, 1156–1161.
223. Staton, R. J., Jones, A. K., Lee, C., Hintenlang, D. E., Arreola, M. M., Williams, J. L., et al. (2006). A tomographic physical phantom of the newborn child with real-time dosimetry. II. Scaling factors for calculation of mean organ dose in pediatric radiography. *Medical Physics*, *33*, 3283–3289.
224. Takahashi, F., Sato, K., Endo, A., Ono, K., Yoshitake, T., Hasegawa, T., et al. (2011). Waza-Ari: Computational dosimetry system for X-Ray Ct examinations. I. radiation transport calculation for organ and tissue doses evaluation using Jm phantom. *Radiation Protection Dosimetry*, *146*, 241–243.
225. Taranenko, V., Xu, X.G. (2009). Foetal dose conversion coefficients for ICRP-compliant pregnant models from idealised proton exposures. *Radiation Protection Dosimetry*, *133*, 65–72.
226. Tresser, M. A., & Hintenlang, D. E. (1999). Construction of a newborn dosimetry phantom for measurement of effective dose. *Health Physics*, *76*, S190.
227. Uusitupa, T. (2010). SAR variation study from 300 to 5,000 MHz for 15 voxel models including different postures. *Radio Science*, *1157*.
228. Valentin, J. (2002). Anatomical and physiological data for use in radiological protection: Reference. *Ann ICRP*, *13*, 2347–2350.
229. Wang, J., Fujiwara, O., Watanabe, S., & Yamanaka, Y. (2004). Computation with a parallel FDTD system of human-body effect on electromagnetic absorption for portable telephones. *Microwave Theory and Techniques, IEEE Transactions on*, *52*, 53–58.
230. Wang, B., Xu, X. G., Goldstein, M., & Sahoo, N. (2005b). Adjoint Monte Carlo method for prostate external photon beam treatment planning: An application to 3-D patient anatomy. *Physics in Medicine & Biology*, *50*, 923.
231. Xu, X. G. (2005). Preliminary development of a 4D anatomical model for Monte Carlo simulations. *Medicine*, 1–10.
232. Zhang, J., Na, Y., & Xu, X. G. (2008c). MO-E-AUD B-05: Development of whole-body phantoms representing an average adult male and female using surface-geometry methods. *Medical Physics*, *35*, 2875.
233. Zhang, J., Xu, G. X., Shi, C., & Fuss, M. (2008d). Development of a geometry-based respiratory motion-simulating patient model for radiation treatment dosimetry. *Journal of Applied Clinical Medical Physics*, *9*, 2700.
234. Ziriak, J. M., Smith, K. I., Nelson, D. A., Ryan, K. L., Gajsek, P., D’Andrea, J. A., et al. (2000). Effects of frequency, permittivity, and voxel size on predicted specific absorption rate values in biological tissue during electromagnetic-field exposure. *IEEE Transactions on Microwave Theory and Techniques*, *48*, 2050–2058.
235. Hammersley, J.M., & Handscomb, D.C. (1964). *Monte carlo methods*. London: Chapman & Hall. ISBN:9780412158704.

236. Shi, C.Y. (2004). Development and application of a tomographic model from CT images for calculating internal dose to a pregnant woman. *Dissertation*, Rensselaer Polytechnic Institute, Troy, New York.
237. McGurk, R., Seco, J., Riboldi, M., Wolfgang, J., Segars, P., & Paganetti, H. (2010). Extension of the NCAT phantom for the investigation of intra-fraction respiratory motion in IMRT using 4D Monte Carlo. *Physics in Medicine and Biology*, 55, 1475–1490.
238. Kramer, R. (2010). FASH and MASH: female and male adult human phantoms based on polygon mesh surfaces: II. *Dosimetric calculations*, 163.
239. Caracappa, P. (2006). Development and evaluation of a new algorithm for determining radiation dose to the red bone marrow. *Dissertation*, New York: Rensselaer Polytechnic Institute, Troy.
240. Zhang, J.Y. (2009). A pair of mesh-based phantoms representing ICRP-89 50th-percentile adult males and females for radiation protection dosimetry using Monte Carlo simulations. *Dissertation*, New York: Rensselaer Polytechnic Institute, Troy.
241. Na, Y.H. (2009). Deformable adult human phantoms for radiation protection dosimetry: methods for adjusting body and organ sizes to match population-based percentile data. *Dissertation*, New York: Rensselaer Polytechnic Institute, Troy.
242. Gu, J.W. (2010). Development of CT scanner models for patient organ dose calculations using Monte Carlo methods. *Dissertation*, New York: Rensselaer Polytechnic Institute, Troy.
243. Mille, M. (2013). A study of shape-dependent partial volume correction in pet imaging using ellipsoidal phantoms fabricated via rapid prototyping. *Dissertation*, New York: Rensselaer Polytechnic Institute, Troy.
244. Eckerman, K.F., Stabin, M.G. (2000). Electron absorbed fractions and dose conversion factors for marrow and bone by skeletal regions. *Health Physics*, 78, 199–214.
245. Xu, X.G., Eckerman, K.F. (2009). *Computational phantoms for radiation dosimetry: a 40-year history of evolution. Handbook of Anatomical Models for Radiation Dosimetry*. Boca Raton: Taylor & Francis, 1–40.
246. ICRP (1975). Report of the Task Group on Reference Man. *ICRP Publication 23*. Pergamon Press. Oxford, UK: Pergamon Press.
247. ICRP (2002). Basic anatomical and physiological data for use in radiological protection reference values. *ICRP Publication 89*. Oxford, UK: Pergamon Press.
248. Stabin, M.G., Watson, E.E., Cristy, M., Ryman, J.C., Eckerman, K.F., Davis, J.L., Marshall, D., Gehlen, M.K. (1995). *Mathematical models and specific absorbed fractions of photon energy in the nonpregnant adult female and at the end of each trimester of pregnancy ORNL Report ORNL/TM 12907*. Oak Ridge, TN: Oak Ridge National Laboratory.
249. Chen, J. (2004). Mathematical models of the embryo and fetus for use in radiological protection. *Health Physics*, 86, 285–295.
250. Hough, M., Johnson, P., Rajon, D., Jokisch, D., Lee, C., Bolch, W. (2011). An image-based skeletal dosimetry model for the ICRP reference adult male—internal electron sources. *Physics in Medicine and Biology*, 56, 2309–2346.
251. Xu, X.G., Shi, C.Y. (2005). *Preliminary development of a 4D anatomical model for Monte Carlo simulations Monte Carlo 2005 Topical Meeting*. Chattanooga, TN: American Nuclear Society, LaGrange Park (IL).

Chapter 13

Applications of Computational Phantoms

Bryan Bednarz

13.1 Introduction

Significant progress has been made in the development of computational anthropomorphic phantoms over the last few decades. A historical overview and discussion on computational phantoms can be found in [Chap. 12](#). Such progress would not have been possible without the availability of large amounts of affordable random access memory (RAM). The evolution of computational phantoms from simple spheres to stylized phantoms, and eventually to voxelized phantoms, and beyond can be directly attributed to the capacity to save large amounts of information on a single memory chip as outlined in [Fig. 13.1](#). Furthermore, the increase in allowed transistors per microprocessor has facilitated the integration of highly resolved anthropomorphic phantoms within Monte Carlo codes to simulate human exposure situations for radiation dosimetry applications. As shown in [Fig. 13.1](#), the approximately exponential increase in processing speeds has shadowed the increase in RAM. Historically, the majority of simulations utilizing phantoms were done for health physics applications, but advancements in radiation therapy and imaging have created a need for anthropomorphic phantoms in medicine. As a result, computational phantoms are playing an important and timely role in accessing the amount of absorbed dose received by patients during medical procedures, helping to quantify the overall health impact of these procedures.

The earliest computational phantoms consisted of simple geometric shapes due to the limited amount of memory and speed available in computers at that time. To reduce the computational burden of Monte Carlo simulations, most of the phantoms were homogeneous, composed entirely of water. The most significant contribution from these simple computational phantoms was made to the field of internal medicine. Point and volumetric source distributions in organs were

B. Bednarz (✉)

Department of Medical Physics, University of Wisconsin, Madison, WI 53705, USA
e-mail: bbednarz2@wisc.edu

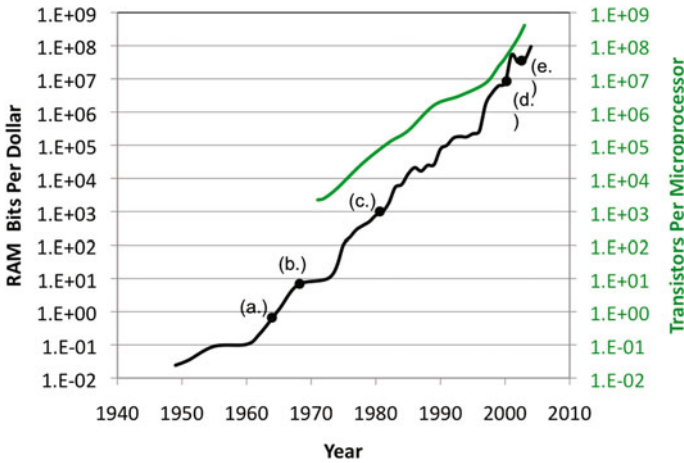


Fig. 13.1 The *left* vertical axis (*black*) plots the RAM bits per dollar available as a function of year [1]. The *right* vertical axis (*green*) plots the transistors per microprocessor as a function of year [1]. Also labeled on the figure are key dates in the evolution of computational anthropomorphic phantoms, including the following: **a** the geometric shape phantoms, **b** stylized phantoms, **c** voxelized phantoms, **d** NURBS phantoms, and **e** BREPS phantoms. See text for definitions

modeled as spheres, cylinders, and disks. For a given photon energy, the absorbed fractions, which is the fraction of emitted energy absorbed in an organ of interest, were calculated using Monte Carlo methods [2]. The absorbed fraction values were then used to estimate the absorbed dose to patients following the delivery of radionuclides during nuclear medicine procedures. The use of absorbed fractions in simple geometric shapes became known as the Medical Internal Radiation Dose (MIRD) method appearing in the first of a series of pamphlets written by the MIRD committee (e.g., see [3]).

Development work on more realistic computational phantoms began as increasingly powerful computers became available. Researchers at Oak Ridge National Laboratory (ORNL) developed an adult phantom that consisted of three distinct regions: a head and neck region, the trunk including arms resting on the side, and the legs [4]. This phantom was known as the “reference man phantom”, since it was based on reference data compiled in ICRP Publication 23 [5]. The original reference man phantom assumed each region was a homogenous mixture of tissue-equivalent material. Soon after, however, 22 organs and more than 100 distinctive sub-regions having the same material composition were defined. Eventually, organ and tissue heterogeneity was included to better represent variations in material composition within these regions. The final version of the phantom developed at ORNL became known as the “MIRD phantom”. The MIRD phantom and phantoms alike are often referred to as “stylized” or “mathematical” phantoms due to the use of surface equations to describe organ and tissue boundaries. The MIRD phantom is considered the first anatomically realistic

computational phantom. It has found an important niche in medicine and health physics being applied to internal and external dosimetry applications. In addition, the MIRDO phantom represents an important transition to anatomically realistic dosimetry, leading the way for more accurate and complex phantoms that would eventually appear decades following its initial release including voxelized phantoms, non-uniform rational B-spline (NURBS) phantoms, and boundary representation (BREP) phantoms.

This chapter is meant to provide an overview of recent and ongoing research projects that have utilized computational anthropomorphic phantoms in health physics and medicine. For more information on the applications of computational anthropomorphic phantoms, the reader should refer to the “Handbook of Anatomical Models for Radiation Dosimetry,” edited by Xu and Eckerman [6].

13.2 Computational Phantoms in Medical Physics

Computational anthropomorphic phantoms have made important contributions to the field of medical physics. For the most part, patient-specific dosimetry efforts are done with limited anatomical data about the patient. For example, radiation therapy uses a segment of the patient body to perform treatment planning dose calculations. Whole-body dose is rarely considered. Likewise, dose from imaging is typically referenced for the length of the body that is included during the scan (e.g., dose-length product) instead of dose to the whole body. This section reviews how computational anthropomorphic phantoms have provided important whole-body dosimetric information about various medical modalities.

13.2.1 Applications to Radiation Therapy

13.2.1.1 The Concern for Dose Outside the Treatment Volume in External Beam Radiation Therapy

The metaphor of a double-edged sword portrays a less-known fact about ionizing radiation’s power to lethally damage cancerous cells. Owing to ever advancing medical technologies, the odds have been steadily improving in the cure of cancer patients treated by radiation alone or combined with surgery and/or systemic therapy (chemical, immunological, and genetic). The radiation can be delivered either internally by means of radioactive sources that are injected near the tumor volume, or externally using high-energy particles to destroy cancer cells or to limit their rate of growth. External beam radiation therapy is the preferred radiation treatment method for most tumor sites.

The main challenge in external beam radiation therapy is to provide the greatest amount of treatment efficacy by delivering a large amount of radiation dose to the

tumor while sparing the dose to healthy tissues adjacent to the tumor. Over its century-long history, external beam radiation therapy has undergone a series of changes in order to address this fundamental challenge. Several types of particles have been used with varying degrees of success, including x-rays, gamma-rays, electrons, protons, neutrons, and heavy ions.

During early radiotherapy treatments, most tumors were treated with single or opposing anterior–posterior and posterior–anterior X-ray fields. Depending on the location of the tumor, the field size was set to a square or irregular shape to avoid high doses to distant internal structures. However, healthy tissue in close proximity to the tumor received very high doses. To help reduce these high doses to adjacent tissues, a technique known as classical conformal X-ray therapy was developed. This technique used patient-specific beam modifiers, such as blocks, wedges, or compensators, to account for changing shapes of the body surface and depth and to conform the radiation beam to the shape of the tumor. In addition, multiple gantry angles were used to spread out the dose to healthy tissue. This was the standard technique used in most clinics up through the 1970s.

X-ray radiation therapy was revolutionized in the early 1970s with the advent of diagnostic imaging modalities. The use of 3D anatomic information from these images led to the development of 3D conformal radiation therapy (3D-CRT). The anatomic information is usually obtained in the form of closely spaced cross-sectional images, which can be processed to reconstruct anatomy in three dimensions. Depending on the imaging modality, visible tumor, adjacent critical structures, and other relevant landmarks are contoured and segmented by outlining the target volumes in each slice with appropriate margins. The segmented anatomy is then implemented into a treatment planning software to design patient-specific fields and beam arrangements. The treatment planning system is used to optimize the dose to the tumor while minimizing the dose to surrounding healthy tissue.

In classical and 3D-CRT, most treatments are delivered with beams that have uniform fluence across the field. In some cases, wedges or compensators are used to modulate the intensity profile to offset irregularities in the tumor contour. It was eventually recognized that spatial modulation of the beam can also be achieved by temporally modulating the fluence within each field and varying the temporal modulation in space [7]. This type of technique is known as intensity-modulated radiation therapy (IMRT), which uses a multileaf collimator (MLC) that dynamically moves in and out of the beam to create a non-uniform fluence across the field. The non-uniform beam is divided into several “beamlets” that enables extra degrees of freedom to deliver the planned dose patterns to the tumor with unprecedented dose escalation and control.

In recent years, proton therapy has also gained momentum with several centers currently operating or being built worldwide. Proton therapy delivers less integral dose deposited in the patient compared to photon therapy while keeping the same amount of prescribed dose to the target volume. This improved conformity near the target region is due to the well-known proton “Bragg peak”, which describes the increase in energy deposition of a proton beam at deeper depths in the body.

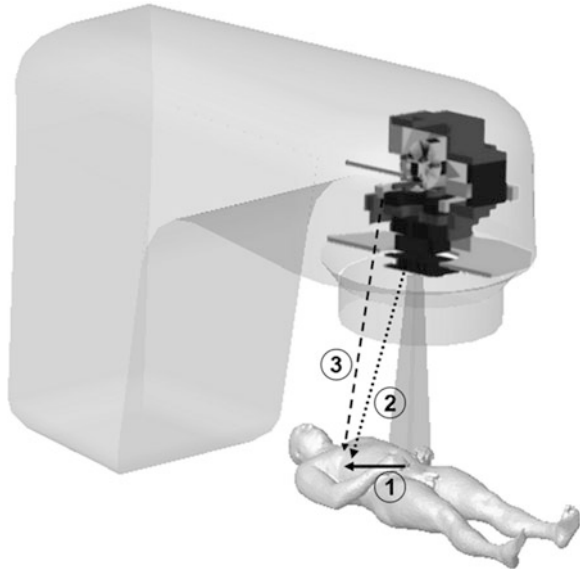
Proton beam therapy is often delivered in one of two modes, passive scattering or beam scanning.

The apparent advantage of healthy tissue dose-sparing in close proximity to the tumor volume provided by both IMRT and proton beam therapy often overshadows the less-known fact that these treatments may result in greater exposures of healthy tissue to intermediate- and low-level doses at increasing distances from the tumor volume compared to older modalities [8–12]. For IMRT, the increase in dose is a consequence of increased “beam-on” time required to deliver the modulated radiation beams used for this treatment, resulting in more leakage radiation that emanates from the medical linear accelerator. In addition, IMRT often uses more fields, which will ultimately expose a larger volume of normal tissues to lower doses. High-energy protons used for proton therapy have the ability to undergo nuclear interactions creating secondary radiation most importantly neutrons. Neutrons are known to be more biologically damaging to tissue compared to photons. These problems incepted a serious and growing concern about radiation-induced second cancers and late tissue injuries among cancer survivors who are now younger and living longer, and thus potentially allowing for such radiation side effects to manifest at a rate faster than ever seen before [8]. A precautionous question remains today: Are we advancing treatment technologies at an ignored latent cost? The history shows that it is prudent to continue to study these radiation treatment technologies as they evolve rapidly in the near future and to develop tools to ensure better tumor control as well as adequate protection of patients against adverse long-term effects.

In a typical radiation treatment that delivers a lethal dose to the tumor, the healthy tissues will inevitably be irradiated by primary and/or secondary radiation at very different levels. Organs adjacent to, near to, and distant from the tumor target can receive high (50 Sv and above), intermediate (5–50 Sv), and low level of equivalent doses (<5 Sv). The dose levels are based on 50 and 5 percentiles of the common total prescribed dose of 100 Gy. Figure 13.2 illustrates the different sources of radiation that contribute to the out-of-field dose in X-ray radiotherapy patients. In regions of high and intermediate dose levels, collimator scatter from the jaws and MLC and patient scatter are predominant sources of radiation dose. In the low-dose-level region, accelerator head leakage is the predominant source of radiation dose. When the primary beam energy is high enough, secondary neutrons are also produced from photonuclear interactions. The threshold energy for photoneutron production lies in the range of 6–13 MeV for most materials. Such neutrons will irradiate the patient uniformly in locations away from the tumor.

The primary contribution to the dose deposited outside of the treatment volume from proton therapy is due to neutrons produced from nuclear interactions in the treatment head and patient. Beam-blocking devices called apertures are the predominant source of neutrons in passively scattered proton therapy. Apertures are used to conform the proton field to the tumor volume and are both patient- and field-specific. Apertures are intentionally made of high-Z materials (e.g., brass), resulting in much of original proton beam being blocked in the device. A fraction of the protons that stop in the aperture will undergo nuclear interactions producing

Fig. 13.2 Contributions of out-of-field photon dose from a medical linear accelerator, which are (1) patient scatter, (2) secondary collimator scatter, and (3) leakage. For high-energy beams neutrons will contribute to the out-of-field dose



a shower of neutrons projected onto the patient. Nuclear interactions also occur in the patient, but with yields that are orders of magnitude less than interactions within the treatment head. Therefore, the neutron dose to patients from passively scattered proton therapy is much greater than dose from beam scanning regimens.

13.2.1.2 The Use of Computational Phantoms to Characterize the Dose Outside the Treatment Volume During External Beam Radiation Therapy

The concern about radiation-induced second cancers and normal tissue toxicity from external beam radiation therapy has led to the use of whole-body computational phantoms to characterize the dose outside of the treatment volume. The original application of computational phantoms for this purpose was to perform dose reconstruction for epidemiological studies on radiation-induced cancer. Stovall et al. [13] performed Monte Carlo simulations to estimate organ doses from conventional radiation treatments for cervical cancer. The group used the MIRD phantom for all of their simulations. Following this work, other groups performed similar dose calculations for conventional radiotherapy using stylized phantoms [14–17].

As the popularity of IMRT increased, the aforementioned concern about the elevated dose to organs outside of the treatment volume from IMRT compared to conventional radiotherapy intensified. To address this concern, several groups performed detailed dosimetric comparisons between the two modalities with measurements or calculations [8]. In combination with a detailed accelerator

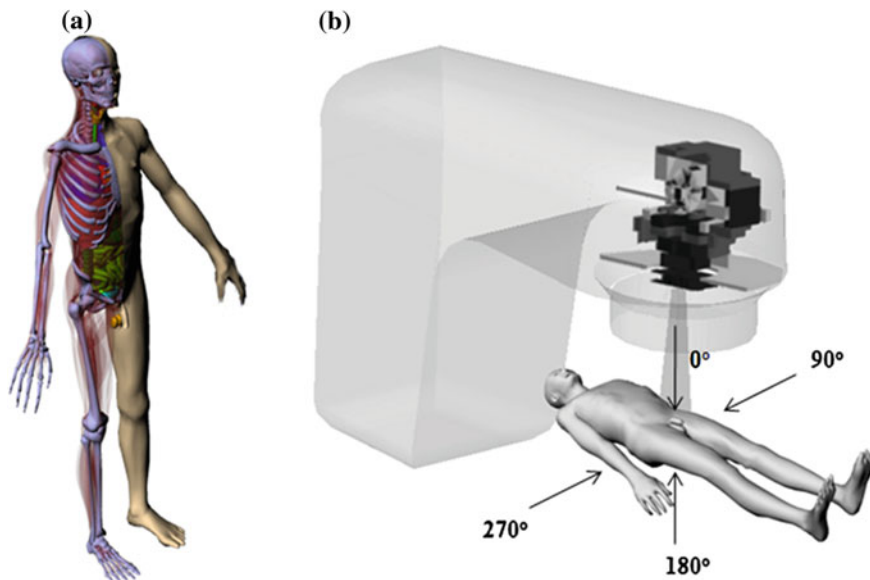
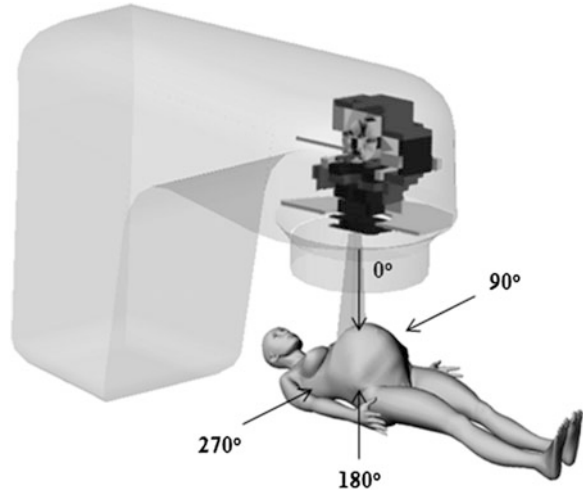


Fig. 13.3 The coupling of (a) RPI Adult Male phantom with (b) a detailed model of the Varian Clinac 2100C in the Monte Carlo Code MCNPX for calculation of dose outside of the treatment volume

model of a Varian Clinac 2100C, Bednarz et al. [18, 19] used the Monte Carlo code MCNPX to calculate organ doses from conventional radiotherapy and IMRT. The group also estimated the radiation-induced second cancer risks to these patients using these volume-averaged organ dose values [20]. The Rensselaer Polytechnic Institute (RPI) Adult Male phantom, consisting of 121 segmented organs, was used for this investigation. Figure 13.3 illustrates the coupling of the detailed accelerator model with the RPI Adult Male phantom.

Another notable application of whole-body computational phantoms is for fetal dose calculations to pregnant patients undergoing external beam X-ray radiotherapy. The number of pregnant patients who undergo radiation therapy has been increasing partially due to the improvements in cancer detection and the tendency for women to delay their pregnancy until later reproductive ages. The safety of the fetus is of particular concern because of its elevated radiosensitivity. Realistic computational phantoms, known as the RPI-P series phantoms, were developed that are compatible with International Commission on Radiological Protection (ICRP) reference values for average pregnant females at the end of 3, 6 and 9-month gestational periods [21]. Combining with the detailed accelerator model discussed above, unshielded [22] and shielded fetal dose [23] were calculated in MCNPX from conventional treatments. A plot of the unshielded treatment setup is provided in Fig. 13.4. Information obtained from these calculations will aid the treatment planning and shielding design process of pregnant patient radiotherapy.

Fig. 13.4 Monte Carlo patient setup using the RPI-P series phantoms for calculating fetal dose from unshielded irradiations of pregnant patients [22]



Whole-body computational phantoms are also used extensively to quantify the neutron dose to patients from proton therapy. The VIP-Man phantom, for example, was used to study neutron dose to patients from passively scattered proton therapy [24]. Simulations were performed using a proton therapy Monte Carlo framework with the code Geant4 that included a detailed model of a passive scattering proton treatment head [25]. This work was later extended to investigate neutron dose to pediatric patients from proton therapy [26]. Pediatric patients have a heightened risk to develop radiation-induced second cancers owing to rapidly proliferating tissues during their development and longer life expectancies to allow for cancers to develop. The UF-series pediatric computational phantoms were used in all simulations. In this study, several proton fields of varying sizes, beam ranges, and modulation widths were considered. Using the same framework, a comparative study was also done investigating the differences in out-of-field dose from proton therapy and IMRT for both adult and pediatric patients [27]. Similar investigations were done using nearly whole-body and partial-body CT scans of proton therapy patients [28, 29].

13.2.2 The Applications to CT Imaging

The number of annual CT examinations has increased from 3.6 million in 1980 to 67 million in 2006 [30]. Although accounting for only 15 % of all medical radiation procedures, CT is responsible for nearly 50 % of the annual effective dose received by Americans. Furthermore, several professional organizations have expressed concern about the recent surge in CT usage [31–34]. It is evident that accurate estimation of organ doses from CT scans is becoming of paramount importance to the radiation dosimetry community.

Stylized computational phantoms have been used extensively to estimate organ doses from CT procedures by means of Monte Carlo simulations. Several software packages have been developed for this purpose such as CTDOSE (<http://www.impactscan.org/index.htm>), CT-Expo [35], and WinDose [36]. CTDOSE is a software tool based on a CT survey done by the National Radiological Protection Board (NRPB) in the United Kingdom. The NRPB survey performed Monte Carlo dose calculations using a stylized phantom with 27 delineated organs or regions based on data gathered from 75 CT scanners operating in the UK at the time. CT-Expo is a similar software package that utilizes survey data gathered in Germany. The WinDose package uses dose data calculated from any single, exposed 1 cm slice thickness for three different beam spectra [36]. For each slice, organ doses were calculated using the adult male and female MIRD phantoms. This data is then extrapolated to estimate the organ dose and effective dose for a variety of different CT procedures. Note, that all of these software packages utilize stylized computational phantoms that do not account for patient-specific size variations. Considering size variations is particularly relevant for pediatric patients who are much smaller than adults. Some authors have assessed organ dose to pediatric patients from CT scans using pediatric stylized phantoms (e.g., see [37]).

More recently, voxel-based phantoms have been used to assess patient doses from CT scans. Demarco et al. [38] utilized the GSF family of voxelized patient models [39, 40] and VIP-man [41] to study the impact of patient size on organ dose from CT scans. All Monte Carlo simulations were performed using the Monte Carlo code MCNPX. Likewise, MCNPX was used by Gu et al. [42] to calculate the fetal dose to pregnant patients from a CT scan delivered by a GE Lightspeed 16. The RPI-P series phantoms representing 3-, 6-, and 9-month gestational stages were used for these computations. The same group also calculated CT organ doses to adult patients using the same scanner model and the RPI-AM and RPI-FM computational phantoms. In addition, a set of realistic body mass index (BMI)-adjustable male and female computational phantoms were developed in order to estimate the CT dose to obese patients [43]. All of the modeling efforts by the RPI group have been integrated into an advanced computational software package for calculating dose from CT scans called VirtualDose [43]. A screenshot of the VirtualDose software is provided in Fig. 13.5.

13.2.3 The Applications to Nuclear Medicine

The use of computational anthropomorphic phantoms in medicine is historically rooted in the development of the MIRD phantom for nuclear medicine dose calculations. Combined with Monte Carlo radiation transport codes, these phantoms were used to generate absorbed fractions for a variety of source and target arrangements. The absorbed fractions were then modified to provide “dose factors” in a series of tables for a variety of radionuclides. For a given source-to-target arrangement, the product of the dose factor and the administered radioactivity would give the absorbed

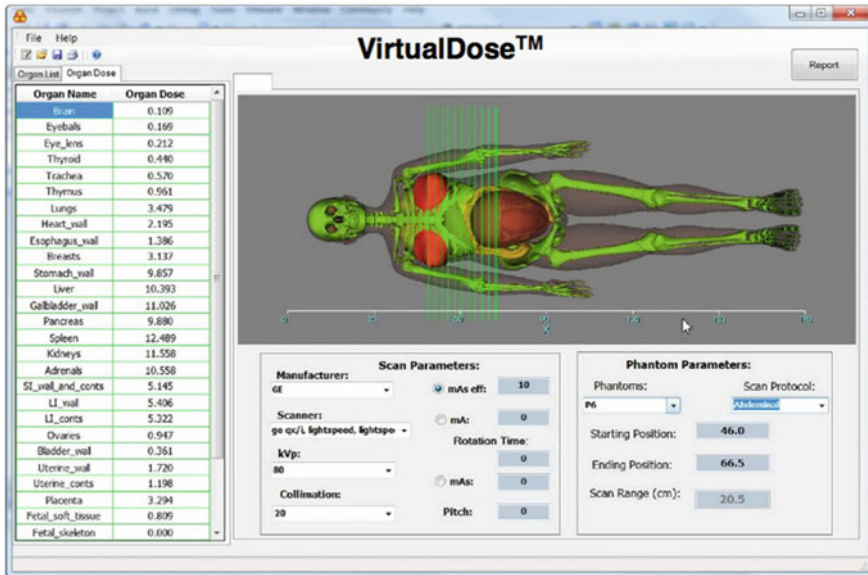


Fig. 13.5 Screenshot of the VirtualDose™ software for calculating absorbed dose from CT scans. Provided by George Xu from Rensselaer Polytechnic Institute

dose to the target. Dose factors are often referred to as dose conversion factors or more commonly as S-values. Eventually, additional stylized computational phantoms were developed to account for individuals of different ages and sizes [44]. While these authors only provided absorbed fractions, S-values from this diverse phantom series were made available in the MIRDOSE software [45].

Likely, the most extensively used software in the nuclear medicine community has been the MIRDOSE software [46]. The MIRDOSE software greatly facilitates the calculation of internal absorbed doses by the MIRD technique. The program utilizes not only the Cristy and Eckerman phantom series, but also a set of stylized computational pregnant phantoms to represent a female during different stages of pregnancy [47]. The program also makes use of the most up-to-date pharmacokinetic models [45]. Recently, the computer code OLINDA/EXM was released as a successor to MIRDOSE. The MIRDOSE contains S-values for 240 radionuclides; the current OLINDA/EXM software contains S-values for over 600 radionuclides. However, despite the vast selection of radionuclides offered to OLINDA/EXM users, the S-values are based on absorbed fractions calculated in stylized computational phantoms. There is an ongoing effort to replace stylized phantoms with anatomically realistic voxelized phantoms to move closer to patient-specific dose calculations.

Several groups have integrated voxelized phantoms into Monte Carlo codes to calculate absorbed fractions for various radionuclides. The VIP-man phantom has been used to calculate absorbed fractions for various electron and photon emitters

[48–50]. Similarly, absorbed fractions from electron and photon emitters were also calculated by Smith et al. [51] using the GSF adult male voxelized phantom. Yoriyaz et al. [52] calculated dose distributions in the Zubal adult phantom [53], but absorbed fractions were not considered in this paper. More recently, several advanced phantoms have been used to calculate absorbed fractions for nuclear medicine procedures including the RPI-AM and RPI-AF phantoms [54], the UF hybrid adult male phantom [55], and the UF hybrid pediatric phantoms [56]. In addition, due to the elevated amount of radiation exposure to pregnant women from diagnostic scanning over the last few years, specific absorbed fractions to the fetus [57] and to newborns [58] have been calculated.

13.3 Computational Phantoms in Health Physics

Computational anthropomorphic phantoms have made important contributions to the field of health physics. This is evident in recent actions by the International Commission on Radiation Protection (ICRP) and the National Council on Radiation Protection and Measurements (NCRP) to transition from radiation protection quantities that depend on dose measured at a point to quantities that depend on dose that is averaged over an entire organ or tissue. A primary example of this transition is the introduction of the quantity known as effective dose equivalent (EDE), which was first proposed in 1977 [59]. This concept was later revised and subsequently named effective dose (E) in 1990 [60] and 2007 [61]. The effective dose is the weighted average of the dose to many organs and tissues in the body. The same value of effective dose can be assumed to produce the same extent of health effects irrespective of the organs or tissues involved in the exposure. Because effective dose cannot be measured directly, the radiation protection community relies on computational phantoms to determine effective dose for a variety of exposure situations. Similarly, radiation quality metrics have also been modified to reflect the shift from pointwise dose quantities to volume-averaged dose quantities. Most notably, the recommending bodies have altered the concept of dose equivalent, which is the dose at a point multiplied by the linear energy transfer (LET) -dependent quality factor ($Q(L)$). The new concept, known as the equivalent dose, is equal to the volume-averaged dose over an organ or tissue multiplied by a radiation weighting factor (w_R). Unlike $Q(L)$, the w_R is not directly dependent on LET. The introduction of effective dose and the modification of the dose equivalent to the equivalent dose demonstrate a paradigm shift taking place from pointwise to volumetric dose quantities and involve the use of computational anthropomorphic phantoms in combination with measurements in radiation protection. The following section overviews applications of computational phantoms in health physics.

13.3.1 Applications to Regulatory Procedures

Although the concept of effective dose recommended by NCRP and ICRP has been established for several decades, the EDE continues to be the primary regulatory quantity used by the US Nuclear Regulatory Commission (NRC) and is defined in the Code of Federal Regulations (CFR). Despite the unwillingness of US regulators to adopt the recent definition, which differs from the EDE by the number and values of tissue-dependent weighting factors (w_T), the effective dose predecessor still relies on volume-averaged organ or tissue doses to properly apply these aforementioned factors. Note, only EDE is referred to when dealing with regulatory quantities.

The EDE is used ubiquitously for regulating radiation from both external and internal radiation fields. As mentioned previously, EDE cannot be measured directly. In the case of external exposures, the effective dose is determined by measuring the occupational quantity known as the personal dose equivalent at a 10 mm depth ($H_p(10)$) by means of a personal dosimeter worn on the chest. In the past, it was assumed that $H_p(10)$ can be used as a direct measure of the effective dose. This consensus was based on measurements in simple spherical phantoms as well as Monte Carlo calculations in the stylized MIRD phantom [62]. As shown in Fig. 13.6, a variety of exposure situations were considered that demonstrated that for most photon energies and irradiation geometries, the ratio of EDE to $H_p(10)$ was between 0.5 and unity [62, 63]. Figure 13.7 diagrams the various irradiation geometries considered in this investigation [63]. However, as shown in Fig. 13.6,

Fig. 13.6 Conversion factor as a function of energy used to determine effective dose equivalent from personal dose equivalent at a 10 mm depth for a variety of different exposure situations. Data extracted from ICRU Report 57 [62]

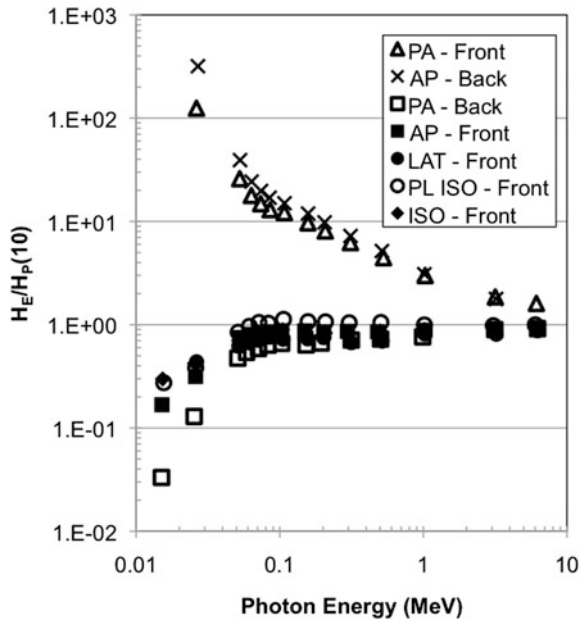
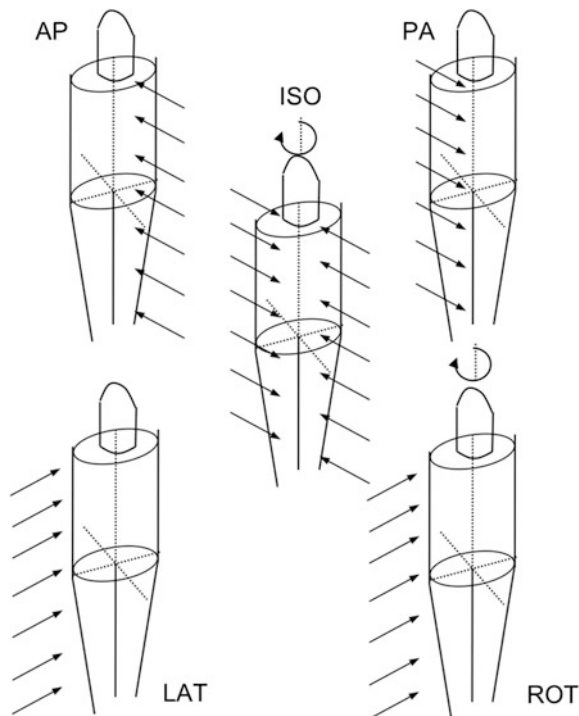


Fig. 13.7 Illustration of exposure situations considered in ICRU 57 [62] used to generate the data provided in Fig. 13.6



the relationship between EDE and $H_p(10)$ is only accurate when the dosimeter that is used to measure $H_p(10)$ is facing the radiation field. For a worker exposed from the back, the measurement of $H_p(10)$ on a chest dosimeter greatly underestimates the EDE.

For these types of generalized exposure situations, several authors have shown that this problem can be addressed with the use of two dosimeters, one placed on the front of the worker and one placed on the back [64–66]. Xu et al. [65] utilized the ICRP-stylized phantom developed by Christy and Eckerman [44] and the Monte Carlo code MCNP to investigate the relationship between effective dose and front and back dosimeters for different irradiation geometries. Based on these calculations, a semi-empirical relationship between the effective dose and the weighted sum of the dosimeter readings was developed. Xu et al. [65] assigned a weighting factor of 0.75 and 0.25 for the higher and lower dosimeter readings, respectively [65, 67]. This relationship is accurate within 11 % for all irradiation geometries considered in their work [65, 67]. We should note while the NCRP acknowledged the relationship developed by Xu et al. in Report No. 122, the council chose to make use of a less accurate relationship derived from simple slab phantoms. Subsequently, Kim et al. [66] used the same stylized phantom but a systematic optimization procedure to determine revised weighting factors for the measured $H_p(10)$. More recently, Kim et al. [68] used a voxelized phantom based

on ICRP reference values to generate a semi-empirical effective dose formulism using the newly released ICRP 103 tissue weighting factors.

EDE from internal exposures is also determined by using computational anthropomorphic phantoms. Most notably, the stylized “family” phantom series developed in the 1980s by Cristy and Eckerman [44] have been used extensively for this purpose in radiation protection. Note, these phantoms are sometimes called “ORNL phantoms” or “ICRP-stylized reference phantoms”. The ICRP methodology for calculating dose from internally deposited radionuclides is essentially the same as the MIRD methodology. However, although they arrive at the same endpoint, the two procedures use different terminology for constructing their formulations. For example, instead of S-values derived from specific absorbed fraction, ICRP uses specific effective energy (SEE). From the SEE values, dose coefficients can be derived, which gives the committed dose equivalent (CDE) to an organ or the committed EDE (CEDE) per unit activity. Therefore, the product of the dose coefficient and the ingested or inhaled activity gives the CDE to a particular organ or tissue or CEDE to the whole body. Using these dose coefficients, it is then possible to determine important regulatory quantities such as the annual limit of intake (ALI) and the derived air concentration (DAC).

Current regulations of occupational exposures rely on dose coefficients that are calculated in the ICRP-stylized reference phantoms [69]. However, there are immediate plans to use the ICRP male and female voxel phantoms to derive internal photon- and neutron-specific absorbed fractions and dose coefficients for occupational intakes of various radionuclides [70].

13.3.2 Applications to Environmental Exposures

The use of computational anthropomorphic phantoms for regulating occupational exposures to external radiation fields was discussed in the previous section. However, a variety of environmental exposures occur when the individuals exposed are not wearing personal dosimeters. In particular, radiation/nuclear accidents might be considered environmental exposure scenarios for which dosimeter data are unavailable. Several groups have derived dose coefficients for environmental exposures from a variety of different radiation fields. Note that dose coefficients from external fields differ from those discussed previously for internal fields in as much as they are typically given in units of dose per unit fluence or dose per unit exposure.

Previously, stylized phantoms have been used to derive dose coefficients from external fields. Initial data were generated using the reference man phantom from exposures to semi-infinite radioactive clouds [71, 72]. Later, the MIRD phantom was utilized to provide organ-specific dose coefficients from submersion in radioactive clouds [73], from planar and volumetric sources on the ground [74, 75], or from both [76].

The first data using voxel phantoms for these types of exposure scenarios were derived from Saito et al. [77] and Petoussi et al. [78]. Both authors used BABY and CHILD, voxel phantoms representing an infant and toddler, to calculate dose coefficients from submersion in a radioactive cloud. These phantoms were developed at the German National Research Center for Environment and Health (GSF, now known as Helmholtz-Zentrum Munchen). Jacob et al. [79] provided additional dose coefficients using these phantoms for submersion and planar and volumetric sources on the ground. Eventually, dose coefficients were calculated by the GSF group in adult male and female phantoms known as ICRP-AM and ICRP-AF. A variety of different source energies and targets were considered [80].

Dose conversion factors in photon, electrons, and neutron fields with geometries shown in Fig. 13.7 have also been derived. An excellent review of the findings from some of initial studies was provided by a joint task group of the ICRP and the International Commission on Radiation Units and Measurements (ICRU) [62]. Several of these studies reviewed by the task group used stylized phantoms for photon [67, 81–83] and neutron [84–90] dose calculations. Eventually, voxelized phantoms replaced stylized phantoms including VIP-man [48, 91, 92], GSF voxel phantoms [40], the Chinese human phantom [93–95], the RPI-P series phantom [96–98], and the RPI-AM and RPI-AF phantoms [99].

13.3.3 Applications to Nuclear Power Plant Exposures

Timely and accurate estimates of absorbed dose to an occupational worker or workers at nuclear power plants are of paramount importance. Unfortunately, Monte Carlo simulations cannot be performed with computational anthropomorphic phantoms because of long simulation times. Computer software tools have been developed to accommodate nuclear power plant health physicists estimate absorbed doses from a variety of exposure situations. A user-friendly software package called PRDC calculates effective dose and absorbed doses to various organs/tissues as well as dosimeters [100]. These quantities are derived from a comprehensive and structured database developed using the Monte Carlo code MCNP- and the MIRD-stylized reference phantoms. Extrapolation between data points is performed in order to quickly provide dosimetric information. Computing time is usually a few seconds or less on a regular personal computer [6].

Another computer program that is available to health physicists in nuclear power plants is known as EPRI EDE Calculator [101]. Figure 13.8 demonstrates the functionality of the EPRI EDE Calculator software. The EPRI EDE Calculator was designed to provide EDE from hot particles. Hot particles, or discrete radioactive particles, are small activation products or fuel fragments ranging between 10 and 250 μm in diameter. Hot particles are rather mobile, and consequently can be found on many parts of a worker's skin or protective clothing. Therefore, the exposure from hot particles results in a highly localized skin dose from beta- and low-energy gamma emitters and a non-uniform whole-body dose

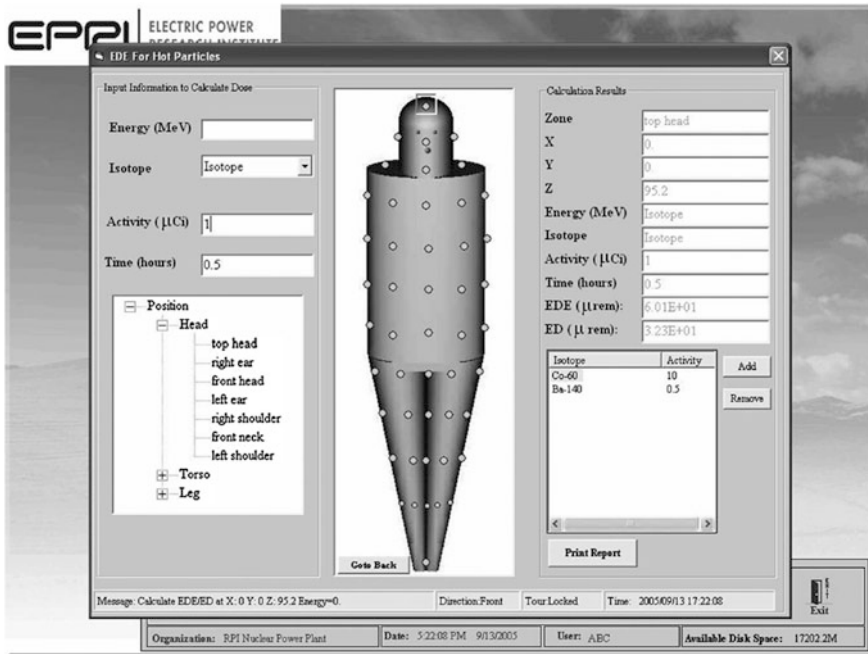


Fig. 13.8 Screenshot of the EPRI EDE Calculator used to calculate EDE and E for hot particles on the skin

from high-energy gamma emitters [6]. The EPRI EDE Calculator considers point sources with photon energies between 0.1 and 2.0 MeV for 74 locations covering the entire body surface. Similar to PRDC, dosimetric data were derived using the MCNP- and the MIRD-stylized reference phantoms. The data structures in the database include location information, energy, EDE, and ED. In addition, there is library of hot particle (i.e., radionuclides) that the user can utilize.

13.4 Discussion

As innovative radiation therapy technologies and techniques become available, it will be imperative to consider possible late effects such as radiation-induced second cancers in addition to acute normal tissue toxicity near the tumor volume, especially in pediatric patients. Due to the limited range of patient image datasets, whole-body computational phantoms may play a greater role in assessing the risk of inducing late effects following radiation therapy. Indeed, in the era of “comparative effectiveness” research, we have already witnessed several studies addressing this issue [20, 27, 102]. Furthermore, current risk models used to estimate second cancer risks from radiotherapy primarily rely on atomic bomb

survivor data, which ill-represents radiotherapy populations. Therefore, there is a need to develop cancer risk models specifically for radiotherapy populations based on past treatments. Retrospective epidemiological studies of this nature necessitate dose reconstruction tools that will rely on computational anthropomorphic phantoms [102].

The alarming increase in CT scans to the US population over the last few decades has fostered concern about the increased absorbed dose associated with these procedures. This unprecedented level of concern has led several professional organizations to join together to form the “Image Wisely” and “Image Gently” campaigns with the objective of lowering the amount of radiation used in medically necessary imaging studies and eliminating unnecessary procedures. In addition, the US Joint Commission has also expressed concern about elevated radiation dose. It appears industry is catching on, as many major companies are now offering low-dose imaging solutions. For example, in 2011 GE, healthcare announced a sizable \$800 million investment in low-dose technologies, including the DoseWatch™ program that tracks, reports, and monitors radiation dose to patients. Based on the overview of CT dosimetry platforms provided in Sect. 2.2.2, it is evident that tracking and monitoring solutions should utilize novel computational anthropomorphic phantoms to provide the most accurate estimates of absorbed dose to the patient.

Furthermore, the growing use of nuclear medicine and molecular imaging raises important questions about elevated radiation dose from these imaging procedures. Due to the nature of these imaging procedures, radioactive material is distributed non-uniformly throughout the body. Therefore, dose assessment from these procedures must rely on computational anthropomorphic phantoms. Evidently, more realistic computational phantoms will help provide more accurate dosimetry data. It is foreseeable that computational anthropomorphic phantoms will also be used for targeted radionuclide therapy (TRT) and radioimmunotherapy (RIT) dosimetry. These therapeutic regimes also involve the distribution of radioactive material throughout the body, but with much higher activities. Therefore, whole-body phantoms could be an exceptional tool to help quantify and optimize the dosimetric regimen for these procedures.

Finally, it is important to recognize the continued use of computational anthropomorphic phantoms in health physics. For the most part, stylized phantoms have been used to predict radiation protection quantities, as discussed in Sect. 1.3. Unfortunately, the implementation of more realistic voxel phantoms has been relatively drawn out. This is primarily due to the contentious interplay between appropriate recommending bodies, regulatory bodies, and the nuclear industry. It is likely that changes to the regulatory framework will occur in forthcoming years, and the use of improved computational phantoms will be reflected in these changes.

The discovery of diverse applications of computational anthropomorphic phantoms has advanced radiation dosimetry in the fields of medical and health physics. It is evident from Chap. 12 that the pace in the development of realistic computational phantoms is accelerating. Accompanying new phantom technology

will have improved dosimetry for the applications in medicine and health physics discussed above. Therefore, these phantoms will only make dosimetry more accurate, helping to ensure the safe and effective use of radiation.

References

1. Kurzweil, R. (2005). *The singularity is near, when humans transcend biology*. USA: Viking/Penguin Books.
2. Reddy, A. R., Ellett, W. H., & Brownell, G. L. (1967). Gamma-ray dosimetry of internal emitters, I. Monte Carlo calculations of absorbed doses for low-energy gamma-rays. *Brit Journal de Radiologie*, 42, 512.
3. Loevinge, R., & Berman, M. (1968). A formalism for calculation of absorbed dose from radionuclides. *Physics in Medicine and Biology*, 13(2), 205.
4. Fisher, H., & Snyder, W. (1967). *Distribution of dose delivered in the body size from a source of gamma rays distributed uniformly in an organ* (p. 245). Oak Ridge, TN: Oak Ridge National Laboratory.
5. ICRP, *Report in the Task Group on Reference Man*, in *ICRP Report 231975*, Oxford, UK: International Commission on Radiological Protection.
6. Xu, X. G., & Eckerman, K. (2010). *Handbook of anatomical models for radiation dosimetry*. Boca Raton, FL: Taylor & Francis Group.
7. Webb, S. (2003). The physical basis of IMRT and inverse planning. *British Journal of Radiology*, 76(910), 678–689.
8. Xu, X., Bednarz, B., & Paganetti, H. (2008). A review of dosimetry studies on external-beam radiation treatment with respect to second cancer induction. *Physics in Medicine and Biology*, 53(13), R193–R241.
9. Followill, D. (1997). Estimates of the whole-body dose equivalent produced by beam intensity modulated conformal therapy (vol 38, pg 667, 1997). *International Journal of Radiation Oncology Biology Physics*, 39(3), 783.
10. Hall, E., & Wu, C. (2003). Radiation-induced second cancers: The impact of 3D-CRT and IMRT. *International Journal of Radiation Oncology Biology Physics*, 56(1), 83–88.
11. Kry, S., et al. (2005). Out-of-field photon and neutron dose equivalents from step-and-shoot intensity-modulated radiation therapy. *International Journal of Radiation Oncology Biology Physics*, 62(4), 1204–1216.
12. Howell, R. M., et al. (2006). Calculation of effective dose from measurements of secondary neutron spectra and scattered photon dose from dynamic MLC IMRT for 6 MV, 15 MV, and 18 MV beam energies. *Medical Physics*, 33(2), 360–368.
13. Stovall, M., Smith, S. A., & Rosenstein, M. (1989). Tissue doses from radiotherapy of cancer of the uterine cervix. *Medical Physics*, 16(5), 726–733.
14. Diallo, I., et al. (1996). Estimation of the radiation dose delivered to any point outside the target volume per patient treated with external beam radiotherapy. *Radiotherapy and Oncology*, 38(3), 269–271.
15. Barquero, R., et al. (2005). Monte Carlo simulation estimates of neutron doses to critical organs of a patient undergoing 18 MV x-ray LINAC-based radiotherapy. *Medical Physics*, 32(12), 3579–3588.
16. Rijkee, A. G., et al. (2006). Assessment of induction of secondary tumors due to various radiotherapy modalities. *Radiation Protection Dosimetry*, 118, 219–226.
17. Mazonakis, M., et al. (2006). Scattered dose to thyroid from prophylactic cranial irradiation during childhood: A Monte Carlo study. *Physics in Medicine and Biology*, 51(8), N139–N145.
18. Bednarz, B., & Xu, X. (2009). Monte Carlo modeling of a 6 and 18 MV Varian Clinac medical accelerator for in-field and out-of-field dose calculations: Development and validation. *Physics in Medicine and Biology*, 54(4), N43–N57.

19. Bednarz, B., Hancox, C., & Xu, X. (2009). Calculated organ doses from selected prostate treatment plans using Monte Carlo simulations and an anatomically realistic computational phantom. *Physics in Medicine and Biology*, 54(17), 5271–5286.
20. Bednarz, B., Athar, B., & Xu, X. (2010). A comparative study on the risk of second primary cancers in out-of-field organs associated with radiotherapy of localized prostate carcinoma using Monte Carlo-based accelerator and patient models. *Medical Physics*, 37(5), 1987–1994.
21. Xu, X. G., et al. (2007). A boundary-representation method for designing whole-body radiation dosimetry models: Pregnant females at the ends of three gestational periods—RPI-P3, -P6 and -P9. *Physics in Medicine and Biology*, 52(23), 7023–7044.
22. Bednarz, B., & Xu, X. G. (2008). A feasibility study to calculate unshielded fetal doses to pregnant patients in 6-MV photon treatments using Monte Carlo methods and anatomically realistic phantoms. *Medical Physics*, 35(7), 3054–3061.
23. Han, B., Bednarz, B., & Xu, X. G. (2009). A study of the shielding used to reduce leakage and scattered radiation to the fetus in a pregnant patient treated with a 6-MV external X-ray beam. *Health Physics*, 97(6), 581–589.
24. Jiang, H., et al. (2005). Simulation of organ-specific patient effective dose due to secondary neutrons in proton radiation treatment. *Physics in Medicine and Biology*, 50(18), 4337–4353.
25. Paganetti, H., et al. (2004). Monte Carlo simulations with time-dependent geometries to investigate effects of organ motion with high temporal resolution. *International Journal of Radiation Oncology Biology Physics*, 60(3), 942–950.
26. Zacharatou Jarlskog, C. (2008). Assessment of organ-specific neutron equivalent doses in proton therapy using computational whole-body age-dependent voxel phantoms. *Physics in Medicine and Biology*, 53(3), 693–717.
27. Athar, B. S., et al. (2010). Comparison of out-of-field photon doses in 6 MV IMRT and neutron doses in proton therapy for adult and pediatric patients. *Physics in Medicine and Biology*, 55(10), 2879–2891.
28. Taddei, P. J., et al. (2009). Stray radiation dose and second cancer risk for a pediatric patient receiving craniospinal irradiation with proton beams. *Physics in Medicine and Biology*, 54(8), 2259–2275.
29. Taddei, P. J., et al. (2010). Risk of second malignant neoplasm following proton versus intensity-modulated photon radiotherapies for hepatocellular carcinoma. *Physics in Medicine and Biology*, 55(23), 7055–7065.
30. Mettler, F. A., et al. (2008). Effective doses in radiology and diagnostic nuclear medicine: A catalog. *Radiology*, 248(1), 254–263.
31. Amis, E. S., et al. (2007). American College of radiology white paper on radiation dose in medicine. *Journal of the American College of Radiology*, 4(5), 272–284.
32. ICRP. (2007). Managing patient dose in multi-detector computed tomography. *Annals of the ICRP*, 37(1), 1–79, iii.
33. McCollough, C., et al. (2008). *The measurement, reporting and management of radiation dose in CT*. College Park, MD: American Association of Physicists in Medicine.
34. NCRP. (2009). *Ionizing radiation exposure of the population of the United States*, Bethesda, MD: National Council of Radiation Protection and Measurements.
35. Stamm, G., & Nagel, H. D. (2002). CT-expo—a novel program for dose evaluation in CT. *Rofo*, 174(12), 1570–1576.
36. Kalender, W. A., et al. (1999). A PC program for estimating organ dose and effective dose values in computed tomography. *European Radiology*, 9(3), 555–562.
37. Khursheed, A., et al. (2002). Influence of patient age on normalized effective doses calculated for CT examinations. *British Journal of Radiology*, 75(898), 819–830.
38. DeMarco, J. J., et al. (2007). Estimating radiation doses from multidetector CT using Monte Carlo simulations: Effects of different size voxelized patient models on magnitudes of organ and effective dose. *Physics in Medicine and Biology*, 52(9), 2583–2597.
39. Petoussi-Hens, N., et al. (2002). The GSF family of voxel phantoms. *Physics in Medicine and Biology*, 47(1), 89–106.

40. Zankl, M., et al. (2002). Organ dose conversion coefficients for external photon irradiation of male and female voxel models. *Physics in Medicine and Biology*, 47(14), 2367–2385.
41. Xu, X. G., Chao, T. C., & Bozkurt, A. (2000). VIP-Man: an image-based whole-body adult male model constructed from color photographs of the visible human project for multi-particle Monte Carlo calculations. *Health Physics*, 78(5), 476–486.
42. Gu, J., et al. (2009). The development, validation and application of a multi-detector CT (MDCT) scanner model for assessing organ doses to the pregnant patient and the fetus using Monte Carlo simulations. *Physics in Medicine and Biology*, 54(9), 2699–2717.
43. Ding, A., et al. (2010). Monte Carlo calculation of imaging doses from diagnostic multidetector CT and kilovoltage cone-beam CT as part of prostate cancer treatment plans. *Medical Physics*, 37(12), 6199–6204.
44. Cristy, M., & Eckerman, K. F. (1987). *Specific-absorbed fractions of energy at various ages from internal photon sources*. Oak Ridge, TN: Oak Ridge National Laboratory.
45. Stabin, M. G. (1996). MIRDose: Personal computer software for internal dose assessment in nuclear medicine. *Journal of Nuclear Medicine*, 37(3), 538–546.
46. Stabin, M., & Bardies, M. (2010). Radiation dose assessment in nuclear medicine. *Handbook of anatomical models for radiation dosimetry*. In X. Xu, & K. Eckerman (Eds.), United Kingdom: Taylor and Francis Group, LCC.
47. Stabin, M., Watson, E., & Cristy M. (1995). *Mathematical models of the adult female at various stages of pregnancy*. (ORNL/TM-12907) Oak Ridge, TN: Oak Ridge National Laboratory.
48. Chao, T. C., Bozkurt, A., & Xu, X. G. (2001). Conversion coefficients based on the VIP-Man anatomical model and EGS4. *Health Physics*, 81(2), 163–183.
49. Chao, T. C., & Xu, X. G. (2001). Specific absorbed fractions from the image-based VIP-Man body model and EGS4-VLSI Monte Carlo code: Internal electron emitters. *Physics in Medicine and Biology*, 46(4), 901–927.
50. Xu, X. G., & Chao, T. C. (2003). Calculations of specific absorbed fractions of the gastrointestinal tract using a realistic whole body tomographic model. *Cancer Biotherapy and Radiopharmaceuticals*, 18(3), 431–436.
51. Smith, T. J., et al. (2001). Impact on internal doses of photon SAFs derived with the GSF adult male voxel phantom. *Health Physics*, 80(5), 477–485.
52. Yoriyaz, H., Stabin, M. G., & dos Santos, A. (2001). Monte Carlo MCNP-4B-based absorbed dose distribution estimates for patient-specific dosimetry. *Journal of Nuclear Medicine*, 42(4), 662–669.
53. Zubal, I. G., et al. (1994). Computerized three-dimensional segmented human anatomy. *Medical Physics*, 21(2), 299–302.
54. Mille, M. N. Y., Zhang, J., Xu, X. G., & Hegenbart, L. (2009). Deformable computational breast phantoms for Monte Carlo based calibrations of detector systems used for assessing internal radioactivity burden in the lungs. *Medical Physics*, 36, 2620.
55. Hough, M., et al. (2011). An image-based skeletal dosimetry model for the ICRP reference adult male—internal electron sources. *Physics in Medicine and Biology*, 56(8), 2309–2346.
56. Lee, C., et al. (2010). The UF family of reference hybrid phantoms for computational radiation dosimetry. *Physics in Medicine and Biology*, 55(2), 339–363.
57. Shi, C., & Xu, X. G. (2004). Development of a 30-week-pregnant female tomographic model from computed tomography (CT) images for Monte Carlo organ dose calculations. *Medical Physics*, 31(9), 2491–2497.
58. Wayson, M., et al. (2012). Internal photon and electron dosimetry of the newborn patient—a hybrid computational phantom study. *Physics in Medicine and Biology*, 57(5), 1433–1457.
59. ICRP. (1977). *Recommendations of the international commission on radiological protection*. Oxford, UK: Pergamon Press.
60. ICRP. (1990). *Recommendations of the international commission on radiological protection, 1991*. Oxford, UK: Pergamon Press.
61. ICRP. (2007). *The 2007 Recommendations of the International Commission on Radiological Protection*. Oxford, UK: Pergamon Press.

62. ICRU. (1998). *Conversion coefficients for use in radiological protection against external radiation*. Bethesda, MD: International Commission on Radiation Units and Measurements.
63. NCRP. (1995). *Use of personal monitors to estimate effective dose equivalent and effective dose to workers for external exposure to low-LET radiation*. Bethesda, MD: National Council on Radiation Protection and Measurements.
64. Lakshmanan, A. R., Kher, R. K., & Supe, S. J. (1991). Estimation of effective dose equivalent using individual dosimeters. *Radiation Protection Dosimetry*, 35, 247.
65. Xu, X. G., Reece, W. D., & Poston, J. W. (1995). A study of the angular dependence problem in effective dose equivalent assessment. *Health Physics*, 68(2), 214–224.
66. Kim, C. H., Reece, W. D., & Poston, J. W. (1999). Development of a two-dosimeter algorithm for better estimation of effective dose equivalent and effective dose. *Radiation Protection Dosimetry*, 81, 101.
67. Reece, W. D., Poston, J. W., & Xu, X. G. (1993). *Assessment of the effective dose equivalent for external photon radiation, volume 1: Calculational results for beam and point source geometries*. Palo Alto, CA: Electric Power Research Institute.
68. Kim, C. H., et al. (2011). Development of new two-dosimeter algorithm for effective dose in ICRP publication 103. *Health Physics*, 100(5), 462–467.
69. Eckerman, K. F., Wolbarst, A. B., & Richardson, A. C. B. (1988). *Limiting Values of Radionuclide Intake and Air Concentration and Dose Conversion Factors for Inhalation, Submersion, and Ingestion*. Washington D.C: U.S. Environmental Protection Agency.
70. Hadid, L., et al. (2010). Application of the ICRP/ICRU reference computational phantoms to internal dosimetry: calculation of specific absorbed fractions of energy for photons and electrons. *Physics in Medicine and Biology*, 55(13), 3631–3641.
71. Poston, J. W., & Synder, W. S. (1974). A model for exposure to a semi-infinite cloud of a photon emitter. *Health Physics*, 26(4), 287–293.
72. Dillman, L. T. (1974). Absorbed gamma dose rate for immersion in a semi-infinite radioactive cloud. *Health Physics*, 27(6), 571–580.
73. O'Brien, K., & Sanna, R. (1976). The distribution of absorbed dose-rates in humans from exposure to environmental gamma rays. *Health Physics*, 30(1), 71–78.
74. Koblinger, L., & Nagy, G. (1985). Calculations on the relationship between gamma source distributions in the soil and external doses. *Science of the Total Environment*, 45, 357–364.
75. Jacob, P., et al. (1986). Effective dose equivalents for photon exposures from plane sources on the ground. *Radiation Protection Dosimetry*, 14, 299.
76. Eckerman, K. F., & Ryan, J. C. (1993). *External exposure of radionuclides in air, water, and soil*. Oak Ridge, TN: Oak Ridge National Laboratory.
77. Saito, K., et al. (1991). Organ doses as a function of body-weight for environmental gamma-rays. *Journal of Nuclear Science and Technology*, 28(7), 627–641.
78. Petoussi, N., et al. (1991). Organ doses for fetuses, babies, children and adults from environmental gamma-rays. *Radiation Protection Dosimetry*, 37, 31.
79. Jacob, P et al. (1990). Calculation of organ doses from environmental gamma rays using human phantoms and Monte Carlo methods, Part II: Radionuclides distributed in the air or deposited on the ground. Neuerberg, Germany: GSF—National Research Center for Environment and Health.
80. Schlattl, H., Zankl, M., & Petoussi-Henss, N. (2007). Organ dose conversion coefficients for voxel models of the reference male and female from idealized photon exposures. *Physics in Medicine and Biology*, 52(8), 2123–2145.
81. Yamaguchi, Y. (1991). *DEEP code to calculate dose equivalents in human phantoms for external photon exposure by Monte Carlo method*. Ibaraki-Ken, Japan: Japan Energy Research Institute.
82. Yamaguchi, Y., & Yoshizawa, M. (1992). *Angular dependence of organ doses and effective dose for external photon irradiation: Proceedings of 8th World Congress International Radiation Protection Association*. International Radiation Protection Association: Montreal, Canada.

83. Yamaguchi, Y. (1994). Dose conversion coefficients for external photons based on ICRP 1990 recommendations. *Journal of Nuclear Science and Technology*, 31, 716–725.
84. Nabelssi, B., & Hertel, N. (1993). Effective dose equivalents and effective doses for neutrons from 30 to 180 MEV. *Radiation Protection Dosimetry*, 48(3), 227–243.
85. Yamaguchi, Y. (1993). Effective dose for external neutron exposure. *Radioisotopes*, 42, 35–36.
86. Stewart, R. D., Tanner, J. E., & Leonowich, J. A. (1993). An extended tabulation of effective dose equivalent from neutrons incident on a male anthropomorphic phantom. *Health Physics*, 65(4), 405–413.
87. Morstin, K., Kopec, M., & Schmitz, T. (1992). Equivalent dose versus dose equivalent for neutrons based on new ICRP recommendations. *Radiation Protection Dosimetry*, 44(1–4), 159–164.
88. Leuthold, G., Mares, V., & Schraube, H. (1992). Calculation of the neutron ambient dose equivalent on the basis of the ICRP revised quality factors. *Radiation Protection Dosimetry*, 40(2), 77–84.
89. Hollnagel, R. (1990). Effective dose equivalent and organ doses for neutrons from thermal to 14 MEV. *Radiation Protection Dosimetry*, 30(3), 149–159.
90. Hollnagel, R. (1992). Calculated effective doses in anthropoid phantoms for broad neutron beams with energies from thermal to 19 MEV. *Radiation Protection Dosimetry*, 44(1–4), 155–158.
91. Bozkurt, A., Chao, T. C., & Xu, X. G. (2000). Fluence-to-dose conversion coefficients from monoenergetic neutrons below 20 MeV based on the VIP-man anatomical model. *Physics in Medicine and Biology*, 45(10), 3059–3079.
92. Bozkurt, A., Chao, T. C., & Xu, X. G. (2001). Fluence-to-dose conversion coefficients based on the VIP-Man anatomical model and MCNPX code for monoenergetic neutrons above 20 MeV. *Health Physics*, 81(2), 184–202.
93. Zhang, G., Liu, Q., & Luo, Q. (2007). Monte Carlo simulations for external neutron dosimetry based on the visible Chinese human phantom. *Physics in Medicine and Biology*, 52(24), 7367–7383.
94. Zhang, G., et al. (2008). The development and application of the visible Chinese human model for Monte Carlo dose calculations. *Health Physics*, 94(2), 118–125.
95. Liu, L., et al. (2009). Organ dose conversion coefficients on an ICRP-based Chinese adult male voxel model from idealized external photons exposures. *Physics in Medicine and Biology*, 54(21), 6645–6673.
96. Taranenko, V., & Xu, X. G. (2008). Fluence-to-absorbed-dose conversion coefficients for neutron beams from 0.001 to 100 GeV calculated for a set of pregnant female and fetus models. *Physics in Medicine and Biology*, 53(5), 1425–1446.
97. Taranenko, V., & Xu, X. G. (2008). Fluence to absorbed foetal dose conversion coefficients for photons in 50 keV–10 GeV calculated using RPI-P models. *Radiation Protection Dosimetry*, 131(2), 159–166.
98. Taranenko, V., & Xu, X. G. (2009). Foetal dose conversion coefficients for ICRP-compliant pregnant models from idealised proton exposures. *Radiation Protection Dosimetry*, 133(2), 65–72.
99. Zhang, J., et al. (2009). RPI-AM and RPI-AF, a pair of mesh-based, size-adjustable adult male and female computational phantoms using ICRP-89 parameters and their calculations for organ doses from monoenergetic photon beams. *Physics in Medicine and Biology*, 54(19), 5885–5908.
100. Kim, C. H., Cho, S. H., & Xu, X. G. (2006). PRDC—a software package for personnel radiation dose calculation. *Radiation Protection Dosimetry*, 118(3), 243–250.
101. Xu, X. G., Su, H., & Bushart, S. (2006). The EPRI EDE calculator—a software package for assessing effective dose equivalent from hot particles on the skin. *Health Physics*, 91(4), 373–378.
102. Newhauser, W. D., & Durante, M. (2011). Assessing the risk of second malignancies after modern radiotherapy. *Nature Reviews Cancer*, 11(6), 438–448.

Index

A

Absorbed dose, 263
Absorbed fractions, 271
Acceptance testing, 91
Accreditation, 116, 129, 130
Acoustic parameters, 162
Acoustic scattering, 166
Acrylic phantoms, 95, 106
AIUM-type 100 ultrasound phantom, 162
Alzheimer's Disease Neuroimaging Initiative Phantom, 187
American College of Radiology, 173, 182, 183
American Institute of Ultrasound in Medicine, 160
Anthropomorphic
Anthropomorphic phantoms, 2, 5, 9–11, 91, 92, 130–133, 151, 152, 169
Attenuation, 165

B

Boundary representation (BREP), 265
Brachytherapy, 77–85
Breast Ultrasound Accreditation Program, 173

C

Calculation, 18, 21, 24, 25, 29–31, 34, 35
Calibration, 18–26, 29, 31, 34
Committed Dose Equivalent (CDE), 276
Committed Effective Dose Equivalent (CEDE), 276
Computational phantoms, 2, 3, 7, 11, 12
Computed tomography, 123, 125, 126, 129, 134, 136

D

Diffusion, 192
Doppler phantoms, 172
Doppler ultrasound, 170
Dose, 226, 229, 230, 236, 239–243, 247–249
Dose conversion factors, 272
Dosimeters, 1, 3–7
Dosimetry, 18–20, 23, 24, 39, 40, 45, 48, 49, 77–80, 84, 85, 143, 147, 150
Dosimetry phantoms, 4, 8–10, 12

E

Effective Dose Equivalent (EDE), 273
External beam radiation therapy, 265

G

Gating, 61–63

H

Heterogeneous, 40, 46

I

Image quality, 127–129, 132, 134–136, 146
Imaging, 77, 79, 81–84
Imaging phantoms, 2, 3, 8, 9, 12
Intensity Modulated Radiation Therapy (IMRT), 266
Interfraction, 54, 55, 58, 59
International Electrotechnical Commission, 160
Intrafraction, 54, 55, 59, 64, 68

L

Leakage, 267
 Linear Energy Transfer (LET), 273
 Localization, 82

M

Magnetic field homogeneity, 189
 Magnetic resonance imaging, 181
 Magphan, 187
 Mammography, 143–153
 MIRDOSE software, 272
 MIRD phantom, 264, 271
 Monte Carlo, 79–81, 226–228, 231, 234, 235, 240, 242, 245, 249, 263
 Motion management, 53, 57, 59, 61
 MRI phantoms, 182

N

National Institute of Standards and Technology, 188
 Non-linear parameter (B/A), 161, 164
 Non-uniform B-spline (NURBS), 265
 Nuclear medicine, 264

O

OLINDA/EXM, 272
 Out-of-field, 268

P

Patient scatter, 267
 Personal dose equivalent at 10 mm depth, 274
 Phannie, 188
 Phantom, 17–36, 39–49, 124–132, 134–136, 143–147, 150–153, 226–242, 244–249
 Alderson, 40–42, 48
 ATOM, 40, 43, 44
 CIRS, 40, 44, 46
 Modus, 46
 RANDO, 40–43, 48
 RSD, 46
 Standard imaging, 46
 Physical phantom, 225
 Prostate motion, 55, 56, 58
 Proton, 48, 49
 Proton therapy, 266

Q

Quality assurance, 26, 34, 53, 59, 66, 67, 94, 96, 119

Quality factor, 273

Quality control, 91

R

Radiation, 17–19, 21–23, 26–29, 31, 34, 35
 Radiation dosimetry, 132
 Radiation-induced second cancers, 270
 Radiation therapy, 263
 Radiation weighting factor, 273
 Radiological Physics Center, 47
 Reference data, 84
 Reference man phantom, 264
 Respiratory motion, 54, 56–58, 60–65, 68
 Relaxation time, 191
 RPI Adult Male, 269
 RPI-P series phantoms, 269

S

Scanning system, 25, 26, 34
 Segmentation, 228, 247, 248
 Setup errors, 54
 Solid water, 28, 34, 35
 Sound speed, 161
 Sources, 77–79, 81
 S-values, 272

T

Temperature dependence, 194
 Test objects, 95, 103–107
 Test tools, 105, 115
 Tissue-dependent weighting factor, 274
 Tissue equivalence, 22, 29
 Tissue equivalent, 1, 2, 4, 6, 7, 39–41, 43–46, 49
 Tissue substitutes, 2, 3
 Tomotherapy, 56, 57, 63
 TM-gel-based phantoms, 163
 Tracking, 55, 58, 61–66
 Training phantoms, 169
 Transducer, 170

U

Ultrasound accreditation program, 173
 Ultrasound phantom, 159
 Ultrasound resolution, 171